UNIVERSITY OF TRENTO
DEPARTMENT OF PHYSICS
Doctoral Programme in Physics
Cycle XXXV

Design of a positron beam for the study of the entanglement in three gamma-rays generated by positronium annihilation

Supervisor
Prof. Roberto Sennen Brusa
Co-supervisors
Prof. Lucio Pancheri
Dr. Sebastiano Mariazzi

Ph.D. Student
Luca Povolo

A Ph.D. Thesis submitted in fulfillment of the requirements
for the degree of Doctor of Philosophy in Physics

Contents

Abbreviations

ACAR	**A**ngular **C**orrelation **A**nnihilation **R**adiation
AE	**A**diabtic **E**xtraction
AEḡIs	**A**ntihydrogen **E**xperiment: **g**ravity, **I**nterferometry, **S**pectroscopy
AWG	**A**merican **W**ire **G**auge
BGT	**B**uffer-**G**as **T**rap
CC	**C**ompton **C**amera
CCD	**C**harge-**C**oupled **D**evice
CERN	**C**onseil **E**uropéen pour la **R**echerche **N**ucléaire
CHSH	**C**lauser, **H**orne, **S**himony, and **H**olt
CMOS	**C**omplementary **M**etal-**O**xide **S**emiconductor
CRT	**C**athode-**R**ay **T**ube
CZT	**C**admium **Z**inc **T**elluride
DBS	**D**oppler **B**roadening **S**pectroscopy
DR	**D**ump **R**elease
EPR	**E**instein, **P**odolsky, and **R**ose
EPRB	**E**instein, **P**odolsky, **R**ose, and **B**ohm
FEM	**F**inite **E**lement **M**ethod
FWHM	**F**ull **W**idth at **H**alf **M**aximum
FWTM	**F**ull **W**idth at **T**enth **M**aximum
GAGG	**G**adolinium-**A**luminum-**G**allium **G**arnet
GHZ	**G**reenberg, **H**orne, and **Z**eilinger
GSOZ	**Z**irconium-doped **G**adolinium **O**xyortho**S**ilicate

HDPE	**H**igh-**D**ensity **P**oly**E**thylene
HPGe	**H**igh-**P**urity **Ge**rmanium
INTEGRAL	**INTE**rnational **G**amma-**R**ay **A**strophysics **L**aboratory
J-PET	**J**agellonian-**P**ositron **E**mission **T**omography
LEED	**L**ow-**E**nergy **E**lectron **D**iffraction
LEPD	**L**ow-**E**nergy **P**ositron **D**iffraction
MCP	**M**icro-**C**hannel **P**late
MFC	**M**ass **F**low **C**ontroller
MUBs	**M**utually-**U**nbiased **B**ase**s**
NAE	**N**on-**A**diabtic **E**xtraction
NC	**N**ormally **C**losed
PALS	**P**ositron **A**nnihilation **L**ifetime **S**pectroscopy
PEEK	**P**oly**E**ther **E**ther **K**etone
PET	**P**ositron **E**mission **T**omography
PMMA	**P**oly(**M**ethyl **M**eth**A**crylate)
PMT	**P**hoto-**M**ultiplier **T**ube
Ps	**P**o**s**itronium
PsICO	**P**o**s**itronium **I**nertial and **C**orrelation **O**bservations
QED	**Q**uantum **E**lectro**D**ynamics
QE-PET	**Q**uantum **E**ntangled - **P**ositron **E**mission **T**omography
RPP	**R**elease with **P**arabolic **P**otential
RW	**R**otating **W**all
SEM	**S**canning **E**lectron **M**icroscope
SEQ	**S**pin **E**xchange **Q**uencing
SiPM	**Si**licon **P**hoto-**M**ultiplier
SpPo	**Sp**in-**Po**larized
SSPALS	**S**ingle **S**hot **P**ositron **A**nnihilation **L**ifetime **S**pectroscopy
TOT	**T**ime-**O**ver-**T**hreshold
UHV	**U**ltra-**H**igh **V**acuum
WGI	**W**hole **G**amma **I**maging

Chapter 1

Introduction

The positron is the antiparticle of the electron. In general, for any particle, there exists a corresponding antiparticle. The two are identical except for the charges, i.e. electric charge, leptonic number, muonic number, ..., which are equal in module but with opposite signs. Thus, while the electron has a negative charge, the positron charge is positive. When a particle and its antiparticle interact all their mass is converted into energy following Einstein's equation $E = mc^2$. This process is called *annihilation*.

The direct annihilation of a positron with an electron generates two photons that, due to the conservation of momentum and energy, are emitted in opposite directions both with 511 keV energy. The direction of emission is random. On the other hand, photons with energy $> 1.022\,\mathrm{MeV}$ can generate a positron-electron couple by interacting with matter. Thanks to the relatively low energy need for their creation, the positrons are the most available antiparticle in the universe, and their characteristic 511 keV annihilation photons have been observed in active galactic nuclei [1], in the sun [2], and even in thunderstorm clouds on Earth [3]. However, in general, the antiparticles are not easily available and the observable universe is mainly composed of matter. From here one of the main unanswered questions of modern physics: given the Big Bang was a high-energy event, it should have generated matter and antimatter in equal quantity, but this symmetry is not observed in the universe around us.

Historically, the positron was the first antiparticle to be observed, its discovery dates back to the 1930s [4, 5]. The bound state of a positron and an electron was first observed in the 1950s [6]. This bound state is called positronium (Ps) and it is the lightest bound matter-antimatter system. It is a hydrogen-like atom, with the positron substituting for the proton. The Ps is not stable, and it has two ground states: para- and ortho-positronium. Para-positronium (p-Ps) is in a singlet spin state $S = 0$ and $m = 0$, where m is the projection of the spin on the z-axis. It annihilates in two counterpropagating photons with 511 keV energy and it has a vacuum lifetime of 125 ps. Ortho-positronium (o-Ps) corresponds to the triplet of spin states $S = 1$ and $m = -1, 0, +1$. It annihilates into three gamma-rays with a lifetime of 142 ns in vacuum. This longer lifetime makes it possible to manipulate the o-Ps level with laser excitation [7], bringing it to longer-lived levels, like 2^3S or Rydberg states, for the study of its properties.

Like in the case of the annihilation of a free positron, the two photons emitted in the p-Ps annihilation have a fixed energy and direction of one with respect to the other, but the emission direction is random. The three photons resulting from the annihilation of o-Ps are emitted on a plane (annihilation plane), with a wide range of energies and direction, the inclination of the annihilation plane is randomly distributed. The conservation of the angular momentum imposes a further constraint on the direction of polarization of the annihilation gamma-rays. For Ps in the ground level, the total angular momentum is given by the spin. For p-Ps and free positrons, the spin conservation imposes that the polarization of a gamma-ray is orthogonal to the polarization of the other [8, 9]. Consequently, the two gammas are expected to be entangled in the degree of freedom of the polarization. For o-Ps, the three gamma polarizations are genuinely multiparticle entangled. The exact entanglement state is expected to depend on the emission direction of the three and from the initial spin state of the o-Ps [10].

The correlation in the annihilation radiation of the two annihilation gammas was first experimentally studied in the 1940s [11–13]. The entanglement in the polarization of the two annihilation gammas is still under investigation [14]. The entanglement in the case of three gammas has never been experimentally attempted. This is due to the complexity of the realization of a detector capable of measuring the polarization of three high-energy gammas at the same time and of a source of positronium in a spin-selected state in a free-field environment (the presence of electromagnetic fields affects the Ps energy levels [15]). This work thesis is centered on the design and study of an apparatus with the objective of studying the entanglement of gamma-ray polarization from the annihilation of ortho-positronium. This apparatus is called PsICO (Positronium Inertial and Correlation Observations) apparatus, and it is under construction at the Antimatter Laboratory (AML) of the Department of Physics of the University of Trento.

With the PsICO apparatus we aim to produce a dense bunched positron beam capable of implanting the positrons in a positron/positronium converter in a field-free region with energy up to tens of kiloelectronvolts. No other positron beamline in the literature satisfies all these requirements. The construction of the PsICO positron beamline is based on four steps:

1. the production of a monoenergetic continuous positron beam,
2. the trapping and cooling of the positrons in a buffer-gas trap (BGT) [16, 17] and the generation of intense bunches of positrons,
3. the extraction of the positron bunches from the magnetic field of the trap,
4. the acceleration and time-compression with a buncher elevator, and the electrostatic focalization of the positron bunches into a positron/positronium converter held in a magnetic and electric field-free region.

Each step corresponds to a stage of the PsICO positron beamline. During this thesis work, all four stages have been designed, the last three stages are now under construction with pieces already in the laboratory, and the first stage has been completed and commissioned.

The production of the monoenergetic continuous positron beam in the first step of the PsICO apparatus requires a radioactive source, a moderator, and a magnetic transport system. The design of this part of the apparatus was based on a previous design from First Point Scientific [18]. The ^{22}Na radioactive source generates positrons with a wide energy distribution. So, a moderator is required to obtain a monoenergetic beam. The beam is magnetically transported to the next section while eliminating the non-moderated positrons that are emitted from the moderator. A solid noble gas moderator, held at cryogenic temperature, is used for the moderation process due to its high efficiency [19]. The speed selection of positrons and their magnetic transport from the moderator to the second stage of the apparatus was optimized by raytracing simulations. From the first stage of the PsICO apparatus, we measured a continuous positron beam with intensities up to $50,000$ positrons per second with a moderator-transport efficiency of 0.2%. Three solid noble gas moderators were tested: Neon, Argon, and Krypton. The advantages and disadvantages of the moderator realized with the three gases were investigated. The commissioning of the continuous positron beam has been completed by measuring the dimension of the beam spot, energy distribution, and polarization at the end of the magnetic transport system.

The second stage of the PsICO apparatus consists of a buffer gas trap (BGT). It is a modified Penning-Malmberg trap, where a 700 G magnetic field confines radially the positrons which are accumulated in an electrostatic potential well along the magnet axis. When the positrons enter the trap, they are cooled by inelastic scattering with gas introduced into the chamber until they fall to the bottom of the potential well. The present design of the BGT presents novelties in the extraction of positron bunches from the 700 G magnetic field into the magnetic field-free region of the buncher-elevator. The positron bunches will be formed in a region with a field homogeneity $\Delta B/B$ better than 0.1%, and the bunches will be released from the trap with a temporal width of less than 5 ns [20].

In the literature, a few configurations for the extraction of positrons from the BGT magnetic field have been proposed and implemented [21–23]. However, the present design is the first one where the positron extraction from the magnetic field is performed directly at the exit of the BGT. According to the simulations of our design, 60% of the positron can be extracted from the magnetic field of the trap [20].

In order to perform the fourth step, a buncher-elevator followed by four lenses has been designed. After the extraction from the BGT, the positrons enter the buncher-elevator whose potential is shaped in 5.5 ns [24]. The final potential is given by a constant voltage bias superimposed by a parabolic potential. The parabolic potential has a height of 1 kV at the start of the buncher-elevator and the vertex at its end, it is required for the time compression of the bunch. The bias gives, instead, the majority of the implantation energy to the positrons and it can reach up to 20 keV [20]. The positron bunch is then focused by the last four lenses onto the target in a spot smaller than 5 mm in diameter and temporal width lower than 2 ns. The focusing point is at 10 cm from the last lens which is kept at ground potential to maintain the region around the positron/positronium converter free from electric and magnetic fields. This will be the first positron beam from a BGT capable of operating at high implantation energy with a positron/positronium converter in a field-free region.

For the study of the entanglement in the polarization of the o-Ps annihilation photons, a good positron/positronium converter is needed. In the literature, there are examples of good converters [25, 26], however, they work in reflection geometry, i.e. they emit Ps on the same side where positrons are implanted. This presents some limitations in the manipulation and study of positronium in vacuum. Positron/positron converters capable of emitting Ps on the other side of the implantation can be found in the literature, but their efficiency is low [27]. So, a new kind of converter has been studied for the production of positronium in transmission [28]. It consists of silicon membranes with a thickness of a few microns where pass-through nanochannels have been electrochemically etched. This kind of converter showed a Ps emission efficiency of at least 16%. After the emission in vacuum, a laser system is required to excite the positronium atoms in a selected spin state in the longer-lived energy level 2^3S. The design and operation of this laser system are outside the scope of this thesis.

The last element needed for the entanglement measurement is the detector. This needs to be capable of measuring the polarization of three gamma-rays at the same time. The only way of measuring the polarization of hundreds of kiloelectronvolts photons is by measuring simultaneously each annihilation gamma and its Compton scattered photon. For each annihilation gamma, the detector has to record the direction and the energy of the annihilation photon and the Compton scattered photon. The measurement of the scattering plane, determined by the annihilation gamma and its Compton scattered photon, allows extracting information about the direction of the polarization of the annihilation gamma. To reconstruct the three polarizations, the detector records six events, this requires a complex detection system. After an extensive study of the literature, we are oriented into the use of modules of plastic scintillators originally developed for PET (Positron Emission Tomography) measurements by a group of the Jagiellonian University (Krakow, Poland) [29]. Two modules have been tested with the continuous positron beam. The two modules were enough to reconstruct the annihilation region with an uncertainty of $\pm 0.26\,\mathrm{cm}$ in the beam direction and of a few centimeters for the other two directions [29]. Further work is needed to test the capability of the two modules in the reconstruction of the polarization of annihilation gammas.

Thanks to all the work done in the design, testing, and implementation of the different components of the PsICO apparatus it makes possible, in the near future, the realization of the first test of entanglement in the polarization of the three gamma-rays generated by annihilation of o-Ps.

The next six chapters are dedicated to the following subjects:

- **Chapter 2:** The physical characteristics and properties of positron and positronium will be briefly described in the first part of the chapter. The second part is dedicated to positron detection, annihilation gammas spectroscopy, and techniques for the measurement of the polarization of positron beams and gamma-rays.

- **Chapter 3:** The entanglement states are explained both in the case of the two and three annihilation gammas. The experiments carried out for the determination of entanglement in the two-gamma case are described.

- **Chapter 4:** The elements for the realization of a continuous positron beam are introduced: positron source, moderator, and transport.

- **Chapter 5:** The design of all four stages of the apparatus is presented highlighting the main elements distinguishing it from existing bunched positron beams.

- **Chapter 6:** The elements composing the first stage of the apparatus are described in the first part of the chapter. In the second part, the characterization of the continuous positron beam is presented.

- **Chapter 7:** A new type of positron/positronium converter in transmission geometry based on nanochanneled membranes is described and its Ps emission is measured. The last part of the chapter is dedicated to the results obtained using two modular J-PET detectors to reconstruct the positron beam spot of the continuous positron beam.

During my Ph.D. work, I designed the PsICO apparatus and performed the raytracing simulations of the positron transport from the moderator to the positron/positronium converter (Chapter 5). I assembled and commissioned the first stage of the apparatus (Chapter 6). Moreover, I actively participated in the development and characterization of transmission positron/positronium converters and in the commissioning of the J-PET (Jagiellonian-PET) detectors for the reconstruction of the beam spot (Chapter 7).

Chapter 2

Positron and Positronium

At the beginning of the XX century, all scientific fields saw great advances. In physics, three great theories were introduced: *Quantum Mechanics* to explain atoms and particles; *General Relativity* to explain the gravitation fields of stars and galaxies; *Special Relativity* to explain the relation between space and time. In this thesis, we are going to talk about positrons, but to introduce them we need to start with quantum mechanics and special relativity, in particular, we start with the first theories to combine them.

Regarding quantum mechanics, it introduced the concept of particle-wave duality, any particle is described in terms of a wavefunction that evolves following the Schrödinger equation:

$$i\hbar\frac{\partial}{\partial t}\Psi = \hat{H}\Psi \tag{2.1}$$

where $\Psi = \Psi[\vec{r},t]$ is the wavefunction of the particle and $\hat{H}$ the Hamiltonian operator of the system. The Hamiltonian can be divided into kinetic and potential components: $\hat{H} = -\frac{\hat{p}^2}{2m} - \hat{U}$, which $\hat{p} = i\hbar\nabla$ the momentum operator and $\hat{U} = \hat{U}[\vec{r},t]$ the potential energy. For free particles $\hat{U} = 0$ and the kinetic energy is associated to $\hat{E} = i\hbar\frac{\partial}{\partial t}$.

Regarding special relativity, the speed of light in vacuum $c = 299792458\,\mathrm{m\,s^{-1}}$ [30] is the same for all observers becoming a limit velocity that can only be reached by particles with zero mass. From the assumptions of special relativity, the total energy of a particle is:

$$E^2 = c^2\vec{p}^2 + m_0^2c^4 \tag{2.2}$$

where $\vec{p}$ is the three-dimensional momentum of the particle of rest mass m_0.

The Schrödinger equation is not valid for high-energy particles, particles with velocities comparable with the speed of light. On the other hand, special relativity does not explain the behavior of the quantum world. The first theories for high-energy particles were developed in the second half of the 1920s' by substituting quantum operators into eq. (2.2). The first example of this operation is the Klein-Gordon equation:

$$\nabla^2 - \frac{1}{c^2}\frac{\partial^2}{\partial t^2}\Psi = \frac{m_0^2c^2}{\hbar^2}\Psi. \tag{2.3}$$

This equation is valid for spinless particles. The next iteration in the process of constructing a combination of the two theories is due to Dirac. He started by factorizing the left part of eq. (2.3) obtaining a relation for the wavefunctions of spin 1/2 particles like positrons and electrons, this results in the Dirac's equation [31]:

$$i\hbar\frac{\partial}{\partial t}\Psi = -i\hbar c(\vec{\alpha}\cdot\vec{\nabla})\Psi \pm m_0c^2\beta\Psi \tag{2.4}$$

in which the rest mass term enters with a plus-minus sign. Considering particles with null-momentum ($-i\hbar c\vec{\alpha}\cdot\vec{\nabla}\Psi = 0$), the previous equation becomes [31]:

$$i\hbar\frac{\partial}{\partial t}\Psi = \pm m_0c^2\beta\Psi \tag{2.5}$$

which permits solutions for particles with negative energies, counterintuitively. Dirac tried to explain the negative energy solution with the introduction of a sea of particles [32]. For example, in the case of electrons, the positive-energy solutions of eq. (2.5) are electrons excited from the sea, and the negative-energy solutions would represent the holes left in the sea by the excited particles [32], similar to the electron-hole theory for semiconductors. While this interpretation is wrong, the negative solutions are associated with special particles with opposite electric charges, these particles were experimentally discovered in the following decades, and we now call them *antiparticles*. In a 1949 paper, Feynman solved this interpretation problem by associating the particles with negative energy to a negative time [33]. Both positive and negative energy solutions are relative to the same particle but, in the first case, the particle propagates forward in time, in the second case, it propagates backward in time, in this way the solutions of eq. (2.5) $\Psi = e^{-i(\pm m_o c^2)t/\hbar}$ have always negative exponent.

To construct the antiparticle from the particle, the charge-conjugation operator $\hat{C}$ was introduced. When it is applied both to particles and to antiparticles it changes one to the other: $\hat{C}\,|Particle\rangle = |Antiparticle\rangle$ and $\hat{C}\,|Antiparticle\rangle = |Particle\rangle$. Specifically, the charge-conjugation operators reverse the particle charges (electrostatic, leptonic, baryonic,...), this particle with reversed charges is called the antiparticle associated with the original particle. Chargeless particles are their own antiparticles and eigenstates of $\hat{C}$, like photons, bosons Z^0, and all metastable particles composed of a particle and its antiparticle. The interaction of a particle and its antiparticle generates a phenomenon called *annihilation*, in which all the energy of the two particles (kinetic, potential, and the rest mass) is converted into energy which goes to form couples of lower energy particle-antiparticles. While, for heavy particles, the annihilation results in a shower of lighter particles, in the case of low-energy light particles, we have mainly the production of photons. In both cases, the annihilations generate particles and their associated antiparticle due to the fundamental conservation laws, in particular, the conservation of all charges, so from the annihilation at least two particles are created: a particle and its antiparticle. In the case of photons, it is its own antiparticle.

From an experimental point of view, the study of antimatter started in the 1930s from the antiparticles of the constituents of the atoms (electrons, protons, and neutrons) and it is continuing today with antiatoms. In 1932, Anderson brought definitive proof of the existence of a particle of the same mass as the electron but opposite charge [4, 5]. By imaging the cosmic rays in a cloud chamber inside a magnetic field, Anderson photographed particles moving in a circular trajectory identical to the electron but in

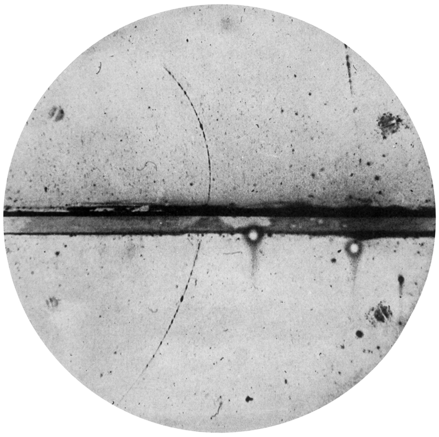

Figure 2.1: One of Anderson's original photographs illustrating the path of a positron in a cloud chamber with a magnetic field. *Image from* [5]

the opposite direction, see fig. 2.1. The positively charged particle was called a positron and it represents the first example of an antiparticle. Anderson won the Nobel Prize in 1936 for this discovery. The discovery of antiproton and antineutron followed much later in the 1950s with the introduction of the first particle accelerators. On the other hand, the first production of an anti-atom, the anti-hydrogen, happened only in 2002 at CERN (Conseil Européen pour la Recherche Nucléaire) by combining a cloud of trapped positrons with a cloud of low-energy anti-protons [34, 35].

2.0.1 Positron

The positron is the lightest stable charged antiparticle and it has mass, electric charge, and spin identical to the electron in module:

- **Rest mass:** $m_0 = 9.10938291(40) \times 10^{-31}\,\mathrm{kg} = 0.510998928(11)\,\mathrm{MeV}$ [30];
- **Charge:** $q = +e = 1.602176565(35) \times 10^{-19}\,\mathrm{C}$ [30];
- **Spin:** $s = 1/2$.

Photons with energy higher than 1.022 MeV, when interacting with material, can produce electron-positron pairs. For this reason since its discovery, evidence of positron presence has been found in many places: astronomical energetic events like black holes and supernovae [1, 36, 37], in stars like our sun [2], and in thunderstorms in Earth's atmosphere [3]. Another advantage of the low mass is in the positron wavelength. At a temperature T (in Kelvin), the De Broglie wavelength of the positron is:

$$\lambda_{DB} = \frac{2\pi\hbar}{\sqrt{3mk_BT}} = (62\,\text{Å})\sqrt{\frac{300}{T}}. \tag{2.6}$$

A positron at room temperature has a De Broglie wavelength of a few nanometers. Thanks to this large De Broglie wavelength, positrons can probe many atomic sizes simultaneously and be trapped in vacancy-like defects. This property makes the positron a good defect probe. It has been demonstrated, in metals, a sensibility to 1 vacancy per

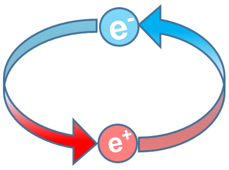

Figure 2.2: Artistic image of a positronium atom

10^7 atoms [38]. Thanks to these characteristics, positrons have been applied in the study of materials for more than sixty years, both to understand the electron density of states and to study the defects of the materials. While studying the positron interaction with materials, it has been observed in particular conditions (see section 2.1.3.1) the bounding of a positron with an electron from the material, the two form an atom-like structure called *positronium* (Ps).

2.0.2 Positronium

If the positron has the same electrostatic charge as the proton, can it form a bound state with the electron like hydrogen? In a 1946 paper, Wheeler proposed the existence of a metastable bound system composed of an electron and its antiparticle, see fig. 2.2, and, in 1951, Deutsch found experimentally this bound system, called positronium [6], and he also discovered that it can annihilate into three gammas [40].

Ps is composed of two spin-1/2 particles, so its total spin can be $S = 0, 1$. Based on the total spin, we call para- (p-) and ortho- (o-) positronium the Ps with total spin $S = 0$ and $S = 1$, respectively. The spin state of a particle $|S, m_S\rangle$ is identified by the total value of its spin S and of the z-component of the spin m_S, so the Ps spin states are:

- $|0, 0\rangle_{Ps}$, the singlet state with antiparallel spins;
- $|1, 0\rangle_{Ps}$, $|1, -1\rangle_{Ps}$, and $|1, +1\rangle_{Ps}$, the triplet states with parallel spins.

The difference between p- and o-Ps is not only reflected in their energy level but also in their lifetimes. From QED (Quantum Electro-Dynamics) calculations, p-Ps has a lifetime in the vacuum of only 125 ps, o-Ps can live in the vacuum much longer with a lifetime of 142 ns [41]. Energy levels of the Ps for principal quantum number $n = 1, 2$ are reported in fig. 2.3 (in the figure like in the rest of the thesis, we follow the standard notation for the atomic levels[1]).

Given the same mass of the two particles composing the positronium atom, the hyperfine structure makes the behavior of p- and o-Ps completely different. To analyze

---

[1] A Ps level is indicated with $n^{2S+1}L_J$ (sometimes the J is omitted), where:

- n is the principal quantum number, $n = 1, 2, 3, ...$;
- S is the total spin, so $2S + 1 = 1, 3$;
- L is the orbital angular momentum reported with letters of the alphabet, $L = 0 \rightarrow S$, $L = 1 \rightarrow P$, ...;
- J it the total angular momentum $\vec{J} = \vec{S} + \vec{L}$.

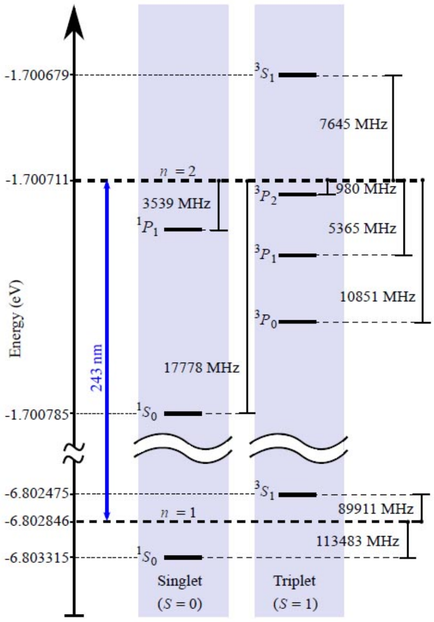

Figure 2.3: Energy level diagram of Ps states up to $n = 2$. The frequencies between each energy level are shown. *Image from* [42].

this, we compare Ps to hydrogen. Both systems are composed of two particles of opposite elementary electrostatic charges, the main difference is in their masses. The reduced mass $\mu = \frac{m_1 m_2}{m_1+m_2}$ of the hydrogen is about double the one of the Ps: $\mu_H = 2\mu_{Ps} \approx 2\,m_0/2$. Considering this correction factor, we can obtain in first approximation the energy of Ps levels as:

$$E_n = \frac{-\alpha^2 mc^2}{4n^2} = -6.803\,\mathrm{eV}n^2 \tag{2.7}$$

where α is the fine-structure constant. This calculation is valid at the first order of α^2, at the next order of α^4 we need to consider corrections due to relativistic effects ($-\frac{5}{64}\alpha^4 mc^2$ for both p- and o-Ps) and due to the spin-spin interaction of the two particles [7]. This last correction is $-\frac{1}{4}\alpha^4 mc^2$ for $S = 0$ and $+\frac{1}{12}\alpha^4 mc^2$ for $S = 1$. In the case of Ps, we have to consider another correction that is not present in hydrogen: the virtual annihilation term. This correction applies only to o-Ps rising its ground energy level by $+\frac{1}{4}\alpha^4 mc^2$. In conclusion, the total split ΔE between the energy of the para- and ortho-positronium in the ground state results [7]:

$$\Delta E = E[1^3S_1] - E[1^1S_0] = E_T - E_S = \frac{7}{12}\alpha^4 mc^2 = 0.84\,\mathrm{meV} = 203\,\mathrm{GHz} \tag{2.8}$$

which is ~ 200 times the hyperfine split in hydrogen.

Figure 2.3 shows the position of another important level in the study of Ps physics: the 2^3S. The Ps in this state is metastable because it cannot relax into the $n = 1$ states through the spontaneous emission of electromagnetic radiation, it can only annihilate.

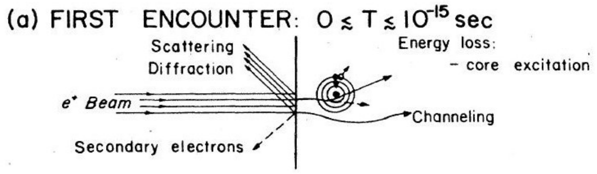

Figure 2.4: Scheme of the first interaction of a positron beam ($E \leq 100\,\mathrm{keV}$) with a material near the surface. *Image from* [51].

Because the distance between the particle and antiparticle increases with the quantum number, it has a lifetime of 1.14 µs, much higher than the 142 ns of the 1^3S level.

Ps is the lightest bound system being formed by two leptons. This characteristic makes Ps the perfect tool for many experiments on fundamental physics to explore the limits of the existing theories in search of new physics. Precise spectroscopy of Ps levels can be used to study the limits of QED [7, 43]. The photons emitted by the annihilation of Ps are used to study the CPT symmetry ($\hat{C}$ charge-conjugation operator, $\hat{P}$ parity operator, $\hat{T}$ time inversion operator) in the leptonic sector [7, 44, 45]. Another important field of study is the interaction of antimatter with forces generated by matter, in particular, the gravitational interaction is of fundamental importance to understand why the universe is composed mainly of matter. It has been proposed the use of Ps in Rydberg states (states with $n \gg 1$) or in 2^3S level to measure the gravitation fall of this system [46–49].

2.1 Positronium Production

This thesis deals with the design of a bunched positron beam for the production of positronium. Ps can be formed by the interaction of positrons with materials. In this section, we analyze the interaction of a mono-energetic positron beam with a material: its implantation, thermalization, diffusion, and finally annihilation with an electron of the medium or Ps formation. We consider beam energy $E < 100\,\mathrm{keV}$. This condition is respected by almost every positron beamline for material study and Ps production.

2.1.1 Implantation

First of all the positrons interact with the surface of the material. As seen in fig. 2.4, the first results of this interaction are:

- some positrons scatter from the surface;
- electrons are emitted into the vacuum (secondary electrons).

Both phenomena give information about the surface of the material. One technique is the Low-Energy Positron Diffraction (LEPD) and it is derived from the electron analogous LEED (Low-Energy Electron Diffraction). The secondary electrons can, instead, be used as the starting signal for the interaction of the positron with the material [50].

The positrons surviving the surface interaction are implanted into the material. They start to lose energy by inelastic scattering.

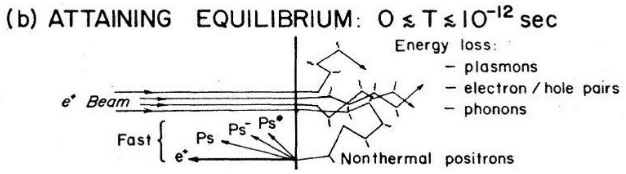

Figure 2.5: Scheme of the thermalization of the positrons after their implantation. *Image from* [51].

2.1.2 Thermalization

As soon as the positrons enter the material, they start to lose energy by interacting with its structure (see in fig. 2.5). The processes with which the positrons lose energy depend on the type of material. In all cases, the energy loss is a fast process, lasting a few picoseconds, after which the positrons are considered thermalized with the material. In more detail, the energy loss processes are:

- **Metals:** At high energy, atomic ionization is the preferred process. Then, as the positrons lose more of the implantation energy, electrons, plasmons, and phonons excitation become the preferred inelastic scattering processes, bringing the final positron energy to quickly equalize the one of the material. For example, in aluminum at 300 K the thermalization time for 1 keV positrons is 6.8 ps [52].
- **Semiconductor:** At high energy the most important process of energy loss is electron excitation. This process dominates for energy higher than a few electronvolts corresponding to the energy gap between the valence and the conduction band of the material. At energy lower than the band gap, electron excitation is no longer possible, and phonon excitation becomes the main thermalization process.
- **Insulator:** The bigger energy gap between the conduction and valence band limits the energy loss process from electron excitation, while at lower energy the thermalization process is not as efficient as the previous two cases.

As seen in fig. 2.5, during the thermalization, non-thermal positron can reach the surface and escape into the vacuum. These positrons are called *epithermal positrons.* Through Monte-Carlo simulations, it is possible to obtain a pretty good analytical approximation of the depth profile for thermalized positrons, which is approximate with Makhovian distributions [53–55].

2.1.2.1 Profile

The profile of thermalized positrons implanted with an energy E is approximately given, as a function of the depth z, by [53–55]:

$$P[z,E] = -\frac{d}{dz}e^{-(z/z_0)^m} = \frac{mz^{m-1}}{z_0^m}e^{-(z/z_0)^m} \tag{2.9}$$

where

$$z_0 = \frac{\bar{z}}{\Gamma[\frac{1}{m}+1]} \tag{2.10}$$

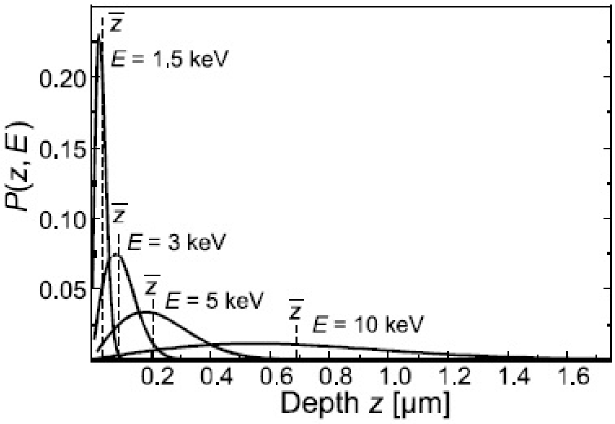

Figure 2.6: Implantation depth profile calculated for different implantation energy in Si. At each energy, the mean implantation depth $\bar{z}$ is indicated by vertical dashed lines. *Image from* [38].

with the gamma function $\Gamma[x] = \int_0^{+\infty} t^{x-1} e^{-t} dt$ and the mean implantation depth $\bar{z} \propto E^n$. In eq. (2.9), m is a parameter of the simulations which in general is set to $m \approx 2$, so the profile $P[z, E]$ becomes:

$$P[z,E] = \frac{\pi z}{2\bar{z}^2} e^{-\frac{\pi}{4}\left(\frac{z}{\bar{z}}\right)^2}. \tag{2.11}$$

The $\bar{z}$ in the previous expression is expressed based on experimental measurements. Two formulas, that are used to approximate the mean implantation depth $\bar{z}$ (in nm) in different material structures, are:

- **Crystal:** $\bar{z} \approx \frac{40}{\rho} E^{1.6}$ [51];
- **Amorphous.** $\bar{z} \approx \frac{28.1}{\rho} E^{1.71}$ [51].

For both expressions, the implantation energy E is given in keV, and the material density ρ is expressed in $\mathrm{g\,cm^{-3}}$. As an example, the implantation profile $P[z, E]$ and the calculated $\bar{z}$ in Si are shown for different implantation energies in fig. 2.6. An increase in the positron implantation energy results in an increase in the mean implantation depth and in the broadening of the distribution.

2.1.3 Diffusion

After thermalization, the positrons do not annihilate immediately, but they start diffusing into the material (see fig. 2.7). This diffusion process is described through the time evolution of the positron density $n[\vec{r}, t]$ as calculated by:

$$\frac{\partial n[\vec{r},t]}{\partial t} = D_+ \nabla^2 n[\vec{r},t] - \Gamma_{bulk}^{eff} n[\vec{r},t] - \frac{\partial}{\partial r}(v_d\, n[\vec{r},t]). \tag{2.12}$$

The first term on the right of eq. (2.12) describes the diffusion of positron with a diffusion coefficient D_+. The second term of the equation represents the annihilation rate of the positron while diffusing in the bulk of the material. The effective rate of this

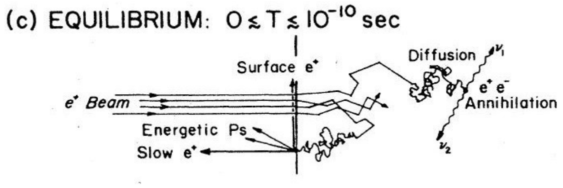

Figure 2.7: Scheme of the diffusion of the positrons after their thermalization. *Image from* [51].

annihilation $\Gamma_{bulk}^{eff} = (\tau_{bulk}^{eff})^{-1}$ (τ represents lifetime, Γ rates) depends on the characteristics of the particular target in which the positrons have been implanted, see section 2.1.4. The last term on the right of eq. (2.12) takes into account the presence of external electromagnetic fields which introduce a drift velocity v_d on the positrons.

For the solution of the diffusion equation (eq. (2.12)), it is necessary to set the boundary conditions related to the trapping rate at the surface and the initial positron density distribution. Regarding the surface, we have at $z = 0$ the possibility to trap with a rate ν the positrons which diffuse from the bulk:

$$D_+ \nabla n[\mathbf{r}, t]|_{z=0} = \nu\, n[0, t] \tag{2.13}$$

Regarding instead the starting density function, as seen in section 2.1.2.1, it is given simply by the implantation profile of the positrons:

$$n[z, 0] = P[z, E]. \tag{2.14}$$

So once thermalized, the implanted positrons have a depth profile $P[z, E]$ given by eq. (2.11), then they start to diffuse in the surrounding material following eq. (2.12). During the diffusion, the positron acts as a probe exploring the volume around the thermalization point. The dimensions of this volume depend on the characteristics of the material with values between tens to hundreds of nanometers. The dimension of the probed volume is characterized by the diffusion length L_+:

$$L_+ = \sqrt{D_+ \, \tau_{bulk}^{eff}}. \tag{2.15}$$

The positron diffusion length brings advantages and disadvantages. A longer L_+ makes positrons capable of exploring greater volume in the material, but at the same time limits the spatial resolution of the positron as a probe.

2.1.3.1 Ps Formation

When a positron interacts with the material, it can take an electron and form Ps, as we discussed in section 2.0.2. Ps formation can happen on the surface or in the material bulk in order to transfer the excess momentum from the initial positron and electron to the atomic structure. While only some materials can have formation in bulk, Ps production on the surface is possible in metals, semiconductors, and insulators.

In any case, to have Ps formation, the process needs to reduce the energy level of the system, i.e. the system with Ps is in a lower energy state than the one with the unbound electron and positron. We now briefly analyze the process of Ps formation on the surface

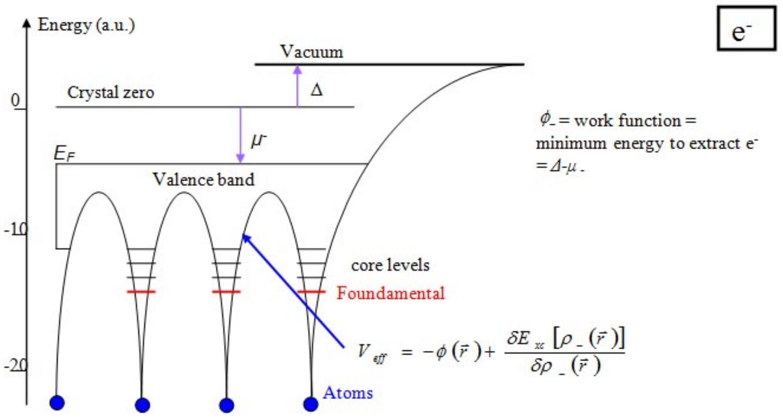

Figure 2.8: Schematic of the electron energy levels near the surface of a metallic crystal, the main parameters are indicated (for explanation see text). *Image from* [56].

using the energy levels for a metallic crystal which are shown in fig. 2.8 for electrons and fig. 2.9 for positrons. The fundamental parameters to consider are:

- **E_F:** Fermi energy, the maximum level of the band structure filled by electrons at $T = 0\,\mathrm{K}$.
- **Crystal Zero:** the average of the electrostatic potential in the infinite crystal.
- **Vacuum Level:** the energy of a particle infinitely distant from the crystal.
- **$\mu^{\pm}$:** chemical potential, $\mu^{-} = E_F -$ Crystal Zero and $\mu^{+} = E_{+} -$ Crystal Zero.
- **Δ:** surface dipole, $\Delta =$ Crystal Zero $-$ Vacuum Level.
- **$\phi_{\mp}$:** electron/positron work function, $\phi_{\mp} = \pm\Delta - \mu_{\mp}$.

In particular, the work function represents the energy needed to extract the particle from the material. ϕ_{-} is always negative, we need to use energy to extract electrons from the material. In the case of positrons, we can have materials with a positive work function, $\phi_{+} > 0$. This property is used in the creation of monoenergetic beams (see chapter 4) [51].

To form Ps, we need to consider the energy to extract the positron and the electron, and the energy to bind them together. With respect to the vacuum level, the binding energy is given by eq. (2.7) (in the following we consider only Ps in the ground state $n = 1$): $E_1 = -6.8\,\mathrm{eV}$. Then the Ps formation potential ϵ_{Ps} is defined as [51]:

$$\epsilon_{Ps} = \phi_{+} + \phi_{-} - 6.8\,\mathrm{eV}. \tag{2.16}$$

Looking at this formula, only if $\epsilon_{Ps} < 0$, we can have Ps formation, and the energy of the formed Ps is $-\epsilon_{Ps}$. In metals and semiconductors, this condition can be satisfied only at the material surface. On the material surface, a contribution to the Ps formation can arise from the positron trapped on the surface potential. In the right conditions, these positrons are thermally detraped as Ps contributing to the total emission of positronium from the material surface [57].

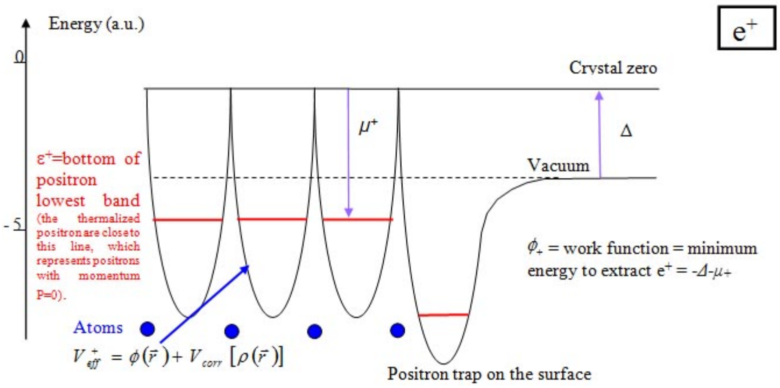

Figure 2.9: Schematic of the positron energy levels near the surface of a metallic crystal, the main parameters are indicated (for explanation see text). *Image from* [56].

Ps formation in the bulk is possible only in insulators where the electron density is lower compared to metals and semiconductors. Once formed into the bulk, Ps diffuse and can reach the surface, so we have to consider the Ps work function ϕ_{Ps} as defined in [51]:

$$\phi_{Ps} = \phi_+ + \phi_- + E_{Bind} - 6.8\,\mathrm{eV} \tag{2.17}$$

where E_{Bind} represents the electron-positron binding energy in the bulk. As for $\phi_{\mp}$, if $\phi_{Ps} < 0$, Ps reaching the material surface is emitted into vacuum with energy ϕ_{Ps}. In the bulk, it is possible to have Ps formation during the thermalization of the positrons, there are two particular processes in which this can happen:

- **Spur:** the positron is cooled down to $30 - 100\,\mathrm{eV}$ by electron excitation, then it bounds to one of the excited electrons to form Ps [58];
- **Ore:** the positron is cooled to $5 - 10\,\mathrm{eV}$ then it ionizes an atom forming Ps with the freed electron [59].

2.1.4 Annihilation

The positron is a stable particle but its lifetime can be unlimited only in vacuum where it does not interact with any electron. On the opposite, when implanted in a material, the final fate of positrons is always the annihilation with an electron of the medium (see fig. 2.10). The annihilation lifetime τ and the rate $\Gamma = \tau^{-1}$ depend on the electron density in the surrounding of the positron:

$$\Gamma = \frac{1}{\tau} = \pi r_0^2 c \int \rho_+[\vec{r}]\rho_-[\vec{r}]\gamma[\rho_+, \rho_-]d\vec{r} \tag{2.18}$$

where $r_0 = 2.82 \times 10^{-15}\,\mathrm{m}$ is the electron classical radius, ρ_+ and ρ_- are the positron and electron density respectively, and $\gamma[\rho_+, \rho_-]$ is the *enhancement factor* that describes the enhancement of electron density around a positron [60].

In general, we can identify two main annihilation paths for the implanted positrons: as free or as bound to electrons (i.e. Ps).

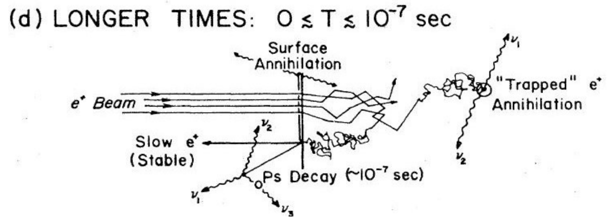

Figure 2.10: Final stage of the interaction, the annihilation of the positrons. *Image from* [51].

2.1.4.1 Positron Annihilation

If the positron annihilates not in the form of Ps, its lifetime depends only on the distribution of the electrons in the material. The material electron density depends on two factors: material composition and open volumes. A negatively charged vacancy, for example, can trap the positron, increasing its lifetime in the material. For each kind of defect, the positron trapping probability is given by the trapping rate $\kappa_i = c_i \mu_i$ which is a function of the concentration of the defect type c_i and its specific trapping rate μ_i. In fig. 2.11, the positron lifetime calculated in pure elements without defects is reported [61]. The lifetime for positrons in a general material, also called *effective lifetime* τ^{eff}, is a combination of the annihilation rate for the defect-free material Γ_{bulk} and the contribution from the defect on the real material:

$$\Gamma^{eff} = \frac{1}{\tau^{eff}} = \Gamma_{bulk} + \sum_i \kappa_i. \tag{2.19}$$

The annihilation of an unbound positron produces a couple of photons. Energetically, the positron is thermalized $E_+ = 0.025\,\text{meV}$ ($T = 300\,\text{K}$), and the electron energy E_- is of the order of few eV, so the main contribution to the photon energy is the rest mass of the particles $m_0 = 511\,\text{keV}$. In the reference system of the center of mass of the two particles, the two photons are emitted at an angle 180° one respect to the other, and both with an energy of $E_\gamma = 511\,\text{keV}$ for the conservation of the energy-momentum in the annihilation process.

Both the electron and the positron have energy and momentum which are not zero in the laboratory reference frame. Then, the measured photon energy is shifted with respect to $m_0 c^2$ by up to a few eV, and the two gammas are not aligned anymore. The major contribution to this shift and misalignment is given by the electrons which are more energetic. By measuring the shift of the energy related to momentum or the angle between the emitted gammas, we can measure the momentum distribution of the electrons [51].

2.1.4.2 Positronium Annihilation

The Ps annihilation can happen in three ways (here we neglect external magnetic fields, their effect on the Ps annihilation will be discussed in section 2.1.6):

- **Self-annihilation:** the positron annihilates with the bounded electron. The lifetime corresponds to the one in vacuum as seen in section 2.0.2, 125 ps for p-Ps and 142 ns for o-Ps.

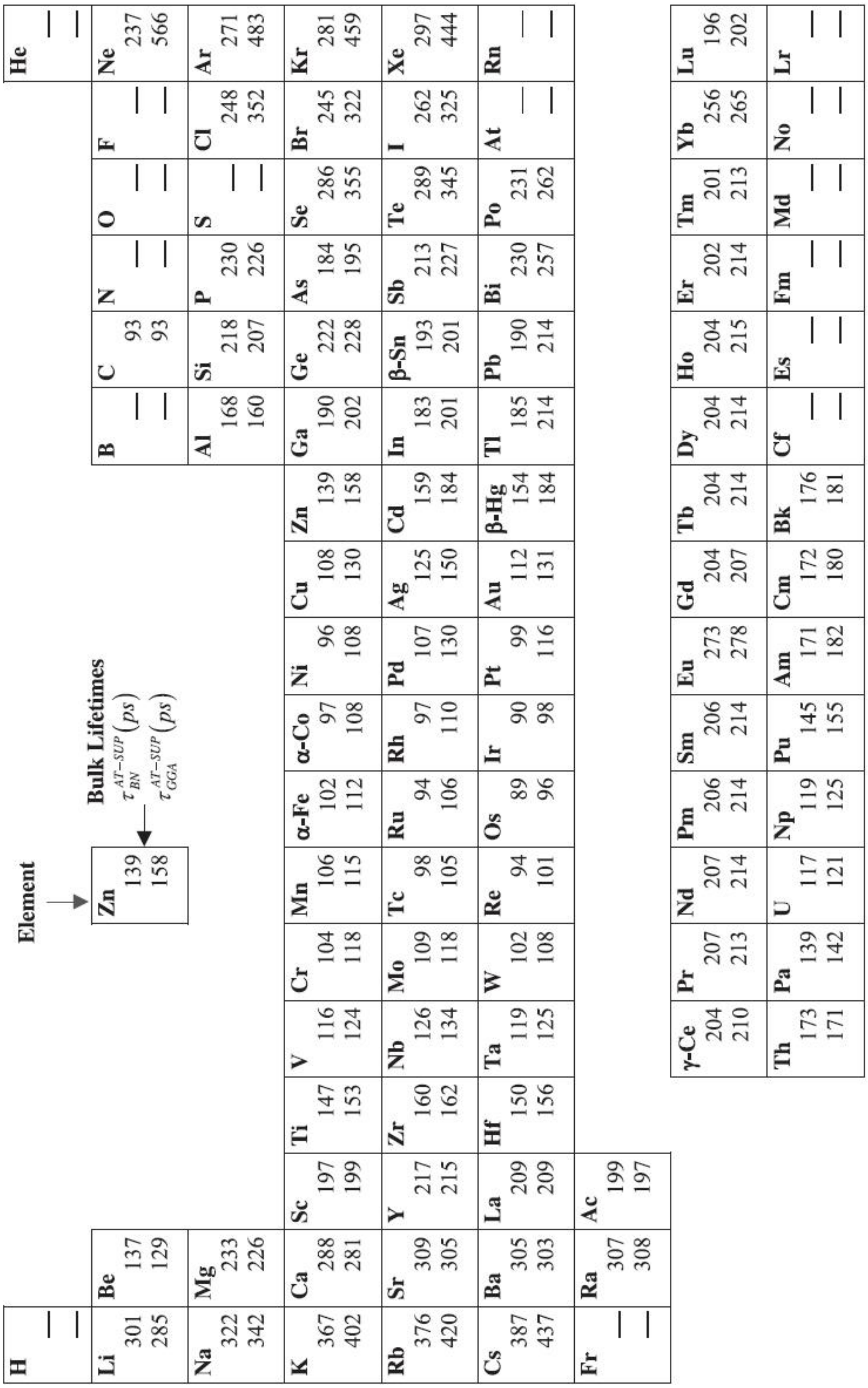

Element

Bulk Lifetimes

$\tau_{BN}^{AT-SUP}(ps)$

$\tau_{GGA}^{AT-SUP}(ps)$

Element	$\tau_{BN}^{AT-SUP}(ps)$	$\tau_{GGA}^{AT-SUP}(ps)$
H	—	—
He	—	—
Li	301	285
Be	137	129
B	—	—
C	93	93
N	—	—
O	—	—
F	—	—
Ne	237	566
Na	322	342
Mg	233	226
Al	168	160
Si	218	207
P	230	226
S	—	—
Cl	248	352
Ar	271	483
K	367	402
Ca	288	281
Sc	197	199
Ti	147	153
V	116	124
Cr	104	118
Mn	106	115
α-Fe	102	112
α-Co	97	108
Ni	96	108
Cu	108	130
Zn	139	158
Ga	190	202
Ge	222	228
As	184	195
Se	286	355
Br	245	322
Kr	281	459
Rb	376	420
Sr	309	305
Y	217	215
Zr	160	162
Nb	126	134
Mo	109	118
Tc	98	105
Ru	94	106
Rh	97	110
Pd	107	130
Ag	125	150
Cd	159	184
In	183	201
β-Sn	193	201
Sb	213	227
Te	289	345
I	262	325
Xe	297	444
Cs	387	437
Ba	305	303
La	209	209
Hf	150	156
Ta	119	125
W	102	108
Re	94	101
Os	89	96
Ir	90	98
Pt	99	116
Au	112	131
β-Hg	154	184
Tl	185	214
Pb	190	214
Bi	230	257
Po	231	262
At	—	—
Rn	—	—
Fr	—	—
Ra	307	308
Ac	199	197
γ-Ce	204	210
Pr	207	213
Nd	207	214
Pm	206	214
Sm	206	214
Eu	273	278
Gd	204	207
Tb	204	214
Dy	204	214
Ho	204	215
Er	202	214
Tm	201	213
Yb	256	265
Lu	196	202
Th	173	171
Pa	139	142
U	117	121
Np	119	125
Pu	145	155
Am	171	182
Cm	172	180
Bk	176	181
Cf	—	—
Es	—	—
Fm	—	—
Md	—	—
No	—	—
Lr	—	—

Figure 2.11: Calculated positron bulk lifetime for elements in the periodic table. *Image from* [61].

- **Pick-off:** the positron annihilates with an electron from the material with opposite spin. The lifetime is reduced with respect to the one in vacuum.
- **SEQ:** when ortho-positronium atoms interact with each other, we have Ps with spin direction opposite to each other. In this situation, the positron tends to annihilate with the electron with the opposite spin, reducing the Ps lifetime with respect to value in vacuum. The process is called spin exchange quenching (SEQ).

2.1.4.2.1 Self-annihilation The lifetime for the Ps in vacuum has been calculated with QED as seen in section 2.0.2, however, the annihilation products have not been indicated. While the photons are the only possible product due to the low positron/ electron mass, the number and characteristics of these photons are determined by the conserved quantities during the annihilation process. As discussed in reference [7], the conservation of $\hat{C}$ in the annihilation process constrains the number of photons from the Ps annihilation.

Ps is chargeless because composed of a particle and its antiparticle, so like the photon, it is an eigenvector of charge-conjugation operator $\hat{C}$. By definition, applying twice the operator, $\hat{C}^2$, we obtain the identity operator $\hat{I}$: the first application sends the particle into its antiparticle $\hat{C}\,|Particle\rangle = q_{\hat{C}}\,|Antiparticle\rangle$, and the second application sends the antiparticle into the original particle $\hat{C}\,|Antiparticle\rangle = \hat{C}^2\,|Particle\rangle = |Particle\rangle = \hat{I}\,|Particle\rangle$. Then, the eigenvalues of $\hat{C}$, $q_{\hat{C}}$, need to satisfy the equation $q_{\hat{C}}^2 = +1$, so $q_{\hat{C}} = \pm 1$. For elementary particles, eigenstates of $\hat{C}$, the eigenvalues are defined as an intrinsic property of the particles, for example, the photon has eigenvalue $q_{\hat{C}}^{\gamma} = -1$ due to the intrinsic parity of the electromagnetic field. Ps is not an elementary particle, the operator $\hat{C}$ exchanges the positron with the electron. This maintains the bound system, but the states of the components are modified: the spin and spatial wavefunction of the particle becomes the one of the antiparticle and vice versa. Consequently, in the general case of a positronium atom in a state $n^{2S+1}L_J$, the eigenvalue of $\hat{C}$, $q_{\hat{C}}^{Ps}$, takes into account the spin exchange $(-1)^{S+1}$, the parity reversal of the spatial wavefunction $(-1)^L$, and the intrinsic parity of the positron and electron (-1) [62]. In conclusion, we have:

$$q_{\hat{C}}^{Ps} = (-1)^{S+1} \times (-1)^L \times (-1) = (-1)^{S+L}. \tag{2.20}$$

Then, considering the Ps annihilation in N photons (so total eigenvalue $(q_{\hat{C}}^{\gamma})^N = (-1)^N$), because $q_{\hat{C}}$ is conserved in the process, we obtain the constrain:

$$(-1)^{S+L} = (-1)^N \tag{2.21}$$

At this point, from the Ps state, we can find the possible number of photons that are generated in the annihilation The smaller number of resulting annihilation photons represents the most likely result. In the case of 1^1S_0, we have $L = S = 0$, so N needs to be even. For o-Ps, 1^3S_1, we have, instead, $L = 0$ and $S = 1$, so $L + S = 1$, and the gammas number needs to be odd. From the conservation of the energy and momentum in the annihilation process, we can conclude:

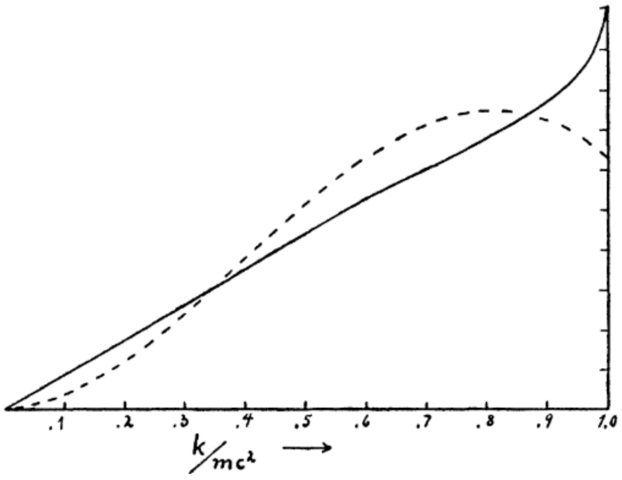

Figure 2.12: Energy spectrum of the annihilation gammas from o-Ps in units of m_0c^2. The solid line shows the probability distribution of the annihilation gamma energy for o-Ps from QED calculations. The dashed line represents the Ore-Powell phase-space prediction of the energy spectrum. *Image from* [63].

- **p-Ps:** the self-annihilation, with a lifetime of 125 ps, gives rise, in most cases, to the formation of two counterpropagating photons with energy exactly $m_0c^2 =$ 511 keV.

- **o-Ps:** the self-annihilation, with a lifetime of 142 ns, gives rise, in most cases, to the formation of three gammas. The photons are emitted in a plane. The energy of each photon is not fixed like in the previous case, but it is distributed as seen in fig. 2.12 following the constraint on the conservation of the total energy $E_{\gamma 1} + E_{\gamma 2} + E_{\gamma 3} = 2m_0c^2$ [63]. For a selected set of three energies satisfying these requirements, the angles between the three photons are fixed by the relation $\vec{p}_{\gamma 1} + \vec{p}_{\gamma 2} + \vec{p}_{\gamma 3} = 0$, where the photon momentum is given by the relativistic relation in eq. (2.2) in the case of massless particles: $p_\gamma = E_\gamma/c$. Regarding the distribution of the annihilation planes: if the o-Ps spin states are equiprobable (non-spin polarized, non-SpPo), all planes around the Ps are equally probable; if a particular spin state is considered, the spin direction breaks the rotation symmetry of the systems, so the inclinations of the annihilation planes are not equally distributed. This case will be described in detail in section 3.3.

2.1.4.2.2 Pick-off In the case of pick-off, the positron from a positronium atom annihilates with an electron of the medium with an opposite spin. In the reference frame of Ps, we have the production of two 511 keV photons in opposite directions, while in the laboratory frame, photon energy is shifted and the two gammas are not aligned anymore.

As previously said, the pick-off process reduces the Ps lifetime with respect to the case of self-annihilation. This reduction depends on the electron density in the open volume surrounding the Ps. This effect is most visible with o-Ps due to its long lifetime. In this case, there are models to relate its reduced lifetime to the open volume, like the Tao-Eldrup model [64, 65]:

$$\Gamma_{pick-off} = \Gamma_A \left(1 - \frac{R}{R + \Delta R} + \frac{1}{2\pi} \sin\left[\frac{2\pi R}{R + \Delta R}\right]\right) \tag{2.22}$$

where

$$\Gamma_A = \frac{1}{4}\Gamma_{p-Ps} + \frac{3}{4}\Gamma_{o-Ps} \approx 2\,\mathrm{ns}^{-1} \tag{2.23}$$

and ΔR is an empirical parameter in general set to be 0.166 nm. The Tao-Eldrup model considers a positronium atom in its fundamental level, in a spherical hole of radius R where the Ps wavefunction is extended for a ΔR inside the hole.

2.1.4.2.3 SEQ The SEQ requires a high density of positronium atoms, so it is a phenomenon observable with o-Ps formed with intense positron bunches produced in the last decades only with the introduction of buffer-gas traps, as we will see in chapter 4. In this case, similarly to the pick-off, the annihilation products are two 511 keV gammas, however, the lifetime reduction depends on the Ps density and spin states distribution. If the Ps density is too low, the positrons cannot annihilate with the electrons from other Ps because their wavefunctions do not overlap. Regarding the distribution of spin states, in SEQ the positron annihilates with an electron with the opposite spin from another positronium atom, so, assuming the density condition is always true, we can have two possibilities:

- **SpPo:** If there is a preferential direction of the Ps spins, the Ps is spin-polarized (SpPo). Then, the positron from the most populated spin state annihilates with the electron of all the other spin states, until only positronium atoms of the most populated state survive. All the positrons and electrons have the same spin direction.
- **Non-SpPo:** If all the spin states have the same Ps population, the SEQ continues until all the Ps atoms annihilate or they are too far to see each other.

2.1.5 Positron/Positronium Converter

When we refer to positron/positronium (e^+/Ps) converters, we intend a category of targets optimized for the emission of Ps in the outside vacuum when implanted with kiloelectronvolt positrons. As discussed in section 2.1.3.1, we can have Ps formation on the material surface for any type of material, however, only in insulators it can also form in the bulk. For this reason, the e^+/Ps converters are based on insulators, in particular, the most used one is SiO_2 due to its high efficiency in producing Ps [66]. To optimize the emission, the material structure is engineered to increase the surface-area-to-volume ratio, creating pores from where the positronium atoms are emitted (see fig. 2.13). As seen from this figure, interconnected cavities offer the best surface-area-to-volume ratio, but they need to be connected to the surface so that the formed Ps can escape into the vacuum.

Both Ps formed in the bulk and at SiO_2 surface can be emitted into the cavity. For thermally de-trapped Ps from the surface, the Ps emission energy is in the range of $10 - 100$ meV (depending on the target surface) [67]. For Ps formed in bulk, the Ps emission energy corresponds to $|\phi_{Ps}|$ and it is between $1 - 3$ eV [68]. Once in the

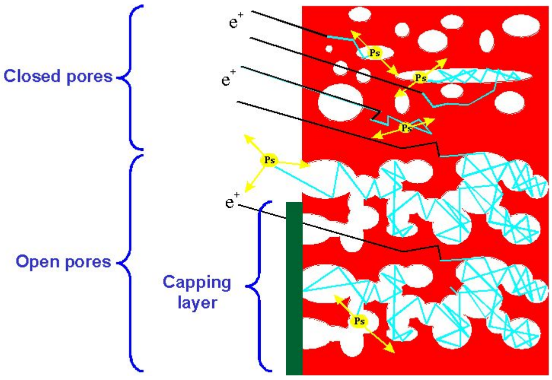

Figure 2.13: Ps formation in insulator material with different defects. *Image from* [78].

cavity, Ps atoms diffuse and a fraction escapes into the vacuum [25, 26]. In the diffusion process, they collide with the cavity surface losing part of their energy [69–76]. These collisions increase the probability of pick-off, decreasing the fraction of Ps that reaches the surface. With well-engineered converters, it is possible to obtain up to $\sim 45\%$ of the implanted positron emitted as Ps from the same side in which the positrons are implanted [76]. In this case, the converter is said to work in reflection, but this geometry can be disadvantageous in some applications. Recently, experiments have been done to generate a e^+/Ps converter that efficiently produces Ps in transmission, i.e. with Ps emission from the opposite side of the target with respect to the one where positrons are implanted. The first targets in this category had an efficiency up to $\sim 9\%$ [27, 77]. In more recent converters, a $\sim 16\%$ efficiency has been reached [28].

For both the reflection and transmission geometry, the e^+/Ps converters are engineered with one of the two following methods:

- **Additive:** depositing silica on a substrate [26, 71, 77];
- **Subtractive:** digging nanochannels in silicon which are then oxidized to form a coating of SiO_2 [25, 28, 72, 76]

In this thesis, we are going to describe the subtractive method developed at AML in Trento.

2.1.5.1 Trento Converter

In the subtractive method, we start with a pure silicon crystal. Thanks to the application of silicon in electronics, wafers of pure silicon with different crystal orientations and resistivities are easily available. At Trento, we use p-type silicon with a crystalline structure (111) and resistivity $0.1 - 1.5\,\Omega\,\mathrm{m}$.

To dig the nanochannels, electrochemical etching is done with the apparatus shown in fig. 2.14:

- The wafer is cut in $\sim 2 \times 2\,\mathrm{cm}^2$ pieces.
- The silicon piece is cleaned and positioned on the aluminum plate in fig. 2.14 right.

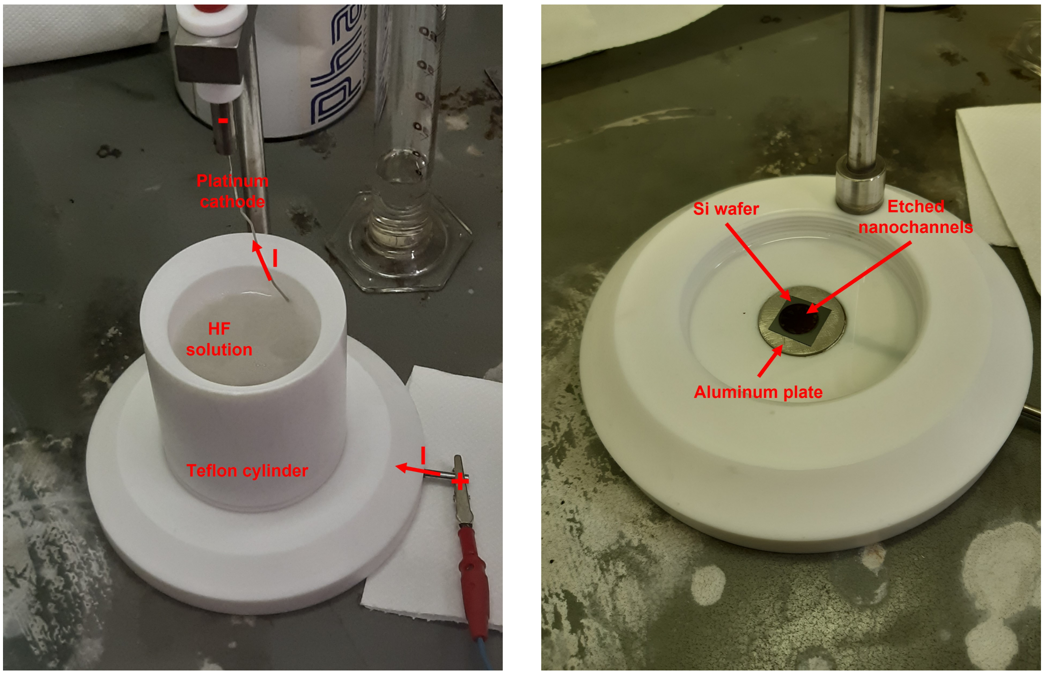

Figure 2.14: Equipment used to produce positron/positronium converter at Trento.

- A Teflon cylinder with a circular 1 cm^2 hole on the basis is screwed in, forming the setup in fig. 2.14 left. The hole in the cylinder is the area of the silicon wafer where the nanochannels are dug. This is shown as a dark disk in the silicon wafer in fig. 2.14 right.
- 75 mL chemical solution is poured in the cylindrical container. The solution is composed by 46.875 mL hydrofluoric acid (HF) at 48% and 28.125 mL of pure ethanol at 99.9%.
- A platinum mesh (platinum cathode) is inserted parallel to the basis of the cylinder in the solution at a distance of around 2 cm from the Si piece. A current is applied between the silicon bottom and the mesh.
- Due to the current flow, the fluoric acid is broken forming ions that attack the defects on the silicon surface digging through it, along the silicon crystal direction. The current density determines the range of diameters of the nanochannels, and the duration of the current is related to the length in depth of the nanochannels.
- After the etching, the target is washed in ethanol and dried in air at 100 °C for 2 h. While the washing eliminates all acid residuals, the heating evaporates the ethanol in the nanochannels, whose surface is then in contact with the oxygen from the air, and a thin layer of silica is formed from the oxidation of the exposed silicon surface.

Due to the crystal orientation of the silicon wafer (111), the nanochannels obtained by electrochemical etching are not perpendicular to the surface but at a 45° with respect to it. Implanted positrons interact with silicon, where they can thermalize and diffuse to the nearby nanochannel.

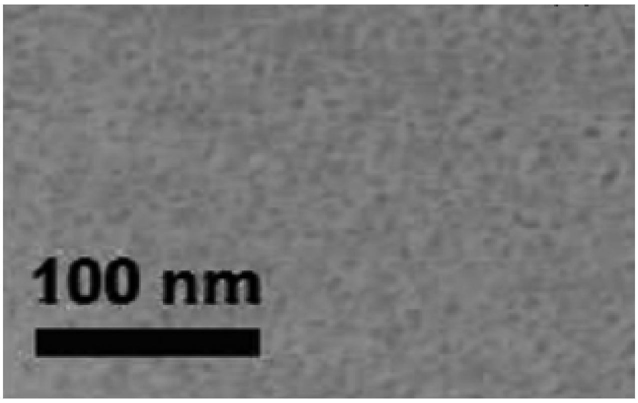

Figure 2.15: SEM image of the surface of a e^{+}/Ps converter etched with $10\,\mathrm{mA\,cm^{-2}}$. The nanochannels are shown as darker areas in the image. *Image from* [28].

In general, we use a $10\,\mathrm{mA\,cm^{-2}}$ current during the etching process. This results in nanochannel diameter in the range of $5-8\,\mathrm{nm}$ separated by distances of a similar order of magnitude (see fig. 2.15). A fine-tuning of the nanochannel diameter can be performed after the etching and the following heat treatment by *re-etching* the target. In this case, the target is immersed for 1 min in the solution of HF and ethanol, and then heat treated for 2 h. In this way, the diameter range of the nanochannels increases to $7-10\,\mathrm{nm}$ [25]. This process can be repeated to further increase the diameter.

These kinds of converters have very high efficiency. First of all, the positron diffusion length in silicon is 200 nm [79], much longer than the typical distance between nanochannels. Then the positrons have a very high probability of diffusing to the silica layer on the nanochannel surface, where Ps is formed and emitted in the pores [66]. At this point, the Ps diffuse in the nanochannels until they reach the vacuum or annihilate. The nanochannel diameter and the e^{+} implantation energy determine the Ps emission yield in vacuum. Ps in larger nanochannels has a longer diffusion length [25], and, tuning the positron implantation energy, a lower temperature of emitted Ps can be obtained [80].

2.1.5.2 Spin-Polarized Positronium

In previous sections, we have discussed how Ps is produced by a target but we did not discuss in which spin state it is formed. At first glance, it appears the Ps population is equally distributed between the four spin states $|0,0\rangle_{Ps}$, $|1,0\rangle_{Ps}$, $|1,-1\rangle_{Ps}$, and $|1,+1\rangle_{Ps}$, so the Ps is non-SpPo. However, this can happen only if the positrons and the electrons that are going to form the positronium atoms do not have a preferred spin direction, which means they are non-spin-polarized. In the case of the positrons, their spin-polarization P is defined with respect to the beam direction:

$$P = \frac{N_{+}^{e+} - N_{-}^{e+}}{N_{+}^{e+} + N_{-}^{e+}} \tag{2.24}$$

where N_{+}^{e+} is the number of positrons with the spin aligned to the beam direction and N_{-}^{e+} anti-aligned to the beam. On the other hand, the electrons in the material do not have a preferred spin direction in general. However, by introducing an external

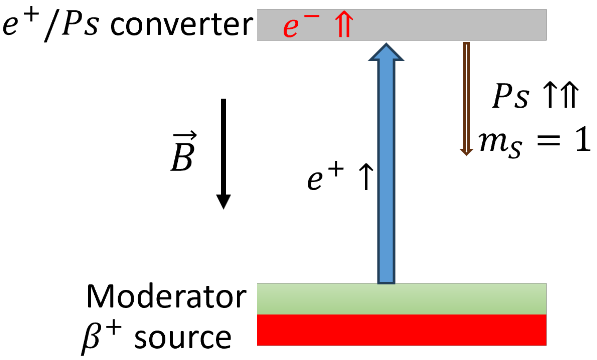

Figure 2.16: Scheme for the production of SpPo Ps with a e^+/Ps converter in a magnetic field $\vec{B}$ using a SpPo positron beam from a source-moderator assembly (see chapter 4 for details). The positron spin is indicated with $\uparrow$, and $\Uparrow$ indicates the electron spin.

magnetic field B, some of the electron spins will align with the field direction, and the electron spin-polarization E is:

$$E = \frac{N_+^{e-} - N_-^{e-}}{N_+^{e-} + N_-^{e-}} \tag{2.25}$$

where N_+^{e-} is the number of electrons with the spin aligned to the B-field direction and N_-^{e-} anti-aligned to the field. In the following, we will always consider the case of static magnetic fields with intensities $B < 1\,\mathrm{T}$ and direction parallel to the positron beam direction. If the positrons and electrons are polarized, we cannot expect the formation of non-SpPo Ps. To see the effect, we need to look into detail the Ps spin states [81]:

$$\begin{aligned} |0,0\rangle_{Ps} &= \frac{\Uparrow\downarrow - \Downarrow\uparrow}{\sqrt{2}} \\ |1,0\rangle_{Ps} &= \frac{\Uparrow\downarrow + \Downarrow\uparrow}{\sqrt{2}} \\ |1,-1\rangle_{Ps} &= \Downarrow\downarrow \\ |1,+1\rangle_{Ps} &= \Uparrow\uparrow \end{aligned} \tag{2.26}$$

where $\uparrow$ and $\downarrow$ represent the positron spin, and $\Uparrow$ and $\Downarrow$ represent the electron spin

As seen in eq. (2.26) and fig. 2.16, SpPo positrons and/or electrons favor forming Ps in the states $|1,\pm1\rangle$. Then the formation probabilities of these four states $F_{|S,m_S\rangle_{Ps}}$ is not 1/4, but [82]:

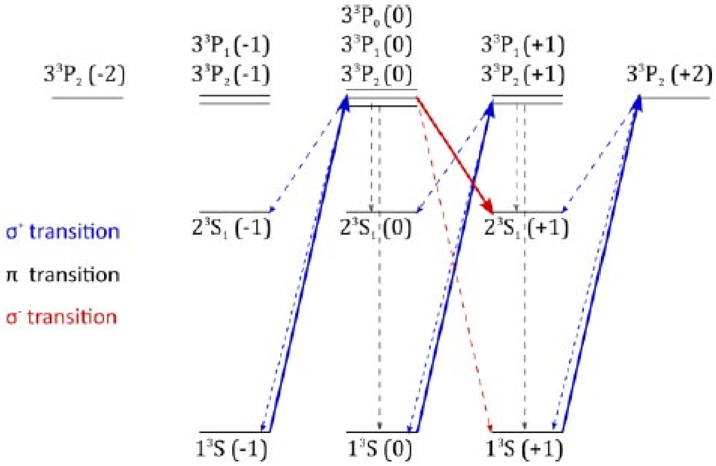

Figure 2.17: Two level $1^3S - 3^3P - 2^3S$ laser transition scheme for the production of single state metastable 2^3S Ps. The solid lines represent the laser excitation with their color indicating the laser polarization. The dashed lines represent the possible spontaneous decay from higher to lower energy levels.

$$\begin{aligned} F_{|0,0\rangle_{Ps}} &= \frac{1-PE}{4} \\ F_{|1,0\rangle_{Ps}} &= \frac{1-PE}{4} \\ F_{|1,-1\rangle_{Ps}} &= \frac{(1-P)(1-E)}{4} \\ F_{|1,+1\rangle_{Ps}} &= \frac{(1+P)(1+E)}{4} \end{aligned} \tag{2.27}$$

This population inequality is important for some experiments where the Ps needs to be prepared in a particular spin state. If the positrons and/or the electrons could be selected with a single spin direction, the Ps would be formed in state $|1,-1\rangle_{Ps}$ or $|1,+1\rangle_{Ps}$. Nevertheless, this fine control is impossible, and the spin state selection is done by manipulating the formed Ps. One way is by quenching the other states. An SEQ process leaves only the most populated of the $|1,\pm1\rangle_{Ps}$ states, while the other two states' lifetime is reduced in a few nanoseconds by the presence of external magnetic field (magnetic quenching, see section 2.1.6). Another way is with polarized lasers. As seen in fig. 2.17, already existing polarization techniques can be used to change the polarization of the lasers used for the two-photon excitation $1^3S_1 \rightarrow 3^3P_1 \rightarrow 2^3S_1$ [83], at the end of the process we obtain metastable Ps in the selected spin state. The laser used at each excitation step can be polarized so the excited atom has the same z-component of the spin $\Delta m = 0$, or changed $\Delta m = \pm 1$. Then by an appropriate selection of the polarization of the two lasers, it is possible to excite from a state $|1,m_i\rangle_{Ps}$ to a state $|1,m_f\rangle_{Ps}$ with $m_i \neq m_f$.

While these techniques can be used also for non-SpPo Ps, by starting with SpPo, we obtain a higher number of positronium atoms in the final selected spin state. While the value of P depends on the positron beam and will be discussed in chapter 4, the electron spin-polarization is related to the electrons in the material which are used to form Ps, in some materials very high values of E can be obtained.

2.1.5.2.1 SpPo electrons in materials In some materials, it is possible to spin-polarize the electron with a strong external magnetic field. In an atom, the electrons occupy the energy level from the lowest until all electrons are positioned. Consequently, most of the electrons are coupled with opposing spin due to the Pauli exclusion principle, except the ones in the most energetic levels. The spin of unpaired electrons can be controlled by an external magnetic field, obtaining SpPo electron which can form Ps in the states following eq. (2.27). SpPo electrons in material can be obtained in ferromagnetic materials, but these are metals, so Ps is formed only at the surface (see section 2.1.3.1). There are some plastic materials that can have SpPo electrons in special conditions. Poly(methyl methacrylate) (PMMA), high-density polyethylene (HDPE), and polypropylene have localized electrons at cryogenic temperatures [84]. In the presence of strong magnetic fields, these materials can reach an electron spin-polarization up to $E = -0.775$ [82], and the positrons tend to bound with these localized electrons [84]. The Ps formation efficiency is $\approx 16\%$ for PMMA [85], 20 % for HDPE [84], and 15 % for polypropylene [84].

To obtain high E values, a strong magnetic field is required, these conditions, however, affect the formed positronium atoms, in the next section we will analyze this influence.

2.1.6 Positronium in a Magnetic Field

The presence of an external magnetic field $\vec{B}$ affects the energy levels of the Ps through its interaction with the magnetic momenta of the positron and electron. The magnetic moment of an electron/positron is given by:

$$\vec{\mu}_{\pm} = \pm\frac{\mu_B}{\hbar}\left(\vec{L} + g_{e^{\pm}}\vec{S}\right) \tag{2.28}$$

where $\mu_B = \frac{e\hbar}{2m_0c} = 9.274\times10^{-24}\,\mathrm{A\,T} = 5.788\times10^{-5}\mathrm{eV\,T^{-1}}$ is the Bohr magneton, and $g_{e^+} = g_{e^-} \approx 2$ are the positron and electron gyromagnetic ratios, respectively. The Hamiltonian of the interaction of the particle with the magnetic field is given by:

$$H_B^{\pm} = -\vec{\mu}_{\pm}\cdot\vec{B}. \tag{2.29}$$

In the following, we consider a static magnetic field of intensity $|\vec{B}| = B$ and direction along the spin projection axis $\hat{z}$.

Up to now, we considered Ps in the S states, so $L = 0$, and only the spin contribution remains in the magnetic momentum of eq. (2.28). Then the interaction term of the Hamiltonian of Ps in a B-field is:

$$H_B^{Ps} = g_{e^-}\mu_B s_{z_{e^-}} B - g_{e^+}\mu_B s_{z_{e^+}} B. \tag{2.30}$$

Considering the Ps spin states reported in eq. (2.26), the perturbation from H_B^{Ps} on the Ps depends on the spin. States $|1,\pm1\rangle_{Ps}$ have the spins of positron and electron in the same direction so the two contributions on the right of eq. (2.29) cancel each other.

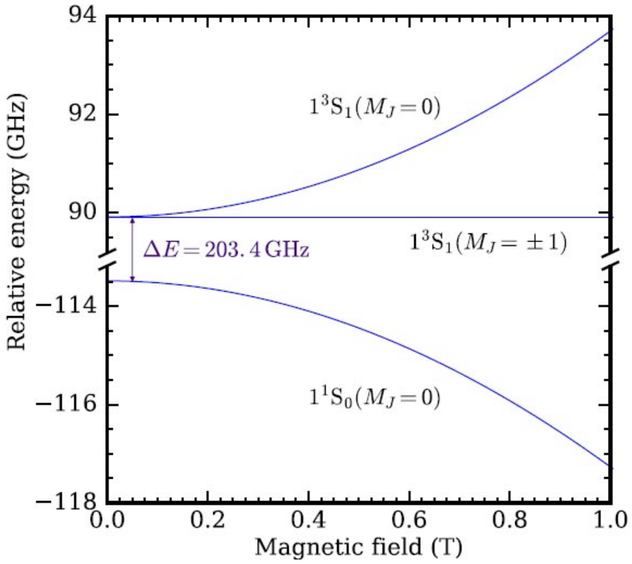

Figure 2.18: Zeeman effect on the ground states of positronium atoms in an external magnetic field. *Image from* [7].

States $|1,0\rangle_{Ps}$ and $|0,0\rangle_{Ps}$ have the two spins in opposite directions so H_B^{Ps} modifies the energy of only these two states.

2.1.6.1 Ps energy levels

In the following, we indicate with E_S and E_T the energy of the singlet state and of the triplet in the absence of external magnetic fields ($B = 0$). The difference between the two is ΔE reported eq. (2.8). In an external B-field, the perturbed energy levels become [15]:

$$\begin{aligned} E_{|0,0\rangle_{Ps}} &= \frac{E_T+E_S}{2} - \frac{\Delta E(1+x^2)^{1/2}}{2} \\ E_{|1,0\rangle_{Ps}} &= \frac{E_T+E_S}{2} + \frac{\Delta E(1+x^2)^{1/2}}{2} \\ E_{|1,-1\rangle_{Ps}} &= E_T \\ E_{|1,+1\rangle_{Ps}} &= E_T \end{aligned} \tag{2.31}$$

where

$$x = \frac{2e\hbar B}{\Delta E} = 0.276B \tag{2.32}$$

The magnetic field is in Tesla, and the perturbed energy levels are shown in fig. 2.18. This shows how the magnetic field mixes the spin states $|0,0\rangle_{Ps}$ and $|1,0\rangle_{Ps}$.

2.1.6.2 Distribution of Ps population

The magnetic field changes the population distribution of the four levels of Ps. In the general case of SpPo positrons and electrons, we have [82]:

$$
\begin{aligned}
F^B_{|0,0\rangle_{Ps}} &= \frac{(1-y)^2(1-P)(1+E)+(1+y)^2(1+P)(1-E)}{8(1+y^2)} \\
F^B_{|1,0\rangle_{Ps}} &= \frac{(1+y)^2(1-P)(1+E)+(1-y)^2(1+P)(1-E)}{8(1+y^2)} \\
F^B_{|1,-1\rangle_{Ps}} &= F_{|1,-1\rangle_{Ps}} = \frac{(1-P)(1-E)}{4} \\
F^B_{|1,+1\rangle_{Ps}} &= F_{|1,+1\rangle_{Ps}} = \frac{(1+P)(1+E)}{4}
\end{aligned}
\tag{2.33}
$$

where $y = \frac{x}{\sqrt{1+x^2}+1}$. The sum of all populations is constant, in fact:

$$
F^B_{|0,0\rangle_{Ps}} + F^B_{|1,0\rangle_{Ps}} + F^B_{|1,-1\rangle_{Ps}} + F^B_{|1,+1\rangle_{Ps}} = 1 \tag{2.34}
$$

2.1.6.3 Ps lifetime

Due to the mixing of the states $|0,0\rangle_{Ps}$ and $|1,0\rangle_{Ps}$, the lifetime of these states is modified, the singlet state can decay in three gammas, and $|1,0\rangle_{Ps}$ can decay in two gammas. For each of the two states, as sketched in fig. 2.19, The annihilation paths and the corresponding rates are [82, 86, 87]:

$$
\begin{aligned}
|1,0\rangle_{Ps} \to 3\,\gamma : \Gamma_{13} &= \frac{\Gamma_T}{1+y^2} \\
|1,0\rangle_{Ps} \to 2\,\gamma : \Gamma_{12} &= \frac{y^2\Gamma_S}{1+y^2} \\
|0,0\rangle_{Ps} \to 3\,\gamma : \Gamma_{03} &= \frac{y^2\Gamma_T}{1+y^2} \\
|0,0\rangle_{Ps} \to 2\,\gamma : \Gamma_{02} &= \frac{\Gamma_S}{1+y^2}
\end{aligned}
\tag{2.35}
$$

where $\Gamma_S = \frac{1}{125\,\mathrm{ps}}$ and $\Gamma_T = \frac{1}{142\,\mathrm{ns}}$ are the annihilation rates for the singlet and triplet state in absence of magnetic field, and Γ_{S,N_γ} is the annihilation rate of the state $|S,0\rangle_{Ps}$ into a N_γ number of annihilation photons. Then, the evolution of the Ps population in the two mixed states in the presence of external magnetic fields $F^B_{|S,m_S\rangle_{Ps}}[t]$ is:

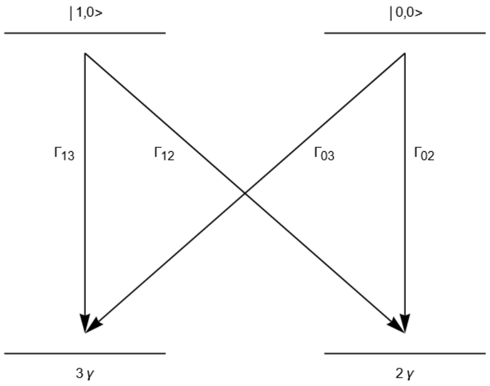

Figure 2.19: Scheme for the mixing of the states $|0,0\rangle_{Ps}$ and $|1,0\rangle_{Ps}$ in a magnetic field. The annihilation rates from these two states into two gammas 2γ or three gammas 3γ are reported as $\Gamma_{S\,N_\gamma}$ with S indicating the total spin of the Ps state and N_γ the number of annihilation photons.

$$\begin{aligned}
\frac{d}{dt}F^B_{|0,0\rangle_{Ps}}[t] &= -(\Gamma_{02}+\Gamma_{03})F^B_{|0,0\rangle_{Ps}}[t] \\
&\Rightarrow\ F^B_{|0,0\rangle_{Ps}}[t] = F^B_{|0,0\rangle_{Ps}}e^{-(\Gamma_{02}+\Gamma_{03})t} = F^B_{|0,0\rangle_{Ps}}e^{-\frac{\Gamma_S+y^2\Gamma_T}{1+y^2}t} \\
\frac{d}{dt}F^B_{|1,0\rangle_{Ps}}[t] &= -(\Gamma_{12}+\Gamma_{13})F^B_{|1,0\rangle_{Ps}}[t] \\
&\Rightarrow\ F^B_{|1,0\rangle_{Ps}}[t] = F^B_{|1,0\rangle_{Ps}}e^{-(\Gamma_{12}+\Gamma_{13})t} = F^B_{|1,0\rangle_{Ps}}e^{-\frac{y^2\Gamma_S+\Gamma_T}{1+y^2}t}
\end{aligned} \tag{2.36}$$

So, the number of annihilations in two $n^B_{2\gamma}[t]$ and three $n^B_{3\gamma}[t]$ gammas from the two mixed states are:

$$\begin{aligned}
\frac{d}{dt}n^B_{2\gamma}[t] &= \Gamma_{02}F^B_{|0,0\rangle_{Ps}}[t]+\Gamma_{12}F^B_{|1,0\rangle_{Ps}}[t] \\
\frac{d}{dt}n^B_{3\gamma}[t] &= \Gamma_{03}F^B_{|0,0\rangle_{Ps}}[t]+\Gamma_{13}F^B_{|1,0\rangle_{Ps}}[t]
\end{aligned} \tag{2.37}$$

whose solutions are:

$$\begin{aligned}
n^B_{2\gamma}[t] &= \frac{\Gamma_{02}}{\Gamma_{03}+\Gamma_{02}}F^B_{|0,0\rangle_{Ps}}\left(1-e^{-(\Gamma_{03}+\Gamma_{02})t}\right)+\frac{\Gamma_{12}}{\Gamma_{13}+\Gamma_{12}}F^B_{|1,0\rangle_{Ps}}\left(1-e^{-(\Gamma_{13}+\Gamma_{12})t}\right) \\
n^B_{3\gamma}[t] &= \frac{\Gamma_{03}}{\Gamma_{03}+\Gamma_{02}}F^B_{|0,0\rangle_{Ps}}\left(1-e^{-(\Gamma_{03}+\Gamma_{02})t}\right)+\frac{\Gamma_{13}}{\Gamma_{13}+\Gamma_{12}}F^B_{|1,0\rangle_{Ps}}\left(1-e^{-(\Gamma_{13}+\Gamma_{12})t}\right)
\end{aligned} \tag{2.38}$$

Finally, the total number of annihilations via two $n^B_{2\gamma}$ and three $n^B_{3\gamma}$ gammas result:

$$\begin{aligned} n^B_{2\gamma} &= \lim_{t\to+\infty} n^B_{2\gamma}[t] = \frac{\Gamma_S}{\Gamma_S + y^2\Gamma_T} F^B_{|0,0\rangle_{Ps}} + \frac{y^2\Gamma_S}{y^2\Gamma_S + \Gamma_T} F^B_{|1,0\rangle_{Ps}} \\ n^B_{3\gamma} &= \lim_{t\to+\infty} n^B_{3\gamma}[t] = \frac{y^2\Gamma_T}{\Gamma_S + y^2\Gamma_T} F^B_{|0,0\rangle_{Ps}} + \frac{\Gamma_T}{y^2\Gamma_S + \Gamma_T} F^B_{|1,0\rangle_{Ps}} \end{aligned} \tag{2.39}$$

And their ratio is:

$$\frac{n^B_{3\gamma}}{n^B_{2\gamma}} = \frac{\Gamma_T}{\Gamma_S} \frac{y^2\Gamma_T(F^B_{|0,0\rangle_{Ps}} + F^B_{|1,0\rangle_{Ps}}) + \Gamma_S(y^4F^B_{|0,0\rangle_{Ps}} + F^B_{|1,0\rangle_{Ps}})}{y^2\Gamma_S(F^B_{|0,0\rangle_{Ps}} + F^B_{|1,0\rangle_{Ps}}) + \Gamma_T(F^B_{|0,0\rangle_{Ps}} + y^4F^B_{|1,0\rangle_{Ps}})} \tag{2.40}$$

In the absence of magnetic fields, $y = 0$, eq. (2.40) is reduced to $\frac{n^B_{3\gamma}}{n^B_{2\gamma}} = 1$ because the singlet state annihilates only as 2 gammas, and $|1,0\rangle_{Ps}$ as three gammas, and the two states have the same populations. More interesting is the case of strong magnetic fields, $y = 1$, then the ratio is reduced to $\frac{n^B_{3\gamma}}{n^B_{2\gamma}} = \frac{\Gamma_T}{\Gamma_S} \approx 8.8 \times 10^{-4}$: the two spin states have a 99.9% probability of annihilates in two gammas with a lifetime $\frac{2}{\Gamma_S+\Gamma_T} \approx 250\,\mathrm{ps}$, much shorter than $|1,\pm1\rangle_{Ps}$ lifetime of 142 ns. In general, the shortening of the state $|1,0\rangle_{Ps}$ lifetime is called *magnetic quenching.* As said in the previous section, by applying an external magnetic field and waiting a few tens of nanoseconds, we obtain Ps only in the $|1,\pm1\rangle_{Ps}$ states.

2.2 Detection techniques for positrons and positronium

In the previous section, we have discussed the properties and interaction of positron and Ps with matter. In the following, we analyze the direct detection of positrons and Ps and the spectroscopy techniques based on the detection of the annihilation gammas.

2.2.1 Direct Detection

The single positrons are detected by charge multiplication, i.e. the signal of a single elementary charge, the positron, is converted by physical processes to thousands or more elementary charges, in general electrons. In this kind of system, the small signal of a single positron is amplified to be detected with much simpler and cheaper detectors. The most used charge multiplication technique for positron detection is based on dynode technology.

2.2.1.1 Dynode

The dynode is composed of materials that emit electrons when a charged particle impinges on its surface, so the number of outgoing charges is greater than the incoming ones. By concatenating this multiplication process, the signal from a single charge is increased by many orders of magnitude. The dynode comes in two forms: discrete and continuous. The first is mainly relegated to photon-multiplier tubes (PMT) which are used in the readout of the signal of scintillators in the process of gamma-ray detection [88]. In the detection of charged particles, continuous dynodes are used. They are cylindrical or conical channels of insulator material with the inner surface coated by a conductive

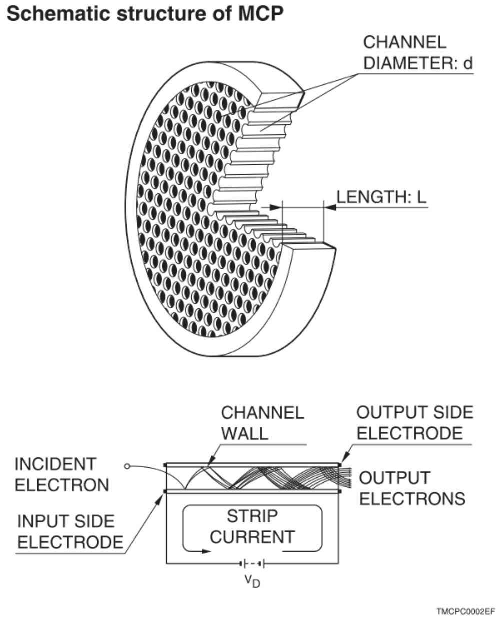

Figure 2.20: Scheme of the structure of an MCP (upper figure) and the working principle of a continuous dynode element of the MCP (lower figure). *Image from* [89]

layer. During operation, the ends are polarized with the side exposed to the incoming particles at a lower potential. By choosing the correct resistive material, the generated secondary electrons are always accelerated towards the opposite end of the devices (see the lower part of fig. 2.20) and, in the process, they interact with the surface multiplying at each interaction the electron number in the dynode. In this way, we obtain even 10^4 electrons from a single particle impinging the detector.

We can have a single dynode or an array of them. In the first case, we can only measure the total number of incoming particles, and the instrument is called channeltron. With an array of dynodes, it is possible to image the particle distribution because the distribution of the generated secondary electrons is proportional to the spatial distribution of the beam. The charge multiplication conserves the information of the particle distribution in the beam spot. If the generated secondary electrodes exit on the back, the device is called a micro-channel plate (MCP).

The MCP is composed of an array of cylindrical dynodes each with a diameter of a few micrometers (see fig. 2.20). Multiple MCPs can be stacked to increase the gain, and the generated electrons are detected through a phosphor screen or a timepix.

2.2.1.1.1 Phosphor Screen The phosphor screens are based on the same process used in the image generation of old Cathode-Ray Tube (CRT) televisions. A glass surface is coated with phosphor atoms. The atoms are excited by inelastic collisions with incoming particles. The excited atoms are then going to de-excite at a rate given by the decay time of the atomic level excitation, and in the process, the atoms emit electromagnetic radiation in/near the visible range. The emission spectrum and decay time of the excited atoms are standardized by phosphor screen type, for details on the most used screens see reference [89].

The phosphor screen transforms this information from the secondary electrons exiting the MCP to photons, which can be recorded electronically with a CCD (charge-coupled device) or CMOS (complementary metal-oxide semiconductor) camera. CCD cameras were the prevalent type until a few years ago, in this type of camera, in each pixel the incoming photons excite electrons that are trapped in the pixel. The electrons from each pixel are collected and translated into a digital signal by the camera board. Differently, each CMOS pixel translates the incoming photons directly into a digital signal. The application of this acquisition chain has been well documented in the positron field [90]. Resolution of 88 µm spatially and 15 ns temporal were obtained [91].

2.2.1.1.2 Timepix The timepix is a pixellated particle detector based on CMOS technology developed at CERN [92, 93]. With this system, each pixel of the sensor interacts with the electrons emitted by the MCP. With timepix, we can obtain a spatial resolution of 12 µm and a temporal resolution of 15 ns with a positron beam [94].

2.2.1.2 Detection of neutral particles

The electron-positron bound state is electrically neutral, so it cannot be accelerated on a dynode to generate a signal of secondary electrodes. There are only two possible ways for a neutral system to generate a signal in a dynode: it is so fast to scatter secondary electrons when interacting with the surface, or it is broken in electrically charged components that are accelerated on the device and generate the signal. In the case of Ps, only Ps faster than several electronvolts is capable of emitting secondary electrons when hitting the surface of a dynode [95, 96]. To detect Ps with energy $< 1\,\mathrm{eV}$, as in the case of Ps emitted into vacuum, the positronium atom has to be ionized and the positron (or the electron) accelerated on the dynode front. Techniques have been demonstrated for the direct ionization of positronium atoms with proper laser pulses or with excitation in high levels $n \gg 1$ (Rydberg states) in a strong electric field (field-ionization) [97, 98]. Positrons freed by the ionization of Ps were then guided by a stray magnetic field (1 T) towards the MCP [99].

2.2.2 Spectroscopy Techniques

The positron annihilation spectroscopies study the gamma-rays produced during the annihilation to infer information on the positron and its surroundings before the annihilation. Based on the property of the annihilation studied, we can divide the spectroscopy techniques into two categories: time and energy-momentum.

2.2.2.1 Lifetime measurements: *Positron Annihilation Lifetime Spectroscopy* and *Single Shot Positron Annihilation Spectroscopy*

With Positron Annihilation Lifetime Spectroscopy (PALS), the lifetime of e^+ and Ps is measured. The time between the start signal, which corresponds to the injection of a single positron in the material, and the stop signal, given by the detection of the annihilation gamma, is recorded. A PALS spectrum is formed by collecting a great number of events. The spectrum is characterized by an initial peak and a decreasing slope, which corresponds to the sum of the different exponential decays from different positron lifetimes in the material, see sections 2.1.4.1 and 2.1.4.2. The peak is characterized by the

Table 2.1: Basic characteristics of the most used inorganic detectors for positron spectroscopy. *Data from* [88]

Material	Refractive Index	Wavelength [nm]	Decay Time [µs]	Light Yield Photons/MeV
NaI(Tl)	1.85	415	0.23	38000
CsI(Tl)	1.80	540	0.68(64%), 3.34(36%)	65000
BaF_2	1.56	220	0.0006	1400
$PbWO_4$			0.006	200

instrumental response function $R[t]$ which considers both the detector and beam characteristics. It is derived experimentally by the fit with multiple Gaussian of a spectrum of a reference sample with known lifetimes. The lifetime spectrum can be fitted with the following function:

$$Z[t] = -\frac{dn[t]}{dt} = R[t] \otimes \sum_{i=1}^{N} \frac{I_i}{\tau_i} e^{-\frac{t}{\tau_i}} + Background \tag{2.41}$$

where N is the number of different lifetime components in the spectrum. The fit is, usually done, with dedicated programs like POSWIN [100] and LT [101].

In PALS, we need a fast detector and a single positron in the material at a time. The second condition is fulfilled with a continuous beam of around 10^6 positrons per second. Regarding the first condition, a fast scintillator detector is used. The scintillator is a scintillating material where the high-energy photon deposits all or part of its energy which is then converted into thousands of low-energy photons. These photons are detected as an electronic signal through a SiPM (silicon photo-multiplier) or a PMT with a photocathode. The scintillator material determines the characteristics of the detector (see table 2.1), a fast scintillating material like BaF_2 is the most used for PALS measurement.

As we will see in chapter 4, there exist beams that can implant up to 10^6 positrons in a few nanoseconds. In this case, the lifetime spectrum can be acquired in a single implantation shot, from here the technique name Single Shot Positron Annihilation Lifetime Spectroscopy (SSPALS) [102]. In this kind of measurement, the detector decay time is not the only problem, the great number of almost instantaneous annihilation will saturate most detectors, so a detector with a low light yield, like $PbWO_4$ (see table 2.1), is used. Figure 2.21 shows, as an example, an SSPALS spectrum measured with the AE$\bar{\text{g}}$IS positron beam line [103].

2.2.2.2 Energy-Momentum

There are two spectroscopy techniques based on the energy-momentum of the annihilation photons:

- the Angular Correlation of Annihilation Radiation (ACAR) measures the non-collinearity of the annihilation gammas;
- the Doppler Broadening Spectroscopy (DBS) measures the energy shift of the annihilation photon from the expected value of 511 keV due to the Doppler effect.

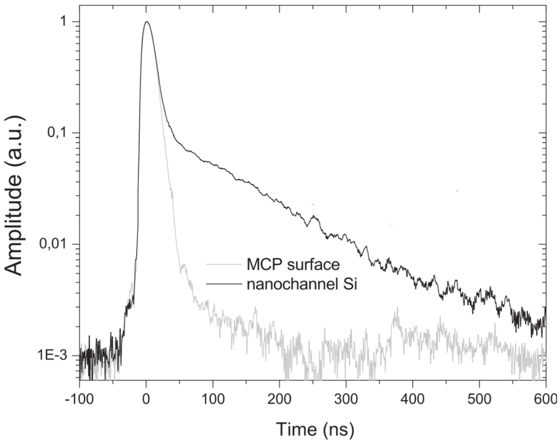

Figure 2.21: Example of SSPALS spectra measured with the AE$\bar{g}$IS positron beam. The spectra measured on the surface of the MCP (no Ps formation, grey curve) and in a silicon sample with nanochannels (Ps formation, black curve) are reported. Each curve is the average of 10 single shots. *Image from* [103].

2.2.2.2.1 DBS The two gammas arising from the positron-electron annihilation in a medium carry the information about the momentum of the electron. In the laboratory frame, the two gammas are non-collinear, forming an angle $\neq 180°$ between them, and are Doppler shifted by a quantity $\pm\Delta E$ with respect $E = 511\,\text{keV}$.

In the DBS technique, the 511 keV annihilation line is measured with a detector with high energy resolution: HPGe (high-purity germanium) detectors. They are a kind of semiconductor detector. The gammas create an electric signal by forming electron-hole pairs in the detector. HPGe detectors have very high energy resolution with respect to typical scintillator detectors like NaI(Tl).

The DBS spectrum corresponds to the density distribution of the electron longitudinal momentum. The 511 keV annihilation line is characterized by the following integral parameters:

$$S = \frac{A}{C} \qquad W = \frac{B}{C} \tag{2.42}$$

where the parameter A, B, and C are defined, as seen in figure 2.22, as:

- A: The *peak area* in the region around the peak, our choice is $\pm\,0.85\,\text{keV}$.
- B: The *wings area* corresponding, in our choice, to the regions $507 - 509.4\,\text{keV}$ and $512.6 - 515\,\text{keV}$.
- C: The *total area* for the normalization is, in our choice, the region of $\pm\,4.25\,\text{keV}$ around the main peak.

The S parameter is related to electrons with low momentum, so it is enhanced when positrons annihilate with valence electrons, while W is related to annihilations with electrons of higher momentum (outermost core electrons).

DBS is also sensible to the formation of Ps. The annihilation of p-Ps would appear as a narrowing of the 511 keV line. As seen in section 2.1.4.2, the o-Ps annihilation gammas

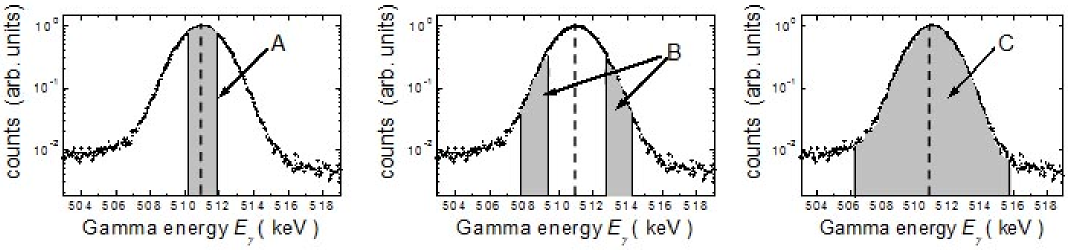

Figure 2.22: Experimental parameters of the DBS measurements. The vertical dashed line corresponds to 511 keV. The grey regions indicated the area corresponding to the parameters A, B, and C as defined in the text. *Image from* [56].

have a continuum of energies from 0 to 511 keV, so they increase the number of counts on the left of the 511 keV peak. For quantifying o-Ps annihilations, two other parameters are introduced:

- V_F: The *valley area* corresponding, in our choice, to the region $410 - 500$ keV.
- P_F: The *peak area* corresponding, in our choice, to the region 511 ± 4.25 keV.

The 3γ-2γ ratio of Ps is defined as as $R_F[E] = \frac{V_F[E]}{P_F[E]}$, and the positron fraction annihilating in 3γ as [104–106]:

$$F_{3\gamma}[E] = \frac{3}{4}\left(1 + \frac{P_1(R_1 - R_F[E])}{P_0(R_F[E] - R_0)}\right)^{-1} \tag{2.43}$$

where R_1 (P_1) and R_0 (P_0) are the R_F (P_F) value when 100% and 0% of the implanted positrons annihilate as 3γ [105–107].

2.3 Polarimetry

The techniques introduced in the previous section cannot provide any information about the spin of positrons and Ps. In this section, we are going to analyze the polarimetry techniques that can be applied to extract the spin-polarization of positron and Ps. Moreover, we will also introduce techniques to measure the polarization of photons with hundreds of kiloelectronvolts energy.

2.3.1 Positron

The polarimetry techniques for positrons can be divided into two big categories:

- high-energy positrons, $E_+ > 1$ MeV,
- low-energy positrons, $E_+ < 1$ MeV.

In the first category a large number of techniques have been studied and applied, due to the usage in positron-electron colliders [108–112]. In the case of low-energy positrons, of interest for this thesis, few techniques were developed for the measurement of the polarization P of the positrons in a beam. These techniques are based on the formation of Ps, which has a population distribution in the spin states not uniform as seen in eq. (2.27). The non-uniformity in the population distribution is then detected with one of the spectroscopy techniques identified in section 2.2.2. To extract the information on the value of P, it is necessary to subject the positronium atoms to an interaction dependent on their spin state. In the case of high-density positron bunches, the SEQ of the Ps cloud is dependent on the population distribution of the states (see section 2.1.5.2), and the positron polarization is determined by SSPALS measurement of the cloud [113]. In the case of continuous beams, PALS [50], ACAR [114], and DBS [87] techniques can be used to reconstruct the positron polarization from the variations in the measured spectrum of Ps annihilation in the presence of an external magnetic field varying its magnetic field. In the scope of this thesis, we will analyze in detail the polarimetry technique based on DBS.

2.3.1.1 Ps DBS Polarimeter

The Ps DBS Polarimetry technique is based on the variation of the S parameter due to the magnetic quenching of Ps. It is based on the measurement of the DBS spectrum of a e^+/Ps converter at different values of the magnetic field. As previously seen, the S parameter represents the annihilations in 2γ with energy near the 511 keV peak, so it contains the Ps self-annihilation in two gammas. The unbound positron annihilation is not dependent on the magnetic field, so the S parameter dependence on the B-field is given by the variation of Ps annihilation changing the magnetic field. The Ps self-annihilation into two gammas $n^B_{2\gamma}$ is given by eq. (2.39). In the measured spectrum, the pick-off annihilations are present, so we add to $n^B_{2\gamma}$ a pick-off rate Γ_{PO} and the positron-electron contact density κ. This last parameter takes into account the change in the Ps wavefunction in the material due to the electric potential generated by the material electrons. The parameter is defined as $\kappa = |\psi_S[\vec{0}]|^2/|\psi_V[\vec{0}]|^2$ where $\psi_V[\vec{r}]$ is the Ps wavefunction in the vacuum, and $\psi_S[\vec{r}]$ in the sample [59]. The self-annihilation rate in two gammas of the Ps becomes [87]:

$$\begin{aligned} n'^B_{2\gamma} = {} & \frac{\kappa\Gamma_S}{1+y^2}\left(\kappa\frac{(\Gamma_T+y^2\Gamma_S)}{1+y^2}+\Gamma_{PO}\right)^{-1} F^B_{|0,0\rangle_{Ps}} + \\ & + y^2\frac{\kappa\Gamma_S}{1+y^2}\left(\kappa\frac{(y^2\Gamma_T+\Gamma_S)}{1+y^2}+\Gamma_{PO}\right)^{-1} F^B_{|1,0\rangle_{Ps}}. \end{aligned} \tag{2.44}$$

The magnetic field dependence of the S parameter can be fitted with the function [87]:

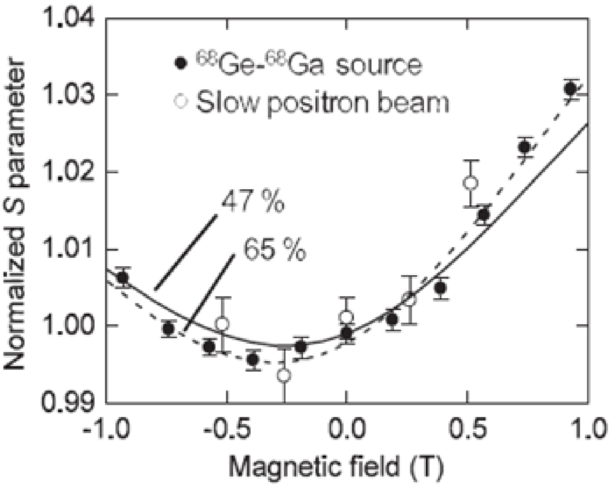

Figure 2.23: Magnetic field dependences of S parameters of fused silica obtained using the ^{68}Ge/^{68}Ga source and a slow positron beam ($E = 15\,\mathrm{keV}$). Solid and broken lines are the fit of the S parameter using eq. (2.45). *Image from* [115].

$$\begin{aligned}
S[B] &= \alpha n_{2\gamma}^{\prime B} + \beta \\
&= \beta + \alpha \frac{\kappa \Gamma_S}{1+y^2} \times \\
&\times \frac{1}{\kappa \frac{(\Gamma_T + y^2 \Gamma_S)}{1+y^2} + \Gamma_{PO}} \frac{(1-y)^2(1-P)(1+E) + (1+y)^2(1+P)(1-E)}{8(1+y^2)} + \\
&+ \alpha \frac{y^2 \kappa \Gamma_S}{1+y^2} \frac{1}{\kappa \frac{(y^2 \Gamma_T + \Gamma_S)}{1+y^2} + \Gamma_{PO}} \frac{(1+y)^2(1-P)(1+E) + (1-y)^2(1+P)(1-E)}{8(1+y^2)}
\end{aligned} \tag{2.45}$$

with α, β, Γ_{PO}, E, and P fitting parameters. α, β, Γ_{PO}, and E depend on the characteristics of the target, in general, the target is an insulator and the electron polarization E is set a priori to zero, $E = 0$. Because the experimental procedure consists of the recording of the DBS spectrum at different magnetic field intensities, we now analyze the effects of the Γ_{PO}, P, and E parameters on the S parameter as a function of B. For any parameter value, $S[B]$ presents a minimum value near $0\,\mathrm{T}$ and it increases for higher magnetic field intensities due to the increased two gamma annihilation from the magnetic quenching of the $|1,0\rangle_{Ps}$ state (see eq. (2.35) and fig. 2.23 in which the measurement from Maekawa et al.'s work are shown [115]). The range of values assumed by $S[B]$ depends on the target characteristics and positron polarization.

The relation between the S parameter and the positron P and electron E polarization comes from the population distribution of the Ps states in the presence of a magnetic field, see eq. (2.33). The two parameters enter linearly in the expression of $S[B]$, then with the chosen target, we can observe an increase in the value range of $S[B]$ for a more polarized positron beam, i.e. higher P translates in a higher variation of $S[B]$ (see

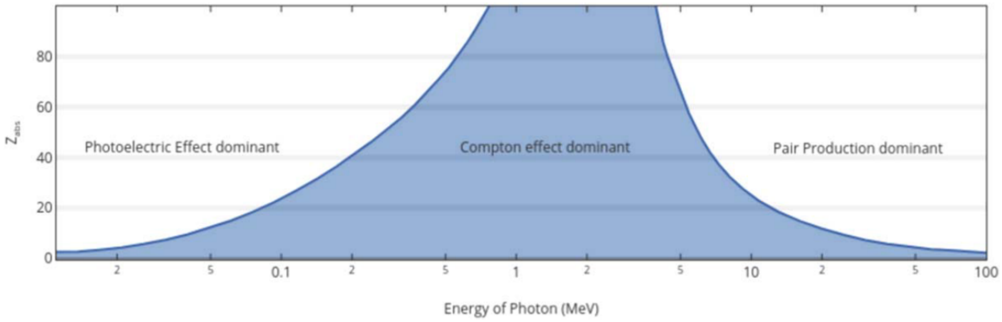

Figure 2.24: Dominant interaction between gamma-ray and material at different photon energies and for sundry atomic numbers. *Image from* [116]

fig. 2.23). The presence of the pick-off is required to emphasize the variation of $S[B]$ at the change of P.

2.3.2 Annihilation Gammas

With regards to the photon, the polarization can be seen as the extension to quantum mechanic of the classical polarization of electromagnetic waves. For optical photons, there exist cheap and easily available filters that allow the passage only of a polarization direction. The only way to measure the polarization of high-energy photons is by measuring the interaction with matter through a polarization-dependent cross-section. These interactions are energy dependent, so the high-energy photons can be divided into three energy ranges and corresponding to three different interactions with matter:

- **X-rays:** energies $0.1 - 100\,\text{keV}$, interaction *Thomson scattering* and *photoelectric effect*;
- **Low-energy gamma-rays:** energies $100 - 2000\,\text{keV}$, interaction *Compton scattering*;
- **High-energy gamma-rays:** energies $> 2\,\text{MeV}$, interaction *Pair production.*

The first two ranges use polarimetry techniques based on the scattering of a photon with an electron. The polarization direction of the incoming photons is obtained by the asymmetry in the direction of the outgoing photons (Compton and Thompson scatterings) or the scattered electrons (photoelectric effect). For x-rays, the photon energy is negligible with respect to the electron rest mass (the electron kinetic energy in the material is of the order of electronvolts), for low-energy gammas, instead, the two particles have similar energies.

With high-energy gamma-rays, the main process is the electron-positron pair production, which is possible only for photon energies $> 1.02\,\text{MeV}$ (see fig. 2.24). In this case, the emission plane of the pair is dependent on the polarization of the incoming photon.

The positron annihilation photons are in the low-energy gamma-rays category, so, to measure their polarization, we need to use Compton polarimeters.

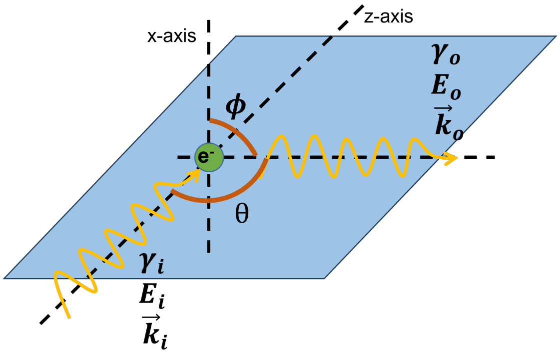

Figure 2.25: Diagram for Compton scattering for unpolarized incoming photons with an electron e^-. The incoming photon γ_i has energy E_i and it is moving in the direction $\vec{k}_i$ along the z-axis. The scattered photon γ_o has energy E_o and it is moving in the direction $\vec{k}_o$. The scattering plane is identified in blue and it is inclined by an angle ϕ with respect to the x-axis. $\vec{k}_i$ and $\vec{k}_o$ reside in the scattering plane with the scattered photon directed at an angle θ with respect to the incoming photon.

2.3.2.1 Compton Polarimeter

Compton in the early 1900s, described an experiment of scattering between light and matter in which there was a frequency shift in the scattered light. The experiment could be described as an inelastic scattering between the electron of the material and the photon. In the following sections, we first introduce Compton scattering starting with unpolarized photons which is the case taught in physics courses, then we pass on to discuss the scattering of linearly polarized photons which is the process behind most Compton polarimeters.

2.3.2.1.1 Scattering of Unpolarized Photons In a Compton scattering, the incoming photon γ_i with energy E_i is scattered by an electron in a scattered (or Compton) photon γ_o with energy:

$$E_o = \frac{E_i}{1 + \frac{E_i}{m_0 c^2}(1 - \cos\theta)} \tag{2.46}$$

where m_0 is the electron rest-mass and θ is the angle between the incoming and scattered photons in the plane defined by the two photons' momentum (scattering plane), as seen in fig. 2.25. In the formulation of the previous equation, neither the incoming photon nor the electron are considered polarized. The distribution of the emission angles for the scattered photons is described by the Klein-Nishina cross-section [117]:

$$\frac{d\sigma_{KN,U}}{d\Omega} = \frac{r_0^2}{2}\frac{E_o^2}{E_i^2}\left(\frac{E_o}{E_i} + \frac{E_i}{E_o} - \sin^2\theta\right) \tag{2.47}$$

where $d\Omega = \sin\theta d\theta d\phi$ with ϕ the azimuthal angle describing the rotation of the scattering plane around the reference axis, see fig. 2.25.

Eq. (2.47) is obtained by integrating over all possible spin directions for the incoming photon (corresponding to its polarization) and for the electron. In these conditions, the scattering process does not have a preferred direction, so the system is symmetric for any

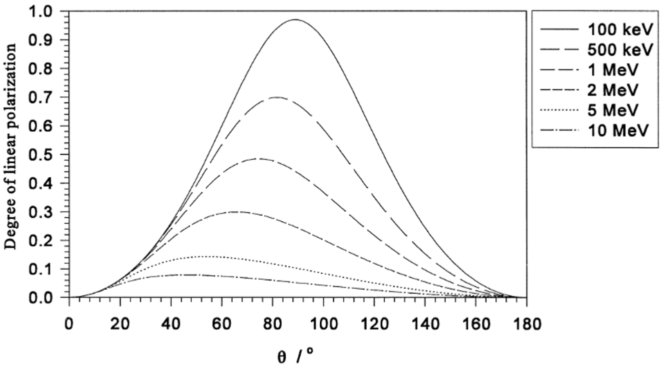

Figure 2.26: Degree of linear polarization Π_U of the scattered photon, as a function of the scattering angle θ in degree, in the Compton scattering process when the incoming photon is unpolarized. *Image from* [118]

rotation of the angle ϕ. Nevertheless, the scattering imprints a linear polarization in the scattered photon which is quantified by the *degree of linear polarization* of the scattered photon Π_U [118]:

$$\Pi_U = \frac{\sin^2\theta}{\frac{E_o}{E_i} + \frac{E_i}{E_o} - \sin^2\theta} \tag{2.48}$$

The process described by eq. (2.48) is sketched in fig. 2.26. The maximum linear polarization of the outgoing photon is observed at lower energies E_i and scattering angles near 90°.

Eq. (2.46) is usually the basis for any teaching of Compton scattering, and it can be used to reconstruct the origin of the incoming photons. By inverting eq. (2.46), we can express the scattering angle as a function of the incoming and scattered photon energies. Using two detectors, the photon from the source performs Compton scattering in the first detector, the scattered photon is then detected by the second detector. If the first detector measured the energy deposited by the incoming gamma (in the form of the scattered electron), and the second detector measured the energy of the scattering photon, it is possible to calculate the scattering angle θ with eq. (2.46). This angle corresponds approximately to the angle between the line connecting the centers of the two detectors and the direction of the incoming photon. A device applying this principle is called a *Compton Camera* (CC) and it has found great applications in high-energy astrophysics [116, 118]. Many space telescopes with CC have been launched in orbit to study the gamma rays from different astronomical sources, including the always present 511 keV photons from the positron annihilation. The most famous telescopes with CC are NASA's Imaging Compton Telescope (COMPTEL) and ESA's International Gamma-Ray Astrophysics Laboratory (INTEGRAL). Recently, Compton cameras have been studied for reconstructing the annihilation point of the positron in a Positron Emission Tomography (PET) [119].

2.3.2.1.2 Scattering of Linearly Polarized Photons The Klein-Nishina cross-section in eq. (2.47) is obtained by integrating over all possible spin directions of the incoming photon (corresponding to its polarization) and of the electron. If we integrate

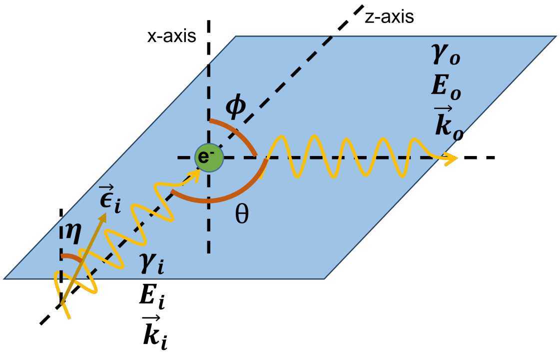

Figure 2.27: Diagram for Compton scattering for linearly polarized incoming photons with an electron e^-. The incoming photon γ_i is moving in the direction $\vec{k}_i$ along the z-axis with energy E_i and polarization $\vec{\epsilon}_i$ at an angle η with respect to the x-axis. The scattered photon γ_o has energy E_o and it is moving in the direction $\vec{k}_o$. The scattering plane is identified in blue and it is inclined by an angle ϕ with respect to the x-axis. $\vec{k}_i$ and $\vec{k}_o$ reside in the scattering plane with the scattered photon directed at an angle θ with respect to the incoming photon.

only over all possible electron spin directions, we obtain the Klein-Nishina cross-section for linearly polarized incoming photons:

$$\frac{d\sigma_{KN,P}}{d\Omega}, = \frac{r_0^2}{2}\frac{E_o^2}{E_i^2}\left(\frac{E_o}{E_i} + \frac{E_i}{E_o} - 2\sin^2\theta\cos^2[\eta - \phi]\right) \tag{2.49}$$

where θ and ϕ are the angles that define the direction of the scattered photon, and η is the angle that defines the direction of the incoming photon polarization $\hat{\epsilon}_i$. The scheme showing the reference system with the angles is reported in fig. 2.27. To better visualize the three angles, we consider a spherical coordinate system with the origin at the scattering point and the incoming gamma direction $\hat{k}_i$ along the z-axis. In this reference frame, the angle θ corresponds to the inclination with respect to the z-axis and it has values ranging between $0 \leq \theta < 90°$, and it is called the scattering angle. The angle ϕ represents the rotation of the projection on the xy-plane of the scattered gamma direction $\hat{k}_o$, it has values ranging between $0 \leq \phi < 360°$ and it is called azimuthal angle. Due to our axis definition, $\hat{\epsilon}_i$ can only be in the xy-plane and its direction is defined by the polarization azimuthal angle η. Furthermore, the scattered photon is still linearly polarized, and eq. (2.48) becomes:

$$\Pi_P = 2\frac{1 - \sin^2\theta\cos^2\eta}{\frac{E_o}{E_i} + \frac{E_i}{E_o} - 2\sin^2\theta\cos^2[\eta - \phi]} \tag{2.50}$$

2.3.2.1.3 Compton Polarimetry A polarimetry measurement needs to extract the polarization degree of the incoming photon and the direction of its polarization η. The polarization of the incoming photon breaks the rotational symmetry of the system around the z-axis. This is traduced by eq. (2.49) in a non-uniformity in the distribution of the cross-section as a function of the azimuthal angle ϕ for a fixed scattering angle θ, as we can see in fig. 2.28. This non-uniformity is periodic with period π and it has maximum and minimum 90° between each other. The intensity of this non-uniformity is

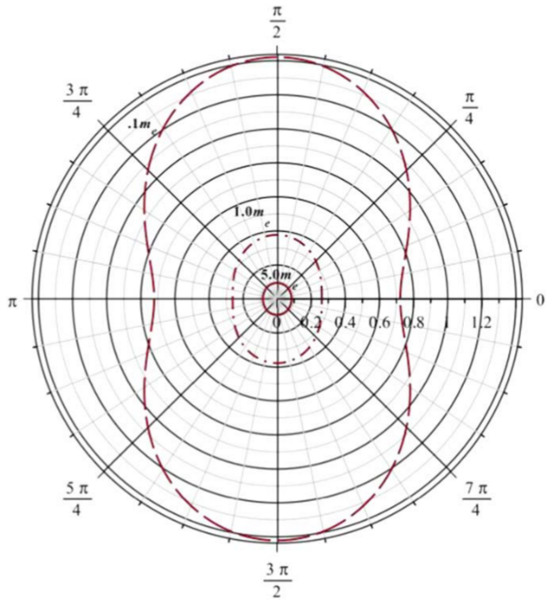

Figure 2.28: Polar plot of the Klein-Nishina cross-section from eq. (2.49) as a function of the azimuthal angle ϕ for different energies of the incoming photon (these energies are shown in units of $m_e = 511\,\text{keV}$). The scattering angle is fixed at $\theta = 45°$, while the polarization of the incoming photon is along the x-axis: $\eta = 0°$. *Image from* [116]

related to the energy E_i and the degree of linear polarization of the incoming photons. The distribution of the cross-section as a function of the angle ϕ, at a given scattering angle θ, gives the direction of the polarization angle η through eq. (2.49).

As seen in fig. 2.28, the energy of the incoming photon represents a limiting factor for Compton polarimeters. Similarly to what was previously discussed for fig. 2.26, the non-uniformity in the cross-section is less pronounced at higher values of E_i, for $E \gg 511\,\text{keV}$ it becomes difficult to identify non-uniformity in the distributions, making the cross-section indistinguishable between unpolarized and linearly polarized photons.

In the energy range where the Compton polarimetry is applicable, the polarization azimuthal angle η corresponds to the value of ϕ which minimizes the distribution of the cross-section at fixed scattering angle θ. In fig. 2.30, the minimum is in 0 with periodicity π. Regarding, instead, the degree of linear polarization for the incoming photon, we start by quantifying the non-uniformity in the cross-section distribution with the *modulation factor* (also called *visibility*):

$$\begin{aligned} Q &= \frac{N_\perp[\phi] - N_{||}[\phi]}{N_\perp[\phi] + N_{||}[\phi]} = \frac{N[\eta + 90°] - N[\eta]}{N[\eta + 90°] - N[\eta]} \\ &= \frac{d\sigma[\theta, \eta + 90°] - d\sigma[\theta, \eta]}{d\sigma[\theta, \eta + 90°] + d\sigma[\theta, \eta]} = \frac{\sin^2\theta}{\frac{E'}{E} + \frac{E}{E'} - \sin^2\theta} \end{aligned} \tag{2.51}$$

Where $N_\perp[\phi]$ and $N_{||}[\phi]$ are the number of photons that are scattered perpendicular and parallel to the direction of the incoming photon polarization, respectively.

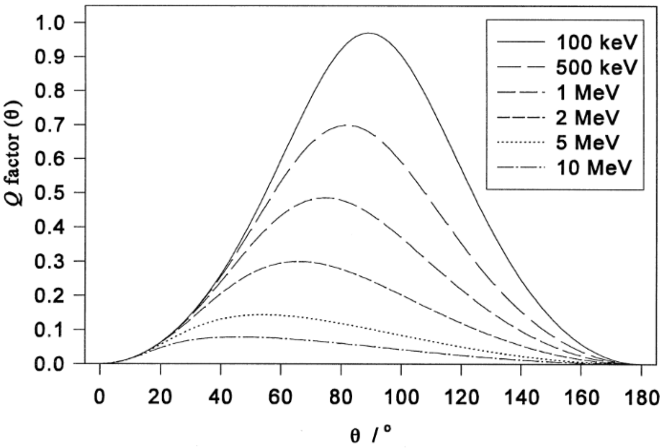

Figure 2.29: Modulation factor Q as a function of the scattering angle (see eq. (2.51)) for different energies of the incoming photons. *Image from* [118]

The modulation factor Q strongly depends on the scattering angle θ. As we can see from the plot of eq. (2.51) in fig. 2.29, the behavior of the modulation factor is similar to the degree of polarization Π_U (eq. (2.48)) of the scattered photons in the case of unpolarized incoming photons, see fig. 2.26. For each energy, we have a maximum Q at a different angle. The angle θ corresponding to the peak of Q decreases with the increase of the incoming photon energy. This helps maximize the non-uniformity in the azimuthal angle ϕ of the cross-section distribution, this optimization is important for incoming photon energies $E_i > 511\,\text{keV}$ where it is more difficult to detect the non-uniformity. In the case of positron annihilation gammas, the maximum of the modulation factor Q is at $\sim 82°$ for 511 keV and $\sim 90°$ for the $\sim 100\,\text{keV}$ photons from o-Ps annihilation.

A Compton polarimeter, usually, works at a fixed scattering angle θ and it acquires the number of scattered photons at different azimuthal angles ϕ. These data can be visualized in polar coordinates (see fig. 2.28) or in linear coordinates (see fig. 2.30). In both cases, the Klein-Nishina cross-section is a function of $\cos^2(\eta-\phi)$, but it is simplified to a shape of the type:

$$C(\eta) = A\cos\left[2\left(\eta-\phi+\frac{\pi}{2}\right)\right]+B \tag{2.52}$$

where A, B, and η are parameters that are fitted on the measured cross-section curve to determine the polarization azimuthal angle η and the degree of polarization of the beam of the incoming photons. To calculate the degree of polarization, we start determining from the fit parameters a quantification of the non-uniformity in the cross-section distribution. We define a *polarization modulation factor* μ_p as:

$$\mu_p = \frac{C_{max}-C_{min}}{C_{max}+C_{min}} = \frac{A}{B} \tag{2.53}$$

From μ_p, it is finally possible to obtain the degree of polarization of the incoming gamma as:

$$P_\gamma = \frac{\mu_p}{\mu_p^{100\%}} \tag{2.54}$$

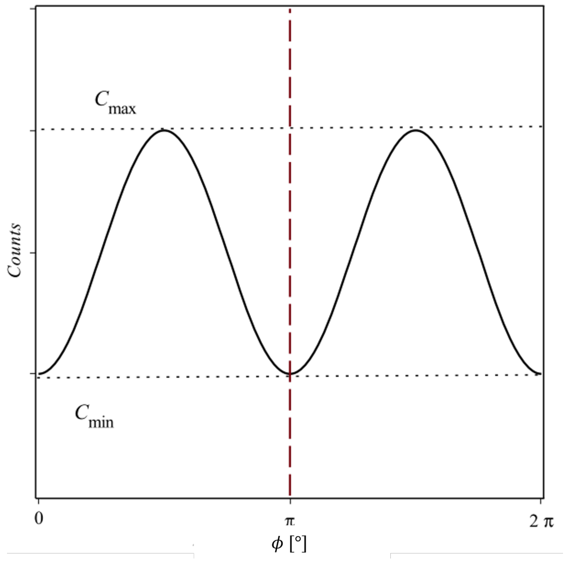

Figure 2.30: Theoretical representation of the non-uniformity in the cross-section distribution for Compton scattering with linearly polarized photons as described by eq. (2.52). The dotted lines show the minimum and maximum of the distribution, while the dashed line indicates the position of the cross-section distribution minimum corresponding to the polarization azimuthal angle $\eta = \pi$. *Image from* [116].

where $\mu_p^{100\%}$ is the modulation factor for a fully polarized photon beam. The value of $\mu_p^{100\%}$ is the calibration of the polarimeter, which sometimes is done with a computational model of the instrument due to difficulties in obtaining a fully polarized beam of gamma-rays.

Another important parameter of a Compton polarimeter is the minimum detectable degree of photon polarization, MDP:

$$MDP = \frac{n_\sigma}{S_f A_{eff} Q}\sqrt{\frac{S_f A_{eff} + B_r}{T}} \tag{2.55}$$

where

- n_σ quantifies the significance level;
- B_r is the background counting rate;
- S_f is the source flux;
- $A_{eff} = \epsilon A$ is the detector effective area given by the detector efficiency ϵ and the detection area A;
- T is the observation time.

2.3.2.1.4 Compton scattering detectors The detectors designed to measure the polarization of low-energy gammas are called *Compton polarimeters* and they can be divided into three categories based on the kind of detection elements used (the categories are analogous to the ones for Compton cameras).

- **Discrete Compton Polarimeter.** The easiest Compton polarimeter to implement makes use of two elements: the scatterer and the absorber. The first element is positioned along the incoming photon path as the scattering point, the second one is positioned on a plane perpendicular to the direction of the incoming photon to detect the scattered photon at a fixed scattering angle. This design was presented by Metzger and Deutsch in a 1950 paper [120]. The design was based on the system proposed for the reconstruction of correlation in annihilation radiation of positron [9], which we will discuss in the next chapter. In the Metzger and Deutsch's design the absorber is moved around the scatter to reconstruct the Klein-Nishina cross-section as a function of the azimuthal angle ϕ, and by fitting eq. (2.52) the polarization direction is obtained. The absorber and scatterer can be the same or composed of materials that are optimized for their application. As shown in fig. 2.24, the gamma-rays have a preferred way of interacting with the material which depends on their energy and on the material. So ideally the scatterer is made of a light material for which Compton scattering is the main interaction process. For the absorber, instead, photoelectric absorption is needed to measure the total energy of the outgoing photon, so scintillator materials like NaI(Tl) are preferred. The setup can be made more complicated. While two scintillators are enough, the reconstruction of the angular distribution of the cross-section requires a long measurement time. The required time can be reduced with the use of multiple detectors to measure the scattered photon [121, 122]. However, the use of more than two detectors increases the cost and complexity of the implementation, and if the detectors are fixed, this limits the number of acquired points of the cross-section distribution. In this case, the solution would be to have the detector near each other and as small as possible, but then we fall into the following polarimeter categories.

- **Pixellated Compton Polarimeter.** The limit case discussed earlier can be realized with a pixellated detector. In this implementation of the Compton polarimeter, any one pixel can work as a scattering center and any other can detect the scattered photon. This compact system does not require moving parts. However, the work on the physical movement of the absorber is changed into computational work of the signals analysis. The signals from each pixel need to be recorded and analyzed. Through the use of thresholds in the hit time and energy deposition, the signal of the incoming photon and of the respective scattered photon can be found. Moreover, in the case of pixellated scintillators, the form and dimensions of the pixel play an important role in the capabilities of the final setup.

  - *Form.* Pixels can be in two main designs: hexagonal or square. The former gives a more uniform response function and so better performance, the square shape is the most used due to the simple design and easier manufacturing process.
  - *Size.* Smaller pixels are needed for higher resolutions, but they are costly and more susceptible to cross-talk and other multi-pixel phenomena.
  - *Thickness.* Thicker pixels have higher efficiency but require more sensible photodetectors and materials.

These complications make pixelate polarimeter costly. Nevertheless, they are still used in applications where the coverage of the detection area is important like the Compton polarimeters for space [118] and PET [123].

- **Cluster Compton Polarimeter.** The cluster Compton polarimeter is a middle ground between the previous two cases. They are composed of a cluster of scintillators similar to a pixellated detector but with a low pixel number (typically four) and pixel size in the centimeter range. An example of this kind of polarimeter is the clover Ge detector where four HPGe crystals are positioned as the leaves of a four-leaf clover [124]. This polarimeter is mostly used in nuclear spectroscopy.

All the previous cases make use of eq. (2.52) to reconstruct the linear polarization of the incoming photon. However there are cases in which the polarization is circular (right- or left-handed), then the previous polarimeters would yield a symmetric cross-section due to the absence of a preferred polarization direction in the xy-plane for the circular polarization. For right- and left-handed polarization of a photon, we intend that its spin is aligned or anti-aligned with the photon momentum, respectively. In this case, we have to use the Klein-Nishina cross-section for polarized electrons and incoming photons [125]. In this condition, the photon is scattered preferably in the forward direction if the spin of the incoming photon and of the electron are aligned. The polarized electrons are obtained, for example, from iron in a magnetic field which is used as the scattering point. This idea came from reference [125] and it was first used with annihilation radiation [126]. This technique found great success in the '50s in the measurement of parity symmetry breaking for the β decay [127–129]. In the case of positron annihilation photons, the work of Clay and Hereford shown in reference [126] is the only one that studies the circular polarization of the emitted photons. We will discuss in detail the experimental setup in section 3.4 of the next chapter.

Chapter 3

Positron Annihilation and Entanglement

In 1935, Einstein, Podolsky, and Rosen questioned the completeness of the quantum mechanics theory with what now is known as EPR (Einstein, Podolsky, and Rose) paradox [130]. Nowadays, visible photons are the best benchmark to test this paradox, however, the annihilation gamma-rays had an extremely important historical role in the experimental study of the EPR paradox.

3.1 EPR paradox & Entanglement

In reference [130], the authors discussed the probabilistic nature of quantum mechanics from the point of view of classical mechanics.

Classical mechanics is deterministic: we can determine the evolution of a system if we know the forces acting on the system and its initial conditions, i.e. the position and velocity vectors of all system elements. However, it is not always possible to determine the initial condition of our system, especially when the system is composed of a high number of elements. For these complex systems, it is not possible to reconstruct the exact evolution of the system but it is possible to describe its behavior with statistical mechanics, which provides a probabilistic description of the system evolution.

Einstein, Podolsky, and Rosen considered nature to always be deterministic. Then, quantum mechanics only gives us, according to them, a non-complete description of the quantum world like statistical mechanics, so we miss some knowledge of the system. This missing knowledge was represented by a variable λ, called *hidden variable*, with which quantum mechanics becomes a complete theory of the quantum world describing it deterministically [130, 131].

The *complete* quantum mechanics, as introduced in reference [130], should also solve the non-locality of quantum phenomena like entanglement. The EPR paradox was constructed to demonstrate the violation of the locality principle of special relativity by quantum mechanics. The EPR paradox and the hidden variables have been at the center of the discussion on the completeness of quantum mechanics since the Einstein, Podolsky, and Rosen's paper. Nowadays the existence of the entanglement has been demonstrated thanks also to decades of work on the study of the two gammas from the positron annihilation, proving the completeness of quantum mechanics. To describe the relation between

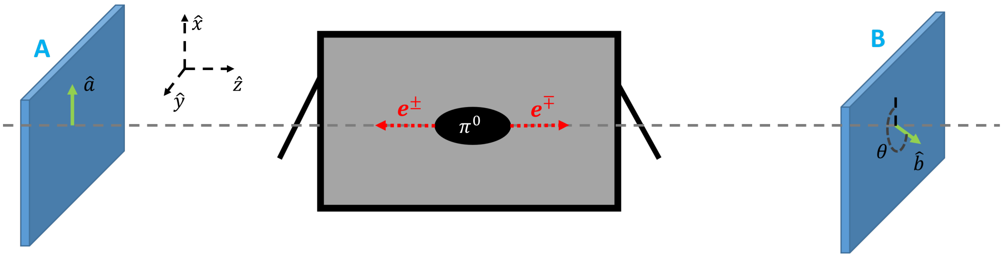

Figure 3.1: Scheme of the EPRB experiment. The neutral pion π^0 decays in a positron-electron couple inside a black box. The two particles are emitted in counterpropagating directions along the z-axis. The polarimeters A and B are used to measure the particle spin along the directions $\hat{a}$ and $\hat{b}$, respectively. The direction $\hat{a}$ is aligned with the x-axis, while there is an angle θ between the direction $\hat{b}$ and the x-axis.

entanglement and positrons, we start with a simplified description of the gedankenexperiment at the basis of the EPR paradox as presented in the 1950s by Bohm, also called the EPRB (Einstein, Podolsky, Rose, and Bohm) experiment [131, 132].

3.1.1 EPRB gedankenexperiment

We start with a neutral pion π^0. It is one of the lightest mesons, a class of metastable hadronic particles composed of a quark and an anti-quark. In particular, π^0 is composed of the two lightest quarks:

$$\pi^0 = \frac{|u\bar{u}\rangle - |d\bar{d}\rangle}{\sqrt{2}} \tag{3.1}$$

where $|u\rangle$ and $|d\rangle$ are the up and down quarks, and $|\bar{u}\rangle$ and $|\bar{d}\rangle$ are the up and down anti-quarks. Like the positronium atom, the neutral pion is a spin-zero chargeless particle, an eigenvector of $\hat{C}$, and it decays mainly into two gammas, however, there are other probable decay paths for the pion. In the EPRB experiment, we consider the decay path of the neutral pion resulting in an electron-positron pair:

$$\pi^0 \rightarrow e^- + e^+ \tag{3.2}$$

For the same reason as discussed in section 2.1.4.2, the particle pair is emitted in the opposite direction for the conservation of momentum. We are now interested in the spins of the positron and electron. In this gedankenexperiment, we have two perfect polarimeters, A and B, which are capable of perfectly reconstructing the polarization direction of the positron/electron along the directions $\hat{a}$ and $\hat{b}$, respectively (see fig. 3.1).

The pion decay happens in a box in which we cannot see. The box has two openings on the opposite sides where the positron and electron can exit and they are then analyzed by the polarimeters A and B measuring their spin in the same direction ($\hat{a} = \hat{b}$). We now block the exit towards B. For any particle reaching the detector A, we have a probability of 50% to measure its polarization up ($\uparrow$ or $\Uparrow$) or down ($\downarrow$ or $\Downarrow$), i.e. the particle is non-spin polarized (non-SpPo). The same results are obtained by blocking the exit towards A and looking only at the polarimeter B. Both quantum mechanics and

Einstein, Podolsky, and Rosen agree on these results, the disagreement is on the results with both exits opened.

For quantum mechanics, the polarization direction of one particle depends on the direction of the other. Because the starting pion has a total angular momentum of zero, the positron and electron are emitted with spin in opposite directions for the conservation of the angular momentum in the decay. Then, if A measures a spin-up, B can only measure spin-down, and vice-versa:

$$|\pi^0\rangle_{e^\pm} = \frac{\Uparrow\downarrow - \Downarrow\uparrow}{\sqrt{2}} \tag{3.3}$$

In the framework of classical determinism, this result was interpreted by Einstein, Podolsky, and Rosen as the incompleteness of the quantum mechanics: after leaving the box the two particles do not interact with each other, so classically they cannot influence each other spin. If the two particles are still influencing each other after the decay, then this system breaks the locality principle which originates from the speed limit in the information transfer given by the speed of light. There are only two possible conclusions for Einstein, Podolsky, and Rosen: the quantum mechanics prediction eq. (3.3) is wrong, or the quantum mechanics is an incomplete theory and there exists a hidden variable that explains the measurement in the framework of classical determinism. Given the experimental verification of quantum mechanics in the first half of the XX century, Einstein, Podolsky, and Rosen concluded, from the EPR paradox, the existence of a hidden variable that completes quantum mechanics in a theory capable to determine the state of the system at any time knowing the evolution law and the initial conditions. This idea started the theoretical work on hidden variable theories, where different hidden variables were postulated, in the hope one of them could be experimentally found to complete quantum mechanics. This theoretical field was very active until the 1980s. However, up to now quantum mechanics has been demonstrated to be a solid theory and the probabilistic nature of reality has become a solid fact in physics. In fact, eq. (3.3) represents an example of the quantum phenomenon of *entanglement*. This does not break the locality principle because the two particles are not communicating with each other, there is no transfer of information.

While the neutral pion is used in this gedankenexperiment, similar behavior can be identified in other particles. Para-positronium is also a neutral chargeless particle that annihilates in two counterpropagating particles (see section 2.1.4.2). So eq. (3.3) can be extended to the linear polarization of the annihilation gammas from p-Ps, and this can be measured with Compton polarimeters as discussed in section 2.3.2.1.

3.1.2 Entanglement: quantification and Bell states

In general, a system is entangled if the state of a part of the system cannot be defined without the knowledge of the state of another part of the system. For example, in the case of eq. (3.3), the spin state of one particle is defined only from the knowledge of the spin state of the other particle spin, the single particle spin is undefined otherwise. Formally, each particle state is defined in a Hilbert space $|particle\rangle \in \mathcal{H}_{particle}$, so a system composed of two particles $|A\rangle \in \mathcal{H}_A$ and $|B\rangle \in \mathcal{H}_B$ is:

- **Entangled:** A system is entangled if its state $|system\rangle$ cannot be separate in the state of particle A and particle B: $|system\rangle \neq |A\rangle \otimes |B\rangle \Rightarrow |system\rangle \notin \mathcal{H}_A \otimes \mathcal{H}_B$, where $\otimes$ is the tensor product.
- **Separable:** A system is not entangled, so separable, if its state can be divided into the states of the single elements: $|system\rangle = |A\rangle \otimes |B\rangle \Rightarrow |system\rangle \in \mathcal{H}_A \otimes \mathcal{H}_B$.

The entanglement of a system can be quantified. Because the entanglement is related to the mixing of the states composing the system, a state $|\psi\rangle = \frac{\Uparrow\downarrow - \Downarrow\uparrow}{\sqrt{2}}$ is more entangled than a state $|\psi\rangle = (\sqrt{p} \Uparrow\downarrow - \sqrt{1-p} \Downarrow\uparrow)$ with $p < 1/2$. In the first case, the two combinations are equiprobable, in the second case, a particular combination of the two particles' spins is preferred. A way to quantify the difference in the entanglement of the two states is with the information that can be gained with a measurement of the state, but first, we need to introduce the density matrix of the system ρ_{system}.

3.1.2.1 Pure and Mixed States

We can describe a quantum system state in terms of the probabilities of the measurement results. A system that can be in states $|\phi_i\rangle \in \mathcal{H}$ with probability p_i is described in terms of its density matrix [133]:

$$\rho_{system} = \sum_i p_i |\phi_i\rangle \langle\phi_i| \tag{3.4}$$

with the conditions: $\sum_i p_i = 1$ and $p_i \geq 0$. Take for example the following systems $|\psi_1\rangle$, $|\psi_2\rangle$, and $|\psi_3\rangle$:

- $|\psi_1\rangle = |\downarrow\rangle \Rightarrow \rho_1 = |\downarrow\rangle\langle\downarrow|$
- $|\psi_2\rangle = \frac{|\Uparrow\uparrow\rangle - |\Downarrow\downarrow\rangle}{\sqrt{2}} \Rightarrow \rho_2 = \frac{1}{2}|\Uparrow\uparrow\rangle\langle\Uparrow\uparrow| - \frac{1}{2}|\Uparrow\uparrow\rangle\langle\Downarrow\downarrow| - \frac{1}{2}|\Downarrow\downarrow\rangle\langle\Uparrow\uparrow| + \frac{1}{2}|\Downarrow\downarrow\rangle\langle\Downarrow\downarrow|$
- $|\psi_3\rangle = \frac{|\Uparrow\downarrow\rangle - |\Downarrow\uparrow\rangle}{\sqrt{2}} \Rightarrow \rho_3 = \frac{1}{2}|\Uparrow\downarrow\rangle\langle\Uparrow\downarrow| - \frac{1}{2}|\Uparrow\downarrow\rangle\langle\Downarrow\uparrow| - \frac{1}{2}|\Downarrow\uparrow\rangle\langle\Uparrow\downarrow| + \frac{1}{2}|\Downarrow\uparrow\rangle\langle\Downarrow\uparrow|$

Each system can be described in matrix form (the elements outside the matrix parentheses are only there as a guide):

$$\begin{gathered}
\rho_1 = \begin{array}{c} \\ |\downarrow\rangle \\ |\uparrow\rangle \end{array} \begin{array}{c} \begin{array}{cc} \langle\downarrow| & \langle\uparrow| \end{array} \\ \begin{pmatrix} 1 & 0 \\ 0 & 0 \end{pmatrix} \end{array}; \quad
\rho_2 = \begin{array}{c|cccc} & \langle\Downarrow\downarrow| & \langle\Downarrow\uparrow| & \langle\Uparrow\downarrow| & \langle\Uparrow\uparrow| \\ \hline |\Downarrow\downarrow\rangle & 1/2 & 0 & 0 & -1/2 \\ |\Downarrow\uparrow\rangle & 0 & 0 & 0 & 0 \\ |\Uparrow\downarrow\rangle & 0 & 0 & 0 & 0 \\ |\Uparrow\uparrow\rangle & -1/2 & 0 & 0 & 1/2 \end{array}; \\
\rho_3 = \begin{array}{c|cccc} & \langle\Downarrow\downarrow| & \langle\Downarrow\uparrow| & \langle\Uparrow\downarrow| & \langle\Uparrow\uparrow| \\ \hline |\Downarrow\downarrow\rangle & 0 & 0 & 0 & 0 \\ |\Downarrow\uparrow\rangle & 0 & 1/2 & -1/2 & 0 \\ |\Uparrow\downarrow\rangle & 0 & -1/2 & 1/2 & 0 \\ |\Uparrow\uparrow\rangle & 0 & 0 & 0 & 0 \end{array}
\end{gathered} \tag{3.5}$$

The density matrix form is fundamental to visualize quantum systems in a mixed state. The systems described until now are represented as a linear combination of the basis vectors, i.e.

- $|\downarrow\rangle$ and $|\uparrow\rangle$ for the spin of a single particle,
- $\langle\Downarrow\downarrow|$, $\langle\Downarrow\uparrow|$, $\langle\Uparrow\downarrow|$, and $\langle\Uparrow\uparrow|$ for the spins of two particle,

and they take the name of *pure states*. If the system cannot be written as a linear combination of basic vectors, it is called *mixed state*. In this case, the system cannot be written as a wavefunction $|\psi_{System}\rangle$, but it can only be described in terms of density matrix ρ_{System}. As well as pure states, also mixed states can be entangled. Mixed states are entangled when the system density matrix cannot be written as the tensor product of the density matrices of the system elements [133].

Experimentally, the procedure to reconstruct the system density matrix (both for pure and mixed states) is called *quantum state tomography* [134]. While this is the direct and complete way to compare the experimental results with the theoretical expectation, the experimental process is complex and costly. As seen in the previous examples, the matrix dimension increases factorially with the element number. Then for a system of two particles, we need to study $2(2!) = 16$ possible configuration of the two-particle states, and we need to measure the probability of each configuration.

3.1.2.2 Von-Neuman Entropy

We consider a system in a pure state with a density matrix ρ, the system is composed of two subsystems A and B. We construct the sub-matrix ρ_A as the tracing out of the other subsystem from ρ: $\rho_A = \mathrm{Tr}_B[\rho] = \sum_i p_i |\phi_i\rangle\langle\phi_i|$, where Tr is the matrix trace and p_i is the probability of the subsystem B to be in the state $|\phi_i\rangle$. We can define ρ_B in the same way. Considering the two-particle systems ψ_1 and ψ_2 from the previous section, we obtain the sub-matrices ρ_A:

- $|\psi_2\rangle = \frac{|\Uparrow\uparrow\rangle - |\Downarrow\downarrow\rangle}{\sqrt{2}} \Rightarrow \rho_2 \Rightarrow \rho_A = \frac{1}{2}(|\Downarrow\rangle\langle\Downarrow| - |\Uparrow\rangle\langle\Uparrow|)$
- $|\psi_3\rangle = \frac{|\Uparrow\downarrow\rangle - |\Downarrow\uparrow\rangle}{\sqrt{2}} \Rightarrow \rho_3 \Rightarrow \rho_A = \frac{1}{2}(|\Downarrow\rangle\langle\Downarrow| - |\Uparrow\rangle\langle\Uparrow|)$

We quantify the entanglement between the two subsystems with the *von Neumann entropy* [135]:

$$S_{VN}[\rho_A] = S_{VN}[\rho_B] = -\mathrm{Tr}[\rho_A \log \rho_A] = -\sum_i p_i \log p_i \tag{3.6}$$

In particular $-\log p_i$ is the information on the system gained if the event $|\phi_i\rangle$ occurs. Some examples:

- $|\psi\rangle = |\Uparrow\uparrow\rangle \Rightarrow \rho = |\Uparrow\uparrow\rangle\langle\Uparrow\uparrow| \Rightarrow \rho_A = |\Uparrow\rangle\langle\Uparrow| \Rightarrow S_{VN}[\rho_A] = -1\log 1 = 0$
- $|\psi_2\rangle = \frac{|\Uparrow\uparrow\rangle - |\Downarrow\downarrow\rangle}{\sqrt{2}} \Rightarrow \rho_2 \Rightarrow \rho_A = \frac{1}{2}(|\Downarrow\rangle\langle\Downarrow| - |\Uparrow\rangle\langle\Uparrow|)$
  $\Rightarrow S_{VN}[\rho_A] = 2(-\frac{1}{2}\log[1/2]) = \log 2$
- $|\psi_3\rangle = \frac{|\Uparrow\downarrow\rangle - |\Downarrow\uparrow\rangle}{\sqrt{2}} \Rightarrow \rho_3 \Rightarrow \rho_A = \frac{1}{2}(|\Downarrow\rangle\langle\Downarrow| - |\Uparrow\rangle\langle\Uparrow|)$
  $\Rightarrow S_{VN}[\rho_A] = 2(-\frac{1}{2}\log[1/2]) = \log 2$
- $|\psi_4\rangle = \sqrt{0.9}\,|\Uparrow\uparrow\rangle + \sqrt{0.1}\,|\Downarrow\downarrow\rangle \Rightarrow \rho_A = (0.1\,|\Downarrow\rangle\langle\Downarrow| + 0.9\,|\Uparrow\rangle\langle\Uparrow|)$
  $\Rightarrow S_{VN}[\rho_A] = -0.1\log[0.1] - 0.9\log[0.9] \in [0, \log[2]]$

In general, the von Neumann entropy gives values in the range $S_{VN}[\rho_A] \in [0, \log[d_A]]$, where $d_A = dim\mathcal{H}_A$ is the dimension of the Hilbert space of the subsystem A. Then, by definition, we have the following relations:

- $S_{VN} > 0$: the system is entangled, the state of one subsystem is inseparable from the other subsystem;
- $S_{VN}[\rho_A] > S_{VN}[\rho_{A'}]$: the first system is more entangled than the second, like $|\psi_3\rangle$ compared to $|\psi_4\rangle$;
- $S_{VN} = \log[d]$: the system is maximally entangled, like $|\psi_2\rangle$ and $|\psi_3\rangle$.

In the case of two-particle systems, the maximally entangled states are called *Bell's states* and they are:

$$|\Phi^{\pm}\rangle = \frac{1}{\sqrt{2}}(|\Uparrow\uparrow\rangle \pm |\Downarrow\downarrow\rangle) \qquad |\Psi^{\pm}\rangle = \frac{1}{\sqrt{2}}(|\Uparrow\downarrow\rangle \pm |\Downarrow\uparrow\rangle) \tag{3.7}$$

All four states have von Neumann entropy log[2], and they form four orthogonal bases.

3.1.3 EPR paradox and Hidden variable theories: Bell's inequality

In 1964, Bell enunciated a theorem allowing the experimental demonstration of completeness of the quantum mechanics, i.e. if the presence of hidden variable can be excluded [136].

Bell's idea is to determine a measurement procedure that highlights the probabilistic nature of the system. We consider the example of the EPRB gedankenexperiment [131]. The neutral pion decays in an electron and a positron and the spins of the two particles are measured with two polarimeters aligned along two generic directions $\hat{a}$ and $\hat{b}$ (see fig. 3.1). So, for each pion annihilation, we record the polarimeters' directions $(\hat{a}, \hat{b})$, and the measured spin for each polarimeter is registered as +1 for ↑ (or ⇑) and −1 for ↓ (or ⇓). For each configuration $(\hat{a}, \hat{b})$, we can define a mean value of the product of the measured spin of the single polarimeter $P[\hat{a}, \hat{b}]$. In the case of π^0 annihilation, if the polarimeters are aligned along the same direction ($\hat{b} = \hat{a}$), we obtain $P[\hat{a}, \hat{b}] = P[\hat{a}, \hat{a}] = -1$ because the particles have opposite spins as seen in eq. (3.3). If, instead, the polarimeters are aligned in opposite directions $\hat{b} = -\hat{a}$, the resulting mean value is $P[\hat{a}, \hat{b}] = P[\hat{a}, -\hat{a}] = +1$.

The two polarimeters are positioned far enough that, within the limit of the speed of light, they cannot influence each other by communicating the results of the measurement before both measurements are done.

Quantum Mechanics The π^0 decay generates an electron and a positron whose spins are related as expressed in eq. (3.3). We define the z-axis along the direction of propagation of the two particles and the x-axis along the direction of polarimeter A ($\hat{a} = \hat{x}$) as seen in fig. 3.1. Then the direction of the polarimeter B is in the xy-plane at an angle θ with respect to the x-axis ($\hat{b} = \cos\theta\hat{x} + \sin\theta\hat{y}$). The mean value of the product of the results of the two polarimeters in the frame of quantum mechanics $P_{QM}[\hat{a}, \hat{b}]$ is [131]:

$$P_{QM}[\hat{a}, \hat{b}] = \frac{4}{\hbar^2}\langle S_{\hat{a}} S_{\hat{b}}\rangle = -\cos\theta = -\hat{a}\cdot\hat{b} \tag{3.8}$$

Hidden variable theory The measurement results of the two polarimeters would be affected by the eventual presence of a hidden variable λ, so we represent the result of the two polarimeters with the functions $A[\hat{a},\lambda] = \pm 1$ and $B[\hat{b},\lambda] = \pm 1$. If $\hat{b} = \hat{a}$, then $B[\hat{a},\lambda] = -A[\hat{a},\lambda]$ for any value of λ. For any configuration of the two directions $\hat{a}$ and $\hat{b}$, the mean value of the product of the results of the two polarimeters in the frame of any hidden variable theory $P_{HV}[\hat{a},\hat{b}]$ is:

$$P_{HV}[\hat{a},\hat{b}] = \int p[\lambda] A[\hat{a},\lambda] B[\hat{b},\lambda] d\lambda \tag{3.9}$$

where $p[\lambda]$ is the probability density of the hidden variable. The value of $p[\lambda]$ depends on the particular hidden variable theory, however, the following discussion is independent of the value of $p[\lambda]$ if it follows the conditions of a probability density, i.e. non-negative values and normalization $\int p[\lambda] d\lambda = 1$. Using the previous relations, we have $P_{HV}[\hat{a},\hat{b}] = -\int p[\lambda] A[\hat{a},\lambda] A[\hat{b},\lambda] d\lambda$. Considering a general direction $\hat{c}$, we construct the following inequality called Bell's inequality [131]:

$$\begin{aligned} |P_{HV}[\hat{a},\hat{b}] - P_{HV}[\hat{a},\hat{c}]| &\leq |\int p[\lambda] \Big(A[\hat{a},\lambda] A[\hat{b},\lambda] - A[\hat{a},\lambda] A[\hat{c},\lambda] \Big) d\lambda| \\ &= |\int p[\lambda] \Big(1 - A[\hat{b},\lambda] A[\hat{c},\lambda] \Big) A[\hat{a},\lambda] A[\hat{b},\lambda] d\lambda| \\ &\leq |\int p[\lambda] \Big(1 - A[\hat{b},\lambda] A[\hat{c},\lambda] \Big) d\lambda| = 1 + P_{HV}[\hat{b},\hat{c}] \end{aligned} \tag{3.10}$$

This inequality is verified for hidden variable theories but not for quantum mechanics. For example, we consider the directions $\hat{a} = \hat{x}$, $\hat{b} = \hat{y}$, and $\hat{c}$ at 45° from $\hat{a}$. Using eq. (3.8), we have: $P_{QM}[\hat{a},\hat{b}] = 0$ and $P_{QM}[\hat{a},\hat{c}] = P_{QM}[\hat{b},\hat{c}] = -0.707$. Then the inequality verified by hidden variable theories is violated:

$$|P_{QM}[\hat{a},\hat{b}] - P_{QM}[\hat{a},\hat{c}]| = |0 + 0.707| \nleq 1 + P_{QM}[\hat{b},\hat{c}] = 1 - 0.707 = 0.293 \tag{3.11}$$

In conclusion, Bell provides a strong instrument to verify experimentally the existence of hidden variables. Given three possible directions of the polarimeters $\hat{a}$, $\hat{b}$, and $\hat{c}$, we calculated the mean value of the product of the measurements of the two polarimeters P_{EXP} in the configurations $(\hat{a},\hat{b})$, $(\hat{a},\hat{c})$, and $(\hat{b},\hat{c})$, then:

- if $|P_{EXP}[\hat{a},\hat{b}] - P_{EXP}[\hat{a},\hat{c}]| \leq 1 + P_{EXP}[\hat{b},\hat{c}]$ is verified, then the quantum world is deterministic and there exist a hidden variable which completes quantum mechanics;
- if $|P_{EXP}[\hat{a},\hat{b}] - P_{EXP}[\hat{a},\hat{c}]| \nleq 1 + P_{EXP}[\hat{b},\hat{c}]$ is verified, then all hidden variable theories with non-negative and normalized probability density are false.

Bell's inequality can be valid only for hidden variable theories that respect the previous condition on the probability distribution $p[\lambda]$. These theories are also called local hidden variable theories because they complete the quantum mechanics preserving the locality principle as they were introduced initially by Einstein, Podolsky, and Rosen.

There are other versions of Bell's inequality, one of the most famous is the Clauser, Horne, Shimony, and Holt (CHSH) inequality [137]. We consider two particles A and

B polarized along the directions $\hat{a}$ and $\hat{b}$, respectively. These directions form, with respect to the x-axis, an angle $\theta_{A/B}$, so the polarization state of the two particles can be written as $|\theta_{A/B}\rangle = \cos\theta_{A/B}\,|H\rangle_{A/B} + \sin\theta_{A/B}\,|V\rangle_{A/B}$ where $|H\rangle$ and $|V\rangle$ are the polarization states along the x and y-axis, respectively. Given the coincidence count for each polarization angle $C[\theta_A, \theta_B]$, the CHSH inequality is obtained from the S-function [134]:

$$S = |E[\theta_A, \theta_B] - E[\theta_A, \theta'_B] + [\theta'_A, \theta_B] + [\theta'_A, \theta'_B]| \leq 2 \tag{3.12}$$

where θ_A, $\theta'_A = 0, 45, 90, 135°$, θ_B, $\theta'_B = 22.5, 67.5, 112.5, 157.5°$,

$$E[\theta_A, \theta_B] = \frac{C[\theta_A, \theta_B] + [\theta_A^{\perp}, \theta_B^{\perp}] - C[\theta_A^{\perp}, \theta_B] - C[\theta_A, \theta_B^{\perp}]}{C[\theta_A, \theta_B] + [\theta_A^{\perp}, \theta_B^{\perp}] + C[\theta_A^{\perp}, \theta_B] + C[\theta_A, \theta_B^{\perp}]}, \tag{3.13}$$

and $\theta^{\perp}_{A/B} = \theta_{A/B} + 90°$.

In 1982, Aspect, Dalibard, and Roger observed experimentally the violation of Bell's inequality, demonstrating the absence of a local hidden variable as defined by most theories [138–140]. In the experiment, entangled optical photons were detected with two detectors far from each other and with detector settings changed just before the photon arrival, in order to limit the possibility of communication between the two detectors. Nevertheless, the low efficiency of the photon detectors introduces a *loophole* that still permits some hidden variable theories [133]. There are many possible ways in which the detectors can influence each other making it difficult to implement a *loophole-free* experiment of Bell's inequality, so some convoluted local hidden variable theories remained possible. Still, even with the demonstration of the violation of Bell's inequality with a loophole-free experiment, this does not exclude non-local hidden variable theories for which the $p[\lambda]$ does not satisfy the condition of a probability density. However, by their nature, these theories do not preserve the locality principle and the original meaning for the introduction of the hidden variables.

Aspect, Dalibard, and Roger's experiment is considered by most the first demonstration of the probabilistic nature of the quantum world. However, in the following sections, we will see how the gamma-rays from the annihilation of positrons have been used to study experimentally the existence of hidden variables before 1982.

3.2 Two Annihilation Gammas: Theory

Both thermal positron and p-Ps annihilate mainly in two counter-propagating gammas (see section 2.1.4). We discussed the conservation of energy and momentum in the annihilation process but not the consequences of the conservation of the angular momentum on the two annihilation gammas. In this section, we will see how the conservation of the angular momentum in the annihilation process defines the spin states of the resulting gammas. We start with the easier case: para-positronium [141].

As p-Ps has total spin and momentum equal to zero, the annihilation gammas are emitted isotropically. We set the z-axis along the direction of the gammas, and we describe their polarization in the circular polarization basis: right-handed ($|R\rangle$) or left-handed ($|L\rangle$). The photons have spin 1, which introduces an angular momentum to the system. If the gamma has polarization $|R\rangle$, the angular momentum is along the direction of motion, and its value is $+1$. If the gamma has polarization $|L\rangle$, the angular momentum

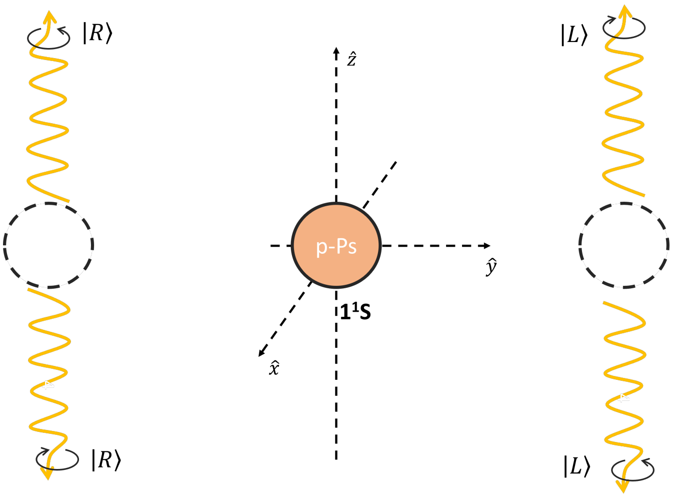

Figure 3.2: Possible polarization configurations of the gamma-rays from the annihilation of p-Ps. The positronium atom is in the energy level 1^1S and it self-annihilates into two counterpropagating gamma-rays along the z-axis.

is opposite to the direction of motion, and its value is -1. But, as previously said, the annihilation process conserves the angular momentum, so the angular momentum of the two annihilation photons needs to be zero: the two spins rotate in opposite directions. In conclusion, because the momenta of the gammas are also opposite, the two annihilation photons have the same circular polarization, and the possible spin states are only: $|RR\rangle$ or $|LL\rangle$, see fig. 3.2. Because both states are equally probable, the system is in a superposition of the two states after the annihilation, and the wavefunction of the two gammas is: $|F_{\pm}\rangle = \frac{1}{\sqrt{2}}(|RR\rangle \pm |LL\rangle)$

Let us now exchange the positron and electron in the p-Ps. Mathematically this corresponds to the application of the parity operator $\hat{P}$. From QED calculations, the parity operator $\hat{P}$ applied to p-Ps gives: $\hat{P}\,|0,0\rangle_{Ps} = (-1)\,|0,0\rangle_{Ps}$ [7, 141]. The parity is conserved during the annihilation, so the wavefunction of the two annihilation gammas has to satisfy the equation $\hat{P}\,|F\rangle_{\pm} = (-1)\,|F\rangle_{\pm}$. The parity operator on the gammas changes its polarization: $\hat{P}\,|R\rangle = |L\rangle$ and $\hat{P}\,|L\rangle = |R\rangle$. So we obtain [141]:

$$\hat{P}\,|F\rangle_{\pm} = \hat{P}\frac{1}{\sqrt{2}}(|RR\rangle \pm |LL\rangle) = \frac{1}{\sqrt{2}}(|LL\rangle \pm |RR\rangle) = \pm\,|F\rangle_{\pm} \tag{3.14}$$

The parity conservation is verified only by $|F\rangle_{-}$, the antisymmetric wavefunction. In conclusion, the two gammas wavefunction is:

$$|F\rangle = \frac{1}{\sqrt{2}}(|RR\rangle - |LL\rangle). \tag{3.15}$$

$|F\rangle$ is a Bell's state (see section 3.1.2), and the two gammas are maximally entangled in the polarization degree of freedom. The annihilation gammas of an unbound positron with an electron are also in the polarization state $|F\rangle$ of eq. (3.15), because also in this annihilation process the angular momentum of the electron-positron system can be considered zero [39].

Measuring the single annihilation gamma, from eq. (3.15), we have 50-50 chance to obtain $|R\rangle$ or $|L\rangle$. Once the polarization is determined for one gamma-ray, we know the circular polarization of the other. In a linear basis, instead, the polarization can be described in terms of horizontal $|H\rangle$, along the x-axis, and vertical $|V\rangle$, along the y-axis, polarization. In terms of electromagnetic radiation, it is polarized circularly when the electric field oscillates in the x and y direction out of phase. Analogously we can write the circular polarization as an out-of-phase ($e^{i\pi}$) superposition of the linear polarization [141]:

$$\begin{aligned} |R\rangle &= \frac{1}{\sqrt{2}}(|H\rangle + i\,|V\rangle) \\ |L\rangle &= \frac{1}{\sqrt{2}}(|H\rangle - i\,|V\rangle). \end{aligned} \tag{3.16}$$

Inserting eq. (3.16) in eq. (3.15), we obtain the linear polarization state of two annihilation gammas as:

$$|F\rangle = \frac{i}{\sqrt{2}}(|HV\rangle - |VH\rangle). \tag{3.17}$$

This is a Bell's state. Differently from the measurement in circular polarization, each of the two photons is unpolarized in a linear basis, but the polarization of the two is correlated: given the polarization direction of one photon, the other has a polarization at 90°.

3.3 Three Annihilation Gammas: Theory

As shown in fig. 3.3, the o-Ps annihilation generates preferably three gamma-rays which are emitted in a plane with a wide range of energy [63]. The analysis of the photons' polarization in this three-body system is complex.

The theoretical analysis of the three gammas polarization started in the second half of the last century with Drisko's results [41, 142, 143]. Nevertheless, Drisko's conclusions had some limitations. Firstly, the o-Ps was assumed non-SpPo, and the annihilation plane was fixed. Secondly, the results are given as the average of the three gammas' polarizations in selected configurations of the photons' emission angle. Only with the new century, new studies of o-Ps annihilation were published.

In 2001, Acín, Latorre, and Pascual explicitly showed, with QED calculations, the existence of an entangled state for all three spin states in the case of annihilation plane orthogonal to the polarization direction [144]. In 2011, Abel, Adkins, and Yoder extended the Drisko's results for SpPo o-Ps and for any configuration of the emission angles [145]. Only recently, these results have been extended to the general case of SpPo o-Ps annihilating from any spin state and annihilation plane [10].

Let us start with o-Ps in the state $|1,0\rangle_{Ps}$. The three gammas a, b, and c are ordered by energy $E_a \geq E_b \geq E_c$, and the Ps spin is aligned along the z-axis. The polarization wavefunction of the three photons is:

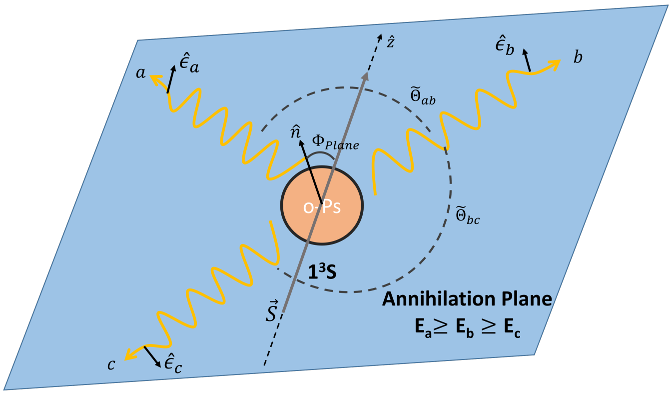

Figure 3.3: Annihilation scheme for the o-Ps. The positronium atom is in the 1^3S energy level with total spin 1 aligned along the z-axis. The o-Ps self-annihilates into three gammas a, b, and c emitted in a plane. The three gamma-rays are released in three directions forming the angles $\tilde{\Theta}_{ab}$ and $\tilde{\Theta}_{bc}$ between them and with a linear polarization $\hat{\epsilon}_a$, $\hat{\epsilon}_b$, and $\hat{\epsilon}_c$, respectively. The normal to the annihilation plane $\hat{n}$ is at an angle Φ_{Plane} with respect to the spin direction.

$$|\psi_{|1,0\rangle_{Ps}}\rangle = \frac{1}{\sqrt{N}}\left(\cos\Phi_{plane}\mathbb{1}^{\otimes 3} + \sin\Phi_{plane}\sigma_x^{\otimes 3}\right)\hat{\mathcal{R}}_{pol}\left[\tilde{\Theta}_{ab},\tilde{\Theta}_{bc}\right]|GHZ\rangle_{abc} \tag{3.18}$$

where

- $\tilde{\Theta}_{ab}$ and $\tilde{\Theta}_{bc}$ are the angles between the photons $a-b$ and $b-c$ as measured on the annihilation plane, see fig. 3.3.
- Φ_{plane} is the angle between the z-axis and the normal to the annihilation plane.
- σ_x, σ_y, and σ_z are the Pauli matrices.
- N is the normalization:

$$\begin{aligned} N = {} & \frac{1}{2}\Big(9+\cos 2\,\tilde{\Theta}_{ab} + \cos\,[2\tilde{\Theta}_{ab}+2\tilde{\Theta}_{bc}] + \cos 2\tilde{\Theta}_{bc} - 4\Big(\cos\tilde{\Theta}_{ab} + \\ & + \cos\,[\tilde{\Theta}_{ab}+\tilde{\Theta}_{bc}] + \cos\tilde{\Theta}_{bc}\Big)\Big). \end{aligned} \tag{3.19}$$

- $\hat{\mathcal{R}}_{pol}\left[\tilde{\Theta}_{ab},\tilde{\Theta}_{bc}\right]$ is the polarisation operator:

$$\begin{aligned} \hat{\mathcal{R}}_{pol}\left[\tilde{\Theta}_{ab},\tilde{\Theta}_{bc}\right] = {} & \sum_{i,j,k=0}^{1}\Bigg((-1)^k\sin^2\frac{\tilde{\Theta}_{ab}}{2} + (-1)^j\sin^2\left[\frac{\tilde{\Theta}_{ab}}{2}+\frac{\tilde{\Theta}_{bc}}{2}\right] + \\ & + (-1)^i\sin^2\frac{\tilde{\Theta}_{bc}}{2}\Bigg) \times |ijk\rangle_{abc}\langle ijk|_{abc}\,. \end{aligned} \tag{3.20}$$

- $|GHZ\rangle_{abc}$ is the Greenberg-Horn-Zeilinger (GHZ) state for three gammas in a circular polarization basis:

$$|GHZ\rangle_{abc} = \frac{1}{\sqrt{2}} |RRR\rangle_{abc} + |LLL\rangle_{abc} \,. \tag{3.21}$$

The polarization for the annihilation photons of the other two spin states can be obtained by applying a rotation of the three gammas' spin space [10]:

$$|\psi_{|1,+1\rangle_{Ps}}\rangle = \sigma_x^{\otimes 3} |\psi_{|1,0\rangle_{Ps}}\rangle \tag{3.22}$$

$$|\psi_{|1,-1\rangle_{Ps}}\rangle = \sigma_y^{\otimes 3} |\psi_{|1,0\rangle_{Ps}}\rangle \,. \tag{3.23}$$

In the following, we will consider the case $|1,0\rangle_{Ps}$, the results can be extended to the other two spin states by applying the rotation in eq.s (3.22) and (3.23).

From eq. (3.18), we can obtain three particular states: a GHZ state, a W state, or a separable state.

Greenberg-Horn-Zeilinger State The GHZ state, eq. (3.21), is similar to the Bell's states in eq. (3.7), and it can be seen as a natural extension of the Bell's state $|\Phi^+\rangle$ to three-particle systems. It is a genuinely multipartite entangled state. As seen from eq. (3.21), the measurement of any elements of the system means a complete determination of the system state with the collapse of the wavefunctions of the other two gammas (i.e. if one gamma is measured to be in the state $|R\rangle$, both the other two gammas are in $|R\rangle$). The GHZ state in eq. (3.21) is written in the circular polarization basis, we can rewrite it in the linear basis using eq. (3.16):

$$\begin{aligned} |GHZ\rangle_{abc} &= \frac{1}{\sqrt{2}} |RRR\rangle_{abc} + |LLL\rangle_{abc} \qquad (3.24)\\ &= \frac{1}{2} \left(|HHH\rangle_{abc} - |VVH\rangle_{abc} - |HVV\rangle_{abc} - |VHV\rangle_{abc} \right) \qquad (3.25) \end{aligned}$$

W State The W state represents a Dicke state for a system of three particles. It is written as:

$$|W\rangle_{abc} = \frac{1}{\sqrt{3}} \left(|LLR\rangle_{abc} + |LRL\rangle_{abc} + |RLL\rangle_{abc} \right) . \tag{3.26}$$

eq. (3.26) is a particular extension of Bell's states to three particles and a genuinely multipartite entangled state. The W state differs from the GHZ state in its behavior when one of the photons is detected. In the case of GHZ states, we have the complete collapse of the wavefunction, for $|W\rangle$, instead, the measurement on a particular photon leaves the remaining particles in an entangled state, i.e. if a gamma-ray is measured to be, for instance, in the polarization state $|L\rangle$, the other two can be either in $|L\rangle$ and in $|R\rangle$.

Separable As we are considering three-particle systems, we can have two-particle separable states, for example, $|\psi_{2-SEP}\rangle = |R\rangle_a \otimes |L\rangle_b \otimes |R\rangle_c$, or single-particle separable states, for example, $|\psi_{1-SEP}\rangle = |R\rangle_a \otimes \frac{1}{\sqrt{2}}(|RR\rangle_{bc} - |LL\rangle_{bc})$.

In the wavefunction of GHZ and W states, it is difficult to directly visualize the entanglement in the gammas' polarization in a similar way as was done for the two gammas' case of eq. (3.15). There is the necessity to distinguish between the two entangled states $|W\rangle$ and $|GHZ\rangle$. We introduce an observable $\hat{Q}$ for which the three annihilation gammas' polarization state is an eigenstate. $\hat{Q}$ has negative eigenvalues for all separable eigenstates and positive values for at least an entangled eigenstate. This kind of observable is called *entanglement witness*, or simply *witness* [133]. For example, we can define a witness $\hat{Q}$ such that $\hat{Q}\,|W\rangle > 0$ and $\hat{Q}\,|GHZ\rangle > 0$. Moreover, it is possible to create multiple entanglement witnesses, one for each entangled state (Theorem of *Completeness of Witnesses*) [133]. Obviously, a single entangled state has different eigenvalues for different witnesses, so we can create a witness whose eigenvalues are maximized for a particular state. Using this idea, Hiesmayr and Moskal defines a class of entanglement witnesses, two of which are optimized for the GHZ and W states, respectively [10]. We analyze the results of the application of these witnesses on the case of SpPo Ps in $|1,0\rangle_{Ps}$ state and non-SpPo Ps.

$\mathbf{|1,0\rangle_{Ps}}$ For SpPo Ps, Hiesmayr and Moskal make calculations for the case in which the annihilation plane is orthogonal to the o-Ps spin ($\Phi_{plane} = 0$). However, the result of these calculations can be extended to the other spin states and plane inclination. The application of the entanglement witnesses in this condition demonstrates the genuine three-particle entanglement nature of the three photons polarization state for all possible values of $\tilde{\Theta}_{ab}$ and $\tilde{\Theta}_{bc}$. It was found that for some emission angles, GHZ state is preferred, and for others W state.

Non-SpPo Ps In this case, the system cannot be described as a pure state as in eq. (2.26). The non-SpPo Ps is a mixed state formed by the distribution probability to be in the pure spin states $|1,0\rangle_{Ps}$, $|1,-1\rangle_{Ps}$, and $|1,+1\rangle_{Ps}$. In the case the three states are equiprobable, the system is described by the density matrix:

$$\rho_{mixed}[\Phi_{plane}] = \frac{1}{3}\,|1,0\rangle_{Ps}\,\langle 1,0|_{Ps} + \frac{1}{3}\,|1,-1\rangle_{Ps}\,\langle 1,-1|_{Ps} + \frac{1}{3}\,|1,+1\rangle_{Ps}\,\langle 1,+1|_{Ps}\,. \quad (3.27)$$

The entanglement witnesses for this mixed stated showed the absence of GHZ states, while the genuine multiparticle entanglement in the W state remains possible, particularly, for the symmetric case ($\tilde{\Theta}_{ab} = \tilde{\Theta}_{bc} = \frac{2\pi}{3}$). Still, for all the other emission angle configurations, the three photons are always entangled, but not maximally entangled [10].

3.4 Two Annihilation Gammas: Experimental history

Experimentally, Compton polarimeters are needed to determine the linear polarization of 511 keV photons (see section 2.3.2). In the literature, almost all experiments on the annihilation gammas polarization make use of discrete Compton polarimeters (see table 3.1). In the first experiments of this kind, the scatterer center was a solid material, and only later the use of two scintillators per polarimeter was introduced (see table 3.1). As discussed in section 2.3.2, the Compton polarimeters reconstruct the linear polarization of the gammas, so we need to consider the expression of the polarization in a linear basis, i.e. eq. (3.17).

The analysis of this kind of experiment starts with the single polarimeter (see section 2.3.2.1 for more details). In terms of modulation factor μ_P from eq. (2.53), the distribution of the scattered gammas (eq. (2.52)) can be rewritten as:

$$C[\eta] = B\left(1 + \mu_P \cos\left[2\left(\eta - \phi + \frac{\pi}{2}\right)\right]\right). \tag{3.28}$$

Now we consider two polarimeters in coincidence, the scattering angle θ of the two polarimeters is fixed (see section 2.3.2.1). The single polarimeter does not measure any linear polarization because the gamma is circularly polarized. As previously discussed, the entanglement is in the relation between the two polarization directions as seen in eq. (3.17), i.e. in the correlation between the measurement of the two polarimeters. Then we express the distribution of the coincidence counts on the two polarimeters as a function of the angle $\Delta\phi$ between the scattering planes identified by the Compton scattering of the two annihilation gammas:

$$P[\Delta\phi] = k\left(1 - \mu_{P1}\mu_{P2}\cos[2\Delta\phi]\right) \tag{3.29}$$

where the subscripts refer to the annihilation gammas 1 and 2, and k is a constant depending on the two-gammas energies and scattering angles [146].

For the two annihilation gammas, the two polarization directions are orthogonal, then with ideal polarimeters $P[\Delta\phi = \pi/2] = 1$. As discussed in section 2.3.2.1, the Compton polarimeters are far from the ideal conditions. Considering the relation between the polarizations (see eq. (3.17)), $P[\Delta\phi]$ is periodic with maximum at $\Delta\phi = \pi/2$ and minimum at $\Delta\phi = 0$. Then, we can simplify the experiment by comparing the measured number of coincidence gammas $P[\Delta\phi]$ at the two angles $\Delta\phi = \pi/2$ and $\Delta\phi = 0$.

Analogously to the single Compton polarimeter in section 2.3.2.1, we construct the modulation factor μ for the two polarimeters from eq. (3.29):

$$\mu = \frac{P[\pi/2] - P[0]}{P[\pi/2] + P[0]} = \mu_{P1}\mu_{P2}. \tag{3.30}$$

The modulation factor μ for the two polarimeters is the product of the modulation factor of the single polarimeters. At this point, it is important to remember the dependence of μ_P by the scattering angle θ and by the incoming photon energy as discussed in section 2.3.2.1 and as shown in fig. 2.29. Then from eq. (3.30), μ depends on the energies and scattering angles of both the gamma-rays. For two gammas at 511 keV, μ_P is maximum for $\theta = 82°$, consequently μ reaches maximum for $\theta_1 = \theta_2 = 82°$ representing the ideal configuration on which set the two Compton polarimeters during the measurement.

The scheme of an annihilation gammas' polarization experiment with four detectors is shown in fig. 3.4. By keeping three detectors fixed to form a plane, the remaining absorber defines with this plane the angle $\Delta\phi$ previously discussed. This reduces the number of moving parts in the experiment to only one detector. As previously discussed,

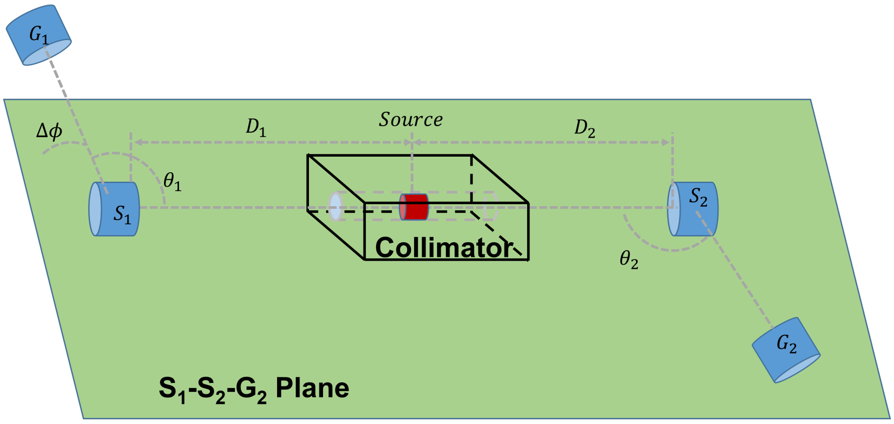

Figure 3.4: Diagram for a simple experimental setup for the measurement of the correlation of annihilation gamma from positrons. The source is positioned in a shielding block with two opposing holes that work as collimators. D_1 and D_2 are distances between the two polarimeters and the source. Each polarimeter is composed of a scatterer S and an absorber G. The absorber detects the Compton gamma-ray that is generated in S with a mean angle θ. S_1, S_2, and G_2 are fixed on a plane, while G_1 is moved forming with the plane the angle $\Delta\phi$.

we are interested in only two angles ($\Delta\phi = 0, \pi/2$), so two positions of this scatterer detector are enough to complete the experiment. At this point, we can reconstruct the ratio between the number of gammas scattered in planes at angle $\pi/2$ and 0 with each other with the use of eq. (3.30):

$$R = \frac{P[\pi/2]}{P[0]} = \frac{1+\mu}{1-\mu}. \tag{3.31}$$

Eq. (3.31) represents the comparison between the experimental results and the theoretical one which is simply given by the characteristics of the detector setup. Sometimes, in the experiment, the generalized version of the previous equation is used: $R[\Delta\phi] = \frac{P[\Delta\phi]}{P[0]}$, which reaches the maximum at $\Delta\phi = \pi/2$.

While this experiment appears simple and easy to implement, its story is long and troubled.

3.4.1 1930-1962: First Stage, Correlation Measurement

Dirac was the first to discuss the polarization of annihilation gammas in the 1930 [147]. However, we have to wait more than a decade for the design of an experiment capable of measuring the polarization correlation. The Klein Nishina cross-section was published only one year before Dirac's paper [117]. Only in 1946, the first setup with two polarimeters was proposed for the measurement of the entanglement in the polarization of the two annihilation gammas [39]. However, the expected value for the ratio R (eq. (3.31)) presented in reference [39] had a calculation error, which was corrected a few years later by Ward in his Ph.D. thesis [148]. While reference [39] was the first to describe the experimental setup, its form as used in the following experiments is attributed to Pryce and Ward. In their 1947 theoretical paper, Pryce and Ward present the explicit design of the apparatus with an image similar to fig. 3.4 [8]. However, the idea of using a similar experimental setup has been attributed to different authors [149]. Other than deriving eq. (3.17) in wavefunction notation from the symmetries of the annihilation, Pryce and Ward calculated for the first time the expected value of R. The theoretical value of $R_{Th} = 2.82$ for scattering angle $\theta = 82°$ is used in most of the experimental papers as the benchmark for the introduction of a series of corrections taking into account the physical dimensions and efficiencies of the detectors used. The results presented in reference [8] were independently derived by Snyder, Pasternack, and Hornbostel in 1948 from Schödinger wave functionals [9]. The expected values R_{Th} shown in the two papers are compatible with each other. In the same year, another paper was published reporting the calculation for the ratio based on the Klein Nishina cross section [150]. Other contemporaries engage themselves with the calculation of R using similar or different methods than the previous authors [149], still all confirmed the calculation in references [8, 9].

With the experimental setup explicitly presented and the expectation value calculated, numerous groups published results on measurements of the correlation in the polarization of the annihilation gammas, often contradicting each other. The year after Pryce and Ward's paper, Hanna published the first experimental result [11], followed in the same year by Bleuler and Bradt [12]. While the experimental implementation was similar, the resulting R was different, as shown in table 3.1. The two groups found opposite results, while Hanna's value was lower than his corrected expectation value, Bleuler and Bradt's one was higher even if still compatible with its corrected R_{Th}. We have to wait a couple of years for a more precise measure by Wu and Shaknov which experimentally confirmed the theoretical value after appropriate correction for the physical dimensions of the setup [13]. The following decade was full of experimental confirmation of Wu and Shaknov's result with different scatterer elements, distances, sources, and detectors as shown in table 3.1 [151–154]. This period culminated with the most precise measurement up to the recent years by Langhoff [155]. To further confirm these results, it was experimentally measured for the first and only time the correlation in the circular polarization of two gamma-rays [126]. The measurement of circular polarization of gamma-rays is extremely complex as mentioned in section 2.3.2.1.4. In reference [126], Clay and Hereford made use of the Compton scattering with SpPo electrons to study the circular polarization of the annihilation gamma. This idea came from reference [125], and it was implemented with two iron foils inside an electromagnet used to orient the electron spins in a given direction. The foils sandwich the source acting as the scatterer center, and two scintillators detect the gammas scattered forward from the source (scattering angle $\theta \sim 180°$). As seen in section 2.3.2.1.4, if the spins of the electrons in the iron foil are aligned along the annihilation gamma direction, the annihilation gamma is preferably scattered forward ($\theta \sim 180°$) in case its polarization is right-handed. Similarly, with anti-aligned electron spins, the annihilation gamma is preferably scattered in the forward direction if left-handed polarized. In this setup, the correlation in the two-gamma polarization is recorded as the difference in the number of scattered gammas arriving at the detectors with the electron spins in the two foils with opposite alignment with respect to the one with the same alignment. In the former case (electron spins with opposite alignment), the two detected gammas have preferably the same circular polarization, while in the latter case (electron spins with same alignment), they have opposite circular polarization. This kind of measurement is noisy because only a few electrons for each iron atom are magnetized, so the detectors receive also gammas scattered by non-SpPo electrons. The results, shown in reference [126], are far from the expected values (see table 3.1). The authors imputed this difference mainly to the low number of SpPo electrons in the iron foil. See reference [126] for details.

While the authors in references [8, 9] managed to reconstruct eq. (3.17), neither of the two groups connected it to the EPR paradox which at the time was in a decade-old paper. In fact, the authors do not make any reference to EPR paradox or entanglement, which is a term coined later, but they refer to this kind of measurement as *correlation in the annihilation radiation* [149]. We have to wait until the end of the '50s before the connection between eq. (3.17) and eq. (3.3) was recognized by Bohm and Aharonov [14]. In this extremely important paper, Bohm and Aharonov presented the Wu and Shaknov's results $R_{Exp} = 2.04 \pm 0.08$ in reference [13] as proof of the existence of entanglement and the implementation of an experiment similar to the EPRB gedankenexperiment. In the paper, the expectation values R_{Th} were derived in the framework of quantum mechanics (see eq. (3.17)) and of hidden variable theory. After correction for the physical condition of Wu and Shaknov's experiment, Bohm and Aharonov found an expected value $R_{Th}^{Sep} < 1.5$ when considering the nature deterministic as assumed by Einstein, Podolsky, and Rosen. This expected value is not compatible with Wu and Shaknov's result of $R_{Exp} = 2.04 \pm 0.08$, which is instead compatible with the expected value calculated from quantum mechanics [14]. The calculations for R_{Th} in both cases were confirmed by an independent derivation [156]. This result is the first confirmation of the probabilistic nature of the quantum world, in fact, it started a period of discussions among different authors on the validity of Wu and Shaknov's result as a demonstration of the completeness of quantum mechanics, see reference [149] for more detail.

3.4.2 1964-2018: Second Stage, Bell's inequality

With the 1964 paper, Bell opened the route to experimentally identify the possible presence of hidden variables [136]. The gammas of positron/electron annihilation were the first benchmark used in the study of Bell's inequality.

A decade after Bell's paper, Faraci et al. studied for the first time the annihilation gammas' polarization to test Bell's inequality [157]. In this work, the authors studied the ratio $R[\Delta\phi]$ as a function of the angle $\Delta\phi$ for different settings of the scattering angles θ_1 and θ_2 of the polarimeters. The experimental results were not compatible with the prediction of quantum mechanics, but they fulfilled the limit of Bell's inequality. This result put into discussion the measurement of the previous period, especially the Bohm and Aharonov's paper. The next year a paper from Wu's laboratory confirmed the measurements of Wu and Shaknov with improved precision (see table 3.1) [158]. The first possible source of discrepancy that was considered was the distance between the source and the scatterers [157]. The entangled state can be destroyed by interacting with the environment during the flight from the annihilation point to the scatterer. The coherence length of 511 keV gammas in the air is expected to be a few centimeters, while the source-polarimeter distance is typical of tens of centimeters (see table 3.1). However, the effect of the source-polarimeter distance on the measurement has been disproved by Wilson, Lowe, and Butt [159]. In this experiment, the ratio R has been measured for source-polarimeter distance from 15 cm up to 2.5 m without showing any appreciable drift in the value as the distance changed. This result eliminates the possible influence on measurement from the loss of coherence in the photon flight [160]. The problem with Faraci et al.'s results seems, instead, related to the experimental setup. Two Italian groups repeated the test of Bell's theorem with different setups and confirmed the violation of Bell's inequality [161, 162]. Both papers studied the ratio $R[\Delta\phi]$ as a function of the angle between the scattering planes of the annihilation gammas $\Delta\phi$. In the first paper, the experimental ratio $R[\Delta\phi]$ was perfectly compatible with quantum mechanics prediction and well above the limit of Bell's inequality [161]. In the second paper, the experimental ratio $R[\Delta\phi]$ was fitted, and the fit parameters, so obtained, were compatible with the prediction of quantum mechanics, confirming the violation of Bell's inequality [162].

These latest results demonstrate the violation of Bell's inequality with the two gamma-rays from positron annihilation. This demonstration was not so straightforward. So, in a 1978 paper, Clauser and Shimony from the CHSH inequality analyzed the experimental setup for the tests of the correlation in the annihilation radiation (see fig. 3.4). The authors identified the main problem in the low analyzing power of the Compton polarimeter. While it is the only instrument capable of detecting the polarization of photons in the hundreds kiloelectronvolt range (see section 2.3.2), its capabilities are extremely limited with very small analyzing power μ as can be seen in table 3.1. Even in the case of an ideal Compton polarimeter, we have an analyzing power very far from the ideal 1 and from the values reached by polarimeters for visible photons. This may be one of the reasons why the results in references [161, 162] were never accepted as a test of the EPR paradox. In fact, the 1982 paper by Aspect, Dalibard, and Roger is considered the first valid test of EPR paradox with Bell's inequality and, for this result, the authors won the Noble prize [138–140]. Aspect, Dalibard, and Roger's work applied the techniques developed in the previous experiments on the polarization of annihilation radiation and the result in Bohm and Aharonov's paper to optical photons. Nowadays optical photons are a fundamental element of most entanglement experiments, and only the experiments in reference [138–140] are considered when discussing the first test of EPR paradox, completely forgetting the results obtained with the annihilation gammas [134].

In 1996, Osuch et al. published a paper with a further test of the violation of Bell's inequality in the annihilation radiation from positrons by using the CHSH inequality [121]. While this inequality originates from Bell's theorem, it is experimentally more demanding in the case of gamma-rays, for a brief overview see reference [146]. As seen in section 3.1.3, to reconstruct the S function (eq. (3.12)), at least four polarimeters are needed, and they are positioned at a 22.5° between each other. In reference [121], the authors used the minimum setup of four discrete Compton polarimeters. They confirmed for the first time the violation of CHSH inequality with a S function (eq. (3.12)) corrected for the physical dimension of the setup. They found $|S_{Corr}| \not< 0.802$, this confirm the entanglement [121]. This result is a further confirmation of the entanglement in the polarization degree of freedom of the two gamma-rays generated in the annihilation of positrons.

Nowadays, the measurement of the ratio R has been proposed as an experiment to introduce undergraduate physics students to the concept of entanglement [164–167]. Moreover, the entanglement of the positron annihilation gammas is studied in the medical field to better discriminate in a PET scan the two events from the same positron annihilation with the constrain on their polarization (Quantum-Entangled PET, QE-PET) [123, 168–170].

3.4.3 2019-Today: Third Stage, What about photons from different annihilations?

In 2019, Hiesmayr and Moskal discussed if the ratio $R[\Delta\phi]$ of two gammas generated by a positron annihilation can be distinguished from the ones generated by two different annihilation events [171]. In reference [171], using the formalism of Mutually-Unbiased Bases (MUBs) for the entanglement witnesses, the authors showed the impossibility of distinguishing between the entangled and mixed state, i.e. they found the same $R[\Delta\phi]$ in the two configurations. This result directly contradicts the one from Bohm and Aharonov (see page and reference [14]). An answer to this result appeared the same year [172]. In this paper, Caradonna et al. repeated Bohm and Aharonov's calculations using the Fano framework [173, 174]. The authors disproved the Hiesmayr and Moskal's paper and confirmed the results of the previous decades of literature in the field [172].

Up to now, the Hiesmayr and Moskal's hypothesis was tested experimentally by scattering one of the two gammas before performing the detection with the polarimeter, i.e. a scattering element is added to one of the two paths to the polarimeters from the source as shown in fig. 3.4. This further scattering should break the entanglement, so the comparison of the two results should show if the entanglement is distinguishable from the mixed state of two uncorrelated gammas. There are two groups that performed experiments with different detectors and scatterers that have published their results in peer-reviewed papers: a British group [123] and a Russian one [122, 146].

British group Watts et al.'s experiment makes use of two cadmium zinc telluride (CZT) pixellated detectors designed for QE-PET application [123]. Each pixellated Compton polarimeter is realized by a single CZT scintillator crystal read by a segmented anode in 121 pixels. Firstly, the authors measured the correlation between two gammas coming from the sodium-22 source. Then, the authors positioned a scattering element in nylon along the path of one of the two gamma-rays, moving also the relative detector 33° outside the path of the annihilation gammas. In this way, the detector can detect only gammas scattered and not the ones coming directly from the source. In both conditions, the pixellated detectors permit the reconstruction of the scattering distribution $P[\Delta\phi]$ (see eq. (3.29)) at the scattering angle $\theta = 90°$. The experiment results in two curves, one for detection directly from the source $P_E[\Delta\phi]$ and one for the case with the scattering element $P_D[\Delta\phi]$. The experimental results show a flat behavior for $P_D[\Delta\phi]$ with values around 1. Instead, when the detection is directly from the source, the curve $P_E[\Delta\phi]$ shows the expected cosine behavior of eq. (3.29). These results were further confirmed with Geant4 simulations [175, 176] which reconstruct a $P[\Delta\phi]$ curve compatible with the experimental results for both cases. Watts et al.'s result seems to confirm the Caradonna et al.'s calculations in reference [172].

Russian group The polarimeter in [122, 146] is completely different from the previous case. Here the authors use plastic scintillators as scatterer centers. At 90° from the scatterer, a ring of 16 NaI(Tl) scintillation detector is positioned with a 22.5° angle between each other, in this configuration they cover the scattering angles $80° - 100°$. This experimental setup is based on a previous system presented in reference [121]. In front of one of the two plastic scintillators, a gadolinium-aluminum-gallium garnet

(GAGG) scintillator is added. By registering the timing and energy of the gamma-rays interacting with all the detectors, it is possible to discriminate different events:

- Entanglement: No interaction is detected on the GAGG, while a gamma-ray scatters on each plastic scintillator at the same time and it is then detected on one of the NaI(Tl) detectors for each polarimeter.
- Decoherent: On the side without the GAGG scintillator, the gamma follows the path as described in the previous case. The other gamma-ray is detected by the GAGG detector, then by the scatterer, and finally by one of the NaI(Tl).

From this, we can see a big difference in the experiment with respect to the British group. The experimental setup remains unchanged in the experiment and much more information can be extracted. By analyzing the deposited energy in the different detectors, the authors manage to differentiate gammas which have different scattering paths between the different detectors. The corrected expectation value of the ratio R is $R_{Th} = 2.4$ for this experimental setup, and it is compared with the measured ratio in the case of detection of the gammas directly from the source $R_{Exp-E} = 2.435 \pm 0.018$ and after scattering in the GAGG scintillator $R_{Exp-D} = 2.41 \pm 0.10$. The experimental results are compatible with the expected value in both cases, meaning we cannot distinguish experimentally if the gammas are entangled. This completely contradicts the result of the British group, confirming the calculation in reference [171]. Moreover, the experimental setup, in this case, permits testing the CHSH inequality. Contrary to the previous result in reference [121], the authors did not find any violation of the inequality.

In conclusion, up to now, we have two opposing theoretical results and two experimental results which support both possibilities. As written by Sharma, Kumar, and Moskal, it is a puzzle in the entanglement of the positron annihilation radiation [177]. A recent paper published in a preprint archive seems to solve this puzzle [178]. In the paper, Parashari et al. implemented an experimental setup like the one from the British group [123] using two pixellated Compton polarimeters with 8 pixel GAGG:Ce (GAGG doped with Cerium) scintillator matrix and a single crystal GAGG:Ce detector as the scattering element. Using the same configuration shown in reference [123], the measurements did not highlight any difference between the ratio $R[\Delta\phi]$ measured with gammas directly from the source from the one measure with one gamma-ray scattered at 30° by the scattering element [178]. This contradicts the results in [123] confirming the results of the Russian group [146]. The Parashari et al.'s result raises some eyebrows by contradicting, using similar configurations, the peer-review result from the British group obtained with pixellated detectors with a higher number of smaller pixel (121 pixels with an area of $0.8 \times 0.8\,\mathrm{mm}^2$ in reference [123] against 8 pixels with an area of $1.9 \times 1.9\,\mathrm{mm}^2$ in reference [178]). While the scattering element in the two experiments are different, this only change the probability of scattering at 30° which is taken into account in the measurements because only the coincident events on the two polarimeters are considered.

We rise also a point not discussed in both papers: the polarization impressed on the gamma from the Compton scattering in the scattering element. The scattered gamma-ray from a Compton scattering presents a linear polarization due to the scattering as discussed in section 2.3.2.1. In the case of annihilation gammas, the degree of polarization of the scattered photon is shown in fig. 2.26 and eq. (2.48). The impressed polarization is minimal at angles near 0° and 180° and maximal near 90°. In the case of the Russian group, the authors considered gammas scattered from the scattering element at small angles [146]. In both references [123, 178], the annihilation gamma scattered at 30° in the scattering element before being analyzed with the polarimeter. The linear polarization of the scattered gamma is not negligible at this angle as shown in fig. 2.26. The polarimeter should detect this linear polarization, however, this influence on the measurement is not discussed in any of the two papers.

There have been proposals to use different detector systems, in particular, the use of detectors, like J-PET (Jagiellonian-PET), with better coverage of the solid angle around the source [177]. In this case, the outgoing gamma-ray is not detected only in a particular direction (discrete and cluster Compton polarimeter) or near the scattering point in a single plane (pixellated Compton polarimeter). With systems like J-PET, it becomes possible to more precisely determine the scattering angle of the gamma-rays, then it becomes possible to select gammas scattered in a narrow range around 82°, maximizing the modulation factor [179, 180].

Nevertheless, a redesign of the experiment eliminating the scattering elements to break the entanglement seems to be the best option. The experiment could be designed: with a quantum state tomography or with better control of the positrons. In the first case, the complete density matrix of the two annihilation gammas is reconstructed, and any possible puzzle can be solved with more precise values of the matrix elements. As discussed previously, quantum state tomography is experimentally complex and costly to implement, so the second way is the easier of the two. Until now, the experiments made use of annihilation gammas from the source, the positrons were produced by the source and they annihilated in loco. There was no control over the annihilation time and positron state at the annihilation: bound or unbound positron, thermalized or non-thermalized. Moreover, there was no control over the number of positrons annihilating in the detection window. The source activity can be controlled low enough not to saturate the detectors. Nevertheless, the experiments up to now used activities with a wide range of values up to tens of decay per nanosecond with no apparent consideration of the possibility of simultaneous hits as shown in table 3.1. This problem can be solved with a positron beam. The beam intensity is known and controllable. The target and implantation energy can be selected to avoid Ps formation and to have complete thermalization of the annihilating positrons. Bunched beams with only one positron per shot would be ideal, giving a better signal-to-noise ratio and only one possible annihilation to detect. This would solve the problem identified by Hiesmayr and Moskal.

3.5 Three Annihilation Gammas: How?

In the previous section, we have seen how the demonstration of a simple formula, eq. (3.15), can be experimentally challenging. Unfortunately, to test eq. (3.18) for three gammas, the experimental measurement is exponentially more difficult than what was discussed for the two gammas. In fact, up to now, no experiments have been done to test the entanglement of the annihilation gammas from o-Ps. Nevertheless, there are some advantages in the entanglement study of three gammas with respect to the two gammas. In fact, in the o-Ps self-annihilation, the gammas can be emitted with different energies making them easier to distinguish with respect to the case of two 511 keV gammas from the unbound positron annihilation, moreover, Ps can be formed in a free environment.

Table 3.1: Experimental measurement of the correlation of two gammas from the annihilation of positrons. The works are organized by year. The source intensity and the source-polarimeter (S.P.) distance are indicated when given in the paper, the same for the expected value of R. R_{Th} represents the expected ratio corrected by the physical dimensions of the setup. R_{Exp} are the reported measured R values for the reported scattering angles.

Year	Source	Scatterer	Absorber	S.P. distance	R_{Th}	$R_{Exp}(MeasureAngle)$	μ_{Exp}	Article
1948	^{64}Cu	Solid Al and Brass	2 Geiger counters		1.55	$1.39 \pm 0.07(90^{\circ\,a})$	0.16 ± 0.03	[11]
1948	^{64}Cu	Solid Al	Geiger counter	7.62 cm	1.7	$1.94 \pm 0.37(82^{\circ\,a})$	0.32 ± 0.13	[12]
1950	^{64}Cu	Solid Al	Geiger counter	10.2 cm	2.0	$2.04 \pm 0.08(82^{\circ\,a})$	0.34 ± 0.03	[13]
1952	^{22}Na	Magnetized Fe	Stilbene		$0.9\%^{b}$	$(3.5 \pm 0.8)\%^{b}$		[126]
1951	$^{64}Cu/^{22}Na$	Solid Pb	Geiger counter		2.0	$1.94 \pm 0.14(90^{\circ\,a})$	0.32 ± 0.05	[151]
1952	^{64}Cu	Stilbene	NaI(Tl)		1.6	$1.62 \pm 0.03(90^{\circ\,a})$	0.240 ± 0.12	[152]
1953	^{22}Na	Solid Al/Pb	Stilbene	17.8 cm	0.77	$0.68 \pm 0.06(90^{\circ\,a})$	0.25 ± 0.02	[153]
1955	^{22}Na	Solid Al	NaI(Tl)	3.4 cm	2.32	$2.18 \pm 0.09(90^{\circ\,a})$	0.371 ± 0.03	[154]
1960	^{22}Na	Scintillator	NaI(Tl)		2.48 ± 0.02	$2.47 \pm 0.07(82^{\circ\,a})$	0.42 ± 0.02	[155]
1974	^{22}Na	Plastic NE202	NaI(Tl)			$2.0 \pm 0.1(80^{\circ\,a})$	0.33 ± 0.4	[157]
1975	^{64}Cu 370 MBq	Plastic	NaI(Tl)	10.2 cm	1.40 ± 0.07	$1.42 \pm 0.02(90^{\circ\,a})$	0.399 ± 0.03	[158]
1976	^{64}Cu 37 GBq	Plastic NE104	NaI(Tl)	$0.15 - 2.54$ m		$1.59 \pm 0.02(82^{\circ\,a})$		[159]
1977	^{22}Na 3.7 MBq	Plastic	NaI(Tl)	2 cm	1.353 ± 0.026	$1.346 \pm 0.007(82^{\circ\,a})$		[161]
1981	^{64}Cu 48 GBq	HPGe	Ge(Li)	42 cm	1.2965 ± 0.0195	$1.301 \pm 0.016(90^{\circ\,a})$		[162]
1996	^{22}Na 185 MBq	Plastic	BaF_2	18.5 cm			0.633	[121]
2018	$^{68}Ga/^{68}Ge$ 4.4 kBq	NaI(Tl)	2 NaI(Tl)	8.1 cm		$2.35 \pm 0.19(90^{\circ\,a})$	0.403 ± 0.006	[165]
2021	^{22}Na 170 kBq	Pixelated CdZnTe		43.5 mm		$1.85 \pm 0.04(70^{\circ} - 110^{\circ})$	0.298 ± 0.015	[123]
2022	^{22}Na 37 kBq	Pixelated GaGG:Ce		4 cm		$1.86 \pm 0.03(72^{\circ} - 90^{\circ})$	0.30 ± 0.01	[181]
2022	^{22}Na 50 MBq	Plastic	16 NaI(Tl) ring	35 cm	2.4	$2.435 \pm 0.018(80^{\circ} - 100^{\circ})$	0.418 ± 0.003	[122, 146]
2023	^{22}Na 370 kBq	Pixelated GaGG:Ce		5 cm		$1.90 \pm 0.01(90^{\circ\,a})$	0.31 ± 0.01	[178]

[a] Average angle over detector dimensions; [b] Difference between the counts for gamma polarization in opposite and same direction

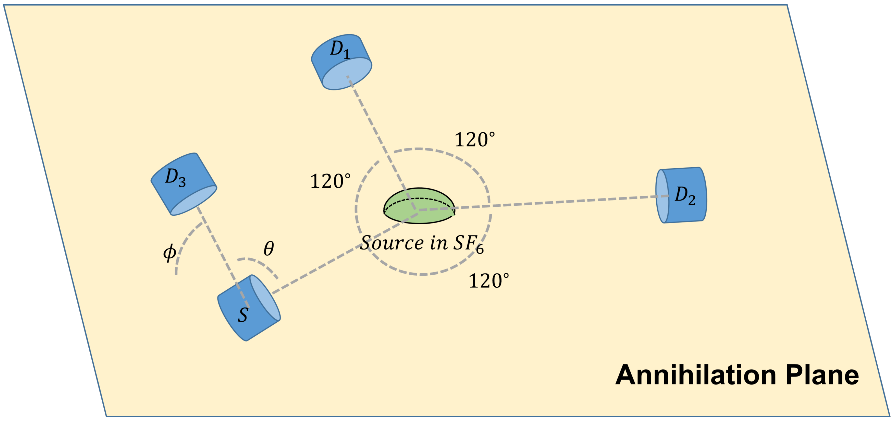

Figure 3.5: Diagram for an experimental setup for the measurement of the polarization of one of three gammas from the annihilation of o-Ps. Detectors D_1, D_2, and S work in coincidence and they are at $\tilde{\Theta}_{ab} = \tilde{\Theta}_{bc} = 120°$ between each other forming an equilateral triangle on the annihilation plane. S is the scatterer of the polarimeter while D_3 is the absorber, which is rotated around the scatterer, to detect the number of gamma-rays scattered at an angle ϕ.

Up to now, we are limited to a few studies, from the second half of the last century, on the polarization of a single gamma from the o-Ps self-annihilation.

In the 1950s, the first measurement of the polarization of o-Ps annihilation radiation was published [182]. The positron source was inserted in a SF_6 environment to produce o-Ps. To detect gammas from the o-Ps annihilation, three detectors in coincidence were fixed on a plane. This defines the annihilation plane of the gammas analyzed, while the detector positions in the plane define the angles between the gammas $\tilde{\Theta}_{ab}$ and $\tilde{\Theta}_{bc}$, as seen in fig. 3.5. One of the three detectors is the scatterer center of the Compton polarimeter. In reference [182], the measurement was done only with the simple setup of the equal triangle $\tilde{\Theta}_{ab} = \tilde{\Theta}_{bc} = 120°$, so the three annihilation gammas have the same energy. The authors measured the number of gammas scattered in the Compton polarimeter parallel and perpendicular to the annihilation plane, the ratio of these two values was 1.87 ± 0.23. This number was compared with the expected value from the theory. In reference [142], Drisko calculated a ratio of $3/1$ in this experimental conditions, i.e. for each gamma scattered perpendicular to the annihilation plane, three are scattered parallel to the plane. Using this as a starting point, Monte-Carlo calculations gave an expected value of 1.80 ± 0.15 for the experiment. The expected and measured values are perfectly compatible [182]. In 1976, Faraci and Pennisi recalculated the theoretical value in the conditions of the experiment in reference [182], the authors obtained a value lower than the measured one [183]. The implementation of successive correction to the expected value from the finite geometry of the experiment decreases the discrepancy between this new calculation and the previous one, however, the two values are still not compatible.

The measurements in reference [182] have a big uncertainty and a discrepancy with the calculation of other groups. In 1978-80, further theoretical analysis of the o-Ps indicated the need for further experimental measurements [184, 185]. Since then, only another result was published in a 1987 paper in Chinese (only the abstract is translated)

[186], but this added little information to the previous results. In reference [186], Jia et al. repeated the previous experiment obtaining 1.82 ± 0.06 for the emission angles $\tilde{\Theta}_{ab} = \tilde{\Theta}_{bc} = 120°$ [186]. This proves the previous result with increased accuracy. Moreover, the Chinese group measured the ratio of 1.53 ± 0.08 for the emission angles $\tilde{\Theta}_{ab} = 90°$ and $\tilde{\Theta}_{bc} = 135°$ [186]. Unfortunately, the authors did not present the corrected expectation value of the ratio for comparison with the theory.

These two experiments were the only ones ever implemented to study the polarization of the gammas emitted by the o-Ps annihilation. So we are at the point where not even the average polarization of the gammas has been determined for most of the emission angle configurations. The measurement of the entanglement of the three gammas requires the simultaneous measurement of the three polarizations, further increasing the complexity of the experimental setup. This complicates the experiment even before the requirements on the o-Ps. In fact, the previous two experiments used non-SpPo Ps, and, as discussed in section 3.3, this reduces the possible entanglement states. We are mostly interested in the detection of the entanglement state of the three gammas from o-Ps in a spin-selected state, i.e. eq.s (3.18), (3.22), and (3.23). We can then reduce the hurdles for the experimental measurement into two main parts: detector and source. In the following, we analyze in detail the two points.

Detector The detector needs to cover most of the solid angle around the annihilation point. Moreover, it should be able to detect the annihilation gammas and select the three gamma-rays from a singular annihilation event, other than being capable of measuring the polarization of each gamma-ray. The first point makes the detector dimension big, increasing the complexity and cost. The second point requires detecting the arrival time, position, and energy of the gamma-rays. With this information for all detection events, it becomes possible to select the gammas emitted simultaneously, in a plane, and with total energy 1022 keV: the three gammas from the same o-Ps annihilation event. These requests increase not only the requirement of the detector material but also the complexity of the analyzing software. To measure the polarization of the three gammas, the detection of the annihilation gammas and the scattered gammas is required, so at least two detector layers placed around the sample are needed. The detector material has to favor Compton scattering with the incoming photons while favoring the absorption of the scattered photon. Moreover, these two events need to happen with high efficiency because a coincidence of 6 events is required for the entanglement measurement. All of these requirements increase the complexity of the detector. There already exist detectors with solid angle coverage and optimized for gamma-ray detection, these are the PET machines. Innovative solutions for PET detectors have been proposed in recent years adding the capability to detect the Compton scattering of the annihilation gammas. These new detectors could be applied to the measurement of entanglement in the gamma-rays from the annihilation of o-Ps. In our case, the most interesting new implementations of PET systems are:

- **QE-PET.** The Quantum-Entangled PET makes use of the constraint on the polarization of the 511 keV annihilation radiation to better select the two gammas originating from the same annihilation event. These would increase the PET resolution as already observed for tomographic detectors of entangled x-ray photons [187]. The QE-PET is composed of a ring of pixellated detectors each working as a pixellated Compton polarimeter [168, 169]. This kind of detector presents a high spatial resolution for the hit events from the interaction with photons, while the time and energy resolution are dependent on the scintillator material. As explained in section 2.3.2.1, pixellated Compton polarimeters require complex analysis to extract the polarization information, so a QE-PET has a high cost due to the pixellated detectors and high requirements in the signal analysis from the pixel to reconstruct the annihilation events and the gamma polarization. While this idea is from the first 2010s [168, 169], most of the work up to now is centered on the simulation and detection of the single pixellated Compton polarimeter [170, 188–192]. Only in recent years, some measurements were done with pixellated Compton polarimeters developed for QE-PET [123, 178, 181]. Nevertheless, the QE-PET still requires many years of development, especially in the software, to reach a level to be applied in the study of the entanglement in the three annihilation gammas.

- **WGI.** A Japanese group presented a new concept of PET called Whole Gamma Imaging (WGI) [119]. In their design, the PET is composed of two concentric rings, the innermost one is formed by pixellated GAGG detectors and works as the scatterer, and the outermost one is formed by pixellated GSOZ (Zirconium-doped Gadolinium OxyorthoSilicate) and works as the absorber. By using the internal ring to generate the Compton scattering and the external ring for the detection of the scattered Compton gamma, the WGI can work as a Compton camera (see section 2.3.2.1), so the direction of the single annihilation gamma can be reconstructed without the need of coincidence detection. An enhancement of the reconstruction capabilities of a normal PET is obtained in the WGI with the increase in the detection capabilities with two detector layers and its use as a Compton camera. In reference [119], the authors presented a prototype and the first results they obtained with the imaging of three sources. Still, while it is possible, there have been no studies of the capability of the WGI to reconstruct the gamma-ray polarization, so there is a lot of work to be done to apply this detector to the three annihilation gammas.

- **J-PET.** The Jagiellonian-PET is implemented with a detector design extremely different from the previous two cases. Instead of going with pixellated detectors which have a very high cost, the J-PET group designed the detector elements using a long plastic scintillator strip with SiPM at both ends, see fig. 3.6. While this detector is simple and inexpensive, the main work for the reconstruction is done electronically. Knowing the light speed in the plastic material, the measured difference in the arrival time of the scintillation light at the two extremes is used to determine the hit position of the gamma along the scintillator length. Then, by implementing a ring of such detectors, we can reconstruct the time and position of the gamma-rays' interaction with the detector ring. So by geometric and time constraints, the gammas from the same annihilation can be selected and the annihilation point can be reconstructed. However, while the plastic scintillator is a cheap material, it has a low absorption efficiency, given that photons with hundreds of kiloelectronvolts energy tend to Compton scatter when interacting with this scintillator. J-PET makes use of this property, the detectors are positioned in three concentric rings and the ring inter-distance is optimized for the detection of the scattered gammas. This makes the J-PET geometry perfect for the reconstruction

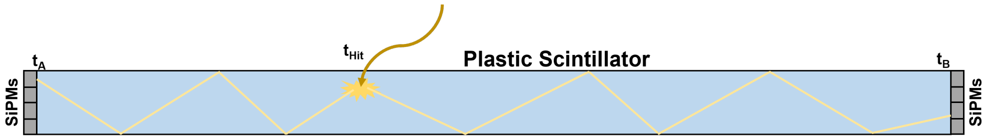

Figure 3.6: Sketched of a plastic scintillator element of the J-PET.

of the gamma polarization. A first version of the J-PET has been implemented and its capabilities have been studied including the reconstruction of the two gammas polarization [179, 180], and the detection of positron/electron annihilations [193] and o-Ps annihilation [194–196]. Now a new detector version is being realized, in which the J-PET is composed of independent modules each formed by 13 plastic scintillator strips read at both ends by four SiPM, see fig. 3.6. This new modular design makes it possible to adapt the detector to best fit its application.

Of these three systems, the most advanced one is the J-PET, where studies have already been done on the reconstruction of gamma polarization and the detection of o-Ps. With its modular design, J-PET can be adapted to specific experimental setups. With a single module, one can detect the hit time and position of a gamma. With two modules near each other, one can detect the photon scattering from the first to the second working as a polarimeter. By positioning two modules opposite to the source, one can reconstruct the annihilation position. If two couples of modules are positioned opposite to the source, the entanglement of the two annihilation gammas can be measured. This can be extended to the three annihilation gamma, by positioning three modules or three couples in a particular angle configuration around the gamma source, it is possible to reconstruct the annihilation and/or the polarization of the o-Ps for a particular set of emission angles. However, the plastic material as scintillator material results in the drawback of a low detector efficiency, so a very strong source or a very long measurement time is required. Still, while the other two systems previously introduced use detectors with higher efficiency than J-PET, they are very far away from the level of system implementation and study reached by the J-PET collaboration.

Source Another major hurdle in the study of entanglement in o-Ps annihilation is the source of ortho-positronium atoms which needs to be high-intensity and capable of selecting its spin state. As seen in section 2.1.5.2, it is possible to produce efficiently o-Ps in a vacuum with the use of a e^+/Ps converter, and the spin state of the emitted Ps can be selected. This requires a beam of positrons for efficient production and emission into the vacuum of o-Ps. The realization of such a beam is the scope of this thesis, in the following chapter we will see the requirements for the construction of this beam.

Chapter 4

Positron Beams

As discussed in section 2.1, the positron implantation energy is usually of the order of tens of kiloelectronvolts. With these energies, it is possible to use the positrons to study material properties (see section 2.2.2) and efficiently produce Ps (see section 2.1.5). Beams with these low energies are also called *slow positron beams.* Due to this low energy, the apparatus dimension, cost, and complexity are much more manageable with respect to beams based on cyclotrons or synchrotrons.

The slow positron beams can be deconstructed into a few fundamental elements as shown in fig. 4.1:

- **Source:** where the positron are generated;
- **Moderator:** where the wide energy distribution of the particles from the source is narrowed down to a mono-energetic beam;
- **Transport:** where the particles are guided from the source-moderator assembly to the target region;
- **Speed-Selector:** where only the particles with the desired energy are selected and the target is shielded from a direct view of the source/moderator that would cause noise in the measurement;
- **Target Region:** where the positrons are implanted into a target with the desired beam spot dimension, timing, and number.

Electron optical systems are used for the manipulation of the positrons from the source-moderator to the target. The method used in the manipulation of the positrons determines the different applications. As seen in fig. 4.1, we can classify the slow positron beams into three categories:

- **Continuous Positron Beam:** the beam from the speed-selector is accelerated and focused on the target. The beam kinetic energy can be tuned from a few electronvolts to tens of kiloelectronvolts. Different energies allow implanting of the positrons at different depths into the target (see section 2.1.2.1). They are mainly used for material study with DBS and $3\gamma/2\gamma$ spectroscopy (see section 2.2.2.2.1).

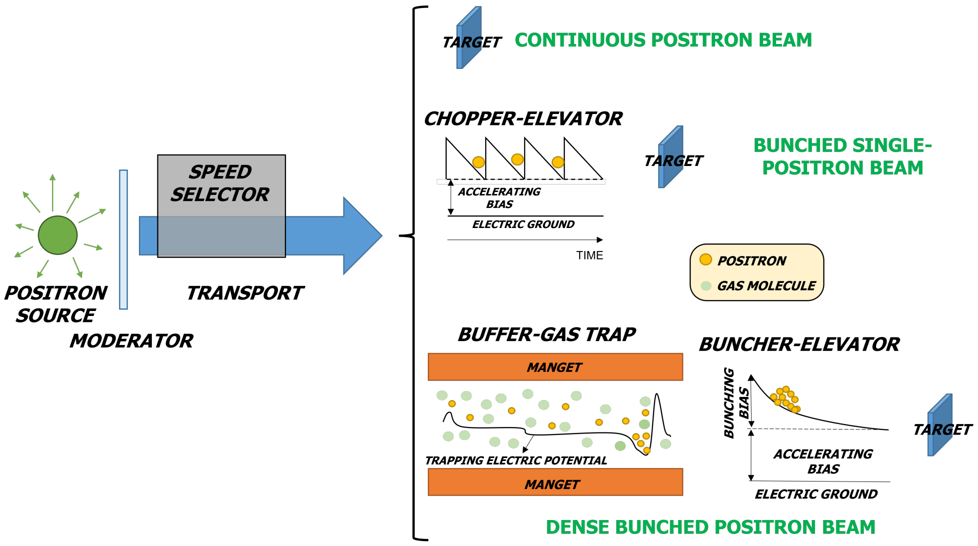

Figure 4.1: Diagram for the generation of a positron beam and the classification of the beam types.

- **Bunched Single-Positron Beam:** The positrons from the speed-selector pass through three electron optical elements: a pre-buncher, a chopper, and a buncher [197, 198]. These elements are powered with a periodic electric potential with frequency in the range $25 - 50\,\mathrm{MHz}$ bunching the beam at the target. With this electron optical system, only one positron is selected by the periodic potential to form the bunch which reaches the target with a temporal width $< 200\,\mathrm{ps}$ [197, 198]. This type of beam is used for solid state and material studies with the PALS technique (see section 2.2.2.1): the buncher gives the start signal for a positron that reaches the target, and the annihilation gamma gives the stop signal. The elapsed time between the two signals is the measured lifetime of the positron in the target [197, 198].

- **Dense Bunched Positron Beam:** After the speed-selector, the positrons are accumulated in a Buffer-Gas trap (BGT) [16, 17], and then dumped in shots of $10^4 - 10^5$ positrons in tens of nanoseconds. After the BGT, the positrons can be further accumulated in an accumulator up to 10^8 positrons [199], or bunched in $2 - 8\,\mathrm{ns}$ at the target [20]. These beams are mainly applied for the production of clouds of o-Ps in vacuum for fundamental studies [7].

In this thesis, we are mainly interested in continuous and dense bunched beams. In the following, we will present a brief description of the source, moderator, speed-selector, and transport required for the production of a slow positron beam.

4.1 Source

We can obtain positrons from:

- **Pair production:** a high-energy photon ($E_\gamma \gg 1.02\,\mathrm{MeV}$) interacts with a material producing positron-electron pairs.

Table 4.1: Most used positron source by β^+ decay. I_{e^+} is the positron yield. E_{MAX} is the end-point energy and E_{AV} the average energy of the β^+ decay spectrum. $H = v/c$ is helicity, E_γ and I_γ are the energy and intensity of the most dominant γ transition. *Table from* [209]

Nuclide	Half life	I_{e^+}	E_{MAX} [keV]	E_{AV} [keV]	v/c	E_γ [keV]	I_γ
^{22}Na	2.60 y	0.898	545.4	215.5	0.711	1275	0.999
		0.001	1819.7	835.0	0.925		
^{58}Co	70.8 d	0.150	475.2	201.3	0.697	811	0.994
^{64}Cu	12.7 h	0.179	652.5	278.1	0.762	1346	0.005
^{68}Ge/^{68}Ga	271 d	0.880	1899.0	836.0	0.925	1077	0.030
		0.011	821.7	352.6	0.806		

- **Radioactive Source:** some metastable nuclides decay with a β^+ process producing positrons.

Pair production permits to obtain higher intensities of the positron beam than the ones obtained with radioactive sources. In the first case, intensities up to $\sim 10^9$ e$^+$/s are available [200]. In the second case, intensities up to $\sim 10^6$ e$^+$/s can be reached [201]. The high-energy photons for the pair production are obtained using linacs [202–206] or nuclear reactors [200, 207, 208], and in both cases, a facility is required. Differently, a beam from a radioactive source can be compact, more cost-effective, and it can be installed in a university laboratory.

4.1.1 Radioactive Source

When a nuclide decays by β^+, we have the production of a positron and an electronic neutrino:

$$^{A}_{Z}X \rightarrow {}^{A}_{Z-1}X + e^+ + \nu_e \tag{4.1}$$

In the atomic nucleus, this corresponds to the decay of a proton in a neutron changing the atomic number of the atom:

$$p^+ \rightarrow n^0 + e^+ + \nu_e \tag{4.2}$$

Given N_0 the initial number of active nuclei in a source, the number of active nuclei at a time t, $N[t]$, is given by:

$$N[t] = N_0 e^{-\frac{t}{\tau/\log[2]}}, \tag{4.3}$$

where τ is the half-life of the radioactive nuclides. In table 4.1, some of the most used radioactive nuclides are shown. The half-life of the nuclides is extremely different spanning from hours/days to years, like sodium-22. The positrons emitted in a β^+ decay are not monoenergetic, the β^+ decay spectrum has a wide energy distribution as seen in the case of cobalt-59 shown in fig. 4.3 The energy distribution depends on the nuclide, table 4.1 reports the average and maximum energy of the positron from some radioactive sources. A source with an activity of the order of Curie [159, 162] can be obtained, but

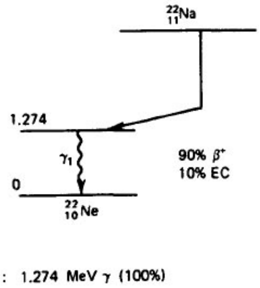

Figure 4.2: Decay scheme for ^{22}Na. From [88]

it requires to be activated in loco with an accelerator facility. For example, ^{68}Ge/^{68}Ga requires a 20 MeV proton beam impinging on a GaN target [115]. On the other hand, a sealed source can be done with ^{22}Na but with lower activity. At present, there is only one producer, iThemba labs in South Africa, that trades sources with a maximum activity of 50 mCi. The decay scheme of sodium-22 is shown in fig. 4.2. This radioactive nuclide has the advantage of a long lifetime (2.6 y) and a high yield of positrons, 90% of the decays produce a positron. This sealed source is used for slow positron beams in laboratories.

4.1.1.1 Generation of SpPo positrons

In the mid-1950s, Lee and Yang suggested that the weak interaction might violate the parity symmetry so the system and its mirror image are not the same [210]. A few years later, using measurements on the decay of ^{60}Co nuclei, Wu et al. experimentally demonstrated that the weak interaction violates parity [211], earning Lee and Yang the 1957 Nobel Prize in Physics. This discovery shocked the scientific community and brought a period of studies and measurements for the different decays. Because the β^+ decay is due to the weak interaction, the positron spin direction was studied, demonstrating the emission of SpPo positron from the radioactive source [129, 212, 213]. The positrons are emitted with spin preferably aligned with the direction of motion. This probability is given by the helicity $H = v/c$ in table 4.1, and as we can see from this table ^{68}Ge/^{68}Ga creates the most SpPo positron beam. The spin-polarization of the positron from the source is decreased by other factors, mainly by the positron backscattering on the source support. In the backscattering, the spin direction is unchanged, so backscattered positrons have spin aligned opposite to the beam direction, this increases the value of N_- reducing the beam polarization P (see eq. (2.24)). The positron backscattering is reduced by engineering the source support using a low-Z material resulting in a suppression in the backscattering of positrons from the source [214].

In the case of positrons created by pair production, their polarization is directly related to the photon polarization, maximum positron polarization is obtained with circularly polarized gamma-rays [215, 216].

4.2 Moderator

As seen in fig. 4.3, the positrons are emitted with a wide range of energy from radioactive sources. These positrons cannot be directly used to create a monoenergetic positron

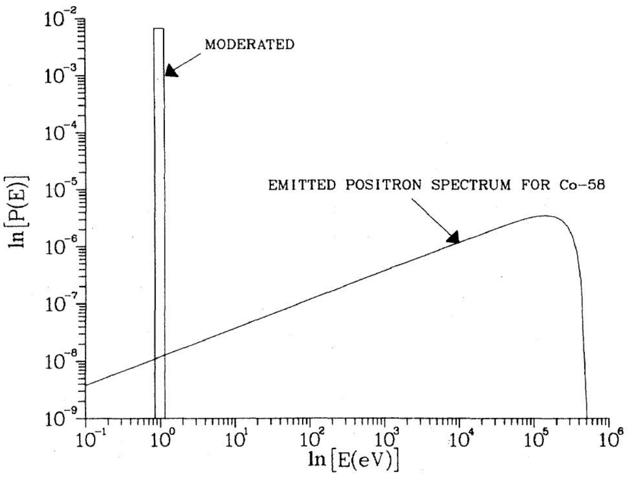

Figure 4.3: Positron energy distribution as emitted by a β^+ ^{58}Co source (normalized) and after the moderator. *Image from* [51].

beam. To produce a beam by cutting a small energy portion of the β^+ spectrum is highly inefficient. Differently, considering the positron interacting with a material (see section 2.1.2), a higher number of positrons can be obtained in a narrow energy distribution during the positron thermalization in the material. Nevertheless, these positrons need to exit the material in order to form the monoenergetic beam. When slowed positrons are emitted with good efficiency, the material is called a *moderator*. The difference between a moderator and a cut in the energy distribution can be seen in fig. 4.3: the number of positrons in the energy range after the moderator is orders of magnitude higher than the positrons in the same energy range when emitted by the source [217]. We can identify some characteristics that a good moderator should have:

- no defect that limits the positron diffusion to the surface,
- high Z number to stop many positrons,
- long diffusion length so the positron can reach the surface,
- negative positron work function so the positrons reaching the surface are emitted.

Only thanks to the introduction of the moderators, intense slow positron beams could be formed. The first slow positron beams had very low intensities with typical values of few positrons per second in the 1970s [218, 219]. Nowadays beam intensities are much higher even up to $\sim 10^6$ e^+/s with a radioactive source [201]. Figure 4.4 shows some geometries used in the formation of slow positron beams. Nowadays, the most used source-moderator geometries are two both making use of a thin film of moderator material in front of the source being it a crystal foil (fig. 4.4c) or solid noble gas film (fig. 4.4d). This reflects the two classes of moderators in use for slow positron beams:

- moderators with negative positron work function ϕ_+,
- solid noble gas moderators.

This distinction is due to the moderation physical phenomena for the emission in vacuum of the moderated positrons.

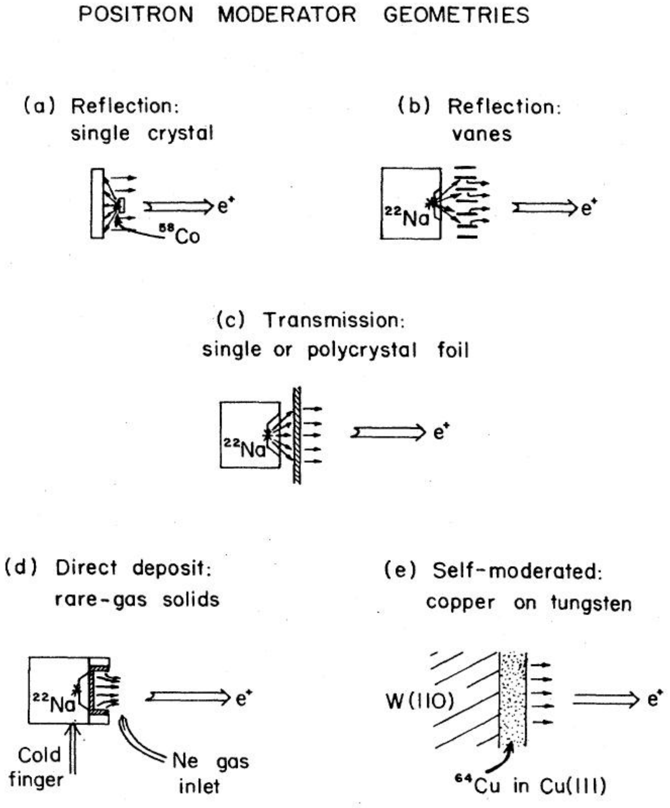

Figure 4.4: Some geometry for assemblies of a β^+ radioactive source and a moderator. *Image from* [51].

4.2.1 Moderator with negative positron work function

All those metals in which the positron work function is negative ($\phi_+ < 0$) can work as moderators. As discussed in section 2.1.3.1, in these materials, the implanted positrons thermalize and a fraction of them diffuse to the surface. Here, if the $\phi_+ < 0$ they are emitted with a narrow energy distribution around a few electronvolts. Examples of this class of moderators are thin foils of tungsten, copper, or nickel [220]. Of these, the most used is the tungsten which emits in vacuum with an efficiency of 0.1% positrons at an energy of $\sim 3\,\mathrm{eV}$ in narrow energy distribution with spread of $\sim 0.3\,\mathrm{eV}$ FWHM (Full Width Half Maximum) [220, 221].

The moderators with negative positron work function operate at room temperature in ultra-high vacuum (pressure $< 10^{-7}$ mbar). The efficiency loss for these moderators is slow and they are operated for months if the vacuum conditions are kept. Nevertheless, with time, there is a build-up of adsorbed molecules on the moderator surfaces which decreases the positron yield. To recuperate the lost moderator efficiency, the moderator is heat treated in vacuum [220]. For example, a tungsten moderator is heated up to $\sim 2000\,\mathrm{K}$ for a few minutes before it is slowly cooled down to room temperature [221].

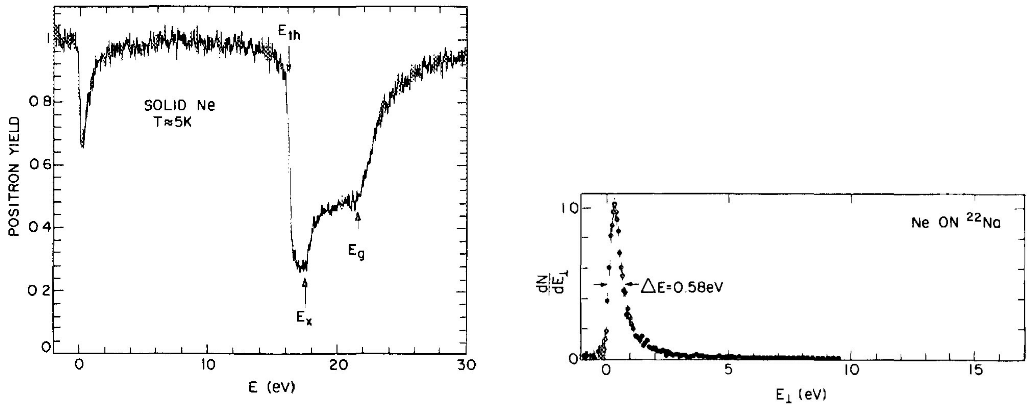

(a) *Positron yield in function of implantation energy.*

(b) *Energy spectrum of positron from ^{22}Na source.*

Figure 4.5: Interaction of positrons with a solid neon moderator. Figure (a) shows the positron reemission from a solid neon target for different positron implantation energies. The major material thresholds are shown: E_{th} is the inelastic threshold for the formation of Ps; E_x is the threshold for the formation of exciton; and E_g is the material band gap (see text for details). Figure (b) shows the distribution of the slow positrons emitted from a solid neon moderator at different values of the component of the positron emission energy normal to the moderator surface of the emission energy. *Images from* [19].

4.2.2 Solid Noble Gas Moderator

The solid noble gas moderators were introduced in 1986 by Mills and Gullikson [19]. Four gases were studied for this application: Neon, Argon, Krypton, and Xenon [19, 222, 223]. In all four cases, the positron work function is positive and the material is an insulator [224]. Then a positron can be emitted from these materials only if it reaches the surface not thermalized but with energy $E > \phi_+$. This is possible with good efficiency due to the low thermalization rate and high diffusion rate of positrons in solid noble gasses [224].

Figure 4.5a shows the behavior of positron implanted into solid neon (a similar figure can be seen for argon in reference [224]). Analyzing the figure from the left, we observe a decrease in the positron yield in vacuum below $\sim$ 1eV. This dip is due to positrons losing their incident energy in the solid and remaining trapped by the positive positron work function of the material. The energy width of this dip is related to the mean energy loss per collision [224]. For implantation energies up to the inelastic threshold E_{th}, the positrons can lose energy only by phonon scattering, however, this process is highly inefficient in solid noble gasses, so the diffusion process happens without positrons losing energy. Then the positrons, thanks to the long diffusion length in these materials, can diffuse to the surface where they are emitted because their energy is higher than the material work function. E_{th} represents the threshold for Ps formation in the solid. It is possible to have Ps emission in vacuum before the inelastic threshold due to electron pickup at the surface. This results in positron yield values lower than unity for energies $< E_{th}$ and decreasing yield for energies near the threshold [224]. Nevertheless, this process is not efficient, in solid neon the decrease in the positron yield at energies lower than the threshold is minimal. After the inelastic threshold, the positron yield of solid neon dips because the positrons are more probably emitted as Ps. This changes at energies higher than E_x, the threshold for the exciton formation, i.e. the formation of an electron-hole bound pair. When the positron forms an exciton, it loses energies below the inelastic threshold, so it cannot form Ps and it can be emitted as positron [224]. In fact, figure 4.5a shows an increase in the positron yield for implantation energies above E_x. After this threshold, the positron yield has a steep increase for implantation energies higher than the material band gap E_g. In this region, the positrons efficiently lose energy by electron excitation. By losing the tens of electronvolt of energy from this process, the positrons do not have enough energy for efficient Ps formation, so if the remaining energy is still higher than the positron work function, they are emitted by the solid.

From a solid noble gas, the positrons are emitted with energy between 0 eV and the inelastic threshold of the material [224]. Positrons emitted with energies near zero correspond to positrons with energies, in the material, slightly bigger than ϕ_+. Positrons with energy higher than E_{th} and lower than E_g are mainly emitted as Ps. In the case of higher energy positrons, the electron excitation cools them down by E_g, until the positron energy is lower than the band gap. Up to now, we considered the implantation of monoenergetic positrons. In the case of a radioactive source, the energy distribution is wide (see fig. 4.3). Figure 4.5b shows the energy distribution of positrons emitted by an assembly of a sodium-22 source and a neon moderator. The distribution is centered around ~ 1 eV similar to the case of moderator with negative work function. However, the FWHM of the energy distribution is 0.58 eV, much worse than the case of tungsten moderators shown in the previous section. Nevertheless, while the neon moderators have a larger energy distribution, they have an advantage in the positron yield: neon moderators have a reported moderation efficiency of 0.7% [19] against the 0.04% of tungsten [225]. The high efficiency makes this kind of moderator best suitable for dense bunched positron beams, where the positron energy distribution at the target is mainly related to the BGT, accumulator, and buncher. On the other hand, the higher intensities obtainable with solid noble gas moderators permit a higher rate of bunches from the BGT.

In the previous section, when talking about moderators with negative positron work function, we presented materials that are solid at room temperature and commercially available as foils. Solid noble gases are commercially available in gas bottles and are required to solidify on metallic supports held at cryogenic temperature. These moderators require a relatively complex apparatus to generate the ultra-high vacuum and cryogenic conditions to grow the moderator. The vacuum conditions are required so that on the cooled surfaces only the noble gas injected into the vacuum chamber from the gas bottle can solidify. The process of formation of a solid noble gas moderator requires following complex procedures. In section 6.2.1, the recipe we use for the formation of the solid noble gas moderator is presented. As we will see in chapter 6, the automation of the formation process of solid noble gas moderators is a necessary step for all apparatus using this kind of moderator due to the frequency at which a new moderator needs to be deposited. In fact, noble gases have one of the lowest melting points. So, at the cryogenic condition at which the moderator is operated, all other molecules in the air can solidify: the cooled surfaces act as a vacuum pump. These molecules adsorbed on the moderator surface decrease the moderation efficiency. So instead of the months of operation we

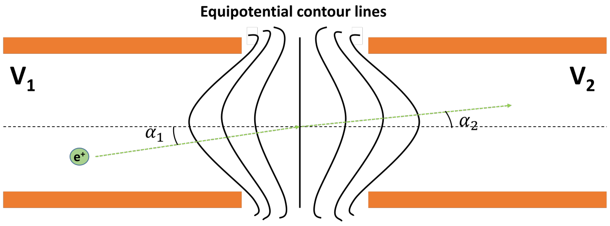

Figure 4.6: Immersion lens with cylindrical electrodes

can obtain from a moderator with a negative positron work function, a solid noble gas moderator is regrown up to two-three weeks to keep a good moderation efficiency.

4.2.3 SpPo positrons from the moderator

The interaction of the positron with the moderator atoms does not involve the particle spin, so the emitted positrons from the moderators present the same spin as they were emitted from the source. The beam is formed by the positron emitted within an acceptance angle α with respect to the source surface normal. The beam spin-polarization is given by the source helicity ($H = v/c$, see table 4.1) and the acceptance angle α [127]:

$$P = \frac{v}{c}\frac{1+\cos\alpha}{2} \tag{4.4}$$

From a radioactive source, the beam spin-polarization is around 30 % [127, 226].

4.3 Transport

The positrons emitted from the moderator need to be transported to the target. Positron transport can be obtained with electric potentials or magnetic fields.

Electric Potential In this case, the positrons are deflected by the difference in the electric potential between two surfaces [227, 228]. Most of the time, cylindrical electrodes are used like the one seen in fig. 4.6. In a cylindrical electrode, the electric potential is only constant inside the electrode. In the case of two cylindrical electrodes like in fig. 4.6, the potential of one influences the other. The penetration length of this influence in the electrode depends on the electrode diameter. It is this electrostatic potential distribution between the two electrodes that, acting on the particle velocity vector, changes the particle direction. Considering a system like the one in fig. 4.6, if the particles are near the electrode axis, the electric potential deflects the direction of the particle velocity with respect to the electrode axis following the formula [228]:

$$\frac{\sin\alpha_2}{\sin\alpha_1} = \sqrt{\frac{V_1}{V_2}} \tag{4.5}$$

where V_1 and V_2 are the electrode potentials, α_1 and α_1 are the angles between the particle trajectory and the electrode axis in the two electrodes. The beam transport makes use of a series of cylindrical electrodes whose electric potentials are set in a way to transport and focus the beam.

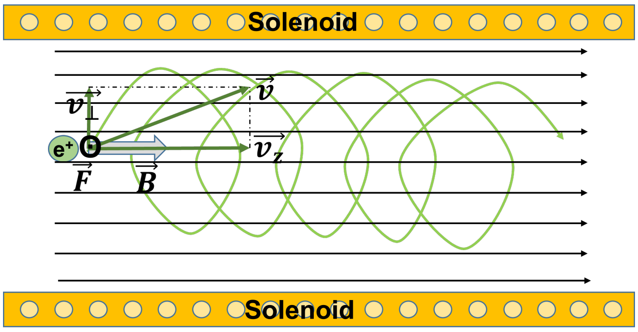

Figure 4.7: Transport of a low-energy beam with magnetic field

Magnetic Field In a static magnetic field $\vec{B} = B\hat{z}$, a positron moves with a velocity $\vec{v} = \vec{v}_z + \vec{v}_\perp = v_z\hat{z} + v_r\hat{r} + v_\theta\hat{\theta}$ (in cylindrical coordinates) and it is subject to the Lorentz force:

$$\vec{F}_L = +e\vec{B} \times \vec{v} = +eB\hat{z} \times (v_z\hat{z} + v_r\hat{r} + v_\theta\hat{\theta}) = +eBv_r\hat{\theta} - eBv_\theta\hat{r} \tag{4.6}$$

This force induces a cyclotron motion around the z-axis with radius $R = \frac{m_0 v_\perp}{eB}$, while the particle still moves along the z-axis with velocity $\vec{v}_z$. the combination of the two effects forms a helix for the particle trajectory, as shown in fig. 4.7. The magnetic field is generated by electromagnets, multiple separated coils, or a long solenoid around the vacuum chamber. In general, fields of the order of hundreds of Gauss are used for positron transport.

Regarding the spin-polarization of the transported beam, the positrons maintain their spin polarization until the beam direction is not changed.

4.3.1 Simulation

At present, personal computers have become powerful enough to simulate particle trajectories even in complex electromagnetic fields through *finite element method* (FEM). In the case of low-energy positron beams, there are two main programs used for simulating the transport fields and the particle trajectories: SIMION® and COMSOL®.

SIMION® It generates the electric maps for a given geometry of a system, and it calculates the particle trajectories through electric and magnetic fields. The magnetic field maps can be imported into the program, in the latest versions, it is possible to calculate the field from simple magnetic coils. SIMION® mainly works with symmetric systems for which it is possible to reduce the dimensions of the system. In the latest version, it can solve systems in a true 3D environment.

COMSOL® It is a program for the solution of any differential equation with FEM. It is a complex software with continuous updates and new features. For our applications, COMSOL® can compute the electromagnetic field map for any system geometry with the Magnetic Fields (mf) and the Electrostatics (es) modules, and it calculates the particle trajectories interacting with these fields with the Charged Particle Tracing (cpt) module.

4.4 Speed Selector

Fast positrons crossing the moderator can be a source of noise in the target region. To separate the source-moderator region from the target region, speed selectors are used. The selection is done by deflecting the slow positrons with electric or magnetic fields, while fast positrons are undeflected.

Examples of speed selectors are deflectors that change the direction by 90°. This can be done with a magnetic field perpendicular to the beam trajectory or using electrostatic deflectors. In this last case, the positron passes between two electrodes shaped like two sections of a cylinder or a sphere [228]. In principle, the beam after the speed selector could have a different spin polarization than the one from the source-moderator assembly.

If we want to maintain unchanged the beam direction before and after the speed selection, $\vec{E} \times \vec{B}$ filters can be used. Another possibility is to deflect the slow positrons by an electric potential or a magnetic field in an out-of-axis small hole along the beam direction. The hole is in a material that blocks undeflected positrons. Only positrons with a velocity slow enough to be deflected in the hole can pass. In the following chapter, we will see how we implemented this deflector using magnetic fields.

Chapter 5

PsICO apparatus: Design

The study of the annihilation photon entanglement (see chapter 3) requires the production of Ps in a selected spin-state. To this end, dense positron bunches have to be produced, implanted in a target capable to form and emit Ps into the vacuum (see section 2.1.5), and manipulated Ps to select its spin-state (see section 2.1.5.2). This section is centered on the design of the PsICO (Positronium Inertial and Correlation Observations) apparatus for the production of a dense bunched positron beam (see chapter 4).

In the design of the PsICO apparatus, we paid particular attention to the target region. As discussed in chapter 4, the creation and transport of positron beams require the use of magnetic or electric potentials. The presence of these fields influences the state of the Ps by introducing the Stark effect [15] and the motional Stark effect [15, 98, 229] (see also section 2.1.6).

The target region can be electric field-free by putting the vacuum chamber and the last electrode at ground potential. The task of obtaining a magnetic field-free region around the target was more challenging. There are two ways to decrease the magnetic field: increase the distance from the coils generating it or the use of a field terminated. In the first case, the magnetic field slowly decreases, then the charged particles would follow its line causing an expansion of the beam spot, this configuration is called adiabatic extraction (AE) [230]. In the second case, the introduction of ferromagnetic materials guides the field line away from the beam. In this case, the magnetic field decreases quickly. When this decrease happens so fast particles cannot follow the magnetic field lines anymore, we talk about non-adiabatic extraction (NAE).

In the literature, there are already a few examples of dense bunched positron beams capable of implanting the positron in a target in free-field, i.e. absence of electromagnetic field, making use of combined AE and NAE [21–23]. In these systems, the positron bunch leaving the BGT travels in a region with a slowly decreasing magnetic field (AE) until its intensity reaches a few tens of Gauss, then a magnetic circuit of ferromagnetic material is positioned to guide the remaining field around the target region (NAE). After this extraction, the bunch is in a magnetic field-free region, however, electrostatic lenses are still needed to focalize the beam on the target. The electric field termination is guaranteed by a grounded last electrode [21, 22] or by a grounded grid [23]. Nevertheless, these designs present some limitations that prevent their application for the study of the annihilation photon entanglement. First of all, the free field region around the target is

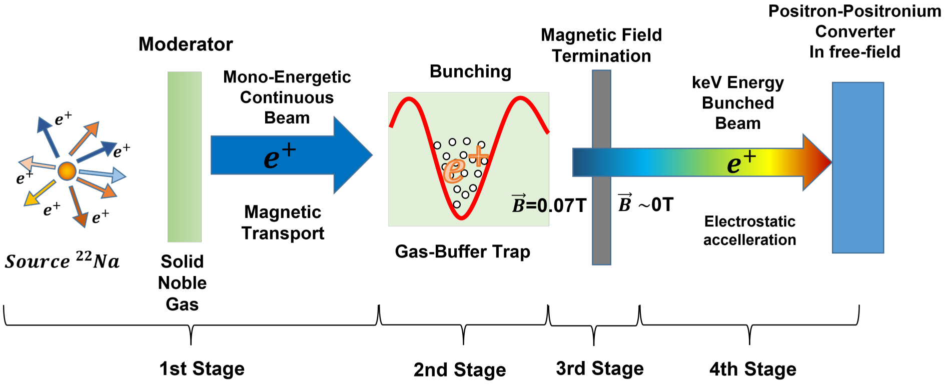

Figure 5.1: Scheme of the design of the PsICO apparatus divided into four stages, for each stage the main elements are sketched.

limited [21, 23], this impedes the free expansion of the Ps cloud emitted by the e^+/Ps converter. A second hurdle is the low implantation energy (< 5 keV) achieved until now with the existing designs [23]. This low implantation energy hinders the possible use of the new e^+/Ps converters in transmission that will be presented in section 7.1. These new converters are capable of emitting Ps cloud on the opposite side with respect to the positron beam, but they require implantation energies > 10 keV. A third limitation of the AE+NAE design is the distance between the BGT and the target. The adiabatic extraction requires an increase in the length of the apparatus after the trap, and more space is required for the electrodes that focalize the positron bunch into the target after the NAE. The increase in this length means an increase in the temporal spread of the positron bunches from the trap. In principle, the bunch could be re-compressed with a buncher [23, 24, 102, 103, 231–233] during the AE [23], but the buncher would operate in a magnetic field gradient. Moreover, with this design, the buncher is separated from the target by the presence of the magnetic circuit for NAE and the following electrostatic refocusing lenses. A fourth hurdle in the design is the magnetic circuit, that should surround the target region. The high density of ferromagnetic material will block the annihilation photons from the target region reducing the events reaching the detector surrounding the chamber. Considering the above limitations, in the design of the PsICO apparatus, we went with a different approach based on the use of NAE directly after the BGT.

The scheme of the PsICO apparatus is sketched in fig. 5.1. We can identify four stages:

- **1st Stage:** a continuous positron beam obtained from a radioactive source coupled to a solid noble gas moderator and magnetically transported;
- **2nd Stage:** a BGT operating at a 700 G magnetic field;
- **3rd Stage:** a NAE positioned immediately after the BGT;
- **4th Stage:** a buncher-elevator [24] and a system of electrostatic lenses to compress, focalize, and implant the positron bunch with energies up to 20 keV in a target in a free-field region.

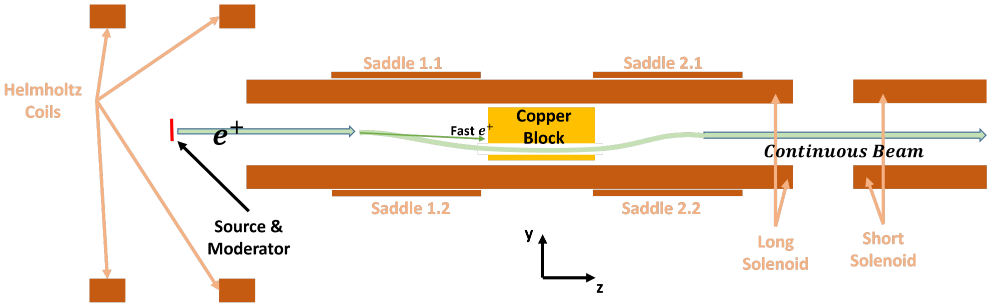

Figure 5.2: Scheme for the transport and speed selection of the positrons from the source-moderator assembly. The coils are identified in dark red. The path of the beam is shown in green. The copper block for the in-line speed selection is shown in orange.

The first two stages have been designed by reproducing and improving the already existing systems. The speed-selector in the first stage has now a more fine control on the beam path. In the BGT, two electrodes are added before the NAE to operate as a pre-buncher to compress the positron bunch temporally before the extraction from the trap. The last two stages have been designed from the ground for the PsICO apparatus. In the following, the design of the four parts will be described and discussed. The design of the apparatus, except for the first stage, is detailed in reference [20].

5.1 1st Stage: Source and Continuous Beam

The purpose of the first stage is the creation of a continuous positron beam with an intensity as high as possible to be used to feed the buffer-gas trap. In chapter 4, we have discussed how to generate this kind of beam. The stage design is based on the use of a radioactive source coupled with a solid noble gas moderator to slow positrons down to a few electronvolts and to obtain the maximum moderation efficiency. The beam is then transported by a magnetic field. The positron speed selection is done with the use of magnetic fields in the in-line configuration.

The design of this stage has been based on the design of the positron beamline of the AE$\bar{g}$IS (Antihydrogen Experiment: Gravity, Interferometry, Spectroscopy) experiment [103]. Such a system operates at CERN and was acquired from First Point Scientific [18]. However, our design presents a change in the operation of the speed selector with respect to the design presented in [103].

5.1.1 Transport & Speed selector

The sketch of the transport and speed selection is shown in fig. 5.2. The positrons are emitted by the source and slowed down by the moderator, then they are guided away from the source-moderator region by the magnetic field generated by the Helmholtz Coils. The positrons are then injected in the hundreds of Gauss magnetic fields generated by two solenoids: one long after the Helmholtz coil followed by a short one. The two solenoids drive the continuous positron beam to the second stage, the positrons travel for the most part along the solenoid axis. There are two separated solenoids due to the presence of a pumping line for the generation of vacuum along the beamline, this will be discussed in

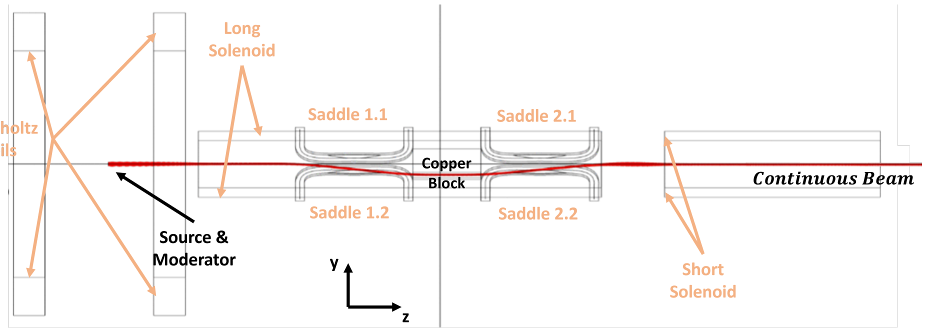

Figure 5.3: The results of the simulation with the positron trajectory in red considering positrons emitted from the source-moderator assembly with energy of about 19 eV and spot diameter 8 mm.

detail in chapter 6. In the following, the z-axis is along the solenoid axis, while the y-axis corresponds to displacement from the solenoid center with the source as the origin.

As discussed in section 4.4, we need to eliminate the positron emitted by the moderator with high energy. In the design presented in fig. 5.2, the speed selection is done inside the long solenoid without changing the beam direction before and after the speed selection. The positrons from the source-moderator region arrive at the copper block shown in the middle of the long solenoid in fig. 5.2. This block has a hole with a diameter of 6 mm displaced from the solenoid axis (see fig. 5.2). The slow positrons are guided out-of-axis in the hole and back on the solenoid axis after the copper block by the speed selector, the fast positrons annihilate on the copper block. The solenoid is required to confine the slow positron beam inside the hole. The deviation of the beam is done with two couples of coils called saddle coils, each couple generates a magnetic field perpendicular to the direction of the beam along the y-axis. The positrons follow the magnetic field lines generated by the sum of the field from the solenoid and the one from the saddle coils. The saddle coils are circular coils deformed to follow the surface of the solenoid.

In the original design of reference [103], the four saddle coils are identical and they are powered with the same current. While this design is simpler, it requires the introduction of correction magnets to center the beam back on the solenoid axis. Then, for the design of the PsICO apparatus's first stage, we decided to change the second couple of saddle coils to reduce the magnetic field they generate. With this change, the beam is guided back directly in the solenoid axis after the speed selection, and no correction magnetic field is required. Simulations of the positron transport have been performed to identify the correct current and turn number of the coils for the beam transport to happen as sketched in fig. 5.2.

5.1.1.1 Simulation

The simulations of the positron transport make use of the capability of COMSOL® to simulate the field generated from coils of any form. The position and form of the coils can be seen in fig. 5.3. In this figure, the raytracing of the positron beam is also shown using as starting condition positrons emitted from the source-moderator with energy 19 eV and spot diameter 8 mm, similarly to the system in reference [103]. While the

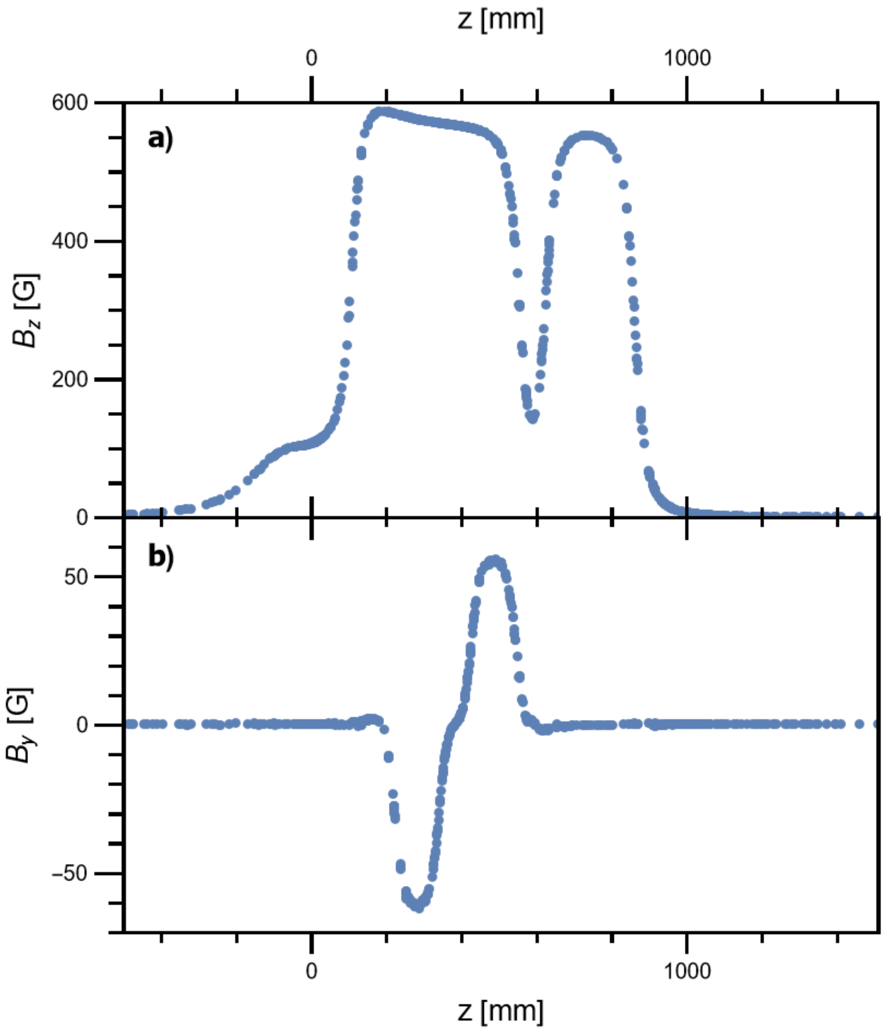

Figure 5.4: Simulated magnetic field. Components of the magnetic field along the solenoid axis: (a) z component, (b) y component. The origin is set at the center of the radioactive source.

spot dimensions are due to the moderator geometry which we will discuss in chapter 6, the positron energy is given by the average energy of the positrons emitted from the moderator (see section 4.2.2) and the moderator electric potential 18.75 V referred to the rest of the system that is grounded.

As discussed in section 4.3, the magnetic field needs to be aligned along the beam direction to obtain a beam transport as shown in fig. 5.3, while the fields from the saddle coils are perpendicular to the beam direction. The raytracing shown in fig. 5.3 was obtained with the transport magnetic field shown in fig. 5.4a. As seen from this figure, the magnetic field produced by the Helmholtz coils in the source-moderator region has an intensity of a hundred Gauss. The solenoids, instead, generate a stronger field $> 500\,\mathrm{G}$ to obtain a small beam spot that fits inside the hole in the copper block. As expected from the coil geometry shown in fig.s 5.2 and 5.3, figure 5.4a shows two separated regions at high field intensity corresponding to the two solenoids: the long solenoid positioned after the moderator and over which the saddle coils are installed, and a short solenoid after some distance from the long one. While this separation is required from construction constraints, it has been minimized to reduce as much as possible the drop in the field intensity in this region. A too-drastic decrease in the magnetic region could produce a mirror effect inverting the particle motion and reflecting it back. As seen from the raytracing in fig. 5.3, the distance of the two solenoids was optimized to avoid the magnetic mirror effect. Figure 5.4b shows the field generated by the two couples of saddle coils. Saddle 1.1 and 1.2 generates a $-61\,\mathrm{G}$ magnetic field in their center which is higher, in absolute value, than the $55\,\mathrm{G}$ magnetic field obtained at the center of saddle 2.1 and 2.2. With this asymmetry in the generated field, the beam is centered on the solenoid axis after the speed-selector without the need for further corrections (see fig. 5.3).

The coil currents and turn number to obtain the raytracing shown in fig. 5.3 are:

- **Helmholtz coils:** 576 turns, 2.82 A
- **Saddle 1.1 & 1.2:** 131 turns, 2.099 A
- **Saddle 2.1 & 2.2:** 125 turns, 2.004 A
- **Long solenoid:** 1664 turns, 12 A
- **Short solenoid:** 894 turns, 12 A

5.2 2nd Stage: Buffer-Gas Trap

The BGT [16, 17] transforms a continuous positron beam into a dense bunched positron beam by allowing cooling, storing, and bunching of many positrons. The BGT is based on the principles of the Penning-Malmberg trap: a strong magnetic field confines the particle radially, and an electrostatic potential well confines the positrons axially. To efficiently trap the positrons, they must be cooled. The cooling is obtained by inelastic scattering with gas molecules introduced in the vacuum chamber. The positrons are progressively cooled in a stair-shaped potential well and until trapped in its bottom where they are stored [16]. With BGT like the one in fig. 5.5, bunches are emitted with more than 10^4 positron per bunch with a temporal length of a few tens of nanoseconds [23, 232, 234, 235]. This positron number is more than enough for most of the applications, however sometimes a large number of positrons is needed, so multiple bunches are accumulated in a separate part of the beamline called an *accumulator*, and the final bunches can contain up to several $10^7 - 10^8$ positrons [103, 199].

For our planned experiment, the positron number released from the BGT is more than enough. We designed a BGT based on the one of the positron beamline of the AE$\bar{\mathrm{g}}$IS [103]. The design of the new PsICO apparatus BGT is shown in fig. 5.5. The main novelties are the optimization of the positron release from the trap and the extraction from the magnetic field. In the following, we discuss the elements and operation of this design.

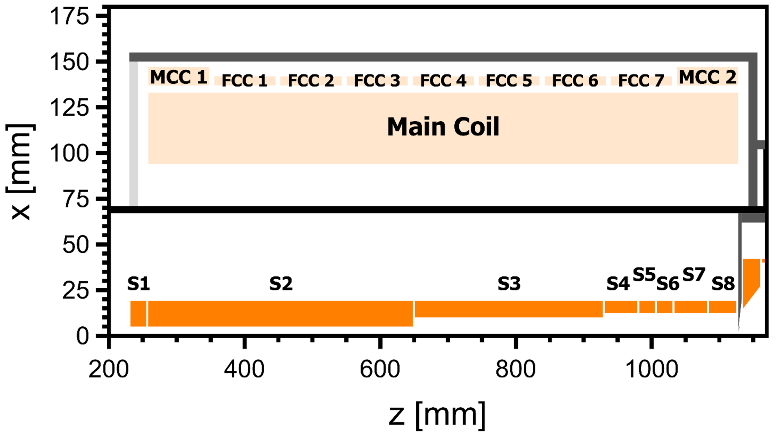

Figure 5.5: Scheme of the two stages buffer-gas trap of the PsICO apparatus. The BGT is composed of: 1) Main Coil, Main Correction Coils (MCC), and Fine Correction Coils (FCC) of the magnet and 2) electrodes of the BGT trap labeled from S1 to S8. S5 is segmented to apply a rotating electrodynamic field to compress the positron cloud. The different colors indicate different materials: in dark gray are the iron elements, in light gray the elements in stainless steel, in black the vacuum chamber, in dark orange the copper electrodes, and in light orange the coils. The origin of the axes was placed at 23.2 cm to the left of S1 along the electrode axis. *Image from* [20].

5.2.1 Gasses

A combination of two gasses is used in the standard procedure to cool the positrons in a BGT, a main gas in great quantities, and another gas in much smaller quantities. The first gas is nitrogen. The positrons with the energy of tens of electronvolt from the source-moderator assembly are inelastically scattered by N_2. In this scattering process, the positrons efficiently transfer their kinetic energy to the electrons of the gas molecule. Consequently, the positrons do not have enough energy to escape from the trap back to the first stage, so they remain trapped in the electrostatic potential well of the BGT [230]. For the second gas, there are different possibilities: SF_6, CO_2, and CF_4 [230]. The second gas is needed to keep the positrons cooled while they are compressed. By trapping more and more positrons in the potential well, they form a cloud at its bottom. To obtain a bunch with a small spot diameter, the cloud is compressed by driving a segmented electrode with a rotating electric field, this technique is called the rotating wall (RW) technique [17, 235–237]. However, this compression results in a warming of the positrons, so with the second gas, the positrons can lose energy through vibrational excitation of the gas molecules [230].

Obviously, the inelastic scattering is not the only interaction process between the positron and the gas molecules, the gas pressure needs to be low enough for the positrons to have an annihilation lifetime longer than their storage time in the trap. On the other hand, we need to have a number of molecules in the vacuum chamber large enough to cool the positrons. The trick used to solve this problem in the BGT is the electrode dimensions. Their internal diameters are different for the different sections of the trap, so the highest pressure ($\sim 10^{-2}$ mbar) is present at the entrance and the lowest pressure

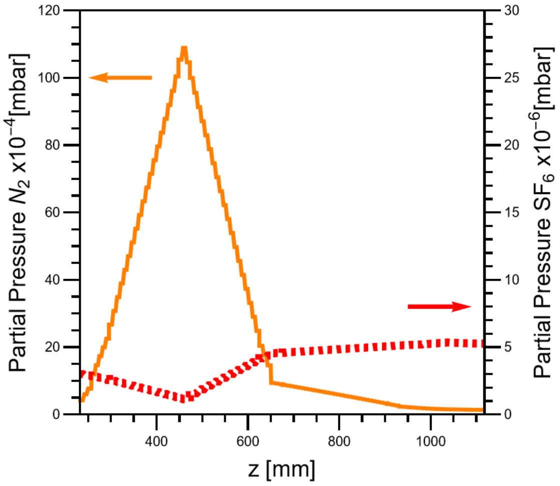

Figure 5.6: Simulated pressure profile inside the BGT electrodes (as shown in fig. 5.5) with fluxes 5.58 sccm for N_2 (orange solid line) and 0.02 sccm for SF_6 (red dashed line) in standard conditions.

($\sim 10^{-5}$ mbar) is obtained at the potential bottom in the electrodes with the largest diameter, where the positrons are trapped [230]. As shown in fig. 5.5, the PsICO apparatus BGT has electrodes with a small diameter at the start (electrodes S1 and S2), which is then increased in the middle (electrode S3), while it is the largest at the end (electrodes S4-S8). In this design, the nitrogen gas is inserted directly through a hole in the middle of electrode S2, while the second gas is released in the vacuum chamber in the interspace between electrodes S5 and S6 in correspondence with the bottom of the electrostatic potential of the trap. For the PsICO apparatus, we ended up choosing SF_6 as the second gas, due to its high cooling rate [230]. With this gas, in a BGT, the trapped positrons are thermalized ($k_B T$=25 meV with k_B the Boltzmann constant) in a few milliseconds [235].

In order to define the gas fluxes to create the required pressure profile inside the BGT electrodes, we simulated the pressure in the PsICO BGT at different fluxes of N_2 and SF_6 by means of COMSOL® using the *Free Molecular Flow (fmf)* module. We considered the gasses in standard conditions (pressure 1 bar and temperature 300 K). We used as reference the pressure profile in the AE$\bar{g}$IS BGT described in reference [103], where a pressure of around $\sim 10^{-2}$ mbar is present at the entrance of the trap and around $\sim 10^{-4}$ mbar in the bottom of the potential well. According to the simulation, in our geometry such values are achievable with fluxes of N_2 of 5.58 sccm and SF_6 of 0.02 sccm, where sccm stands for *Standard Cubic Centimeter per Minute.* More in detail, a pressure of 1.1×10^{-2} mbar is expected in the middle of S2 while 3×10^{-4} mbar in the trapping region of electrodes S5 and S6, as shown in fig. 5.6.

5.2.2 Magnet

The BGT magnet needs to generate a magnetic field to confine the positrons in the electrode and to allow to compress radially the positron cloud at the bottom of the electric potential well. Moreover, other two characteristics are needed for the operation of the trap: a slow increase in the field intensity at the trap entrance, and a homogenous field in the trapping region between electrodes S5 and S6. The first requirement arises from the fact that a pumping station has to be positioned before the first stage and the BGT to limit the gas flux from the trap to the source-moderator region which would pollute the moderator. This results in a drop in the magnetic field intensity between the short solenoid end and the entrance of the BGT magnet. To avoid the formation of a magnetic mirror, the magnetic field of the trap has to increase slowly enough to permit the positron beam to enter the BGT. The homogeneity of the magnetic field in the trapping region is required by the fact that eventual inhomogeneity would result in a heating of the trapped positrons. To trap positrons [103], the BGT magnet needs to generate a stable magnetic field of 700 G with a field homogeneity (measured as the maximum variation of the field intensity in the selected region) of at least $\frac{\Delta B}{B} = 0.1\%$ in the region between electrodes S5 and S6.

The magnet design of the PsICO BGT is shown in fig. 5.5, it is composed of ten separated coils: a main coil capable of generating fields up to 850 G, and nine correction coils to adjust the magnetic field. The main coil is formed by 412 turns of 7.5 × 7.5 mm holed copper wire. The wire has a 5 mm diameter hole for the water needed to cool the magnet. The other nine coils are formed by AWG (American Wire Gauge) 9 copper wires. The two external coils are called *main correction coils* and have 39 turns, and the seven coils in the middle are called *fine correction coils* and have 26 turns. These coils are supported and cooled by the main coil. The correction coils are needed to fine-tune the magnetic field to obtain the required slow increase in the field intensity at the entrance of the BGT and the homogeneous field in the region of electrodes S5 and S6.

From the design in fig. 5.5, the magnetic field profile in fig. 5.7b is obtained using COMSOL® simulations with *magnetic field (mf)* module. The magnetic field shown in fig. 5.7b satisfies all the characteristics previously requested: the field increases slowly enough to avoid magnetic mirroring the positrons back to the first stage, and a field homogeneity $\Delta B/B$ better than 0.1% in the trapping region.

5.2.3 Electrodes

While the gases cool the positrons and the magnetic field confines them radially, the electrodes S1-S8 define the electrostatic potential profile. Three different potential profiles are used during the operation phases of the BGT: *trapping*, *compression*, and *release*. At the start, we have a step potential ending in a well between S5 and S6. As the positrons are gradually cooled by N_2 gas, they are progressively confined in a smaller region and finally trapped in the potential well (see fig. 5.7c). During this *trapping* phase, the positrons are continuously accumulated in the potential well bottom. After a given accumulation time, the potential of electrode S4 is raised to block the entrance of other positrons in the potential well bottom. At the same time, the potentials of electrodes S5 and S6 are raised (see table 5.1). In this second phase (*compression* phase), the positron cloud is trapped in a deep potential well between electrodes S5 and S6. In the process, the cloud is compressed with the RW technique using the segmented electrode S5, while the positrons are kept cool by the addition of the second gas. The *compression* phase prepares the positrons to be released outside the BGT. The release is done by lowering the potential of electrodes S6-S8. In a typical BGT, a cycle of the three phases is completed multiple times per second [103]. The slowest phase is the first, where we have to wait for the accumulation of the positrons that depends on the rate of the continuous positron

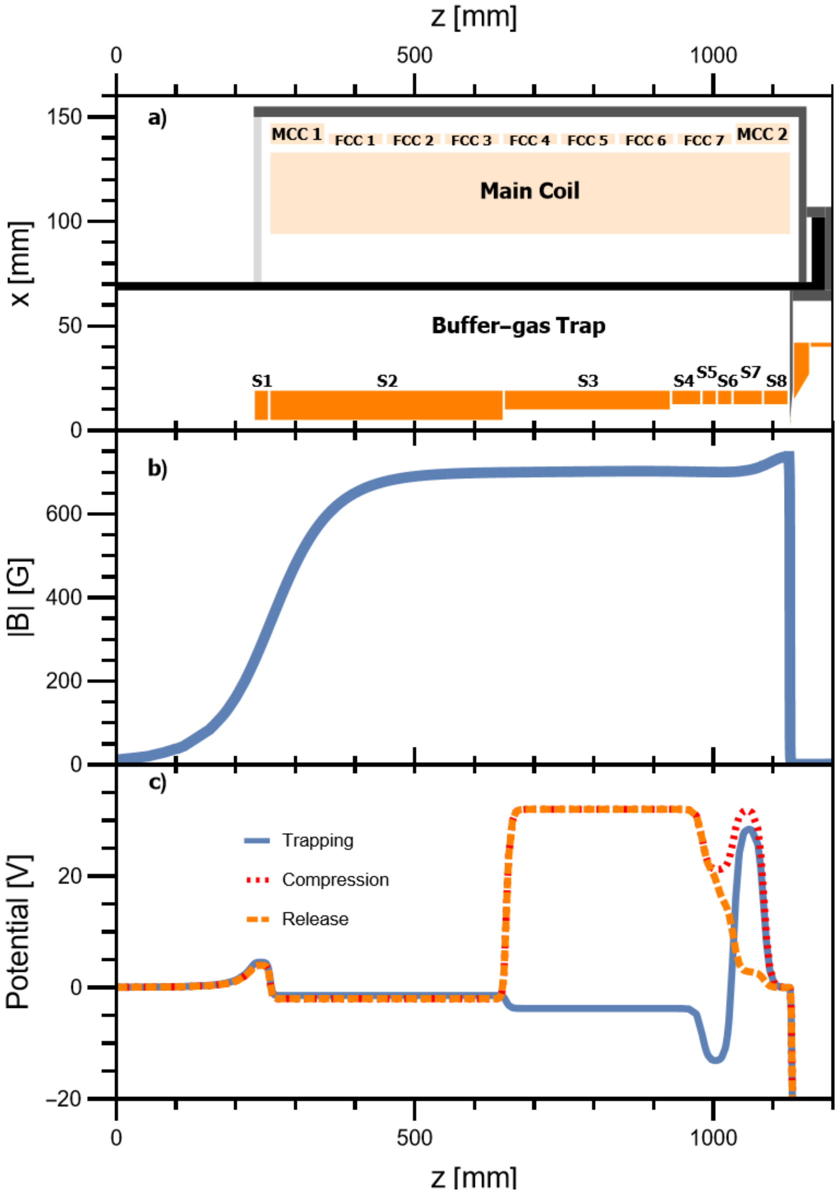

Figure 5.7: (a) Sketch of the BGT with axial dimensions. (b) The intensity of the magnetic field along the axis of the system. (c) Potential along the axis during the three phases: (continuous line) *trapping* phase; (dotted line) *compression* phase; (dashed line) *release* phase. To show the full dynamic of the magnetic field, the origin of the axes was placed at 23.2 cm to the left of S1 along the electrode axis. *Image from* [20].

Table 5.1: Potential of electrodes S1-S8 during the three phases: *trapping*, *compression*, and *release*. The potentials for two possible releases *Dumping Release* and for *Release with Parabolic Potential* are reported. See text for details. *Table from* [20].

Electrode	S1	S2	S3-S4	S5	S6	S7	S8
Potential [V] @ Trapping	4.55	-1.43	-3.75	-13.31	-13.31	28.83	0.00
Potential [V] @ Compression	4.00	-2.00	32.00	21.10	21.10	32.00	0.00
Potential [V] @ Dumping Release	4.00	-2.00	32.00	19.80	19.80	0.00	0.00
Potential [V] @ Release with Parabolic Potential	4.00	-2.00	32.00	21.10	14.90	1.50	0.00

beam. The second phase lasts a few milliseconds. This time is needed for the positron cloud to reach the maximum compression and for the positrons to thermalize [235].

COMSOL® *electrostatics (es)* module has been used to simulate the electrostatic potential profiles for the operation of the PsICO BGT in the three phases (fig. 5.7c). The corresponding electrode potentials are reported in table 5.1. Knowing the electrostatic potential and magnetic field in the S5-S6 region, it is possible to reconstruct the dimension of the positron cloud before its release from the BGT. The positrons at this point are considered thermal, so, given the good magnetic field homogeneity in the region, the cloud is expected to have a cylindrical form [235] with a diameter of 5 mm. Along the trap axis, the positrons fill the potential well up to 25 mV from the bottom, this corresponds to a total length of 9 mm as seen in fig. 5.8.

5.2.3.1 Release form BGT

In BGT like the one in reference [103], the positron cloud is released by simply lowering the potential of electrodes after the trapping region (electrodes S7 and S8 in our design), this is called *dumping release* (DR). The potentials corresponding to this release operation are shown in table 5.1. In this configuration, the positrons spill outside the trap towards the next section of the apparatus. This option is employed in systems where the BGT feeds an accumulator [103]. In this case, the relatively broad time distribution of positrons released from the BGT (a few tens of nanoseconds) is acceptable. In the PsICO apparatus, a minimization of the positron time spread at the exit of the BGT is required in view of their transport to the target. So a different release method has been considered: *release with parabolic potential* (RPP). In RPP, the potentials of S5 and S6 are set at different values (see table 5.1) forming a quasi-parabolic potential with the height of 32 V at S4 and the vertex 0 V at the end of S8 (see fig. 5.8). The two methods have been compared through COMSOL® simulations using the *electrostatics (es)* module.

The simulation was started just before the release, so the positrons are in a cylindrical cloud of length 9 mm and diameter 5 mm. We considered 10^4 positrons distributed as cylindrical slices every 0.45 mm. To each positron, a velocity has been assigned with the three components randomly sampled from a Maxwellian distribution at 300 K. The assigned velocity is independent of the position of the positrons, then the positrons at the extremes of the cloud have an average total energy of 50 meV. For both the released methods, a rise time of 5.5 ns has been considered for the change in the electrostatic

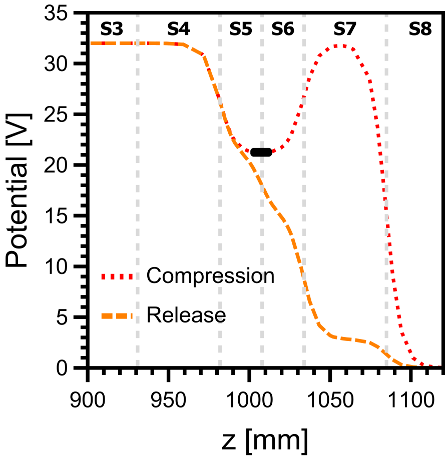

Figure 5.8: Detail of the potential along the main axis during the *compression* phase (dotted line) and the *release* phase with quasi-parabolic potential (dashed line). The cylindrical distribution of the confined positrons before the release is marked in black (see text for details). See fig. 5.7 for the definition of the z-axis. *Image from* [20].

potential between the *compression* and *release* phases, similar to what is obtained with the electronics employed in [24].

In the case of DR, the positron bunch at the end of electrode S8 has a temporal length of 55.2 ns FWTM (Full Width Tenth Maximum). In the case of RPP, we obtain 4.2 ns FWTM, an order of magnitude less with respect to the other method. As compared to the case of reference [24], the electric potentials, in this case, are much lower, so lower rise time, and temporal width, could be achieved. Moreover, due to the low density of the positron cloud, the space-charge effect is still negligible [22], and a similar time spread is expected even with bunches containing up to 10^6 positrons.

The positrons released by the BGT are at the end of electrode S8, still inside the trap magnetic field as seen in fig. 5.7, in the next section, we will see how the extraction from this field has been achieved.

5.3 3rd Stage: Magnetic Field Extraction

In the PsICO apparatus, we want to extract the positrons from the magnetic field as soon as they exit the BGT so that the final part of the beam transport can be purely done with electrostatic potentials. We designed an NAE of the positron bunches after they exit electrode S8. This was done in a way to keep the beam from diverging. The structure of the designed NAE is shown in fig. 5.9. The structure consists of two components: the *iron structure* with the spider, and the electrodes E1-E3. The first component terminates the magnetic field, while the electric potentials on the electrodes E1-E3 guide the positrons and focus them in the next stage of the apparatus.

5.3.1 NAE

The non-adiabatic extraction is obtained by quickly terminating the magnetic field so the particles cannot follow the field lines like in the case of adiabatic extraction [22].

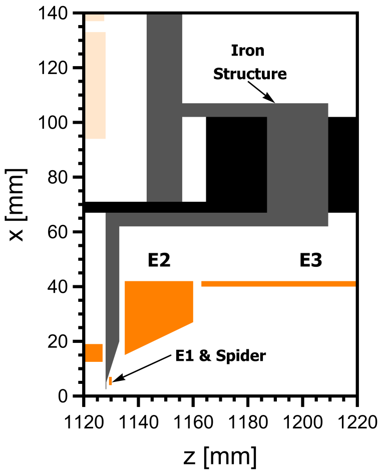

Figure 5.9: Non-Adiabatic Extraction (*NAE*) zone. Dark gray indicates the field terminator in iron. Extraction electrodes in orange. Vacuum chamber in black. See fig. 5.7 for the definition of the origin of the axes. *Image from* [20].

The termination of the field is done with a magnetic circuit that guides the field lines to close away from the area of interest. This circuit is composed of materials with high magnetic permeability.

In the PsICO apparatus, we decided to terminate the magnetic field just after the main magnet (the solenoid) with a complex magnetic circuit in ARMCO® pure iron. The shape of the magnetic circuit is shown as dark gray in fig. 5.9. A cup in ARMCO® is inserted in the vacuum chamber of the BGT. The cup is in contact with the vacuum flange of the chamber (still in ARMCO®) which is then connected to the outside of the BGT magnet that is also in iron (see fig. 5.9). The part of the magnetic circuit inside the vacuum chamber has a thickness of 5 mm, and at its bottom there is the *spider* structure (see fig. 5.10) for the passage of the positrons.

The design of the hole in the field terminator for the passage of the positron beam affects the transverse (i.e. orthogonal to the beam direction) velocity of extracted positrons. This is due to the different directions of the field lines during extraction that influence the direction of the Lorentz forces (see eq. (4.6)) on the particles. In the literature, there are four designs for the hole:

- simple hole [21, 23, 103, 238–240];
- concentric rings [241, 242];
- grids [243];
- spiders [22, 244–246].

The simple hole represents the simplest design. Given the cylindrical symmetry of the hole, the magnetic field lines are extracted radially, then, as seen from eq. (4.6), the Lorentz force is in the angular direction, i.e. the direction perpendicular to the plane formed by the radius and the longitudinal direction. This results in an increase in the angular component of the beam velocity making more difficult the following electrostatic

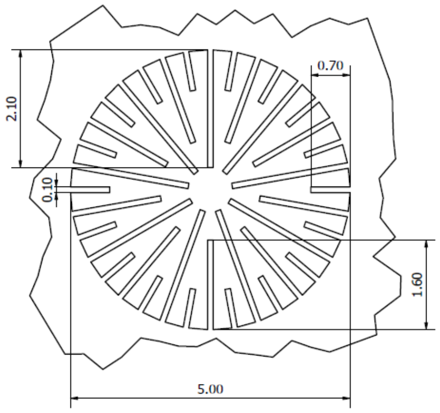

Figure 5.10: Technical design of the 0.25 mm thick spider. The reported dimensions are in mm. *Image from* [20].

transport with cylindrical lenses. The other three designs are the different answers reached to mitigate this problem. All three designs are not axially symmetric, so the magnetic field lines are not extracted only radially but also in the angular direction that corresponds to a radial Lorentz force [242]. Due to the geometry of the spider, this decreases the angular component of the velocity of the extracted particles. Consequently, the following electrostatic transport is much easier [22].

In our design, we chose the spider due to its higher transparency [22, 242]. Our spider design is shown in fig. 5.10. It consists of a 5 mm diameter structure with 0.1 mm tines on a 0.25 mm thick ARMCO® sheet. The spider transparency has been evaluated to be 75%, and this design is manufacturable by photoetching.

With the complete magnetic circuit composed of the iron structure and the spider, we obtain from the simulations a drop in the magnetic field from the hundreds of Gauss of the BGT to less than 1 G in a few millimeters (see fig. 5.11). The simulations do not show any saturation in the magnetic circuit. This is possible thanks to the choice of the material and its thickness. AMRCO® presents a relatively low magnetic permeability ($\sim 10^4$) with respect to other ferromagnetic materials like mu-metal, but it possesses a very high saturation field (up to 2.2 T) that allows to avoid saturation in the spider tines.

5.3.2 Electrodes

While the magnetic circuit reduces the magnetic field intensity, the electrodes E1-E3 manipulate the beam and focus it in the fourth stage. The positron bunch arrives at the spider with a few tens of electronvolt of energy given by the quasi-parabolic potential. COMSOL® simulations of the bunches NAE show the best results when the positron are slowed as they progress through the spider. This is obtained by a retarding electric field generated by electrodes E1 and E2 set at +20 V. Electrode E3, instead, has a -5 kV potential to generate a penetrating electric field that accelerates the positrons after the spider. In fig. 5.11, the potential generated by the three electrodes is shown. Using this configuration of the three electrode potentials, the simulations show a 60% extraction efficiency for the positrons from the BGT magnetic field, while the rest of the bunch annihilates on the spider structure. This efficiency is in line with previous results [22].

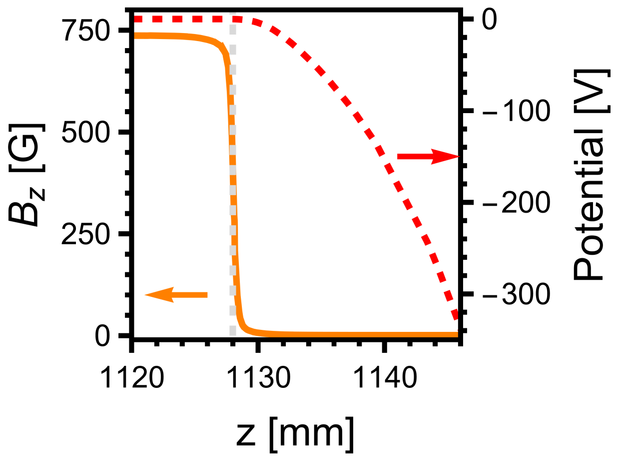

Figure 5.11: Magnetic field (continuous line) and electrostatic potential (dashed line) in the region of positron extraction from the BGT trap. The thick vertical dashed line marks the position of the spider. See fig. 5.7 for the definition of the z-axis. *Image from* [20].

5.4 4th Stage: Bunching and focusing on the target

After the third stage, the positron bunches are in a magnetic-free region and they have to be compressed in time and focused on the target that is required to be in a free magnetic and electric fields for our planned experiment. The fourth stage of the PsICO apparatus consists of two sets of electrodes as shown in fig. 5.12: electrodes B0-B9 form the buncher-elevator, and electrodes L1-L4 are the focusing lenses. The first set of electrodes is used to compress the bunch and give it the final implantation energy. The second set of electrodes focuses the compressed bunches on the target. COMSOL® simulations have been performed to find the set of potentials that ensure the best conditions of the positron beam on the target in terms of beam size and temporal distribution. In these simulations, the starting position and velocity for the positrons in the bunch correspond to the ones resulting from the simulation of the NAE (see section 5.3).

5.4.1 Buncher-Elevator

The concept of the buncher-elevator was previously studied by our group in reference [24].

Initially, electrodes B0-B9 are at $-500\,\mathrm{V}$ potential forming a lens with electrode E3 for focusing the positron bunch in the middle of the electrode set. Electrodes B0 and B9 are designed to be longer than the other electrodes of the buncher to shield the other buncher electrodes from the penetrating field of electrodes E3 and L1, respectively. By using a potential of $-500\,\mathrm{V}$, the bunch is slowed down maintaining part of the compression gained with the RPP release from the BGT. When the positrons are wholly inside the first four electrodes, B0-B3, electrodes B0-B9 are raised with a rise-time of $5.5\,\mathrm{ns}$ to the final potential value. This value is the sum of two components: a bias voltage common to all buncher electrodes and a superimposed electrostatic potential parabola [24]. The bias voltage corresponds to the *elevator* part of the electrode set B0-B9, while

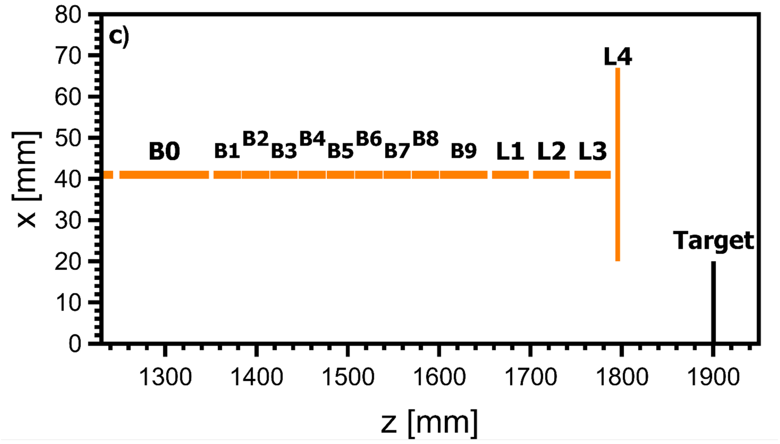

Figure 5.12: Scheme of the fourth stage of the PsICO apparatus. Electrodes of the buncher-elevator (labeled B0-B9) and focusing electrodes (labeled L1-L4). In orange the copper electrodes and in black the target. Between the target and electrode L4, there is a distance of 10 cm. See fig. 5.7 for the definition of the z-axis. *Image from* [20].

the superimposed parabolic voltage is the component compressing the positron bunches. In our design, we considered a parabola with 1 kV maximum on B0 and its vertex at the beginning of B9. The bias voltage has been considered to vary from 0 up to 20 kV (see table 5.2).

The implantation energy of the positron bunches is determined by the sum of three contributions:

- the bias;
- the 500 eV average energy of the positrons when inside the buncher before the rising of the buncher potential;
- the energy from the superimposed parabolic potential, this depends on the position of the positron along the parabolic potential.

As seen from the last three columns of table 5.2, the last two contributions add between 700 and 1400 eV to the energy from the bias.

5.4.2 Lenses

Electrodes L1-L4 are needed to focalize the positrons on the target. The optimization of the four lenses is not simple. For start, their potential is different for different biases of electrode B0-B9, and each bias needs its optimization. Moreover, the target region needs to be also free from electrostatic fields. In order to fulfill this condition L3 and L4 are kept at ground potential. This is further complicated by the request to keep a large free-field space in front of the target with a distance of 10 cm between the target and the electrode. This last point especially increases the difficulty in the beam focusing with respect to previous works in the literature [23]. Simulations of raytracing have been performed by using COMSOL® *electrostatics (es)* module to identify the optimal potential for the electrodes L1-L4. The best sets of values for each positron implantation

Table 5.2: Potential bias of the buncher-elevator and potentials of the focusing electrodes are reported in the first four columns. Spot dimension, temporal spread, and positron implantation energy at the target for each bias are reported in the following columns. The average, maximum, and minimum implantation energy for every bias value is reported in the last three columns. *Table from* [20].

Bias [kV]	L1 [kV]	L2 [kV]	L3/L4 [kV]	Spot FWTM [mm]	Temporal FWTM [ns]	Implantation energy [eV]		
						Average	Maximum	Minimum
0	0	−4.5	0	5.3	0.7	1062	1433	772
1	1	−5.4	0	5.2	1.3	2056	2419	1741
2	2	−4.7	0	4.5	1.5	3055	3440	2789
3	3	−4.0	0	4.5	1.5	4053	4442	3790
4	4	−3.5	0	4.2	1.5	5051	5424	4794
5	5.3	5.3	0	3.5	1.0	6078	6437	5791
7	7	0	0	4.1	1.6	8051	8410	7794
10	10	9.3	0	3.3	1.4	11070	11450	10790
12	12	9	0	3.7	1.6	13060	13420	12780
15	13	8	0	3.4	1.8	16000	16360	15670
20	15	0	0	4.1	1.9	20980	21360	20640

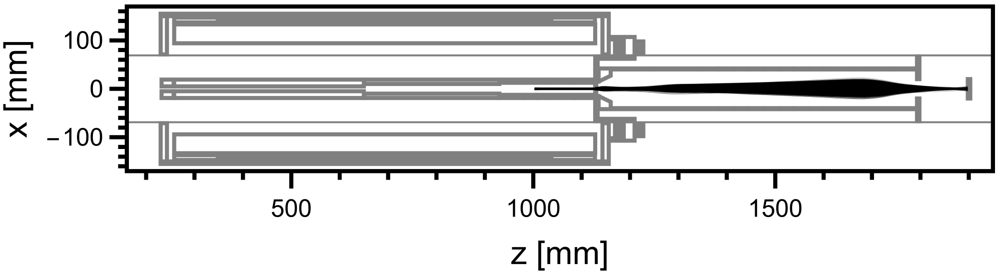

Figure 5.13: Raytracing of positrons with final implantation energy on the target of 11 keV. See fig. 5.7 for the definition of the origin of the axes. *Image from* [20].

energy in the target from around 1 keV up to around 21 keV are reported in table 5.2. From this table, we can differentiate two operation regimes. With biases < 4 kV L2 is at a negative potential, while a positive potential is required for biases from 5 kV to 20 kV.

Figure 5.13 shows the results of the raytracing simulation for the case of 11 keV implantation energy. In this figure, electrodes L1-L4 manage to focus the positron bunch on the target with a spot diameter of 3.3 mm FWTM (see in fig. 5.14). As seen in table 5.2, similar dimensions are obtained for all the simulations with implantation energies greater than 5 keV. For implantation energies smaller than 5 keV, the spot diameter is around ~ 5 mm. According to the simulations, for each positron implantation energy, the positron bunch arrives on the target with a temporal width less than 2 ns. Spot diameters smaller than the ones reported in table 5.2 can be achieved by setting L3 and L4 at a potential different than 0 V. However, this would mean relaxing the constraint to have a region in front of the target free from electrostatic fields.

In the next chapter, we will show the state of the implementation of the PsICO apparatus.

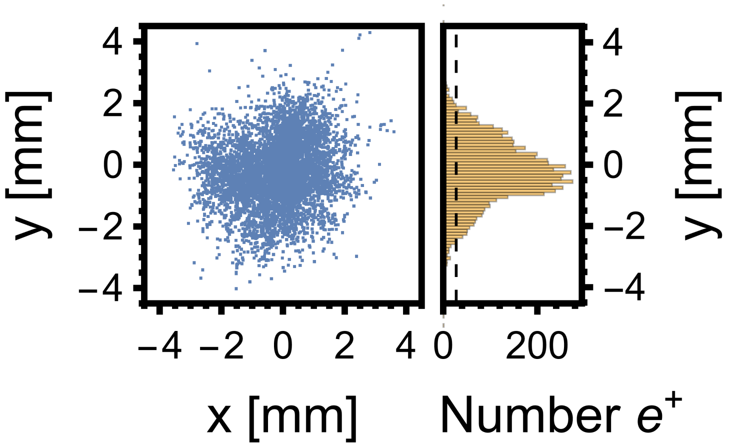

Figure 5.14: On the left: the simulated spot of positrons implanted in the target with 11 keV of average energy. On the right: distribution of positrons along the y-axis. *Image from* [20].

Chapter 6

PsICO apparatus: Commissioning

As previously described, the PsICO apparatus is composed of four stages and their designs have been presented:

- **Stage 1:** Source and Continuous Beam;
- **Stage 2:** Buffer-gas Trap;
- **Stage 3:** Magnetic Field Extraction;
- **Stage 4:** Bunching and focusing on the target.

In this section, we will discuss the construction of these stages.

At the writing of this thesis, the construction of mechanical pieces for the second to the fourth stages has been concluded. During this thesis work, we managed to build and commission the first stage, obtaining the continuous positron beam from a source with a solid noble gas moderator. In the present chapter, the commissioning and characterization of the first stage of the apparatus are presented.

6.1 1st Stage: Construction

The objective of the first stage of the apparatus is the creation of a continuous beam of slow positrons to feed the BGT in the second stage. The commercial design from First Point Scientific was used as a reference for the design of this stage with some changes in the transport system (see section 5.1.1).

Chapter 4 shows the elements required for obtaining a continuous positron beam. Our choices for each beam element are:

- **Radioactive Source:** Sodium-22;
- **Moderator:** Solid noble gas moderator;
- **Transport:** Magnetic transport (see section 5.1.1 for design);
- **Speed-selector:** Using two couples of saddle coils (see section 5.1.1 for design).

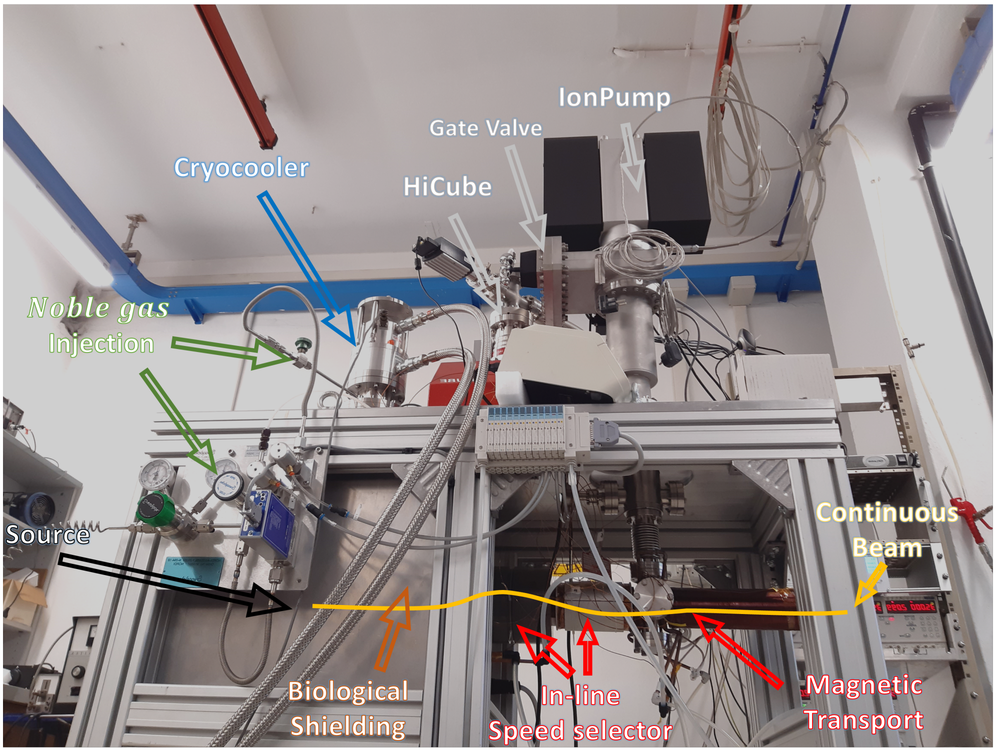

Figure 6.1: First stage of the PsICO apparatus, the different components are highlighted.

From these choices, we identified the systems that need to be constructed for the completion of the first stage:

- **Vacuum System:** To create and maintain the ultra-high vacuum (UHV) conditions (chamber pressure $< 10^{-8}$ mbar) required for the positron transport;
- **Cryogenic System:** To reach and maintain the cryogenic temperatures at the source-moderator assembly required for the growth and operation of a solid noble gas moderator;
- **Gas Injection System:** To inject the noble gas in controlled quantities in the source-moderator region for the deposition of the solid noble gas moderator;
- **Biological Shield System:** To protect the operators and the surrounding environment from the ionizing radiation of the radioactive source;
- **Transport System:** To transport and speed-select the positrons from the source-moderator assembly to the end of the stage towards the second stage;
- **Remote Control System:** To manage the apparatus remotely and automatize the deposition and annealing of the solid noble gas moderator.

Figure 6.1 shows the constructed first stage with the different elements of the apparatus indicated. In the following, the systems composing the first stage will be described in detail.

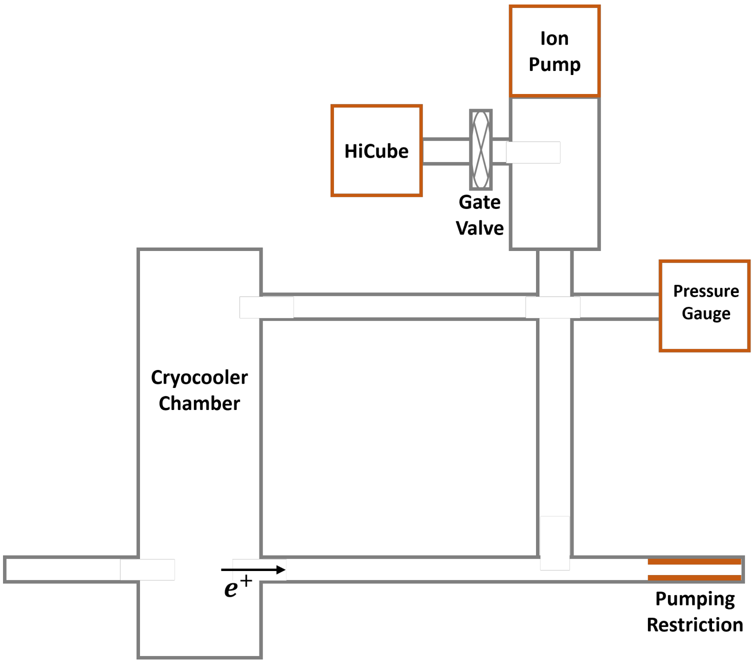

Figure 6.2: Schematic of the vacuum system of the first stage of the PsICO apparatus.

6.1.1 Vacuum System

Figure 6.2 shows the schematic of the vacuum system of the first stage of the PsICO apparatus. In the scheme, the top right part shows the elements dedicated to the creation and monitoring of the vacuum. The bottom part represents the tube in which the positron beam travels. The source-moderator assembly is positioned at the bottom of the *Cryocooler Chamber*. In the sketch, the positron beam travels from the left to the right as indicated by the arrow in fig. 6.2. The beam starts at the bottom of the vacuum chamber where the cryocooler is inserted (see fig. 6.2). As introduced in section 5.2.1, a continuous flux of gases is needed for the operation of the BGT in the second stage of the apparatus. To reduce the impact of these gases on the moderator, a pumping restriction is present at the end of the beam tube as indicated in fig. 6.2.

In order to generate the UHV conditions for the beam transport, a pre-vacuum pump and a UHV pump mounted in cascade are used. The Pfeiffer HiCube 80 Eco is used as a pre-vacuum pump (from here on it is referred to as HiCube). It is a commercial solution composed of a membrane pump and a turbomolecular pump. It operates from ambient pressure and reaches in the vacuum chamber a limit pressure of 2×10^{-6} mbar. The main task of the HiCube is to pump the vacuum chamber at a pressure lower than 10^{-4} mbar, this condition is required for the operation of the UHV pump which is the ion pump Agilent IPCMini 150 StarCell (from here on it is referred to as IonPump). Nevertheless, we generally start to operate the IonPump at a pressure lower than 5×10^{-6} mbar to increase the lifetime of the pump. Because the IonPump operates at a much lower pressure than the HiCube, this pump is usually isolated from the main vacuum chamber of the apparatus by a gate valve (see fig. 6.2) when the chamber pressure decreases below $\sim 9 \times 10^{-7}$ mbar. The pressure in the vacuum chamber is monitored all the time by a full-range vacuum gauge: the Pfeiffer HPT200. This gauge is capable of measuring pressures from ambient pressure (1 bar) to 5×10^{-10} mbar. We observe a limit pressure in the vacuum chamber of $\sim 2 \times 10^{-8}$ mbar with only the IonPump operating. This base pressure is lowered during the operation of the cryocooler because it acts as a cryopump. The low-temperature surfaces of the cryocooler adsorb the molecules of the gas in the chamber, so the cryocooler is started only with vacuum pressures near the limit reached by the IonPump. With both the IonPump and cryocooler operating, we register pressure $< 5 \times 10^{-10}$ mbar, which is lower than the limit of operation of the pressure gauge.

6.1.2 Cryogenic System

The temperature of a few Kelvin is a fundamental requirement for the growth of a solid noble gas moderator (see section 6.2.1.1 for detail). To reach the required conditions, we use a cryocooler fed by compressed helium at 200 bar. The compressed helium is generated by the Sumitomo HC-4E compressor which feeds the Sumitomo CH-204S-N cryocooler shown in fig. 6.3 left. As seen from this figure the cryocooler has two stages a larger first stage and a smaller second stage at the top. The two stages operate at different temperatures and cooling powers:

- **First Stage:** it can reach temperatures ~ 20 K, it has tens of Watt of cooling power;
- **Second Stage:** it can reach temperatures < 10 K, but its cooling power is smaller (< 3 W).

On the first stage of the cryocooler, three elements are mounted: an aluminum block, a tungsten (W) shield, and a tungsten cap. These elements surround completely the second stage and its elements (see fig. 6.3 right) and they operate as a thermal and a biological shield. The thermal radiation from the vacuum chamber at ambient temperature (300 K) is absorbed/reflected by the first stage which has a lot of cooling power. In this way, the second stage is surrounded by an environment at a few tens of Kelvin and the power of the thermal radiation reaching it is negligible. This reduces the cooling power required to keep the low temperature in the source support. The tungsten elements also work as a biological shield (see section 6.1.4). The tungsten shield has two holes on opposite sides, one for the passage of the positrons and the other for the insertion of the radioactive source.

On the second stage of the cryocooler, two elements are mounted: the copper block and the source support. The copper block works as a biological shield (see section 6.1.4), but its main role is another. The temperature in the second stage of the cryocooler is not stable, it fluctuates by ± 0.25 K due to the pulsed operation on which the cryocooler operates. Then the thermal capacity of the copper block acts as a dumping of these oscillations, so the temperature fluctuates by ± 0.05 K at the source support. The moderator is deposited in the source support which is mounted on top of the copper block, at the tip of the second stage as shown in fig. 6.3. The two pieces are in thermal contact but electrically insulated by a disk of aluminum nitride while four screws in polyether ether ketone (PEEK) keep the two components attached. This allows to set the potential of the source up to a few tens of volts. The source support is the most important element of the entire structure mounted on the cryocooler. The sketch of its structure can be seen in fig. 6.4. There are two openings, one on the front with a conical shape and another on

Figure 6.3: Photos of the cryocooler of the PsICO apparatus. The two-stage commercial cryocooler Sumitomo CH-204S-N (left), the copper block and source support mounted on the second stage with elements to control the moderator temperature (middle), and the aluminum block and tungsten elements mounted on the first stage (right).

the back for the insertion of the source holder on which the source is mounted (the two openings are aligned with the holes in the W shield mounted on the first stage). The conical opening is the one on which the noble gas molecules are going to deposit to form the moderator. The conical surface is mirror-finished to present as few imperfections as possible to the deposited gas.

As we will see in section 6.2.1, the creation of a noble gas moderator requires changes in the temperature of the source support. However, the cryocooler can only be started or stopped, it cannot be used for the fine-tuning of the temperature in the second stage. When on, the cryocooler brings the attached structure to the lowest possible temperature given its thermal load. When off, the thermal radiation from the vacuum chamber warms the entire cryocooler until it thermalizes at room temperature. To control the moderator temperature, a resistive heater is used. The temperature of the first stage is monitored by two diodes. The position of these elements is shown in fig. 6.3 center: the diode B and the heater are attached to the copper block near the second stage of the cryocooler, the diode A is attached at the top of the source support to monitor the moderator temperature. With this system, we manage to reach temperatures of $7.00 \pm 0.05\,\mathrm{K}$ at the moderator, diode B measures lower temperature in the high $6\,\mathrm{K}$. Giving power to the heater, we can regulate the moderator temperature up to $\sim 29\,\mathrm{K}$. A temperature controller is used to read the temperature and to operate the heater to reach a desired set temperature.

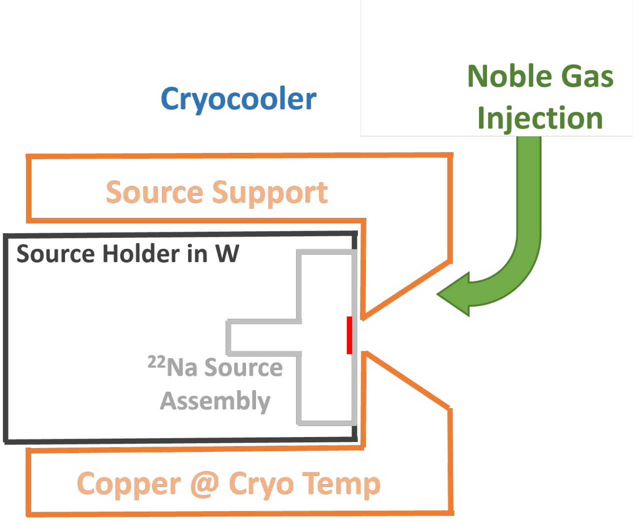

Figure 6.4: Schematic of the element mounted on the top of the second stage of the cryocooler.

6.1.3 Gas Injection System

The deposition of the moderator requires the injection of a noble gas on the front face of the source and on the conical surface in front of the source (see fig. 6.4). The gas to the source support is delivered by a tube attached to the outside of the tungsten shield on the first stage of the cryocooler. From there the tube follows the cryocooler structure until the CF adapter (see fig. 6.3 center), where it is connected outside the vacuum chamber to the system required to feed the noble gas in a precise amount. This system is shown in fig. 6.5. The noble gas with a purity of $> 99.999\%$ and pressure > 100 bar is contained in the gas bottle. The gas pressure is decreased to 1 bar by the pressure regulator, while the Mass Flow Controller (MFC) quantifies and fine-tunes the flux of gas to the requested quantity. Finally, a pneumatic valve controls the delivery of gas to the vacuum chamber. Typical gas fluxes for the moderator deposition are 3 sccm for 3 min, these two parameters quantify the amount of gas injected into the chamber (see section 6.2.1). As shown in fig. 6.5, the delivery system is also connected to the HiCube through two valves: a pneumatic valve and a manual valve. The first connects the HiCube to the region between the MFC and the pneumatic valve which controls the flux of gas towards the source-moderator assembly. This region is cleaned before each moderator deposition from any gas that permeated from the connection and the MFC. The manual valve connects the HiCube to the gas delivery system before the MFC. This valve is open to clean the connection to the gas bottle each time it is changed.

6.1.4 Biological Shield System

As previously indicated, a radioactive source positioned on the top of the second stage of the cryocooler is employed to produce the positrons. For the protection of the operators from the ionizing radiation produced by the source, the environment around the apparatus needs to be shielded as much as possible. In the PsICO apparatus, the biological shielding of the source is obtained using three shields of high-density material.

Figure 6.5: The system used to inject a specific quantity of noble gas on the front face of the source and on the conical surface in front of it. The gas flux, from the gas bottle, is regulated by the Mass Flow Controller and the pressure regulator.

The structure of the biological shielding is shown in fig. 6.6, in it, we can identify three main shields:

- **Shield 1:** the cryocooler structure. As shown in fig. 6.3, on the first and second stages of the cryocooler, components in copper and tungsten are mounted. They work also as a biological shield.
- **Shield 2:** the lead balls. The vacuum chamber of the cryocooler is installed in a box that is filled with 1.5 mm diameter lead balls for a total weight of ~ 400 kg. These balls do the main work in the attenuation of the radiation. By using small lead balls instead of lead blocks, the space around the vacuum chamber is more efficiently filled. Given the complex structure of the chamber, it would require lead blocks with a complex design and greater installation difficulty. Due to the small dimensions of the lead balls, they behave almost like a liquid, so by filling from the top, the balls distribute themselves to fill all the space. With a faucet on the bottom of the box, we can empty the box in a short time.
- **Shield 3:** the external structures. It is composed of two elements. First of all, we have the box containing the lead balls, it is formed by 1 cm thick stainless steel

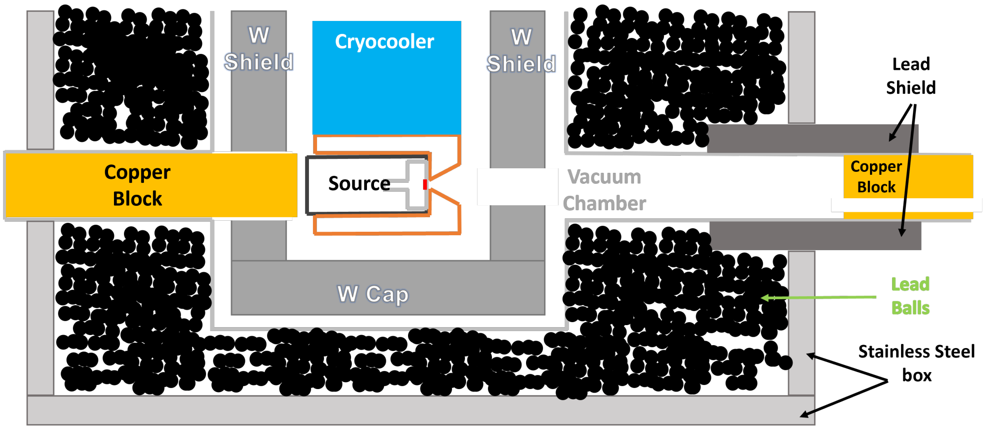

Figure 6.6: Schematic of the shielding system of the first stage of the PsICO apparatus required to suppress the ionizing radiation from the source.

sheets. While the sheet thickness is required to support the heavy weight of the lead balls, it also works as a biological shield given that 36% of 511 keV radiation from the positron annihilation is attenuated by traversing 1 cm of stainless steel. The two copper blocks and the lead shield in fig. 6.6 compose the second element of the third biological shield. They are needed to block the radiation along the vacuum chamber in the back and front of the source. The vacuum chamber in the two directions expands outside the lead ball box due to operational requirements. The section of the vacuum chamber on the back of the source permits the insertion and removal of the source without the removal of the lead balls, increasing the safety of the operation. On the front, the vacuum chamber needs to exit the lead ball box to permit the positron beam to reach the second stage of the PsICO apparatus. In order to stop the radiation in the direction of the beam while permitting its passage, a copper block with an off-axis hole is placed in the beam tube (see fig. 6.6). This copper block works as speed-selector for slow positrons (see sections 5.1.1 and 6.1.5 for details). The shielding of the source in the beam direction is further augmented by the lead shield positioned around this copper block. This lead element has the further task of shielding the operator from the radiation originating in the annihilation of fast positrons during the speed selection process.

The shields are sized for the use of a 50 mCi radioactive source. During our commissioning of the first part of the PsICO apparatus, we used a ~ 1 mCi sodium-22 source. With this small activity, no radiation value over the laboratory background was observed in the working region around the apparatus.

6.1.5 Transport System

The design of the transport system of the positron beam for the first stage of the PsICO apparatus was presented in section 5.1.1, now we look at how the design has been implemented. The scheme for the transport and coils' position can be seen in fig. 6.7. Moderated positrons travel along the magnetic field generated by the Helmholtz coils and the long solenoid sketched in the figure (see section 5.1.1). In the middle of the long solenoid, positrons are speed selected by two pairs of saddle coils that generate a

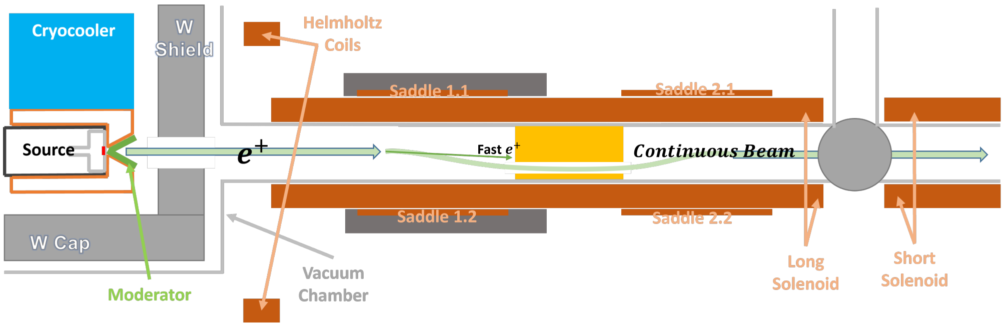

Figure 6.7: Schematic of the transport system of the first stage of the PsICO apparatus for the generation of the positron beam.

magnetic field guiding the slow positron through the hole of the copper block. Positrons with higher speed annihilate on the copper block. The positrons, after crossing the speed-selector, travel to the short solenoid which guides them to the end of the first stage of the PsICO apparatus. As previously said the energy of the beam is mainly given by the source support potential which is set at 18.76 V while the rest of the structures are at ground potential.

All the coils were built in the laboratory. Figure 6.8a shows the two Helmholtz coils mounted around the vacuum chamber that contains the cryocooler. They are inside the lead ball box, so they are not visible in fig. 6.1. The two coils are powered in series and water-cooled with a turn of 6 mm copper tube soldered on the structure supporting the coil turns. Figure 6.8b shows the two solenoids as we finished winding them. Both solenoids have been winded on a copper tube surrounding the vacuum chamber. Between the copper tube and the vacuum chamber, four 6 mm copper tubes along the chamber length provide water-cooling to the solenoids. In the operation, the four tubes are connected in series so only an inlet and an outlet for water are required. As indicated in fig. 6.7, the saddle coils are mounted around the long solenoid with the saddles 1.1 and 1.2 inside the lead shield. The assembly is also depicted in fig. 6.8c.

The water tubes of the solenoids and the Helmholtz coils are connected in series with the cold water entering the solenoids and leaving through the Helmholtz coils. With a water flux of $2.5\,\mathrm{L\,min^{-1}}$, the Helmholtz coils are kept at around room temperature. In the case of the solenoids, the forced air cooling has been added to keep the temperature at the solenoid surface below 55 °C. The forced air cooling system consists of a tangential fan capable of generating a flux of $340\,\mathrm{m^3\,h^{-1}}$. The fan is positioned under the solenoids. While part of the heat from the saddle 1.1. and 1.2 is dissipated by conduction with the lead shield, the heat from saddle 2.1 and 2.2 do not have this possibility, so the forced air cooling is fundamental to keep the two coils at temperature $< 75\,°\mathrm{C}$. During the coil operation, the coils are monitored in two ways: with thermocouples in strategic positions, and by registering the voltage and current that are applied to each coil set with the remote control system (see section 6.1.6). In a normal operation, we have:

- **Helmholtz coils:** 2.820 ± 0.001 A, 29.3 ± 0.1 V, 22 °C
- **Saddle 1.1:** 2.099 ± 0.001 A, 26.0 ± 0.1 V, 65 °C
- **Saddle 1.2:** 2.099 ± 0.001 A, 23.4 ± 0.1 V, 65 °C

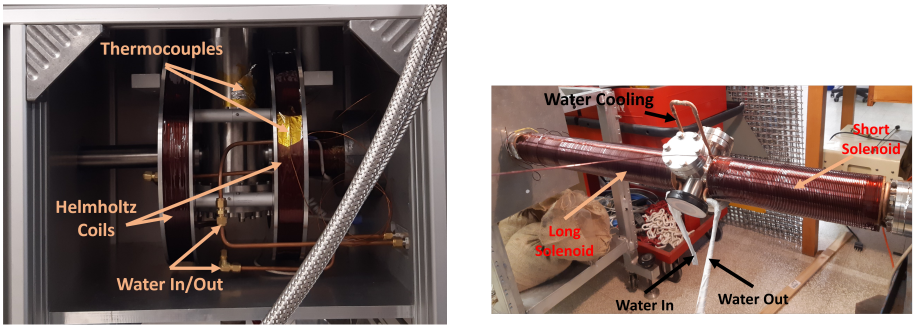

(a) *Helmholtz Coils.* **(b)** *Solenoids.*

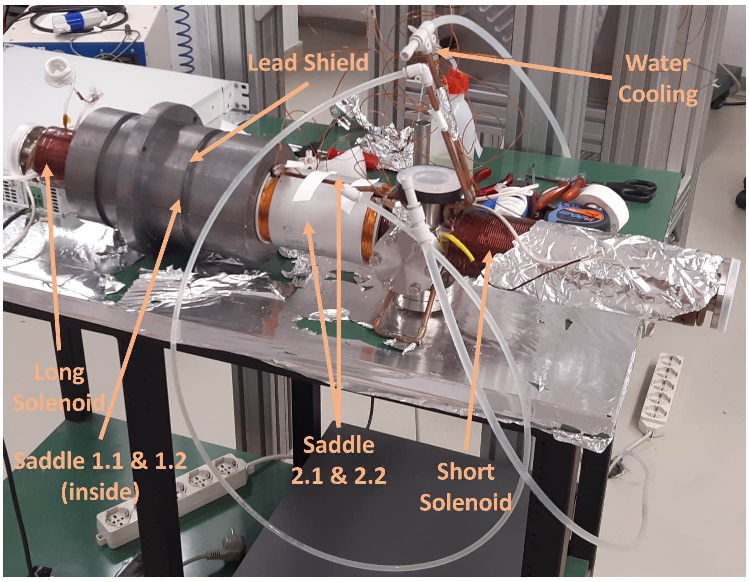

(c) *Solenoids and saddle coils assembly.*

Figure 6.8: The coils for the magnetic transport and speed selection of the positron beam in the first stage of the PsICO apparatus. (a) The Helmholtz coils as mounted around the vacuum chamber of the cryocooler inside the lead ball box. (b) The two solenoids outside the source region. (c) The assembly of the solenoids and saddle coils for coils during the coil testing.

- **Saddle 2.1:** $2.004 \pm 0.001\,\mathrm{A}$, $21.8 \pm 0.1\,\mathrm{V}$, $72\,^{\circ}\mathrm{C}$
- **Saddle 2.2:** $2.004 \pm 0.001\,\mathrm{A}$, $17.7 \pm 0.1\,\mathrm{V}$, $50\,^{\circ}\mathrm{C}$
- **Long and short solenoid:** connected in series, $12.0 \pm 0.1\,\mathrm{A}$, $68.0 \pm 0.5\,\mathrm{V}$, $50 - 65\,^{\circ}\mathrm{C}$

In all cases, the coils are supplied with a constant current by the different power supplies, so the applied voltage depends on the temperatures in the laboratory.

6.1.6 Remote Control System

In the previous section, we have identified the different elements of the first stage of the PsICO apparatus necessary for the production of a slow positron beam. In this section, the remote control of these elements is described. We divide the elements to be controlled into two categories: the one related to the transport system and the other for the elements of the vacuum, cryogenic, and gas injection systems. In the first category, we have the power supply for the coils and the power supply for the voltage on the moderator. Except for the power supply of the moderator, all the other elements are connected to a computer as seen in fig. 6.9. The elements are controlled with a MATLAB code. During the operation of the beam, there are two codes monitoring in parallel the apparatus, one for each category.

In the construction of the control system, we used the serial port to communicate with most of the elements. There are two main protocols for the serial port: RS232 and RS485. Both require a minimum of two wires. While the RS232 permits the connection to one element per connection, the RS485 protocol allows a daisy chain of different elements by giving to each element an address. It is possible to convert a signal from an RS232 protocol to an RS485 protocol, but the lack of the address on the RS232 element makes it difficult to stably control elements with RS232 protocols in an RS485 chain.

While the serial protocols are available for most of the elements of the apparatus, the connectors used by the manufacturers of the elements are not the same. Most of the time, an instrument has, as a serial port, a DB9 connector which is a 9-pin rectangular connector, whose wiring depends on the choices of the manufacturer. Sometimes instead the connector used is a USB. Pfeiffer, in its products, tends to use the RS485 protocol on an M12 connector which is a circular connector with four pins: two pins for the RS485 protocol, a grounding pin, and a power pin. While the M12 connector is more beautiful and easy to connect than the DB9, there does not exist any adapter to pass from one connector to the other, and given the more historical presence of the DB9 connector and its cheapness, most of the instruments with a serial port use it. While in old computer serial ports for RS232 protocol were ubiquitous, with the introduction of the USB they disappeared. So to connect the serial ports to the computer we need to convert from the serial protocol on DB9 or M12 connectors to the serial port on USB connectors.

In summary, the elements of the apparatus we need to control are:

- **Vacuum System:**
  - IonPump: RS485 protocol, DB9 connector
  - HiCube: RS485 protocol, M12 connector
  - Pressure gauge: RS485 protocol, M12 connector
  - Gate valve: 2 pressure lines, one for opening, the other for closing the valve
- **Cryogenic System:**
  - Cryocooler: the power is controlled by a relay that has an RS485 protocol and DB9 connector
  - Temperature controller: RS232 protocol converted to RS485 protocol, DB9 converter
- **Gas Injection System:**
  - Valves: the two pneumatic valves require a pressure line each
  - MFC: RS485 protocol, DB9 connector

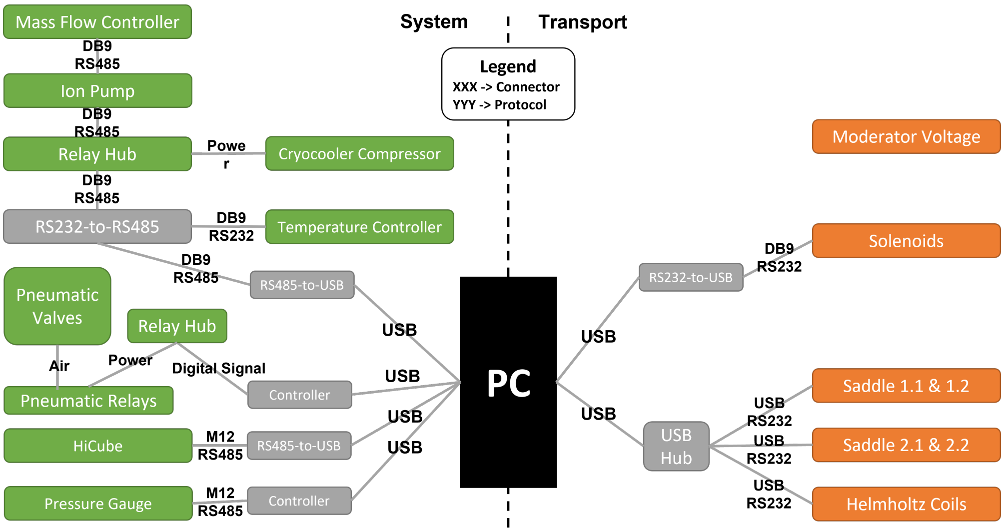

Figure 6.9: Schematic of the control system of the first stage of the PsICO apparatus. Each element is indicated, for the most part, they are controlled with a computer, in that case, the protocol and connector type are indicated.

- **Transport System:**
  - Moderator Power supply: not connected to the computer
  - Solenoids Power supply: RS232 protocol, DB9 connector
  - Saddle 1.1 and 1.2 Power supply: single element with two outputs, RS232 protocol, USB connector
  - Saddle 2.1 and 2.2 Power supply: single element with two outputs, RS232 protocol, USB connector
  - Helmholtz coils Power supply: RS232 protocol, USB connector

Figure 6.9 shows how the elements are connected to the PC. In particular, we create a long chain using the RS485 protocol connecting in series the MFC, the IonPump, the relay of the cryocooler, and the temperature controller. On the other hand, the pneumatic elements need a complex chain for their control as seen in fig. 6.9. The pressure line to each element is connected to a main pressure line through a hub of pneumatic relays. The main pressure line available in the laboratory uses compressed dry air at 4 bar of pressure. The pneumatic relays are powered by electric relays, which are controlled by a digital signal from a controller that is connected with a USB to the computer. The controller sends a signal 1 or 0 which closes or opens the electric relay, which then switches off or on the power to the pneumatic relay. This sends the pressure line to a pressure of 1 bar or 4 bar changing the state of the pneumatic valve. In the case of the gas system, we have two normally closed (NC) pneumatic valves, i.e. when the pressure line is at 1 bar they are closed and they need a 4 bar pressure on the line to open. In the case of the gate valve, there are two lines, when one is pressurized the valve is open, and when the other is pressurized the valve is closed. If both lines are pressurized, it is closed. In the case neither line is pressurized: if the valve is closed remains such; if it is open, it goes in an almost closed state.

6.2 1st Stage: Characterization

In this section, we will see the commissioning of the first stage of the PsICO apparatus. In particular, we studied: the moderator-transport efficiency, the energy distribution and the spot of the continuous positron beam; the spin-polarization of the positrons using different noble gases as moderators. We start by showing the recipe used for the growth of the moderator with different gasses.

6.2.1 Moderator Growing Procedure

As discussed in section 4.2.2, most of the positron beamlines with a solid noble gas moderator make use of neon. The growth of the neon moderator is well-studied. Because of the similar apparatus design, we decided to use the same recipe used in the AEgIS experiment [103]:

- **Conditioning:** the chamber containing the source and the conical support is evacuated only by the IonPump to reach a vacuum $< 10^{-7}$ mbar. Then the cryocooler is switched on to reach the minimum temperature;
- **Cleaning:** the gases adsorbed on the second stage of the cryocooler are evaporated by increasing the temperature to 25 K;
- **Deposition:** the temperature is stabilized at 8.8 K and the IonPump is switched off. In this way, the vacuum chamber is isolated. Then the neon gas is injected for 3 min with a flux of 3 sccm obtaining a pressure slightly less than 10^{-5} mbar;
- **Annealing:** the temperature is increased to 9.3 K and kept stable for 15 min for the annealing of the moderator. The pressure in the vacuum chamber in this phase stabilizes at slightly less than $< 10^{-4}$ mbar;
- **Crystallization:** the temperature is brought to the minimum reachable by the cryocooler and the IonPump is switched on;
- **Use:** the formed moderator is used for a couple of weeks with decreasing efficiency;
- **New Moderator:** to grow a new moderator one start again from the *cleaning*.

These operations are also shown in fig. 6.10, where the state of the moderator is sketched for each step. The cleaning step eliminates the previous moderator by bringing the second stage of the cryocooler to a temperature well above the melting point of neon. This prepares the surface of the source and source support for the deposition of the new moderator. During the deposition, the surfaces are at a temperature lower than the melting point so neon is physically adsorbed to them. The vacuum chamber is saturated with the injected noble gas, so multiple layers of adsorbed gas molecules are formed. By measuring the moderator-transport efficiency (as shown in section 6.2.2) with different injected quantities of neon gas, we determined the optimal quantity of gas needed in the chamber to grow a good moderator. Because the total amount of gas injected in the vacuum chamber is given by the product of the flux for the deposition time, we decided to keep for all the test the same gas flux while we changed the deposition time. Figure 6.11 shows an increase in the moderator-transport efficiency with higher deposition times.

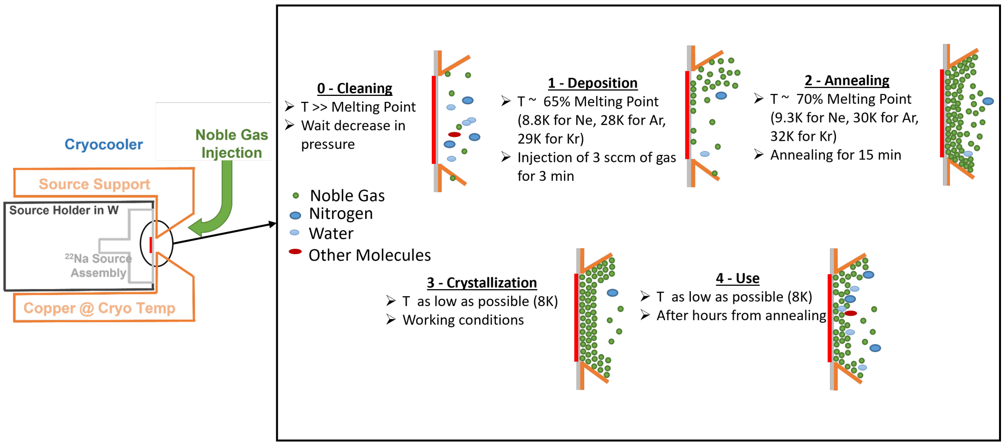

Figure 6.10: The steps to grow a solid noble gas moderator. For each step, the behavior of the gases (sketched as disks or ellipses) is shown: in green the noble gas, in dark blue the nitrogen gas, in light blue the water molecules, and in red all other residual gasses.

This increase saturates around 180 s which represents the optimal condition of the gas flux.

The deposited gas layers form a disordered structure. During the following annealing, the temperatures of the neon molecules are brought near the melting point (70% of the melting point) so they can reorganize. After the heat treatment, the temperature is decreased as much as possible to block the molecules in the crystalline form obtained with the annealing. Unfortunately, over time, defects are going to form due to the motion of neon molecules and the deposition over the moderator of molecules from residual gases in the vacuum chamber. This has the effect of reducing the efficiency of the moderator.

In the PsICO apparatus, we tested argon and krypton moderators other than neon. Also for these two gases, we used the same moderator recipe as neon but with different deposition and annealing temperatures. Nevertheless, for all three gases, similar conditions are required for the recipe to work. To find these conditions, we need to look at the melting point for the three gasses.

6.2.1.1 Antoine equation

The melting point of a gas is obtained from the vapor pressure p that is a function of the temperature T. Their relation is expressed by the Clapeyron equation:

$$\frac{d}{dT}\log[p] = \frac{\Delta H_v}{RT^2} \tag{6.1}$$

where ΔH_v is the evaporation enthalpy and R is the gas constant. The vapor pressure curve is derived by integrating the Clapeyron equation, but this operation is complicated by the temperature dependence of the enthalpy. It is possible to assume the enthalpy constant in a small range of temperatures, then knowing the evaporation enthalpy at a temperature we can calculate from eq. (6.1) the vapor pressure. However, the experimental approach was preferred. In the 1960s the vapor pressures of most of the common gases were measured for a wide range of temperatures [247]. So selecting a temperature region, we can fit this data with the Antoine equation:

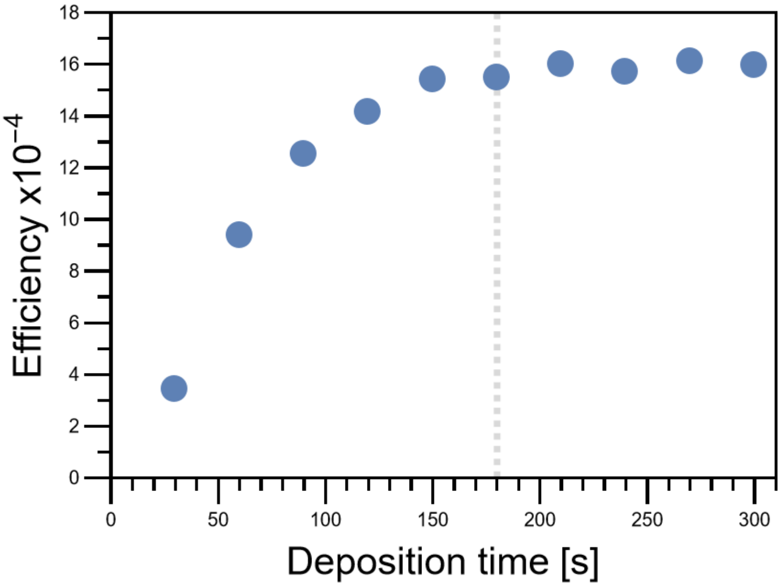

Figure 6.11: The moderator-transport efficiency of the first stage of the PsICO apparatus for different quantities of neon gas injected during the deposition of the moderator. The gas quantity has been changed by modifying the duration of the gas injection while the gas flux of 3 sccm has been kept constant. The moderator-transport efficiency has been measured with the procedure shown in section 6.2.2 waiting always the same time after the end of the annealing. The deposition time used for the growth of the moderator in this thesis is indicated with a vertical dashed line.

$$\log_{10}[p] = A - \frac{B}{T + C} \tag{6.2}$$

where the vapor pressure p is expressed in bar, the temperature T in Kelvin, and A, B, and C are fit parameters for the considered temperature region. The values for these fit parameters have been calculated for different temperature ranges and gases [248]. In the case of neon, argon, and krypton, the behavior of the vapor pressure as a function of the temperature as predicted by the Antoine equations is shown in fig. 6.12. As it can be seen from this figure argon and krypton melt at temperatures of the order of tens of Kelvin in a vacuum, while neon requires temperatures of a few Kelvin.

By referring to the vapor pressure of neon in fig. 6.12, we can identify the 8.8 K and 9.3 K as corresponding to the 65% and 70% of the melting point at the operating pressures, respectively. In order to apply a comparable recipe for the production of the solid noble gas moderators, the deposition and annealing of the moderator have been performed at 65% and 70% of the melting point for each noble gas, respectively. These conditions correspond to 28 K and 30 K for argon, and 29 K and 32 K for krypton.

Thanks to the higher melting point, argon and krypton moderators can be even operated at a much higher temperature than neon moderators, reducing the requirement on the limit temperature of the cryocooler. However, this means that a greater variation in the moderator temperature is needed during the creation of a moderator. Consequently, longer times are required to form a new moderator. Due to the small range of variation in

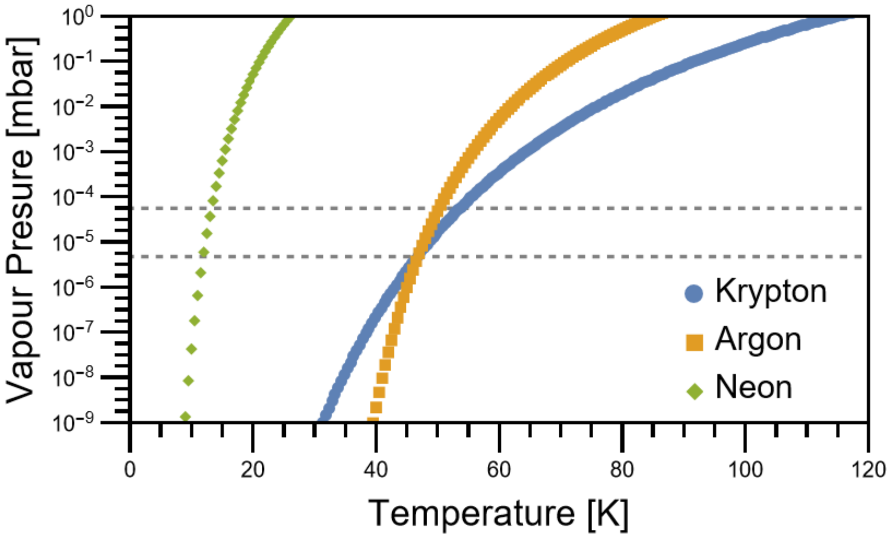

Figure 6.12: Antoine equation for the three noble gases: Neon (green diamond), Argon (orange square), and Krypton (blue disk). The dashed horizontal lines correspond to the vacuum chamber pressure during deposition (bottom) and annealing (top).

temperature, a neon moderator requires less than one hour to form. In the case of argon and krypton moderators, the entire growth procedure can last more than two hours.

6.2.2 Moderator-Transport Efficiency of the Continuous Beam

In this section, we present the measurements of moderator-transport efficiency of the first stage of the PsICO apparatus. This efficiency takes into account: the moderation efficiency of a given noble gas moderator, the speed selection efficiency, and the transport efficiency to the end of the short solenoid. The evolution of the moderator-transport efficiency, due to the aging of the moderator, over time is also investigated.

6.2.2.1 Experiment Design

By referring to fig. 6.1, we determine the apparatus efficiency by detecting the positrons annihilating at the end of the short solenoid with a NaI(Tl) detector. By operating the coils at the currents indicated in section 6.1.5, the positrons are transported from the positron-moderator to the end of the short solenoid where they annihilate on a blank vacuum flange of 1 cm thick stainless steel. The detector is positioned in front of the flange at 25.5 cm distance. The detector is a calibrated 3 × 3 inches crystal with a 40% photopeak efficiency for 511 keV gamma-rays. The detector PMT has been shielded with mu-metal to reduce the effect of the coil magnetic field on the reading. A background measurement is operated periodically with the detector keeping all the coils operative, except the saddle 1.1 and 1.2 to stop the positrons from reaching the short solenoid.

Typically, 10 min long spectra from the detector were registered. For each spectrum, the number of events in the photopeak at 511 keV energy is recorded. From this number, we obtain the moderator-transport efficiency by normalizing the measurement time and subtracting the background rate. Then, this result is corrected by:

- detector efficiency;
- detector solid angle coverage;
- number emitted photons per annihilation;
- blank flange attenuation;
- probability of ^{22}Na decay via positron emission;
- source activity (measured 51.6 mCi at July 22nd 2007).

With this procedure, we obtained the moderator-transport efficiency of the continuous positron beam, i.e. the probability of the positron reaching the blank flange when emitted by the radioactive source.

6.2.2.2 Efficiency: Short Term

First of all, we studied the effect on the efficiency of the temperature at which the moderator is kept during operation. For the three gases considered (neon, argon, and krypton), we studied the evolution of the moderator-transport efficiency for 24 h after the annealing of a new moderator. Test at different temperatures of operation for the three noble gases are reported in fig. 6.13.

6.2.2.2.1 Neon Moderator Figure 6.13a shows the moderator-transport efficiency using neon moderators operating at temperatures between $7.4 - 8.5\,\mathrm{K}$. As we expected from the discussion in section 6.2.1.1, the system has higher efficiency at lower temperatures. For temperatures $\geq 8\,\mathrm{K}$, the efficiency decays in a few hours to less than 0.05%. If the moderator operates at lower temperatures, the moderator efficiency reaches higher values and it remains more stable during the first day of operation.

6.2.2.2.2 Argon Moderator Figure 6.13b shows the moderator-transport efficiency using argon moderators operating at temperatures between $8 - 20\,\mathrm{K}$. Also in this case the operating temperature of the moderator affects the efficiency of the system. Nevertheless, the temperature range considered is much larger than the case of neon and the efficiency variation is much smaller. In fact, all three temperatures shown in fig 6.13b are far from the melting point of argon, and the efficiency behaves in similar ways. In the first hours after the growth of the new moderator, the efficiency progressively increases reaching a plateau. Then the efficiency remains stable for 24 h. The measured peak efficiency of 0.2% is equal if not higher than the one measured from the neon moderator with the lowest temperature.

6.2.2.2.3 Krypton Moderator Figure 6.13c shows the moderator-transport efficiency using krypton moderators operating at temperatures between $7.4-14\,\mathrm{K}$. Krypton, like argon, has a much higher melting point than neon. In the case of krypton, the efficiency is much smaller from the start with respect to the other two gases, but the efficiency remains almost constant in the first 24 h from the growth of a new moderator. Moreover, the efficiency does not seem to be affected by the operation temperature in the considered range $7.4 - 14\,\mathrm{K}$.

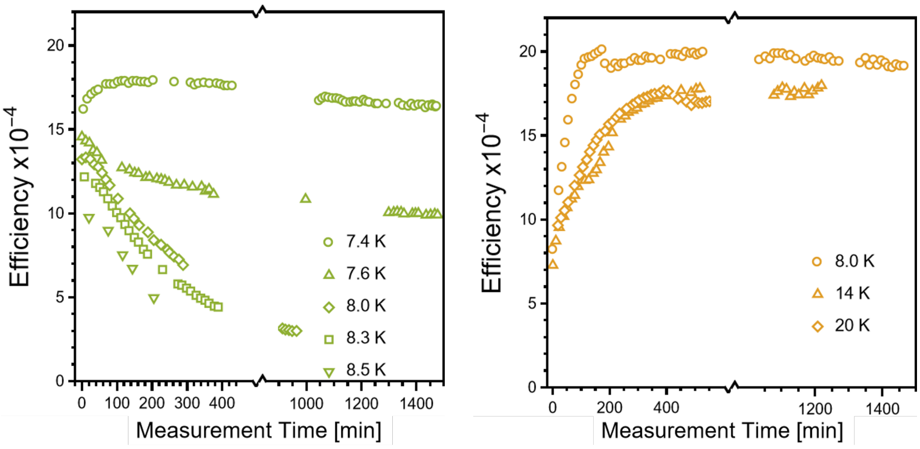

(a) *Neon moderator.* **(b)** *Argon moderator.*

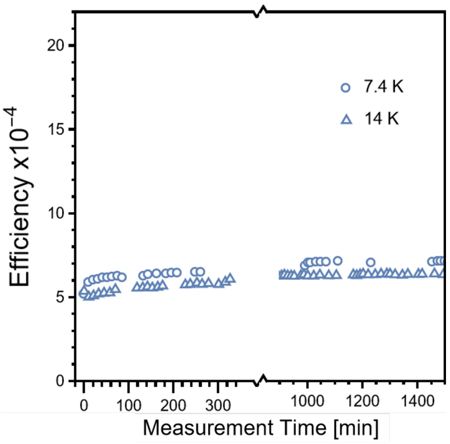

(c) *Krypton moderator.*

Figure 6.13: The moderator-transport efficiency of the continuous beam with different moderators and operating temperatures. The starting time of the measurement is at the end of the annealing.

6.2.2.3 Efficiency: Long Term and Annealing

If we consider the moderator-transport efficiency using the three moderators grown at around 7 K and we measure it for a few days (see fig. 6.14), the following considerations can be made:

- Using an argon moderator, the highest efficiency was reached, in the first 24 h from the growth. For longer times, the efficiency showed a quite fast decrease.

- Using a neon moderator, an initial efficiency slightly lower than the one using argon has been observed. However the decrease of the efficiency is less steep, and after two days the efficiency using a neon moderator is higher than the one using argon.

- Using a krypton moderator, the initial efficiency is smaller than the ones obtained using the other two noble gases. Nevertheless, the efficiency in this case decreases at a very low rate remaining almost constant over a few weeks.

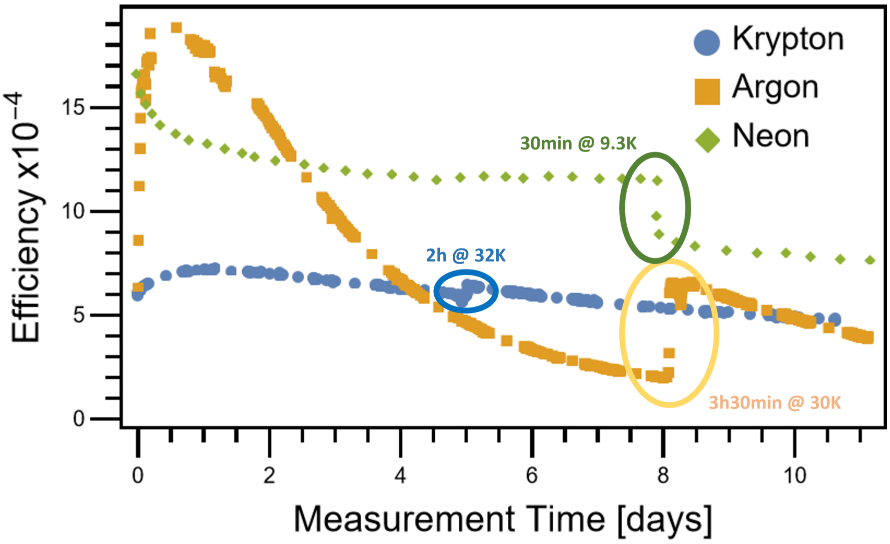

Figure 6.14: The efficiency of the first stage of the PsICO apparatus when operating at around 7 K for different moderators: Neon (green diamond), Argon (orange square), and Krypton (blue disk). The circled regions indicate the effect of the moderator re-annealing on the moderator-transport efficiency. The re-annealing temperatures and durations are: Neon 9.3 K for 30 min; Argon 30 K for 3.5 h; Krypton 32 K for 2 h.

With negative work-function moderators, a thermal treatment allows to regain the lost efficiency during the operation (see section 4.2). For solid noble gas moderators, a new moderator is typically deposited every two-three weeks. As discussed in section 6.2.1, the growth of an argon or krypton moderator can last more than two hours. In order to avoid this deadtime in the measurements, the possibility to recover the efficiency with a thermal treatment has been tested. For this treatment, we bring the moderator to the annealing temperature while the positron beam is continuously monitored. The heat treatments on the three moderators are shown in fig. 6.14, the effects are different for the three noble gases.

6.2.2.3.1 Neon Moderator As shown in the lower right of fig. 6.14, after 30 min of re-annealing at 9.3 K (70% of melting point), we observed a net drop in the system efficiency. In this case, we can regain the lost efficiency only by growing a new moderator.

6.2.2.3.2 Argon Moderator Argon moderator presents the opposite effect of the one observed in neon. By increasing the moderator temperature up to 30 K (70% of the melting point). After a couple of hours, the efficiency stabilizes, at this point the treatment is concluded and the moderator temperature is lowered. For the argon moderator, the re-annealing of 3.5 h at 30 K results in a doubling of the efficiency and in a decrease of the following decay rate. This can increase the operation duration of the argon moderator, we obtain a higher efficiency without the need to stop the beam operation as it would be required by the growth of a new moderator. The gains from the re-annealing and the high peak efficiency make the argon a good candidate to substitute neon in

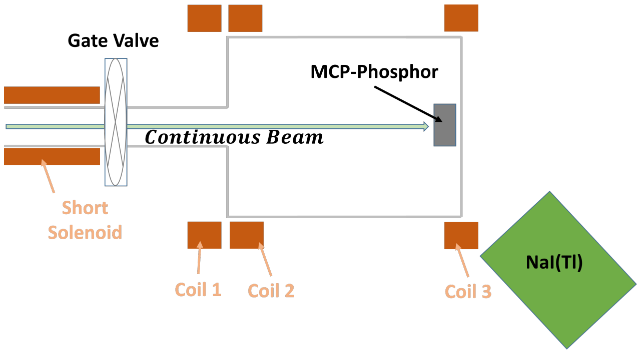

Figure 6.15: The scheme of the setup used to measure the energy distribution of positrons using different noble gas moderators. The measurement is done in a vacuum chamber connected through a gate valve to the end of the first stage of the PsICO apparatus. Three coils are used to guide the beam from the short solenoid to the front of the MCP which is polarized up to +30 V. The annihilations on the MCP are recorded with the same NaI(Tl) detector used for the efficiency measurements.

the formation of solid noble gas moderator, especially in the case where the cryocooler cannot reach temperature around or lower than 7 K.

6.2.2.3.3 Krypton Moderator As shown in fig. 6.14, the change in efficiency induced by thermal treatment is almost negligible. After 2 h at 32 K (70% of the melting point), no great variation in the efficiency has been observed. Only after cooling, a small increase in the efficiency has been measured.

6.2.3 Energy Distribution of Continuous Beam

A second parameter that has been tested at the exit of the first stage of the PsICO apparatus is the energy distribution of the positrons moderated by using the three noble gasses investigated in the previous section.

6.2.3.1 Experiment Design

The scheme of the apparatus used to measure the beam energy distribution is sketched in fig. 6.15. Here, we have to stress that the energy distribution with our setup is the convolution of the energy distribution of the positrons emitted by the source-moderator assembly and the transfer function of the speed-selector. A cylindrical vacuum chamber is connected to the end of the first stage of the PsICO apparatus. A gate valve is present between the two chambers. The vacuum in the cylindrical chamber is generated with a rotative pump and a turbomolecular pump, and pressures in the high 10^{-8} mbar have been reached. The cylindrical chamber is surrounded by three coils that, when the gate valve is open, are used to magnetically transport positrons from the end of the short solenoid to an MCP-phosphor screen assembly (see section 2.2.1). Coil 1 and 2 operated at 2.5 A while coil 3 at 4.0 A. According to COMSOL® simulations, this configuration guarantees beam spot on the MCP of 4 mm.

The used MCP-phosphor assembly was a Hamamatsu F2222-21P251 composed of a two-stage MCP and a $P46$ phosphor screen. During the measurements, the front face

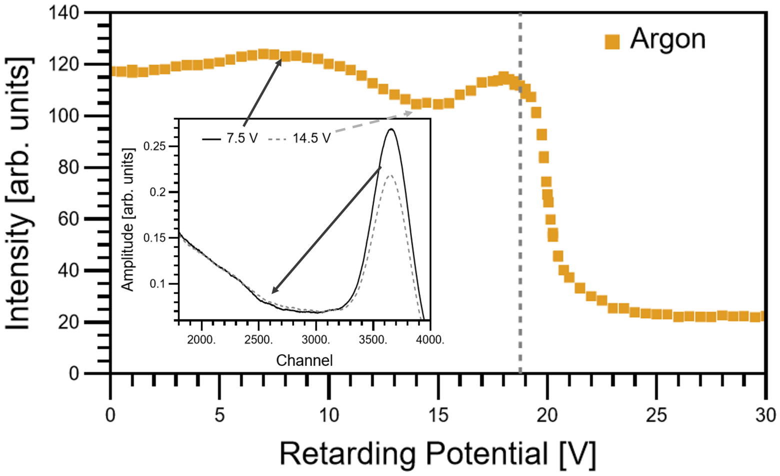

Figure 6.16: Measurement of the annihilation of positrons from an argon moderator on the MCP set at different potentials. The vertical dashed line represents the electric potential of the moderator. The insert shows the spectra recorded by the detector for MCP potentials 7.5 V (continuous line) and 14.5 V (dashed line), the spectra have been cleaned as indicated in the text. The arrow indicates the excess in the valley region for the 14.5 V case.

of the MCP was polarized with positive electric potential so that only positrons with energy higher than the set potential can annihilate on the MCP face while positrons with lower energy are back-reflected. The positron annihilation on the MCP is recorded with a NaI(Tl) detector. The MCP is used as a retarding field analyzer.

The potential on the front face of the MCP was varied between 0 and 30 V. Figure 6.16 shows the annihilations recorded in the 511 keV photopeak by the NaI(Tl) detector at different MCP potentials for an argon moderator. For the other moderators, similar behaviors have been observed. From this figure, we can identify two regions: one for potential smaller than 18.76 V, corresponding to the moderator potential, and one at higher potential. In this latter region, we observe a monotonic decrease in the annihilation count, which reaches almost zero at a few volts over the moderator potential. The rate of this intensity variation represents the integral distribution of the beam energy component parallel to the beam direction. For potential smaller than the one of the moderator, the number of counts is not constant like one could expect. Indeed, the number of counts in the 511 keV photopeak shows a deep centered at around 14.5 V. In order to investigate the origin of this deep, the energy spectra measured with the NaI(Tl) at the bottom of the deep (14.5 V) and at potential lower than the decrease (7.5 V) have been compared (inset in fig. 6.16). Both spectra have been cleaned from the background and normalized on the height of the Compton shoulder. Moreover, we applied a moving average to better visualize the difference between the two behaviors. The spectrum recorded at 14.5 V shows a lower 511 keV photopeak, while the valley region has a higher number of events with respect to the spectrum measured at 7.5 V. This indicates the formation of Ps which shifts annihilations from the peak to the valley. So the observed deep in the number of counts around 14.5 V can be ascribed to the formation of Ps from the Ore process (see section 2.1.3.1) on the surface of the MCP

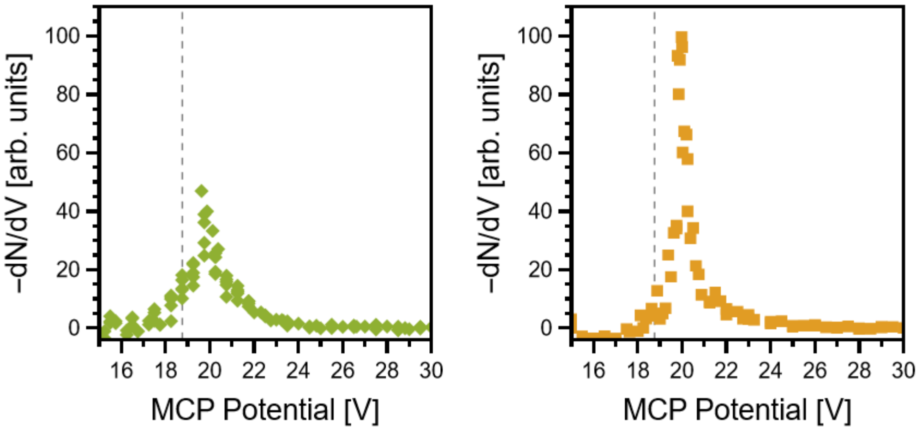

(a) *Neon moderator.* **(b)** *Argon moderator.*

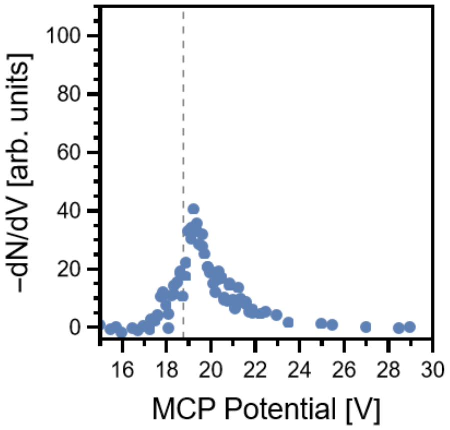

(c) *Krypton moderator.*

Figure 6.17: The energy distribution of the positron beam generated with different solid noble gas moderators. The vertical dashed lines indicate the moderator potential used for the beam transport.

6.2.3.2 Energy Distribution

From measurements like that shown in fig. 6.16, we have extracted the energy distribution of the beam. Indicating with N the number of counts in the 511 keV photopeak and with V the MCP potential used to acquire the spectrum, the rate of the intensity variation $-dN/dV$ is shown for the three moderators in fig. 6.17. The vertical dashed line marks the moderator potential.

There are differences in the energy distribution when using the three moderators. In the case of argon moderator, the distribution has a higher and narrower peak (FWHM of 0.4 eV) at 20.0 eV. The neon and krypton moderators give a larger energy distribution and a lower peak. The energy distribution with the neon moderator has FWHM of 1 eV with center at 19.5 eV. The energy distribution with the krypton moderator has FWHM of 1 eV with center at 19 eV. The difference in the energy distributions obtained using the krypton and argon moderators with respect to the neon one could have a different effect on the bunch formation in the BGT. This is a matter to be studied.

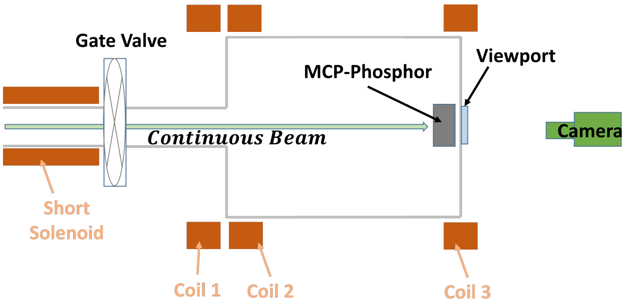

Figure 6.18: The scheme of the setup used to measure the beam spot. The measurement is done in a vacuum chamber connected through a gate valve to the end of the first stage of the PsICO apparatus. Three coils are used to guide the beam from the short solenoid to the front of the MCP-phosphor assembly. The image from the phosphor screen is recorded by a CMOS camera.

6.2.4 Continuous Beam Spot Dimension

A third parameter that has been tested at the exit of the first stage of the PsICO apparatus is the spot dimension. As discussed in references [249, 250], the beam spot shape for a solid noble gas moderator is determined by the geometry of the moderator. In our case, we expect a ring-shaped beam due to the conical geometry of the moderator (see fig. 6.4) [249, 250].

6.2.4.1 Experiment Design

The setup used for the measurement of the beam spot (see fig. 6.18) is almost identical to the one used for the measurement of the positron energy distribution. Also in this case, the positrons that have reached the end of the short solenoid are guided by the three coils to the MCP-phosphor assembly (Hamamatsu F2222-21P251). For this measurement, the front and back of the MCP were set at the electric potentials $-100\,\mathrm{V}$ and $+900\,\mathrm{V}$ respectively, while the phosphor was set $+3800\,\mathrm{V}$. To shield the positron beam from the electric potentials on the connectors of the MCP-phosphor assembly, an aluminum shield connected to ground was installed (see fig.s 6.19a and 6.19b). As shown in fig. 6.19a, the shield covers the front of the MCP-phosphor assembly leaving visible to the beam only the MCP active front part.

The positrons are accelerated on the front of the MCP where they generate secondary electrons. The signal from these electrons is amplified as they are accelerated to the back of the MCP, from which they are emitted and implanted into the phosphor screen where they induce light emission. The light signal is recorded by a CMOS camera (LUCID Triton 16.2MP Monochromatic) on the back of the assembly looking at the phosphor screen through a dedicated viewport (see fig. 6.18).

6.2.4.2 Spot

The beam spot imaged by the MCP-phosphor assembly with the CMOS camera is reported in fig. 6.19c. The spot is an almost perfect ring with an external diameter of 4.4 mm. This diameter is in agreement with the expected spot dimensions simulated with

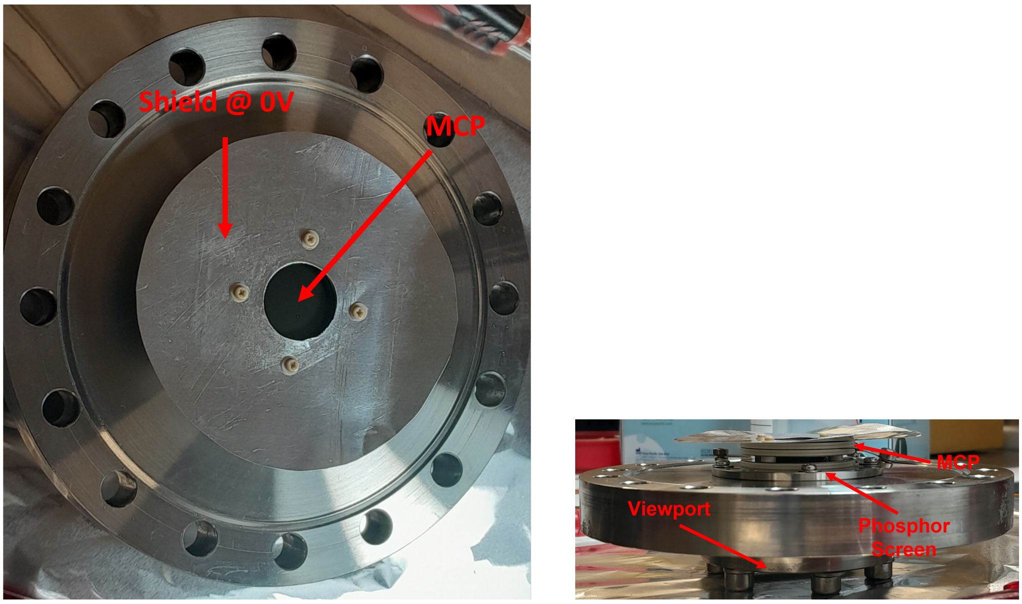

(a) *MCP front view in the apparatus.* **(b)** *MCP section.*

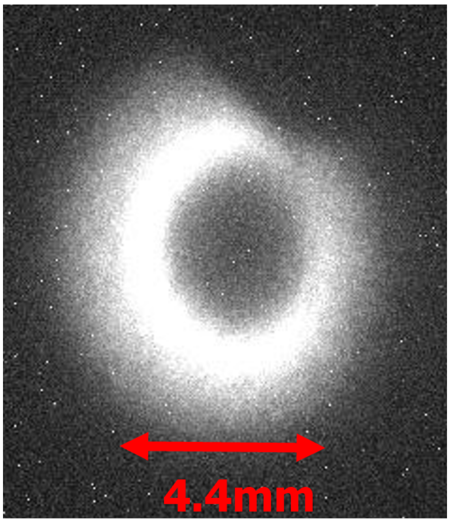

(c) *Beam spot.*

Figure 6.19: The beam spot measurement uses the Hamamatsu F2222-21P251 MCP-phosphor assembly. Figures (a) and (b) show the assembly and its components. Figure (c) shows the beam spot.

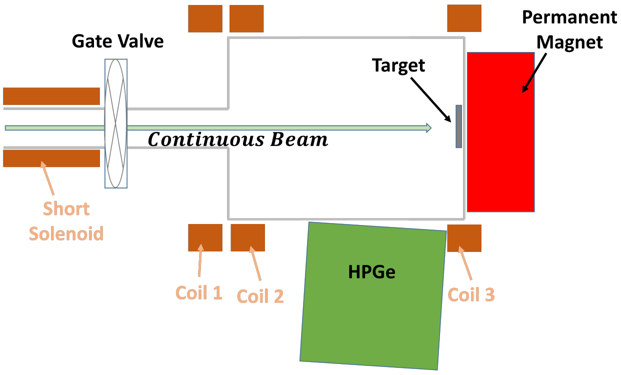

Figure 6.20: The scheme of the setup used to measure the positron spin-polarization from different noble gas moderators. The measurement is done in a vacuum chamber connected through a gate valve to the end of the first stage of the PsICO apparatus. Three coils are used to guide the beam from the short solenoid to the target at $-3\,\mathrm{kV}$. The target is immersed in the magnetic field generated by the coil 3 and a permanent magnet. The annihilation photons are recorded by an HPGe detector.

COMSOL® and considering the geometry and the magnetic fields of our system. The lower density on the top-right corner of the positron spot is ascribable to the presence of the tube injection of noble gas in front of the source.

6.2.5 Continuous Beam Spin-Polarization

As previously discussed, the positron beam generated by a radioactive source is spin-polarized (see section 2.1.5.2). In this section, we describe the measurement of the positron spin-polarization using the three noble gas moderators.

6.2.5.1 Experiment Design

For the polarimetry measurements, we applied the technique described in section 2.3.1.1. Using the same chamber as the previous sections, the positrons are guided and focused into a e^+/Ps converter (see section 2.1.5). The converter was generated with the recipe in section 2.1.5.1 but with a non-constant current:

- for the first 5 min, we kept a constant current of 2.1 mA;
- for the next 10 min, the current was increased from 2.1 mA to 20.1 mA with a constant rate $1.8\,\mathrm{mA\,min^{-1}}$;
- for the last 5 min, we kept a constant current of 20.1 mA.

With this procedure, we should obtain nanochannels with a small diameter on the surface and much bigger deeper into the silicon. This is expected to result in the decrease of Ps escaping the target and in a large fraction of Ps annihilating inside the converter via pick-off (as required by eq. (2.45) to emphasize the dependency of the magnetic quenching of Ps from the positron polarization). The other element for the Ps DBS Polarimetry technique is the magnetic field. The total field on the target is generated by two elements:

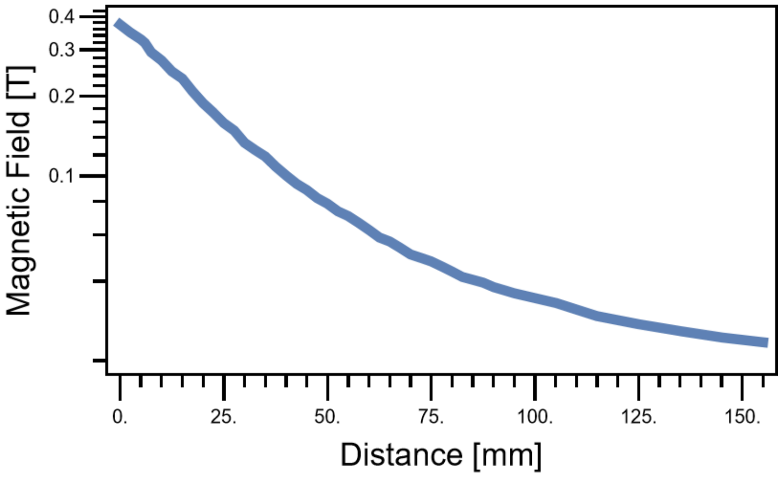

Figure 6.21: The magnetic field measured at the converter position for different distances of the 0.5 T permanent magnet in the presence of the magnetic field generated by coil 3.

coil 3 and a permanent magnet producing a magnetic field of 0.5 T on its surface. The permanent magnet is mounted in a linear movement allowing displacement of about 16 cm. To change the magnetic field on the target, the distance between the converter and the permanent magnet is changed from 0.5 cm up to 16 cm with a resolution less than 1 mm. The calibration magnetic field on the converter as a function of the distance from the permanent magnet was measured with the Gaussmeter F.W. Bell Model 640 and it is shown in fig. 6.21. As the magnet is moved away the magnetic field decreases until the 160 G from correction coil 3 becomes the main contribution.

The three coils are fundamental to guide and focus the beam on the target, especially in the presence of the permanent magnet that strongly affects the magnetic field in the target region. Figure 6.22 shows the COMSOL® simulation of the effect of the permanent magnet on the positron transport towards the converter. When the magnetic field of the permanent magnet is aligned with the other coils (region of positive magnetic fields in the figure), all the positrons from the short solenoid reach the target in a spot smaller than 4.4 mm. The spot dimensions are a consequence of the strong magnetic fields, while the transport efficiency is due to the three coils which generate a magnetic field strong enough to eliminate the mirror effect from the 0.5 T permanent magnet even when near the target. As seen in fig. 6.22, when the permanent magnet generates a field opposite to the one from the coils (region of negative magnetic fields in the figure), the positrons are reflected by the change in the field intensity, then the probability of reaching the target decreases and the beam spot dimension increases over the target dimension. For this reason, we decided to proceed with the measurement only with the magnetic field of the permanent magnet aligned with the coils.

At each position of the permanent magnet, the annihilation photons are recorded with an HPGe detector, and the S parameter is calculated (see section 2.2.2.2.1). This operation is performed both when moving the magnet away and closer to the converter. No difference in the two data sets has been identified.

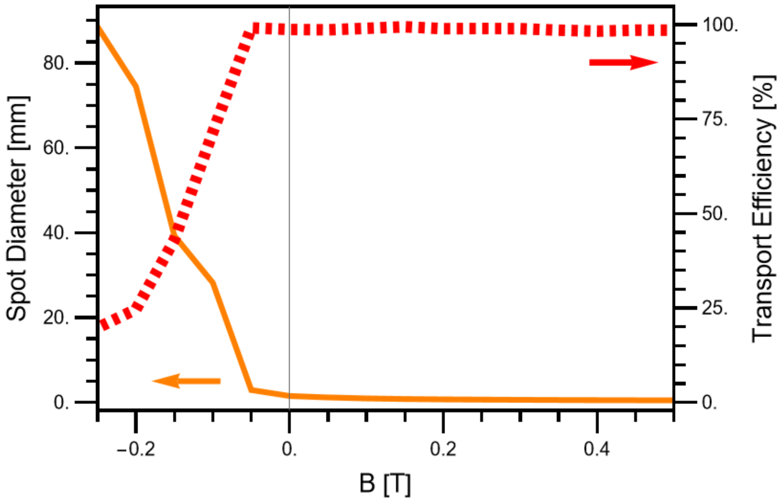

Figure 6.22: COMSOL® simulation of the beam transport from the short solenoid to the target for different fields generated by the permanent magnet. The probability of positron arrival on the converter (dashed red line) and the diameter of the beam spot at the converter (continuous orange line) are shown.

6.2.5.2 Positron Spin-polarization

Figure 6.23 shows the measurement results. The S parameter increases with the magnetic field for all three moderators. The points are fitted with eq. (2.45) obtaining the fit parameters α, β, Γ_{PO}, and P shown in table 6.1. In the fitting, the parameter k was set to $k = 0.95$ [59]. The values of α, β, and Γ_{PO} are compatible between the different moderators, this is expected because they depend only on the e^+/Ps converter. The spin-polarization of the beam from the neon moderator is $(30 \pm 1)\%$ compatible with previous results [226]. The results for the other two moderators were compatible with the one for neon.

Table 6.1: Results of the Ps DBS polarimetry measurement with the three solid noble gas moderators.

Parameter	Neon	Argon	Krypton
α	1.6 ± 0.5	1.9 ± 0.6	1.9 ± 0.5
β	0.64 ± 0.11	0.59 ± 0.13	0.58 ± 0.11
$\Gamma_{PO}[\mathrm{ns}^{-1}]$	1.3 ± 0.7	1.3 ± 0.9	1.2 ± 0.8
P	0.30 ± 0.01	0.29 ± 0.01	0.29 ± 0.01

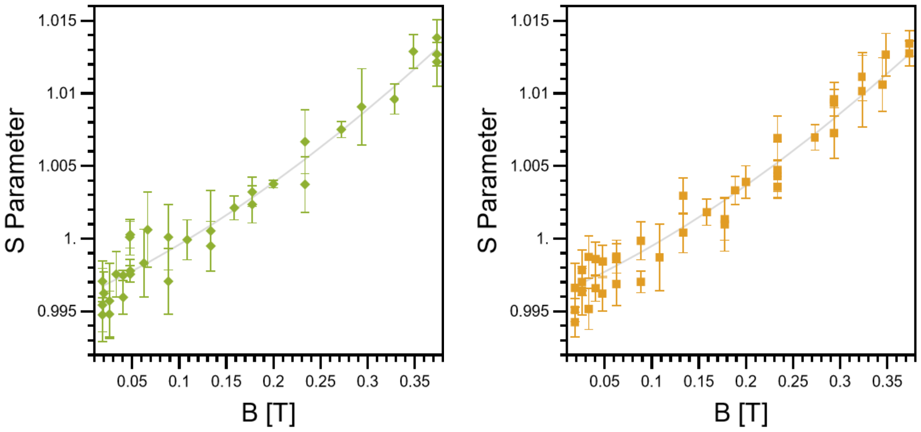

(a) *Neon moderator.* **(b)** *Argon moderator.*

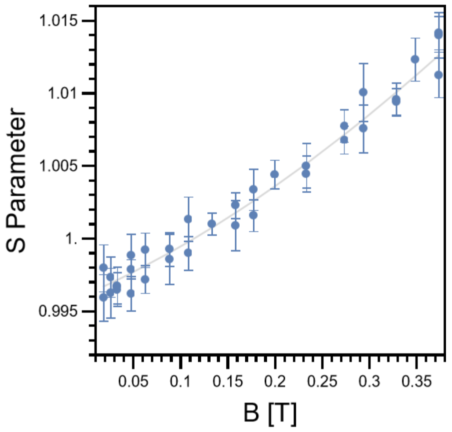

(c) *Krypton moderator.*

Figure 6.23: Ps DBS polarimetry results using the three noble gas moderators. The points represent the measured S parameter at different magnetic field intensities at the converter. The line represents the fit of the data with eq. (2.45) with the fit parameters α, β, Γ_{PO}, and P shown in table 6.1.

Chapter 7

PsICO apparatus: Further Studies

In the previous two chapters, we introduced the design and status of the PsICO apparatus, a positron beamline for the study of entanglement in the polarization of gamma-rays emitted by Ps annihilation. In order to reach this goal, in addition to the laser system to excite the Ps in a specific quantum state, other two elements are required: the e^+/Ps converter and the detector. In this chapter, we are going to present some preliminary results for these two components.

7.1 Transmission e^+/Ps Converter

In section 2.1.5, we introduced the state of targets engineered for Ps production. The most efficient converters work in reflection (i.e. with Ps emission from the same side of the target where positrons are implanted), but an efficient production of Ps in the transmission (i.e. with Ps emission from the opposite side of the target where positrons are implanted) would be ideal for the manipulation and formation of Ps beam.

Ps formation in transmission was obtained with thin silica film deposited on a carbon foil [27, 77, 251, 252], but this kind of converter has a low efficiency $\sim 9\%$ [27]. A new concept for the production of the e^+/Ps converter in transmission is needed to increase this efficiency.

We were able a new kind of e^+/Ps converter based on the nanochanneled silicon described in section 2.1.5.1.

7.1.1 Production

These new converters are synthesized with the same recipe shown in section 2.1.5.1, with a silicon p-type wafer (111) with resistivity $0.1 - 1.5\,\Omega\,\mathrm{cm}$ as base material. However, instead of leaving the nanochannelled layer embedded on the silicon bulk, we wanted to detach the nanochannelled layer from the bulk obtaining a thin membrane with passtrough nanochannels. We modified the procedure of the electrochemical etching to detach the nanochannels from the substrate with a current burst. Because the etching current is related to the nanochannel diameter, with the current burst we increased the nanochannel diameter until they connected each other in depth, forming a cavity underneath the nanochanneled layer. This cavity produced the detachment of the nanochanneled membrane. The duration and intensity of the burst current depend on

Table 7.1: Parameters for the electrochemical etching of the produced membranes. The tested parameters of burst current for each duration of the primary etching are indicated with D (Detachment) or ND (No Detachment), the blank spaces indicate combinations not studied. Only the combinations of electrochemical etching duration and burst current indicated with D generate a detached membrane with a surface larger than 6 × 6 mm. *Table from* [28].

Duration of the electrochemical etching [s]							Burst Current	
3000	2300	1800	1400	1000	750	500	Intensity [mA]	Duration [s]
D	ND	ND					240	24
	D	ND	ND				400	60
		D	ND	ND			500	90
			D	ND	ND		1000	90
				D	ND	ND	2000	90
					D	ND	2500	90
						D	3000	30

the length in depth of the nanochannels, i.e. the duration of the electrochemical etching. Table 7.1 shows the burst current tested for the generation of a nanochannelled membrane of at least 6 × 6mm. To obtain such membranes, we require burst currents with intensities between 240 and 3000 mA for durations between 24 and 90 s.

The membranes obtained from the electrochemical etching are extremely fragile, so they were laid on a grating with 90% transparency to proceed with the oxidation in air at 100 °C for 2 h. After the oxidation, we tested the possibility of a re-etching to increase the nanochannel diameter by immersing the membranes in the HF solution for 1 min followed by a new cycle of oxidation in air. Only membranes with first etching times longer than 750 s survive to a single re-etching, while other membranes with etching times longer than 3000 s survive a second re-etching. In the other membranes, the formation of tensile stresses after each etching results in the fragmentation of the membrane [253].

7.1.2 Physical characteristics

First of all, we need to know the positron implantation profile in these targets. According to reference [254], in this nanochannelled silicon targets, the positron implantation profile can be still reproduced by a Markhovian profile (see section 2.1.2.1). What has to be taken into account is the reduced density in the nanochanneled silicon with respect to the silicon bulk density of $2.33\,\mathrm{g\,cm^{-3}}$. Moreover, the thickness needs to be measured. The surface and side of the membranes were imaged with a high-resolution JEOL JSM-7001F thermal field emission scanning electron microscope (SEM). The membrane density was determined from interferometric analysis using a Cary5000 instrument equipped with the near-normal reflectance tool.

7.1.2.0.1 SEM Imaging The diameter of the nanochannels has been determined via SEM measurements. As seen in fig. 7.1, the nanochannels appear in SEM images as a reduction in the brightness with respect to the not-etched regions. Consequently, the nanochannel diameter distribution can be extracted by the analysis of the SEM pictures.

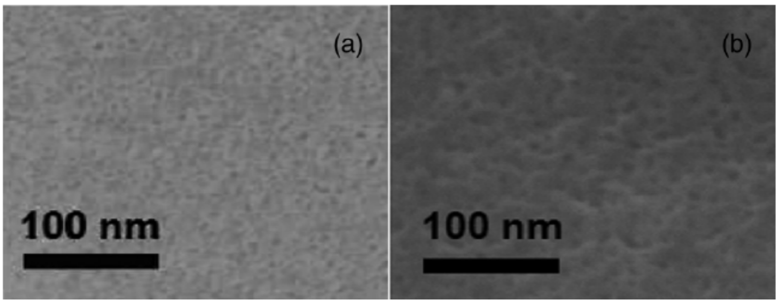

Figure 7.1: SEM images of the surface of the membrane generated with an electrochemical etching time of 3000 s, without re-etching (a) and with one re-etching (b). *Image from* [28].

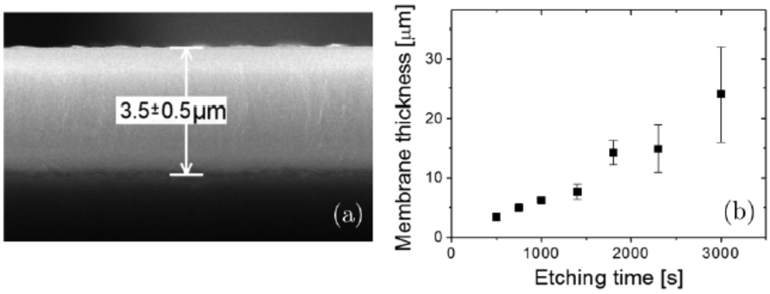

Figure 7.2: (a) Cross-section SEM image of the membranes synthesized with an electrochemical etching time of 500 s. The distance between the front and the back of the membrane is reported with an error associated with the semi-dispersion of the thickness along the sample (see text). (b) Measured membrane thickness for different durations of the electrochemical etching. *Image from* [28].

From fig. 7.1a, we obtain an average size of $5-8$ nm for the membrane electrochemically etched for 3000 s. After a re-etching of the membrane, the nanochannel size increases to an average of $7-10$ nm as shown in fig. 7.1b.

By imaging the cross-section of the membranes with the SEM (see the example in fig. 7.2a), it is possible to measure the thickness of the membranes. As seen from this figure, the thickness is not uniform. The uncertainty on its value is reported as the maximum semi-dispersion along the sample. Moreover, the thickness inhomogeneity increases with the membrane thickness as seen in fig. 7.2b. Hereafter, the membranes will be labeled according to their average thickness, the relation between thickness and electrochemical etching duration is reported in table 7.2.

7.1.2.0.2 Interferometric Analysis Interferometric analysis was performed to determine the membrane density. The reflectance spectra of the membranes were acquired with wavelengths in the visible range $800-300$ nm. The light reflected from the front surface interferes with the one from the back surface of the membrane, this results in a periodic fluctuation in the amount of light reaching the detector and recorded in the reflectance spectrum. For each spectrum, the number of periods $N \geq 6$ was identified in a selected region W of the spectrum. Then the membrane thickness d and refractive index n are related by the equation:

Table 7.2: Average thickness associated with the membrane at different electrochemical etching durations. The thickness error is reported as the maximum semi-dispersion of the membrane thickness. *Table from* [28].

Etching Time [s]	Thickness [µm]
500	3.5 ± 0.5
750	5.0 ± 0.3
1000	6.3 ± 0.2
1400	7.7 ± 1.3
1800	14.3 ± 2.0
2300	14.9 ± 4.0
3000	24 ± 8

$$d = \frac{N}{2W(n^2 - \sin^2\theta)^{0.5}}, \tag{7.1}$$

which in our case, due to the small incline of the beam $\theta = 5°$, can be approximated to:

$$nd = \frac{N}{2W}. \tag{7.2}$$

From the SEM images of the membrane cross-sections, we obtained the membrane thickness (see table 7.2), through which we can calculate the refractive index of each membrane by eq. (7.2). At this point, we can use the Bruggeman approximation to obtain the fraction of porosity f_{air} of the samples:

$$n = n_{air} f_{air} + n_{Si}(1 - f_{air}) \tag{7.3}$$

where the rifractive index of air and silicon are: $n_{air} = 1$ and $n_{Si} = 3.8$ [255]. From eq. (7.3), it is possible to derive the fraction of porosity of each sample obtaining $f_{air} = 0.46 \pm 0.02$ for electrochemically etched membranes, and $f^{re}_{air} = 0.52 \pm 0.06$ for re-etched membranes. At this point, we have all the information to calculate the membrane density $\rho = (1 - f_{air}) \times \rho_{Si} = (1 - f_{air}) \times 2.33\,\mathrm{g\,cm^{-3}}$, and we obtained: $\rho = 1.3 \pm 0.1\,\mathrm{g\,cm^{-3}}$ for electrochemically etched membranes and $\rho^{re} = 1.1 \pm 0.2\,\mathrm{g\,cm^{-3}}$ for re-etched membranes.

7.1.3 Apparatus for Membrane Characterization

To perform the study of Ps yield from the membranes, we used the positron beam of the AML laboratory. The apparatus, called SURF, is shown in fig. 7.3. It generates a continuous positron beam using a sodium-22 radioactive source. The positrons are moderated with a tungsten film, and they are guided electrostatically to the target [225]. The target is kept at ground potential while the source, moderator, and electrodes are raised up to tens of kilovolts of electrostatic potential to provide the positron implantation energy. In this study, the positrons were implanted with energy ranging from 1.5 to 26 keV. In this energy range, the apparatus transmission function is constant [225].

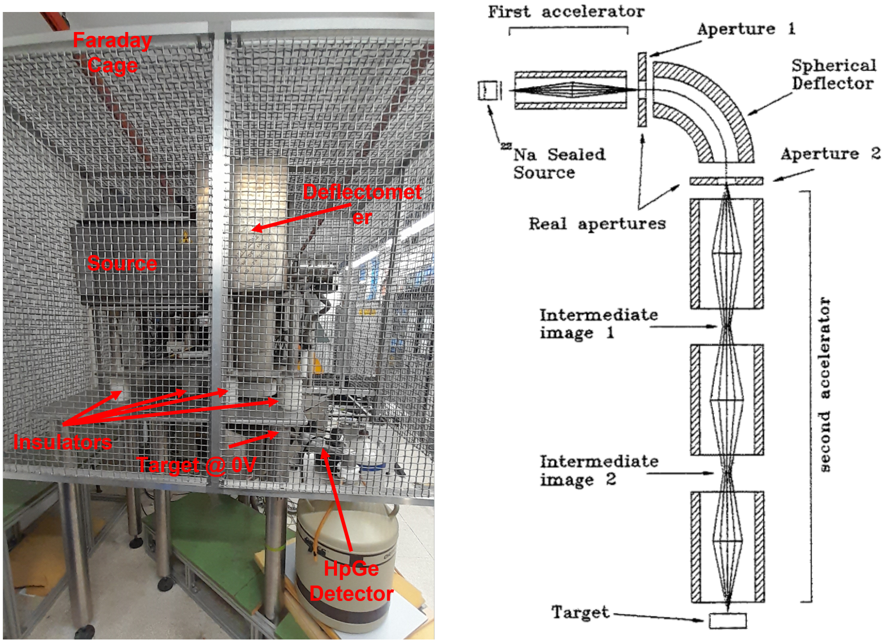

(a) *SURF.* **(b)** *SURF scheme..*

Figure 7.3: The electrostatic positron beam at the Antimatter Laboratory of Trento. The image on the right is from [225].

At each implantation energy considered, the DBS spectrum (see section 2.2.2.2) of the positron annihilation was recorded with an HPGe detector placed at 3.5 cm on the side of the target. The detector efficiency is 45% and its resolution at 511 keV is 1.4 keV [106]. The Ps formation is estimated from the $3\gamma - 2\gamma$ annihilation ratio $F_{3\gamma}[E]$ (see eq. (2.43)). The two regions of the target chamber in front and behind the membrane are perfectly symmetric. With this geometry, the detector probes the region in front and behind the target with the same solid angle.

7.1.4 Measurement of Positronium Yield

Figure 7.4 shows the measured fraction of annihilation into three gammas for the membranes. In the figure, we distinguish the three thickest membranes (14.3, 14.9, 24 µm) and the four thinnest membranes (3.5, 5.0, 6.3, 7.7 µm). At implantation energies > 4 keV the first group has an almost identical behavior. On the opposite, the thinnest membranes show different behavior for $E > 4$ keV.

7.1.4.0.1 14.3, 14.9, 24 µm membranes We start by analyzing the low-energy region ($\leq$ 3 keV) of fig. 7.4a. The decrease in the $F_{3\gamma}$ in this region comes from two processes:

- a lower Ps formation at the surface due to Spur process (see section 2.1.3.1);

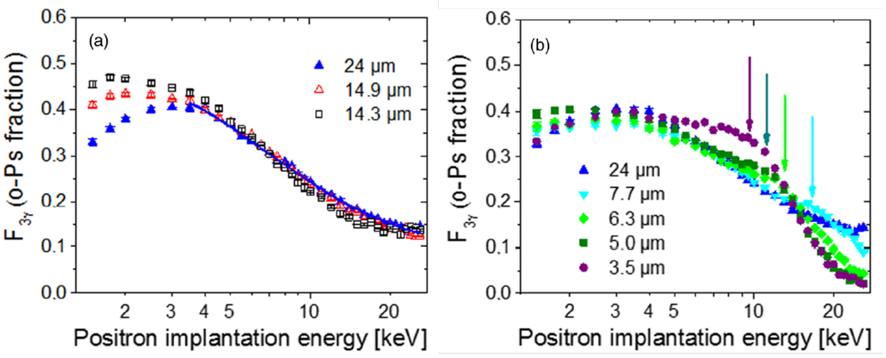

Figure 7.4: Fraction of 3γ annihilation $F_{3\gamma}$ measured at different positron implantation energies. (a) Measurements on membranes 24 µm (up full triangle), 14.9 µm (up empty triangle), and 14.3 µm (empty square). The continuous line is the best fit of the diffusion model [25] on the data for the 24 µm membrane (see text for details). (b) Measurements on membranes 24 µm (up full triangle), 7.7 µm (down full triangle), 6.3 µm (full diamond), 5.0 µm (full square), and 3.5 µm (full disk). The excess annihilations attributable to Ps emission in transmission are indicated by vertical arrows. Statistical errors are reported. *Image from* [28].

- the Ps escapes from the nanochannels after few interactions and so with high kinetic energy, consequently the annihilation gammas see the detector under a small solid angle (i.e. they are detected with lower efficiency).

While all three membranes show a decrease in the $F_{3\gamma}$ near the surface, the behavior is different. This can be attributed to a difference in the surface roughness due to different durations of the electrochemical etching [256]. At implantation energies > 3 keV, the three curves overlap indicating a quite similar nanochannel structure in the three membranes, i.e. similar density and dimension. At increasing implantation energies, the positronium atoms are more likely to annihilate with the electrons from the nanochannel surface decreasing the fraction of Ps emitted from the membrane front face. This is evident from the monotonic decrease in the $F_{3\gamma}$ curves at higher energies. This behavior is compatible with what is obtained from e^+/Ps converters in reflection [25, 72, 75]. In fact, the probability of positron and Ps reaching the back surface of these thick membranes is low:

- **e^+:** using the density previously calculated in the positron depth profile (see eq. (2.11)), less than 3% of the positrons reaches depth higher than 12 µm when implanted at 26 keV;
- **Ps:** by fitting the monotonic decrease region of the $F_{3\gamma}$ (see fig. 7.4), it is possible to extract the Ps diffusion length using the model in reference [25]. In the case of the 24 µm thick membrane, we obtain a diffusion length of 760 ± 80 nm, and similar results are obtained from the other two curves measured in the thickest membranes. This means that even in the case of Ps forming at the maximum implantation depths, it has a low probability of reaching the back surface of the membrane.

In the following, we are going to use the 24 µm thick membrane as a reference in the discussion of Ps formation in the thinnest membranes.

7.1.4.0.2 3.5, 5.0, 6.3, 7.7 µm membranes Figure 7.4b shows the same behavior of the thinnest membranes at low energy (< 3 keV) as seen in the thickest membrane. Even at implantation energies > 3 keV, the behavior is similar with a decrease in the $F_{3\gamma}$ curves. However, the similarities are broken increasing the positron implantation energy. For example, by examining the 7.7 µm membrane, we can identify a similar behavior of the $F_{3\gamma}$ curve with respect the 24 µm membrane up to 13 keV implantation energy. After this energy, we can identify a bump in the curve up to 20 keV, after which we observe $F_{3\gamma}$ values below the reference. The bump can be attributed to the emission of Ps from the back surface of the membrane. The lower values at higher energies can be attributed to positron implantation depth comparable to the membrane thickness. This not only means that a fraction of the implanted positrons escapes the membrane (20% of e^+ escapes at 26 keV), but also the Ps is formed near the back surface. This Ps can escape at high speed after a few interactions and it is detected with less efficiency. If we consider now the other thinnest membranes, we can observe that the energy at which the bump starts is very dependent on the membrane thickness. As seen in fig. 7.4b:

- 7.7 µm: excess center 15 keV;
- 6.3 µm: excess center 12 keV;
- 5.0 µm: excess center 11 keV;
- 3.5 µm: excess center 9.5 keV.

The $F_{3\gamma}$ curves in fig. 7.4 offer only a starting point in the quantification of the Ps emission both in reflection and transmission. Indeed, precise quantification of the amount of Ps emitted in transmission (as well as in reflection at low energy) cannot be obtained directly by the measured $F_{3\gamma}$ curves without correcting them for the undetected fraction of Ps atoms mentioned above. In the next section, the method to correct the data is reported.

7.1.5 Positronium Corrected Yield

To evaluate the fraction of undetected Ps we need to analyze the values of counts in the peak $P[E]$ and the valley $V[E]$ as a function of the positron implantation energy E [25]. These curves are shown in fig. 7.5 for the 24 and 7.7 µm membranes, representing the case without and with the emission of Ps in transmission. However, as previously discussed in both cases we have undetected events, so the $P[E]$ and $V[E]$ values for a virgin silicon sample are used as references. The $P[E] + V[E]$ curve of the silicon is constant as shown in fig. 7.5. This is expected from the constant transmission function of the apparatus as discussed in section 7.1.3. In the case of the two membranes, the counts are always lower than the one from silicon, for all implantation energies. This reduction can be due to two effects:

(a) In the presence of three-gamma annihilation, the detected annihilation photon can have energy outside the peak and valley windows;

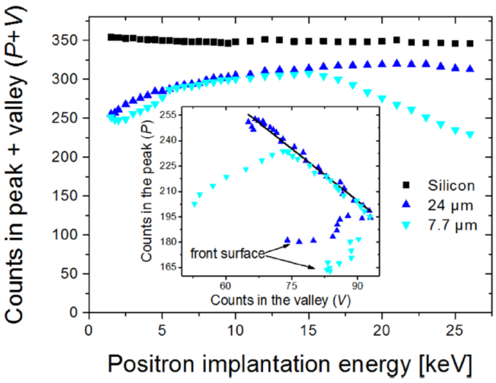

Figure 7.5: Total counts, peak $P[E]$ plus valley $V[E]$, at different implantation energies: (square) virgin silicon, (up triangle) 24 µm membrane, and (down triangle) 7.7 µm membrane. The insert shows the peak vs valley counts for the two membranes. The black line is the best fit of the linear part of the 24 µm membrane curve (see text). For both plots, the statistical errors are smaller than the symbol size. *Image from* [28].

(b) The emitted Ps with high kinetic energy annihilates far from the membrane, so it is detected with lower efficiency.

In the case of the 24 µm membrane, both (a) and (b) contribute to the low counts at low E. At higher energies, instead, the fraction of positron and Ps escaping is negligible as previously discussed, so in this region (a) is the main factor for the loss in $P[E]+V[E]$ counts.

In the case of the 7.7 µm membrane, the $P[E]+V[E]$ curve behaves very similarly to one of the thickest membranes up to 16 keV. Then for this energy region, the same factors contribute to the count loss as previously discussed. However, for this thinner membrane, we have an increase in the count loss at $E > 16$ keV, indicating undetected positron or Ps emitted in transmission.

In a target with Ps formation, the peak and valley counts can be expressed with the following equation [28]:

$$\begin{aligned} P[E] &= P_{Si} - N_{escaped}[E] - N_{2\gamma3\gamma}[E] \\ V[E] &= V_{Si} + \frac{N_{2\gamma3\gamma}[E]}{\alpha} \end{aligned} \tag{7.4}$$

where $P_{Si} = 45 \pm 2$ and $V_{Si} = 304 \pm 2$ are the peak and valley count for the virgin silicon target, $N_{2\gamma3\gamma}[E]$ is the counts that disappeared from the peak area due to o-Ps annihilation, $N_{escaped}[E]$ is the counts that disappeared from the peak area due to the non-detection of emitted positron and Ps, and α is a parameter accounting for the fraction of $N_{2\gamma3\gamma}[E]$ which are recorded in the valley area.

First of all, it is necessary to calculate the parameter α, so we consider the $P[E]\ vs\ V[E]$ curve for the 24 µm membrane as shown in the insert of fig. 7.5. In this curve, we can identify most of the points as residing along a straight line. This data corresponds to the measurement for implantation energies > 6 keV. As previously discussed, in this situation the number of escaped positron and Ps is negligible ($N_{escaped}[E] \approx 0$), so eq. (7.4) is reduced to:

$$P[E] = P_{Si} - \alpha(V[E] - V_{Si}). \tag{7.5}$$

By fitting this equation on the selected data of the thickest membrane, we obtain the value of the parameter $\alpha = 2.05 \pm 0.06$.

Deviations from the linearity in the $P[E]\,vs\,V[E]$ curve represent the presence of a non-negligible amount of escaping positron and Ps ($N_{escaped}[E] \neq 0$), which can be quantified with eq. (7.4) as:

$$N_{escaped}[E] = P_{Si} - P[E] - \alpha(V[E] - V_{Si}). \tag{7.6}$$

In thick membranes, the deviation is present only at low positron implantation energy pointing out that emission of positron and Ps can occur only from the front face. In thin membranes (like 7.7 µm in fig. 7.5), $N_{escaped}$ is different than 0 also at high implantation energy. By using eq. (7.6), the fraction of lost counts from escaped positron and Ps can be estimated in the different membranes. The results are shown in fig. 7.6 with similar behavior for all four thinnest membranes. We can identify three regions in the curves: low-energy (< 5 keV), medium-energy (> 5 and < 10 − 15 keV depending on the membrane thickness), and high-energy (> 10 − 15 keV depending on the membrane thickness). In the low-energy region, the four curves start at a rate of around 50 counts per second which quickly decreases to 0 counts per second at implantation energies > 5 keV. Undetected Ps atoms emitted in reflection are the major contributors to these lost counts at low energies. Indeed, the low-Z material that constitutes the membrane has a low probability of positron backscattering or reemission [25]. In the medium-energy region, the value of $N_{escaped}[E]$ is negligible indicating a very low number of undetected positrons and Ps escaping the membranes. In the high-energy region, the number of undetected events increases quickly. This effect can be ascribed both to positrons crossing the membrane ($N_{e^+}[E]$) and fast Ps forward emitted by the membranes ($N_{Ps}[E]$).

The number of positrons crossing the membrane, $N_{e^+}[E]$, can be estimated by integrating the Makhovian profile of eq. (2.11) beyond the membrane thickness and normalizing to the measured P_{Si}. Then the number of escaped positronium atoms can be estimated by:

$$N_{Ps}[E] = N_{escaped}[E] - N_{e^+}[E]. \tag{7.7}$$

As seen in fig. 7.6, $N_{e^+}[E]$ is negligible at low energy and becomes important at high implantation energies where its value tends to explode. For high implantation energies, $N_{e^+}[E]$ presents large errors due to the uncertainty in the membrane thickness and its density used for its calculation. In particular, the situation where $N_{e^+}[E] > N_{escaped}[E]$ in the case of the two thinnest membranes indicates an underestimation in the membrane thickness and/or density.

Regarding, instead, the estimation of the undetected Ps events $N_{Ps}[E]$, two regions with high values are evident in fig. 7.6. The first region is positioned at low energy and it is compatible with the underdetection of Ps emitted in reflection shown also in converters in reflection [25]. The second region in the $N_{Ps}[E]$ curve corresponds to the bulge in

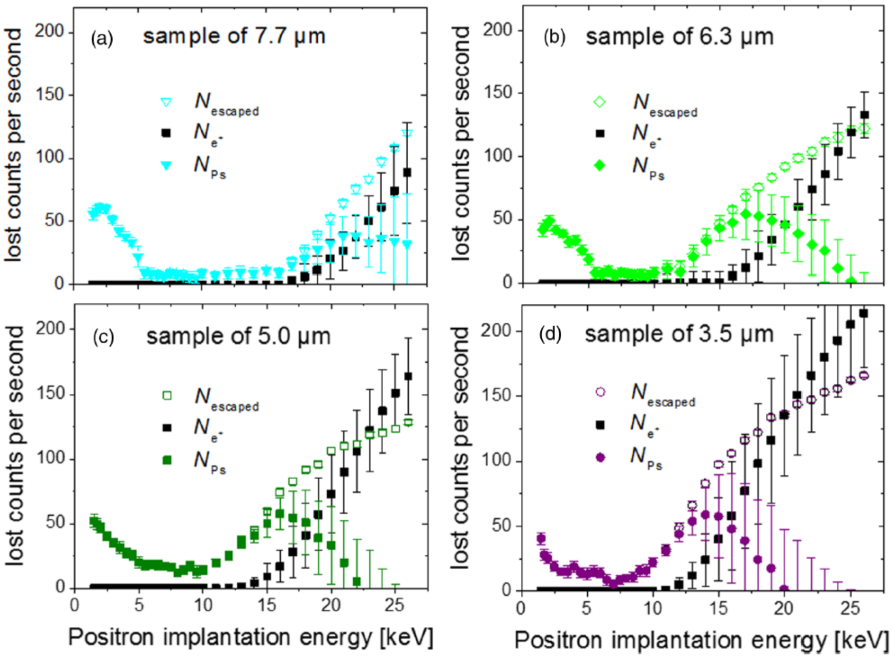

Figure 7.6: Counting rate of the lost events due to: positron and Ps escaping $N_{escaped}[E]$, positron crossing the membrane $N_{e^+}[E]$, and undetected Ps $N_{Ps}[E]$. Statistical errors are reported. *Image from* [28].

the $F_{3\gamma}$ curves in fig. 7.4b. This bulge is ascribable to Ps emission in transmission. The four membranes in fig. 7.6 show different behavior in the second region with high $N_{Ps}[E]$ values. In the 7.7 µm membrane, the region shows just a slight decrease at very high energy. For the other three membranes, it is evident the presence of a peak with a maximum at 17, 16, and 14 keV for the 6.3, 5.0, 3.5 µm membranes, respectively.

By introducing the corrected values of the valley and peak counts using eq. 7.4 in the calculation of the $F_{3\gamma}$ (see eq. (2.43)), we obtain the corrected $F_{3\gamma}$ curve for the four thinnest membranes. These are shown in fig. 7.7 together with the respective measured $F_{3\gamma}$ curve. The difference between the corrected and the measured curves for each membrane is highlighted in the figure as a region with homogeneous coloration. This region represents the undetected Ps emitted in reflection and in transmission, and in the following is referred to as *corrected amount*. As expected after the discussion above about $N_{Ps}[E]$, for each membrane, the corrected amount is concentrated into two energy regions, one at low energy and another at higher energies. While the first is similar to the four membranes, the second behaves extremely differently depending on the membrane thickness with an increase in the $F_{3\gamma}$ curve starting at lower energy for membranes with progressively lower thickness. At low energy, the corrected amount accounts for the lost counts due to the Ps emission from the membrane front (in reflection), while at high energy it accounts for the Ps emitted from the back surface of the membrane (in transmission) and not accounted in the measured $F_{3\gamma}$.

In addition to this corrected amount of forward emitted Ps, we also need to account for the measured Ps emitted by the back surface of the membranes. To calculate this quantity, we use the 24 µm membrane as a reference. Its $F_{3\gamma}$ curve is ascribed to the emission of Ps only in reflection, in fact, as previously discussed, the values are similar

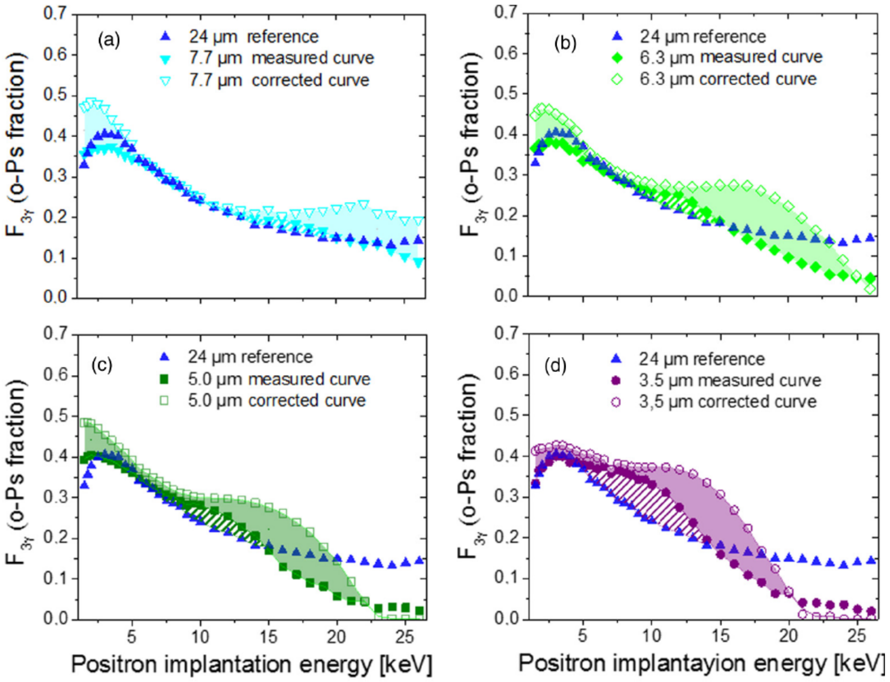

Figure 7.7: $F_{3\gamma}$ curves as measured and corrected (see text) for the four thinnest membranes [7.7 (a), 6.3 (b), 5.0 (c), and 3.5 µm (d)]. The difference between the corrected and measured curves is shown as homogeneous colored bands. $F_{3\gamma}$ curve for 24 µm is shown for reference. The parallel lines pattern highlights the excess in the measured $F_{3\gamma}$ with respect to the reference. The error bars are not reported for clarity. *Image from* [28].

to converters in reflection. At this point the excess in the measured $F_{3\gamma}$ for the four thinnest membranes in the 10 keV region is related to the emission of Ps in transmission. In fig. 7.7, this region is marked by a parallel lines pattern and it will be called the *measured amount* in the following.

This measured amount is an underestimation of the real value due to the missing events that are undetected in the measured $F_{3\gamma}$. The total amount can be estimated by summing the measured and corrected values. The total amount is shown in fig. 7.8 for the four thinnest membranes. In this figure, there are two regions of o-Ps production, one at implantation energies < 5 keV (this threshold is indicated by vertical dashed lines in the figure), and the other at higher energies. In the lower region, the Ps is emitted from the front surface of the membrane as previously discussed, while at high energy, the contribution from Ps emitted in reflection is negligible, and the curves on the right of the vertical dashed line in fig. 7.8 represent our estimation of the Ps emitted in the forward direction.

All four thinnest membranes present an emission of Ps in transmission. The maximum amount has been observed in the 3.5 µm membrane and it is at least $16 \pm 4\%$ (see table 7.3). In general, we observe a shift on the right of the corrected Ps emission with respect to the measured amount. This is consistent with a lower number of interactions with the nanochannel surface for Ps formed near the back surface of the membrane. As a

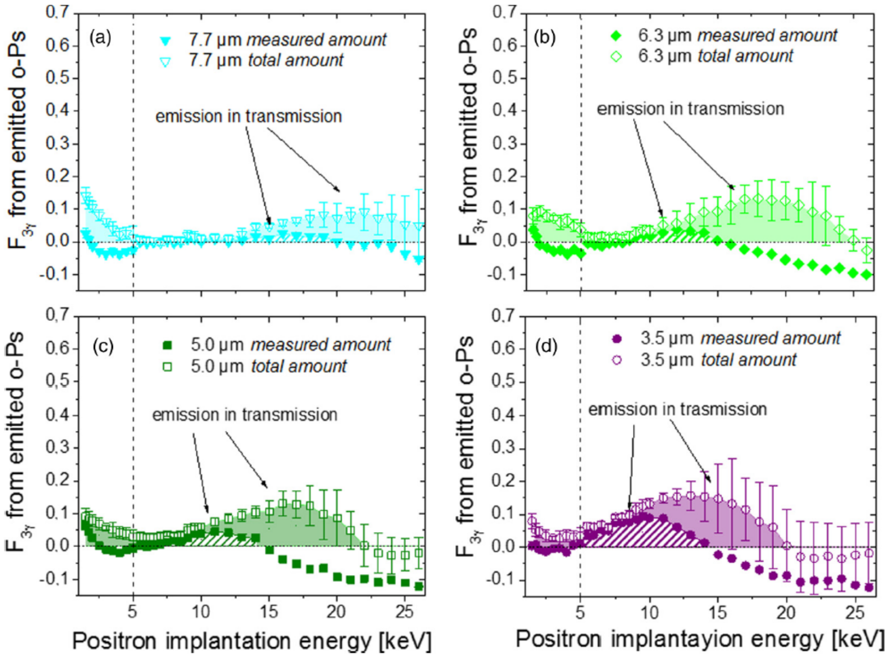

Figure 7.8: Estimation of the o-Ps self-annihilation measured (full symbols) and measured+corrected (empty symbols) for the four thinnest membranes for 7.7 (a), 6.3 (b), 5.0 (c), and 3.5 µm (d). The region with parallel lines pattern indicates the *measured amount*, while the region with homogeneous color indicates the *corrected amount* (see text and fig. 7.7). The vertical dashed lines divide the curves in two, one at low energy where the contribution comes mainly from the Ps emitted in reflection, and the other where the curve values are attributed to Ps leaving from the back surface of the membrane. The error bars are reported. *Image from* [28].

consequence, this Ps is expected to be forward emitted with higher Ps emission energy, so its self-annihilation has a lower probability of being detected by the HPGe detector.

7.1.6 Re-etched Membranes

The membranes discussed up to now are produced with a single etching cycle. As indicated in section 7.1.1, for some membranes it was possible to re-etch them to increase the nanochannels dimension from the original $5-8$ nm to $7-10$ nm. In the following, we are going to discuss three of these re-etched membranes whose thicknesses are: 24, 7.7, and 5.0 µm. Their measured $F_{3\gamma}$ curves are shown in fig. 7.9.

We start from the thickest membrane. As seen in fig. 7.9a, the 24 µm re-etched membrane shows a similar behavior to the not-re-etched 24 µm membrane but with a different slope. By fitting the measured curves with the diffusion model in the monotonic decreasing region, similarly to what was done in the previous section, we extracted the Ps diffusion length. While in the no-re-etched membranes, it was from 760 ± 80 nm, it results 1800 ± 200 nm in the re-etched membranes. Also for the re-etched membranes, the diffusion length is too small to observe Ps emission in transmission from the 24 µm membrane. Therefore, the $F_{3\gamma}$ values for the 24 µm re-etched membrane are indicative

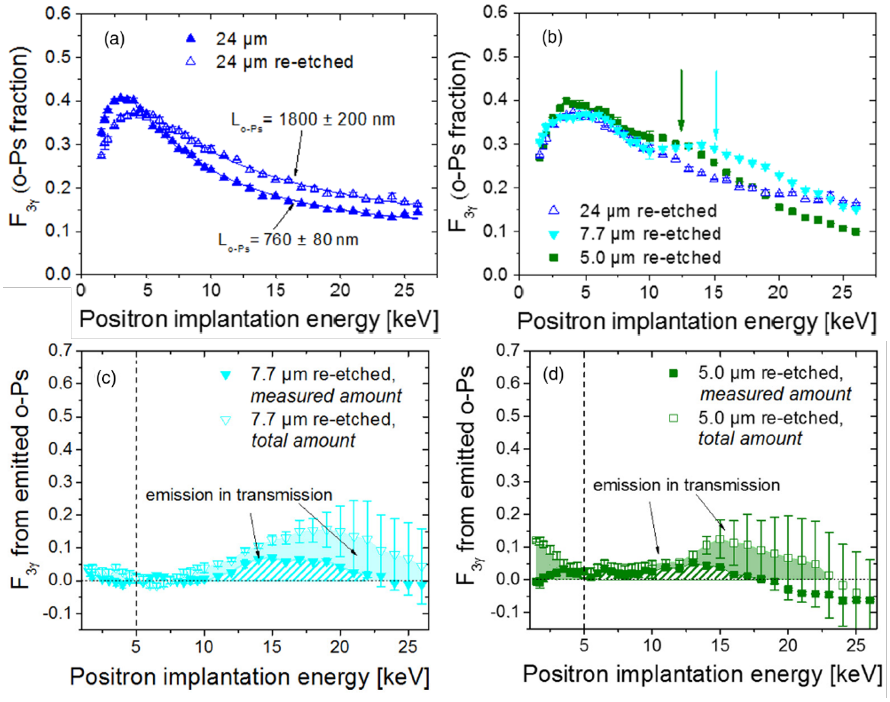

Figure 7.9: (a) $F_{3\gamma}$ curves for 24 µm (full up triangle) and 24 µm re-etched (empty up triangle), the continuous lines represent the best fit of the diffusion model (see text). (b) (c) (d) $F_{3\gamma}$ curves for 24 µm re-etched (empty up triangle), 7.7 µm re-etched (full down triangle), and 5.0 µm re-etched (full square). The continuous lines represent the best fit of the diffusion model (see text). The vertical arrows indicate excess in the $F_{3\gamma}$ value due to Ps emission in transmission. (c) (d) Estimation of the o-Ps self-annihilation measured (full symbols) and measured+corrected (empty symbols) for the 7.7 µm re-etched (c) and 5.0 µm re-etched (d). The region with parallel lines patterns indicates the *measured amount*, while the region with homogeneous color indicates the *corrected amount* (see text and fig. 7.7). The vertical dashed lines divide the curves in two, one at low energy where the contribution comes mainly from the Ps emitted in reflection, and the other where the curve values are attributed to Ps leaving from the back surface of the membrane. The error bars are reported. *Image from* [28].

of Ps emission in reflection similar to the case of the non-re-etched membrane, so we can use this membrane as a reference in the calculation of the Ps emission in transmission.

For the two thinnest membranes, we can still observe a bump in the $F_{3\gamma}$ curves at high energy with respect to the reference (see fig. 7.9), indicating also in the re-etched membranes the emission of Ps in transmission. By using the same procedure as for the non-re-etched membranes, it becomes possible to calculate the total (corrected and measured) amount of Ps formation, this is shown in fig. 7.9c and d. The Ps production in the re-etched membranes shows similar behavior to that of non-re-etched membranes.

7.1.7 Conclusion about Transmission Converters

Table 7.3 summarized the maximum efficiency in the measured and total (measured and corrected) amount of Ps emitted in transmission for all the membranes discussed

Table 7.3: Maximum of the total and measured amount of Ps emission in transmission and the corresponding energy for the 7.7, 6.3, 5.0, and 3.5 µm non-re-etched membranes and the 5.0, and 7.7 µm re-etched membranes. *Table from* [28].

membrane	Ps forward emission Maximum			
	Measured		Total	
	Efficiency [%]	E_{e^+} [keV]	Efficiency [%]	E_{e^+} [keV]
3.5 µm	3.4 ± 1.0	9.5	16 ± 4	13
5.0 µm	4.5 ± 0.4	11	13 ± 4	16
5.0 µm re-etched	5.2 ± 0.5	13	13 ± 6	15
6.3 µm	3.8 ± 0.5	12	13 ± 5	18
7.7 µm	2.6 ± 0.4	16	9 ± 5	22
7.7 µm re-etched	7.1 ± 0.7	15	16 ± 5	19

in this chapter. For non-re-etched membranes, the maximum measured and the total amount of Ps production increase with a decrease in the thickness of the membranes, with the thinnest membrane (3.5 µm) showing a maximum of at least $16 \pm 4\%$. In the case of re-etching, the membranes show maximum efficiency similar to one of thinnest non-re-etched membranes, with a maximum of $16 \pm 5\%$ for the 7.7 µm re-etched membrane.

These efficiencies are at least two times greater than the best previously obtained with transmission converter [252], but still lower than what is obtainable with converters optimized for the reflection geometry. Nevertheless, the transmission geometry could be more advantageous in all those studies that make use of beams of positronium atoms.

7.2 Detector

As mentioned at the beginning of this chapter, another important element for the measurement of the entanglement of the gamma rays generated by Ps self-annihilation is the detector. In section 3.5, we introduced possible solutions for measuring the polarization of the gamma-rays coming from the Ps annihilation. Preliminary tests have been performed on the capabilities of J-PET detectors.

7.2.1 J-PET

In section 3.4, some experimental setups for the measurement of the entanglement in the two-gamma annihilation of positrons were presented. In these setups, two polarimeters are used to reconstruct the polarization of each gamma. The polarimeters described are only capable of detecting gamma-rays coming from one direction. As discussed in section 3.5, this limits their application to the case of Ps annihilation in three gammas. Detector systems, like J-PET, that are capable of covering a good portion of the solid angle around the annihilation spot were described as possible solutions for the study of entanglement in the three annihilation gammas.

J-PET modules can be positioned around the o-Ps annihilation spot covering the majority of the solid angle with multiple layers. In this configuration, the internal layer is used to Compton scatter the annihilation gammas, the external layer, instead, detects the scattered gamma-rays. Knowing the directions of the incoming and the scattered gammas, we can reconstruct the Compton scattering. In particular, it is possible to determine the scattering θ and azimuthal ϕ angles which are necessary to determine the degree and direction of the polarization of the incoming gamma (see section 2.3.2.1).

Two J-PET modules were made available for a first test with a positron beam. We started by studying the capability of the modules to reconstruct the direction of the annihilation gammas. For this purpose, we made use of the 511 keV gamma-rays from annihilations of positrons on a blank vacuum flange positioned at the end of the first stage of the PsICO apparatus (this is the same setup used in section 6.2.2). The two modules were positioned opposite to each other with respect to the positron beam at the center (see fig. 7.10 left). The detection events were skimmed to select only the two counterpropagating gammas from the same annihilation. Consequently, the two modules were able to reconstruct the annihilation spot of positrons from tomographic analysis of the detected gamma-rays. This also corresponds to the determination of the direction of the gammas emitted by the reconstructed annihilation spot. This test is described in detail in reference [29].

7.2.1.1 J-PET modules

Each module can operate as a stand-alone detector with 13 plastic scintillators and the reading electronics incorporated in a single package. Each scintillator has dimension $500 \times 24 \times 6\,\mathrm{mm}^3$ and the scintillating light is recorded by a 1×4 SiPMs matrix glued on both ends of the scintillator. The signals from the SiPMs are read out from the front-end electronic board at each end of the module with an FPGA in triggerless mode [257, 258]. This provides excellent time resolution: the sampling rate of the voltage signal from the SiPMs is 20 ps [257]. Using the time resolution, the energy of the recorded photon is not obtained by charge collection, but from the time-over-threshold (TOT) of the signal of the corresponding event. The TOT is recorded by the onboard electronics as the timestamps at a threshold for rising and falling edges of the SiPM signal, the TOTs at two thresholds (30 mV and 70 mV) are recorded for each signal. The relation between the energy deposited by the photon in the interaction and the TOT has already been established in reference [259]. Considering the electronics and the scintillators, the single module has a length of 90.6 cm, a width of 9 cm, and a weight less than 2 kg. The signals from the electronics at both ends of all modules are collected by a controller board capable of handling up to 6 modules. The controller board is connected to a PC to record the signals for the reconstruction [29].

The reconstruction of the annihilation gamma direction requires the recording of the two counterpropagating 511 keV photons, so the modules are positioned opposite one another. The reconstruction starts with the identification of the hit position and hit time of the gamma interaction with the single scintillator. These two parameters are calculated from the difference in timing between the signals from the SiPMs from the opposite ends of the scintillator (see fig. 3.6). Knowing the speed of light in the scintillator material, the hit time is the average of the two recorded times and the hit position is the speed of the scintillating light times the difference in the timing to reach the two ends [260, 261]. At this point, for each gamma interaction with the module, we have the TOT, hit position, and hit time. From the TOT we can discriminate the photons with the 511 keV energy. Using the other two data points, the events are coupled to have the same hit time and hit position opposite one another, in this way the two

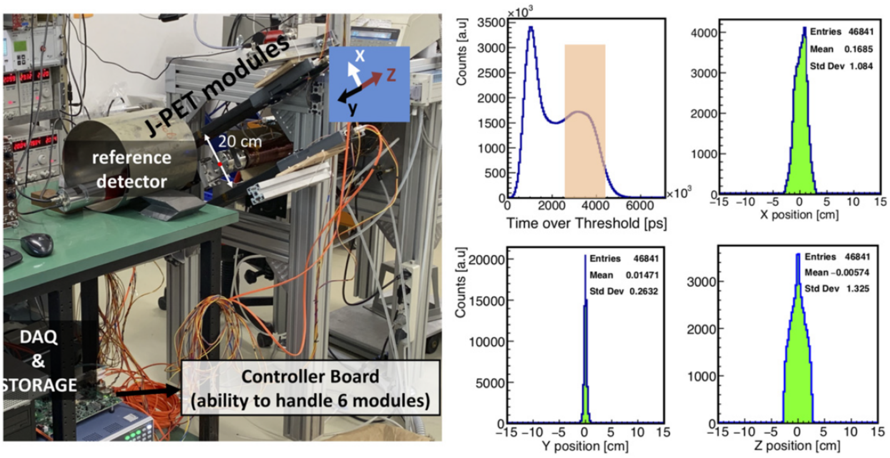

Figure 7.10: On the left, the experimental setup for the test of two J-PET modules with the PsICO apparatus is shown. The positron beam is stopped on a blank flange, the two modules are centered on the flange center and distanced by 20 cm from each other. The directional frame used in the analysis of signals from the two modules is shown: the y-axis along the positron beam and the z-axis along the module length. On the right, the four panels show the measurement results. The upper left panel represents the TOT distribution of the recorded events highlighting the region corresponding to 511 keV photons. The remaining three panels show the projection on the three axes (x, y, z) of the reconstructed vertices. *Image from* [29].

counterpropagating annihilation photons are selected. At this point, the direction of the two annihilation gammas is given by the line connecting the two hit positions. Along this line there is the annihilation spot, its position is calculated from the difference in the hit time of the two events [29]. In the case of three-gamma annihilation of o-Ps, a more complex analysis of the hit events would be required to reconstruct the annihilation spot and the gamma directions due to greater complexity with respect to the two-gamma annihilation of positrons [262].

7.2.1.2 Measurement and results

The experimental setup is shown in fig. 7.10 left. The positron beam from the PsICO apparatus is stopped with a blank flange. The flat surface of the flange provides an ideal situation to test the limits in the reconstruction capabilities of the two modules in the direction of the beam (y-axis in the following discussion). The modules are centered on the center of the flange at a distance of 20 cm from each other to optimize the coverage of the solid angle around the annihilation spot [29]. As seen from the figure, the modules are at a 60° angle with respect to the vertical plane of the apparatus, this is due to the presence of the gate valve before the blank flange limiting the module positioning.

During the measurements with the modules, argon moderators were used for the maximum positron rate, and the positron rate was monitored by the NaI(Tl) detector as in the efficiency studies of section 6.2.2.

The four panels on the right of fig. 7.10 show the results of the measurements. In particular, we have the distribution of the TOT of the recorded signal (upper left panel of fig. 7.10), only the events in the shaded area of the plot are considered coming from the interaction of a 511 keV annihilation photon with the module. Using the procedure indicated in the previous section, it became possible to reconstruct the annihilation spot of the positrons. The remaining panels of the right part of fig. 7.10 show the preliminary result of this reconstruction, and resolution of ±1.01, ±0.26, and ±1.33 cm are obtained in the x, y, and z coordinate, respectively [29]. These three directions correspond to the direction orthogonal to the module surface (x-axis), along the beam direction (y-axis), and along the module length (z-axis).

The best resolution is obtained along the beam direction respect to which the modules are orthogonal. These preliminary results are encouraging in the use of these modules in the determination of: the annihilation point, the hit point of the gammas on the detector, and the determination of the direction of the annihilation gammas. Further tests are needed to study the use of J-PET modules in the measurement of the entanglement in the three gammas from o-Ps annihilation. The next step will be the use of the two modules one over the other to reconstruct the direction of the Compton scattered gamma from a 511 keV gamma. When the capabilities of the J-PET modules to reconstruct the direction of the incoming and scattered gamma have been determined, we will increase the number of modules to create the detector setup to measure the entanglement in the polarization of the annihilation radiation.

Bibliography

[1] N. Prantzos, C. Boehm, A. M. Bykov, R. Diehl, K. Ferrière, et al. “The 511 keV emission from positron annihilation in the Galaxy”. In: *Reviews of Modern Physics* 83 (2011), p. 1001.

[2] R. J. Murphy, G. H. Share, J. G. Skibo, and B. Kozlovsky. “The Physics of Positron Annihilation in the Solar Atmosphere”. In: *The Astrophysical Journal Supplement Series* 161 (2005), p. 495.

[3] G. J. Fishman. “Positrons observed to originate from thunderstorms”. In: *Eos* 92 (2011), p. 185.

[4] C. D. Anderson. “The apparent existence of easily deflectable positives”. In: *Science* 76 (1932), p. 238.

[5] C. D. Anderson. “The positive electron”. In: *Physical Review* 43 (1933), p. 491.

[6] M. Deutsch. “Evidence for the Formation of Positronium in Gases”. In: *Physical Review* 82 (1951), p. 456.

[7] D. B. Cassidy. “Experimental progress in positronium laser physics”. In: *European Physical Journal D* 72 (2018), p. 53.

[8] M. H. L. Pryce and J. C. Ward. “Angular correlation effects with annihilation radiation”. In: *Nature* 160 (1947), p. 435.

[9] H. S. Snyder, S. Pasternack, and J. Hornbostel. “Angular Correlation of Scattered Annihilation Radiation”. In: *Physical Review* 73 (1948), p. 440.

[10] B. C. Hiesmayr and P. Moskal. “Genuine Multipartite Entanglement in the 3-Photon Decay of Positronium”. In: *Scientific Reports* 7 (2017), p. 15349.

[11] R. C. Hanna. “Polarization of Annihilation Radiation”. In: *Nature* 162 (1948), p. 332.

[12] E. Bleuler and H. L. Bradt. “Correlation Between the States of Polarization of the Two Quanta of Annihilation Radiation”. In: *Physical Review* 73 (1948), p. 1398.

[13] C. S. Wu and I. Shaknov. “The angular correlation of scattered annihilation radiation”. In: *Physical Review* 77 (1950), p. 136.

[14] D. Bohm and Y. Aharonov. “Discussion of experimental proof for the EPR paradox”. In: *Physical Review* 108 (1957), p. 1070.

[15] S. M. Curry. “Combined zeeman and motional stark effects in the first excited state of positronium”. In: *Physical Review A* 7 (1973), p. 447.

[16] T. J. Murphy and C. M. Surko. “Positron trapping in an electrostatic well by inelastic collisions with nitrogen molecules”. In: *Physical Review A* 46 (1992), p. 5696.

[17] J. R. Danielson, D. H. E. Dubin, R. G. Greaves, and C. M. Surko. “Plasma and trap-based techniques for science with positrons”. In: *Reviews of Modern Physics* 87 (2015), p. 247.

[18] C. M. Surko, S. J. Gilbert, and R. G. Greaves. “Progress in Creating Low-energy Positron Plasmas and Beams”. In: *Non-neutral plasma physics III*. Ed. by John J. Bollinger, Ross L. Spencer, and Ronald C. Davidson. Melville, New York: AIP Conference Proceedings, 1999, p. 3.

[19] A. P. Mills and E. M. Gullikson. “Solid neon moderator for producing slow positrons”. In: *Applied Physics Letters* 49 (1986), p. 1121.

[20] L. Povolo, S. Mariazzi, L. Penasa, R. Caravita, and R. S. Brusa. “Generation of a bunched positron beam extracted nonadiabatically from a buffer-gas trap and focused in a free field region”. In: *Physical Review Accelerators and Beams* 26 (2023), p. 051601.

[21] T. R. Weber, J. R. Danielson, and C. M. Surko. “Electrostatic beams from tailored plasmas in a Penning-Malmberg trap”. In: *Physics of Plasmas* 17 (2010), p. 123507.

[22] N. C. Hurst, J. R. Danielson, and C. M. Surko. “Magnetic field extraction of trap-based electron beams using a high-permeability grid”. In: *Physics of Plasmas* 22 (2015), p. 073503.

[23] D. A. Cooke, G. Barandun, S. Vergani, B. Brown, A. Rubbia, and P. Crivelli. “Positron extraction to an electromagnetic field free region”. In: *Journal of Physics B* 49 (2016), p. 014001.

[24] L. Penasa, L. Di Noto, M. Bettonte, S. Mariazzi, G. Nebbia, and R. S. Brusa. “Positron bunching system for producing positronium clouds into vacuum”. In: *Journal of Physics: Conference Series* 505 (2014), p. 012031.

[25] S. Mariazzi, P. Bettotti, S. Larcheri, L. Toniutti, and R. S. Brusa. “High positronium yield and emission into the vacuum from oxidized tunable nanochannels in silicon”. In: *Physical Review B* 81 (2010), p. 235418.

[26] L. Liszkay, F. Guillemot, C. Corbel, J. P. Boilot, T. Gacoin, et al. “Positron annihilation in latex-templated macroporous silica films: Pore size and ortho-positronium escape”. In: *New Journal of Physics* 14 (2012), p. 065009.

[27] S. Aghion, C. Amsler, T. Ariga, G. Bonomi, R. S. Brusa, et al. (AE$\bar{\mathrm{g}}$IS collaboration). “Characterization of a transmission positron/positronium converter for antihydrogen production”. In: *Nuclear Instruments and Methods in Physics Research B* 407 (2017), p. 55.

[28] S. Mariazzi, B. Rienäcker, R. Magrin Maffei, L. Povolo, S. Sharma, R. Caravita, L. Penasa, P. Bettotti, M. Doser, and R. S. Brusa. “Forward emission of positronium from nanochanneled silicon membranes”. In: *Physical Review B* 105 (2022), p. 115422.

[29] S. Sharma, J. Baran, R. S. Brusa, R. Caravita, N. Chug, et al. (AML & J-PET collaboration). “J-PET detection modules based on plastic scintillators for performing studies with positron and positronium beams”. In: *Journal of Instrumentation* 18 (2023), p. C02027.

[30] P. J. Mohr, B. N. Taylor, and D. B. Newell. “CODATA Recommended Values of the Fundamental Physical Constants: 2010”. In: *Journal of Physics and Chemistry of Solids* 41 (2012), p. 043109.

[31] P. A. M. Dirac. “The Quantum Theory of the Electron”. In: *Proceeding of the Royal Society A* 117 (1928), p. 610.

[32] P. A. M. Dirac. “A Theory of Electrons and Protons”. In: *Proceeding of the Royal Society A* 126 (1930), p. 360.

[33] R. P. Feynman. “The theory of positrons”. In: *Physical Review* 76 (1949), p. 749.

[34] M. Amoretti, C. Amsler, G. Bonomi, A. Bouchta, P. Bowe, et al. (ATHENA collaboration). “Production and detection of cold antihydrogen atoms”. In: *Nature* 419 (2002), p. 456.

[35] G. Gabrielse, N. S. Bowden, P. Oxley, A. Speck, C. H. Storry, et al. (ATRAP collaboration). “Background-Free Observation of Cold Antihydrogen with Field-Ionization Analysis of Its States”. In: *Physical Review Letters* 89 (2002), p. 213401.

[36] J. Knödlseder, P. Jean, V. Lonjou, G. Weidenspointner, N. Guessoum, et al. “The all-sky distribution of 511 keV electron-positron annihilation emission”. In: *Astronomy and Astrophysics* 441 (2005), p. 513.

[37] C. Keith and D. Hooper. “511 keV excess and primordial black holes”. In: *Physical Review D* 104 (2021), p. 63033.

[38] R. Krause-Rehberg and H. S. Leipner. *Positron annihilation in semiconductors: defect studies*. Springer Science & Business Media, 1999.

[39] J. A. Wheeler. “Polyelectrons”. In: *Annals of the New York Academy of Sciences* 48 (1946), p. 219.

[40] M. Deutsch. “Three-quantum decay of positronium”. In: *Physical Review* 83 (1951), p. 866.

[41] S. DeBenedetti and H. C. Corben. “Positronium”. In: *Annual Review of Nuclear Science* 4 (1954), p. 191.

[42] A. M. Alonso, B. S. Cooper, A. Deller, S. D. Hogan, and D. B. Cassidy. “Positronium decay from n=2 states in electric and magnetic fields”. In: *Physical Review A* 93 (2016), p. 12506.

[43] G. S. Adkins, D. B. Cassidy, and J. Pérez-Ríos. “Precision spectroscopy of positronium: Testing bound-state QED theory and the search for physics beyond the Standard Model”. In: *Physics Reports* 975 (2022), p. 1.

[44] P. A. Vetter and S. J. Freedman. “Search for CPT-odd decays of positronium”. In: *Physical Review Letters* 91 (2003), p. 263401.

[45] J. Raj. “Test of T, P and CP Symmetry in the decay of ortho-Positronium using the J-PET detector”. PhD thesis. Jagiellonian University, 2022.

[46] A. P. Mills and M. Leventhal. “Can we measure the gravitational free fall of cold Rydberg state positronium?” In: *Nuclear Instruments and Methods in Physics Research B* 192 (2002), p. 102.

[47] M. K. Oberthaler. “Anti-matter wave interferometry with positronium”. In: *Nuclear Instruments and Methods in Physics Research B* 192 (2002), p. 129.

[48] D. B. Cassidy and S. D. Hogan. “Atom control and gravity measurements using Rydberg positronium”. In: *International Journal of Modern Physics: Conference Series* 30 (2014), p. 1460259.

[49] S. Mariazzi, R. Caravita, L. Glöggler, L. Povolo, L. Penasa, S. Sharma, P. Moskal, and R. S. Brusa. “Development of a Position-Sensitive Detector for Positronium Inertial Sensing Measurements”. In: *Acta Physica Polonica A* 142 (2022), p. 319.

[50] P. W. Zitzewitz, J. C. Van House, A. Rich, and D. W. Gidley. “Spin polarization of low-energy positron beams”. In: *Physical Review Letters* 43 (1979), p. 1281.

[51] P. J. Schultz and K. G. Lynn. “Interaction of positron beams with surfaces, thin films, and interfaces”. In: *Review of Modern Physics* 60 (1988), p. 701.

[52] R. M. Nieminen and J. Oliva. “Theory of positronium formation and positron emission at metal surfaces”. In: *Physical Review B* 22 (1980), p. 2226.

[53] A. F. Makhov. “The penetration of electrons into solids. 1. The intensity of an electron beam, transverse paths of electrons”. In: *Soviet Physics-Solid State* 2 (1961), p. 1934.

[54] A. F. Makhov. “The penetration of electrons into solids. 2. The distribution of electrons in depth”. In: *Soviet Physics-Solid State* 2 (1961), p. 1942.

[55] A. F. Makhov. “The penetration of electrons into solids. 3. The absorption of the energy of an electron beam”. In: *Soviet Physics-Solid State* 2 (1961), p. 1945.

[56] S Mariazzi. “Application of Positron Spectroscopy for Defect Characterization”. PhD thesis. University of Trento, 2005.

[57] K. G. Lynn and D. O. Welch. “Slow positrons in metal single crystals. I. Positronium formation at Ag(100), Ag(111), and Cu(111) surfaces”. In: *Physical Review B* 22 (1980), p. 99.

[58] O. E. Mogensen. “Spur reaction model of positronium formation”. In: *The Journal of Chemical Physics* 60 (1974), p. 998.

[59] A. Dupasquier. “Positroniumlike systems in solids”. In: *Positron Solid State Physics, Proceedings of the International School of Physics, Enrico Fermi, Course LXXXIII*. Ed. by W. Brandt and A. Dupasquier. Amsterdam, North-Holland: SIF- Società Italiana di Fisica, 1981, p. 510.

[60] M. J. Puska and R. M. Nieminen. “Theory of positrons in solids and on solid surfaces”. In: *Reviews of Modern Physics* 66 (1994), p. 841.

[61] J. M. C. Robles, E. Ogando, and F. Plazaola. “Positron lifetime calculation for the elements of the periodic table”. In: *Journal of Physics: Condensed Matter* 19 (2007), p. 176222.

[62] P. A. M. Dirac. *The principles of quantum mechanics*. Oxford University Press, 1930.

[63] A. Ore and J. L. Powell. “Three-Photon Annihilation of an Electron-Positron Pair”. In: *Physical Review* 75 (1949), p. 1963.

[64] S. J. Tao. “Positronium annihilation in molecular substances”. In: *The Journal of Chemical Physics* 56 (1972), pp. 5499–5510.

[65] M. Eldrup, D. Lightbody, and J. N. Sherwood. “The temperature dependence of positron lifetimes in solid pivalic acid”. In: *Chemical Physics* 63 (1981), pp. 51–58.

[66] S. Van Petegem, C. Dauwe, T. Van Hoecke, J. De Baerdemaeker, and D. Segers. “Diffusion length of positrons and positronium investigated using a positron beam with longitudinal geometry”. In: *Physical Review B* 70 (2004), p. 115410.

[67] P. Sferlazzo, S. Berko, and K. F. Canter. “Experimental support for physisorbed positronium at the surface of quartz”. In: *Physical Review B* 32 (1985), p. 6067.

[68] Y. Nagashima, Y. Morinaka, T. Kurihara, Y. Nagai, T. Hyodo, et al. “Origins of positronium emitted from SiO_2”. In: *Physical Review B* 58 (1998), p. 12676.

[69] T. Chang, M. Xu, and X. Zeng. “Effect of the Energy Loss Process on the Annihilation of orthopositronium in silica aerogel”. In: *Physics Letters A* 126 (1987), p. 189.

[70] R. S. Vallery, P. W. Zitzewitz, and D. W. Gidley. “Resolution of the orthopositronium Lifetime Puzzle”. In: *Physical Review Letters* 90 (2003), p. 203402.

[71] D. B. Cassidy, P. Crivelli, T. H. Hisakado, L. Liszkay, V. E. Meligne, et al. “Positronium cooling in porous silica measured via Doppler spectroscopy”. In: *Physical Review A* 81 (2010), p. 012715.

[72] S. Mariazzi, P. Bettotti, and R. S. Brusa. “Positronium cooling and emission in vacuum from nanochannels at cryogenic temperature”. In: *Physical Review Letters* 104 (2010), p. 243401.

[73] K. Ito, R. S. Yu, K. Sato, K. Hirata, Y. Kobayashi, et al. “Pore interconnectivity of nanoclustering silica porous films as studied by positronium time-of-flight spectroscopy”. In: *Journal of Applied Physics* 98 (2005), p. 094307.

[74] H. K. M. Tanaka, T. Kurihara, and A. P. Mills. “Positronium time of flight measurements of an open-pored spin-on low-k mesoporous film”. In: *Journal of Physics Condensed Matter* 18 (2006), p. 8581.

[75] C. He, T. Ohdaira, N. Oshima, M. Muramatsu, A. Kinomura, et al. “Evidence for pore surface dependent positronium thermalization in mesoporous silica/hybrid silica films”. In: *Physical Review B* 75 (2007), p. 195404.

[76] S. Mariazzi, R. Caravita, C. Zimmer, B. Rienäcker, A. Camper, et al. (AE$\bar{g}$IS collaboration). “High-yield thermalized positronium at room temperature emitted by morphologically tuned nanochanneled silicon targets”. In: *Journal of Physics B* 54 (2021), p. 085004.

[77] S. L. Andersen. “Positronium formation and cooling in meso-structured silica films”. PhD thesis. Aarhus University, 2015.

[78] D. W. Gidley, K. G. Lynn, M. P. Petkov, M. H. Weber, J. N Sun, and A. F. Yee. “Depth-profiled Positron Annihilation Spectroscopy of Thin Insulation Films”. In: *New Directions in Antimatter Chemistry and Physics*. Ed. by C. M. Surko and F.A. Gianturco. Kluwer Academic Publishers, 2001, p. 151.

[79] E. Soininen, J. Makinen, D. Beyer, and P. Hautojarvi. "High-temperature positron diffusion in Si, GaAs, and Ge". In: *Physical Review B* 46 (1992), p. 104.

[80] F. Guatieri, S. Mariazzi, C. Hugenschmidt, and R. S. Brusa. "Classical modeling of positronium cooling in silicon nanochannel plates". In: *Physical Review B* 106 (2022), p. 035418.

[81] G. Gerber, D. Newman, A. Rich, and E. Sweetman. "Precision measurement of positron polarization in ^{68}Ga decay based on the use of a new positron polarimeter". In: *Physical Review D* 15 (1977), p. 1189.

[82] T. Hirade. "Positronium formation at low temperatures in polymers and other molecular solids". In: *Acta Physica Polonica A* 107 (2005), p. 615.

[83] M. Antonello, A. Belov, G. Bonomi, R. S. Brusa, M. Caccia, et al. (AE$\bar{\text{g}}$IS collaboration). "Efficient 2^3S positronium production by stimulated decay from the 3^3P level". In: *Physical Review A* 100 (2019), p. 63414.

[84] T. Hirade, F. H. J. Maurer, and M. Eldrup. "Positronium formation at low temperatures: the role of trapped electrons". In: *Radiation Physics and Chemistry* 58 (2000), p. 465.

[85] C. A. Palacio, J. De Baerdemaeker, D. Van Thourhout, and C. Dauwe. "Emission of positronium in a nanometric PMMA film". In: *Applied Surface Science* 255 (2008), p. 197.

[86] G. Consolati. "Magnetic quenching of positronium". In: *Journal of Radioanalytical and Nuclear Chemistry* 210 (1996), p. 273.

[87] Y. Nagai, Y. Nagashima, J. Kim, Y. Itoh, and T. Hyodo. "Measurement of positron spin polarization by using the Doppler broadening method". In: *Nuclear Instruments and Methods in Physics Research B* 171 (2000), p. 199.

[88] G. F. Knoll. *Radiation Detection and Measurements*. John Wiley and Sons, 1979.

[89] *MCP and MCP assembly - Hamamatsu Photonics K.K.* URL: `https://www.hamamatsu.com/content/dam/hamamatsu-photonics/sites/documents/99_SALES_LIBRARY/etd/MCP_assembly_TMCP0003E.pdf`.

[90] G. B. Andresen, W. Bertsche, P. D. Bowe, C. C. Bray, E. Butler, et al. "Antiproton, positron, and electron imaging with a microchannel plate/phosphor detector". In: *Review of Scientific Instruments* 80 (2009), p. 123701.

[91] R. Caravita, M. Antonello, A. Belov, G. Bonomi, R. S. Brusa, et al. (AE$\bar{\text{g}}$IS collaboration). "Hybrid imaging and timing ps laser excitation diagnostics for pulsed antihydrogen production". In: *Acta Physica Polonica A* 137 (2020), p. 96.

[92] T. Poikela, J. Plosila, T. Westerlund, M. Campbell, M. De Gaspari, et al. "Timepix3: A 65K channel hybrid pixel readout chip with simultaneous ToA/ToT and sparse readout". In: *Journal of Instrumentation* 9 (2014), p. C05013.

[93] A. S. Tremsin and J. V. Vallerga. "Unique capabilities and applications of Microchannel Plate (MCP) detectors with Medipix/Timepix readout". In: *Radiation Measurements* 130 (2020), p. 106228.

[94] L. T. Glöggler, R. Caravita, M. Auzons, B. Bergmann, R. S. Brusa, et al. (AE$\bar{\text{g}}$IS collaboration). "High-resolution MCP-TimePix3 imaging/timing detector for antimatter physics". In: *Measurement Science and Technology* 33 (2022), p. 115105.

[95] A. P. Mills Jr. and W. S. Crane. “Beam-foil production of fast positronium”. In: *Physical Review A* 31 (1985), p. 593.

[96] D. W. Gidley, R. Mayer, W. E. Frieze, and K. G. Lynn. “Glancing angle scattering and neutralization of a positron beam at metal surfaces”. In: *Physical review letters* 58 (1987), p. 595.

[97] A. C. L. Jones, A. M. Piñeiro, E. E. Roeder, H. J. Rutbeck-Goldman, H. W. K. Tom, and A. P. Mills. “Large-area field-ionization detector for the study of Rydberg atoms”. In: *Review of Scientific Instruments* 87 (2016), p. 113307.

[98] M. Antonello, A. Belov, G. Bonomi, R. S. Brusa, M. Caccia, et al. (AE$\bar{\text{g}}$IS collaboration). “Rydberg-positronium velocity and self-ionization studies in a 1T magnetic field and cryogenic environment”. In: *Physical Review A* 102 (2020), p. 13101.

[99] C. Amsler, M. Antonello, A. Belov, G. Bonomi, R. S. Brusa, et al. (AE$\bar{\text{g}}$IS collaboration). “A 100 μm-resolution position-sensitive detector for slow positronium”. In: *Nuclear Instruments and Methods in Physics Research B* 457 (2019), pp. 44–48.

[100] D. Bochert. “Optimierte Analyse von Lebenszeitspektren aus Positronenstrahlsystemen”. Master’s Thesis. Universität der Bundeswehr Munchen, 2004.

[101] J. Kansy. “Microcomputer program for analysis of positron annihilation lifetime spectra”. In: *Nuclear Instruments and Methods in Physics Research A* 374 (1996), p. 235.

[102] D. B. Cassidy, S. H. M. Deng, H. K. M. Tanaka, and A. P. Mills Jr. “Single shot positron annihilation lifetime spectroscopy”. In: *Applied physics letters* 88 (2006), p. 194105.

[103] S. Aghion, C. Amsler, A. Ariga, T. Ariga, A. S. Belov, et al. (AE$\bar{\text{g}}$IS collaboration). “Positron bunching and electrostatic transport system for the production and emission of dense positronium clouds into vacuum”. In: *Nuclear Instruments and Methods in Physics Research B* 362 (2015), p. 86.

[104] M. Eldrup, A. Vehanen, P. J. Schultz, and K. G. Lynn. “Positronium formation and diffusion in crystalline and amorphous ice using a variable-energy positron beam”. In: *Physical Review B* 32 (1985), p. 7048.

[105] E. Soininen, A. Schwab, and K. G. Lynn. “Positron-induced Auger-electron study of the Ge(100) surface: Positron thermal desorption and surface condition”. In: *Physical Review B* 43 (1991), p. 51.

[106] R. S. Brusa, C. Macchi, S. Mariazzi, and G. P. Karwasz. “Porosity of low-κ materials studied by slow positron beam”. In: *Acta Physica Polonica A* 107 (2005), p. 702.

[107] A. P. Mills. “Positronium formation at surfaces”. In: *Physical Review Letters* 41 (1978), p. 1828.

[108] V. N. Baier and V. M. Katkov. “Quasiclassical theory of bremsstrahlung by relativistic particles”. In: *Soviet Physics JETP* 28 (1968), p. 807.

[109] H. Kolanoski and E166 Collaboration. “The E166 Experiment: Undulator Based Production of Polarized Positrons”. In: *AIP Conference Proceedings*. Vol. 1149. AIP. 2009, p. 841.

[110] C. Sun, J. Zhang, J. Li, W. Z. Wu, S. F. Mikhailov, et al. “Polarization measurement of stored electron beam using Touschek lifetime”. In: *Nuclear Instruments and Methods in Physics Research A* 614 (2010), p. 339.

[111] J. Dumas. “Feasibility studies of a polarized positron source based on the bremsstrahlung of polarized electrons”. PhD thesis. Université de Grenoble, 2011.

[112] S. Tashenov, T. Bäck, R. Barday, B. Cederwall, J. Enders, et al. “Electron polarimetry with bremsstrahlung”. In: *Journal of Physics: Conference Series* 488 (2014), p. 12057.

[113] D. B. Cassidy, V. E. Meligne, and A. P. Mills. “Production of a Fully Spin-Polarized Ensemble of Positronium Atoms”. In: *Physical Review Letters* 104 (2010), p. 173401.

[114] Y. Nagashima and T. Hyodo. “Effects of positron spin polarization on orthopositronium and parapositronium formation in a magnetic field”. In: *Physical Review B* 41 (1990), p. 3937.

[115] M. Maekawa, Y. Fukaya, A. Yabuuchi, I. Mochizuki, and A. Kawasuso. “Development of spin-polarized slow positron beam using a ^{68}Ge–^{68}Ga positron source”. In: *Nuclear Instruments and Methods in Physics Research B* 308 (2013), p. 9.

[116] C. Ilie. “Gamma-ray polarimetry: A new window for the nonthermal universe”. In: *Publications of the Astronomical Society of the Pacific* 131 (2019), p. 111001.

[117] O. Klein and T. Nishina. “Über die Streuung von Strahlung durch freie Elektronen nach der neuen relativistischen Quantendynamik von Dirac”. In: *Zeitschrift für Physik* 52 (1929), p. 853.

[118] F. Lei, A. J. Dean, and G. L. Hills. “Compton polarimetry in gamma-ray astronomy”. In: *Space Science Reviews* 82 (1997), p. 309.

[119] E. Yoshida, H. Tashima, K. Nagatsu, A. B. Tsuji, K. Kamada, et al. “Whole gamma imaging: A new concept of PET combined with Compton imaging”. In: *Physics in Medicine and Biology* 65 (2020), p. 125013.

[120] F. Metzger and M. Deutsch. “A study of the polarization-direction correlation of successive gamma-ray quanta”. In: *Physical Review* 78 (1950), p. 551.

[121] S. Osuch, M. Popkiewicz, Z. Szeflinski, and Z. Wllhelmi. “Experimental test of bell’s inequality using annihilation photons”. In: *Acta Physica Polonica B* 27 (1996), p. 55.

[122] D. Abdurashitov, A. Baranov, D. Borisenko, F. Guber, A. Ivashkin, et al. “Setup of Compton polarimeters for measuring entangled annihilation photons”. In: *Journal of Instrumentation* 17 (2022), P03010.

[123] D. P. Watts, J. Bordes, J. R. Brown, A. Cherlin, R. Newton, et al. “Photon quantum entanglement in the MeV regime and its application in PET imaging”. In: *Nature Communications* 12 (2021), p. 2646.

[124] Y. Kojima, K. Imai, S. Ohno, R. Chaya, K. Yamamoto, and M. Shibata. "Optimum detector arrangement of a Compton polarimeter using a clover detector for β -delayed γ rays". In: *Nuclear Instruments and Methods in Physics Research A* 990 (2021), p. 164984.

[125] O. Halpern. "Detection of Circularly Polarized Gamma-Rays and the Production of Polarized Electrons". In: *Nature* 168 (1951), p. 782.

[126] F. P. Clay and F. L. Hereford. "The scattering of 0.5 MeV circularly polarized photons in magnetized iron". In: *Physical Review* 85 (1952), pp. 675–676.

[127] H. Schopper. "Circular polarization of γ-rays: Further proof for parity failure in β decay". In: *Philosophical Magazine* 2 (1957), p. 710.

[128] H. Schopper. "Measurement of Circular Polarization of γ-rays". In: *Nuclear Instruments* 3 (1958), p. 158.

[129] M. Deutsch, B. Gittelman, R. W. Bauer, L. Grodzins, and A. W. Sunyar. "Polarized Positrons from ^{66}Ga and ^{66}Cl". In: *Physical Review* 107 (1957), p. 1733.

[130] A. Einstein, B. Podolsky, and N. Rosen. "Can quantum-mechanical description of physical reality be considered correct?" In: *Physical Review* 47 (1935), p. 777.

[131] D. J. Griffiths. *Introduction to Quantum Mechanics.* Second Edi. Pearson Education, Inc., 2005.

[132] D. Bohm. *Quantum Theory.* New York: Prentic-Hall, Inc., 1951.

[133] O. Gühne and G. Tóth. "Entanglement detection". In: *Physics Reports* 474 (2009), p. 1.

[134] K. Edamatsu. "Entangled photons: Generation, observation, and characterization". In: *Japanese Journal of Applied Physics, Part 1: Regular Papers and Short Notes and Review Papers* 46 (2007), p. 7175.

[135] S. Aaronson. *Lecture 11, Tues Feb 21: Quantifying Entanglement, Mixed State Entanglement.* 2016. URL: `https://www.scottaaronson.com/qclec/11.pdf`.

[136] J. S. Bell. "On the Einstein Podolsky Rosen Paradox". In: *Physics* 1 (1964), p. 195.

[137] J. F. Clauser, M. A. Horne, A. Shimony, and R. A. Holt. "Proposed experiment to test local hidden-variable theories". In: *Physical Review Letters* 23 (1969), p. 880.

[138] A. Aspect, J. Dalibard, and G. Roger. "Experimental Test of Bell's Inequalities Using Time-Varying Analyzers". In: *Physical Review Letters* 49 (1982), p. 1804.

[139] A. Aspect, P. Grangier, and G. Roger. "Experimental Tests of Realistic Local Theories via Bell's Theorem". In: *Physical Review Letters* 47 (1981), p. 460.

[140] A. Aspect, P. Grangier, and G. Roger. "Experimental Realization of Einstein-Podolsky-Rosen-Bohm Gedankenexperiment: A New Violation of Bell's Inequalities". In: *Physical Review Letters* 49 (1982), p. 91.

[141] R. P. Feynman, R. B. Leighton, and M. Sands. *The Feynman Lectures On Physics - Volume III: Quantum Mechanics.* New Millen. New York: Basic Books, 1965.

[142] R. M. Drisko. "Spin and Polarization Effects in the Annihilation of Triplet Positronium". In: *Physical Review* 102 (1956), p. 1542.

[143] S. DeBenedetti and R. T. Siegel. “The three-photon annihilation of positrons and electrons”. In: *Physical Review* 94 (1954), p. 955.

[144] A. Acín, J. I. Latorre, and P. Pascual. “Three-party entanglement from positronium”. In: *Physical Review A* 63 (2001), p. 042107.

[145] F. M. Abel, G. S. Adkins, and T. J. Yoder. “Polarization effects in the decay of orthopositronium to three photons”. In: *Physical Review A* 83 (2011), p. 062502.

[146] A. Ivashkin, D. Abdurashitov, A. Baranov, F. Guber, S. Morozov, et al. “Testing entanglement of annihilation photons”. In: *Scientific Reports* 13 (2023), p. 7559.

[147] P. A. M. Dirac. “On the Annihilation of Electrons and Protons”. In: *Mathematical Proceedings of the Cambridge Philosophical Society* 26 (1930), p. 361.

[148] J. C. Ward. “Some properties of the Elementary Particles”. PhD thesis. Oxford University, 1949.

[149] F. J. Duarte. “The origin of quantum entanglement experiments based on polarization measurements”. In: *European Physical Journal H* 37 (2012), p. 311.

[150] A. Wightman. “Note on Polarization Effects in Compton Scattering”. In: *Physical Review* 74 (1948), p. 1813.

[151] F. L. Hereford. “The angular correlation of photo-electrons ejected by annihilation quanta”. In: *Physical Review* 81 (1951), p. 482.

[152] B. L. Robinson and L. Madansky. “Polarization correlations of the gamma-rays of ^{143}Cs and of annihilation radiation”. In: *Physical Review* 88 (1952), p. 1065.

[153] F. L. Hereford and J. P. Keuper. “The azimuthal distribution of photoelectrons produced by 0.5 MeV polarized photons”. In: *Physical Review* 90 (1953), p. 1043.

[154] G. Bertolini, M. Bettoni, and E. Lazzarini. “Angular correlation of scattered annihilation radiation”. In: *Il Nuovo Cimento* 2 (1955), p. 661.

[155] H. Langhoff. “Die Linearpolarisation der Vernichtungsstrahlung von Positronen”. In: *Zeitschrift für Physik* 160 (1960), p. 186.

[156] L. A. Page. “Polarization effects in the two-quantum annihilation of positrons”. In: *Physical Review* 106 (1957), p. 394.

[157] G. Faraci, D. Gutkowski, S. Notarrigo, and A. R. Pennisi. “An experimental test of the EPR paradox”. In: *Lettere Al Nuovo Cimento* 9 (1974), pp. 607–611.

[158] L. R. Kasday, J. D. Ullman, and C. S. Wu. “Angular correlation of Compton-scattered annihilation photons and hidden variables”. In: *Il Nuovo Cimento B* 25 (1975), p. 633.

[159] A. R. Wilson, J. Lowe, and D. K. Butt. “Measurement of the relative planes of polarization of annihilation quanta as a function of separation distance”. In: *Journal of Physics G* 2 (1976), p. 613.

[160] D. J. Bohm and B. J. Hiley. “Nonlocality and polarization correlations of annihilation quanta”. In: *Il Nuovo Cimento B* 35 (1976), p. 137.

[161] M. Bruno, M. D’Agostino, and C. Maroni. “Measurement of linear polarization of positron annihilation photons”. In: *Il Nuovo Cimento B* 40 (1977), p. 143.

[162] G. Bertolini, E. Diana, and A. Scotti. “Correlation of annihilation γ-ray polarization”. In: *Il Nuovo Cimento B* 63 (1981), p. 651.

[163] J. F. Clauser and A. Shimony. “Bell’s theorem. Experimental tests and implications”. In: *Reports on Progress in Physics* 41 (1978), p. 1881.

[164] P. Knights, F. Ryburn, G. Tungate, and K. Nikolopoulos. “Studying the effect of polarisation in Compton scattering in the undergraduate laboratory”. In: *European Journal of Physics* 39 (2018), p. 025203.

[165] P. Knights, F. Ryburn, G. Tungate, and K. Nikolopoulos. “An undergraduate laboratory study of the polarization of annihilation photons using Compton scattering”. In: *European Journal of Physics* 39 (2018), p. 045202.

[166] J. Hetfleiš, J. Lněnička, and J. Šlégr. “Entangled γ-photons - Classical laboratory exercise with modern detectors”. In: *European Journal of Physics* 39 (2018), p. 025403.

[167] J. Engbrecht and N. Hillson. “A flexible positron spectrometer for the undergraduate laboratory”. In: *American Journal of Physics* 86 (2018), p. 549.

[168] A. L. McNamara, K. Wu, D. Boardman, M. I. Reinhard, and Z. Kuncic. “Positron emission tomography coincidence detection with photon polarization correlation”. In: *Medical Imaging 2013: Physics of Medical Imaging.* Ed. by Christoph Hoeschen Robert M. Nishikawa Bruce R. Whiting. Vol. 8668. SPIE, 2013, 86681U.

[169] A. L. McNamara, M. Toghyani, J. E. Gillam, K. Wu, and Z. Kuncic. “Towards optimal imaging with PET: An in silico feasibility study”. In: *Physics in Medicine and Biology* 59 (2014), p. 7587.

[170] M. Toghyani, J. E. Gillam, A. L. McNamara, and Z. Kuncic. “Polarisation-based coincidence event discrimination: An in silico study towards a feasible scheme for Compton-PET”. In: *Physics in Medicine and Biology* 61 (2016), p. 5803.

[171] B. C. Hiesmayr and P. Moskal. “Witnessing Entanglement In Compton Scattering Processes Via Mutually Unbiased Bases”. In: *Scientific Reports* 9 (2019), p. 8166.

[172] P. Caradonna, D. Reutens, T. Takahashi, S. Takeda, and V. Vegh. “Probing entanglement in Compton interactions”. In: *journal of Physics Communications* 3 (2019), p. 105005.

[173] U. Fano. “Remarks on the Classical and Quantum-Mechanical Treatment of Partial Polarization”. In: *Journal of the Optical Society of America* 39 (1949), p. 859.

[174] W. H. McMaster. “Matrix Representation of Polarization”. In: *Reviews of Modern Physics* 33 (1961), p. 8.

[175] S. Agostinelli, J. Allison, K. Amako, J. Apostolakis, H. Araujo, et al. “GEANT4 - A simulation toolkit”. In: *Nuclear Instruments and Methods in Physics Research A* 506 (2003), p. 250.

[176] J. Allison, K. Amako, J. Apostolakis, P. Arce, M. Asai, et al. “Recent developments in GEANT4”. In: *Nuclear Instruments and Methods in Physics Research A* 835 (2016), p. 186.

[177] S. Sharma, D. Kumar, and P. Moskal. “Decoherence puzzle in measurements of photons originating from electron-positron annihilation”. In: *Acta Physica Polonica A* 142 (2022), p. 428.

[178] S. Parashari, D. Bosnar, I. Friščić, Z. Kuncic, and M. Makek. "Closing the Door on the Puzzle of Decoherence of Annihilation Quanta". In: *arXiv* (2023). URL: `http://arxiv.org/abs/2304.11362`.

[179] P. Moskal, N. Krawczyk, B. C. Hiesmayr, M. Bała, C. Curceanu, et al. (J-PET collaboration). "Feasibility studies of the polarization of photons beyond the optical wavelength regime with the J-PET detector". In: *European Physical Journal C* 78 (2018), p. 970.

[180] N. Krawczyk, B. C. Hiesmayr, J. Chhokar, C. Curceanu, E. Czerwiński, et al. (J-PET collaboration). "Simulation studies of annihilation-photon's polarisation via Compton scattering with the J-PET tomograph". In: *Hyperfine Interactions* 240 (2019), p. 80.

[181] S. Parashari, D. Bosnar, A. Kožuljević, and M. Makek. "Measurement of angular correlations of Compton-scattered gamma quanta from positron annihilation using GAGG:Ce scintillator matrices with single-side readout". In: *Journal of Instrumentation* 17 (2022), p. C09007.

[182] L. Leipuner, R. Siegel, and S. DeBenedetti. "Polarization of the Three-Photon Annihilation Radiation". In: *Physical Review* 91 (1953), p. 198.

[183] G. Faraci and A. R. Pennisi. "Polarization of the annihilation photons of triplet positronium". In: *Il Nuovo Cimento B* 31 (1976), p. 289.

[184] G. Faraci and A. R. Pennisi. "Polarization correlation of a photon pair". In: *Physics Letters A* 66 (1978), p. 15.

[185] G. Faraci and A. R. Pennisi. "Polarization of triplet Ps photons in asymmetrical decay". In: *Il Nuovo Cimento B* 55 (1980), pp. 257–263.

[186] Q. Jia, X. Tang, B. Yang, Y. Li, and J. Ye. "A measurement of the linear polarization of photons emitted from three photon annihilation of positrons and electrons". In: *Chinese Physics C* 11 (1987), p. 293.

[187] Z. Kuncic, A. McNamara, K. Wu, and D. Boardman. "Polarization enhanced x-ray imaging for biomedicine". In: *Nuclear Instruments and Methods in Physics Research A* 648 (2011), S208.

[188] M. Makek, D. Bosnar, and L. Pavelić. "Scintillator Pixel Detectors for Measurement of Compton Scattering". In: *Condensed Matter* 4 (2019), p. 24.

[189] M. Makek, D. Bosnar, A. M. Kožuljević, and L. Pavelić. "Article investigation of GaGG:Ce with TOFPET2 ASIC readout for applications in gamma imaging systems". In: *Crystals* 10 (2020), p. 1073.

[190] M. Makek, D. Bosnar, L. Pavelić, P. Šenjug, and P. Žugec. "Single-layer Compton detectors for measurement of polarization correlations of annihilation quanta". In: *Nuclear Instruments and Methods in Physics Research A* 958 (2020), p. 162835.

[191] A. M. Kožuljević, D. Bosnar, Z. Kuncic, M. Makek, S. Parashari, and P. Žugec. "Study of multi-pixel scintillator detector configurations for measuring polarized gamma radiation". In: *Condensed Matter* 6 (2021), p. 43.

[192] S. Parashari, M. Makek, T. Bokulić, D. Bosnar, A. M. Kožuljević, et al. “Optimization of detector modules for measuring gamma-ray polarization in Positron Emission Tomography”. In: *Nuclear Instruments and Methods in Physics Research A* 1040 (2022), p. 167186.

[193] P. Moskal, D. Kisielewska, R. Y. Shopa, Z. Bura, J. Chhokar, et al. (J-PET collaboration). “Performance assessment of the 2γ positronium imaging with the total-body PET scanners”. In: *EJNMMI Physics* 7 (2020), p. 44.

[194] P. Moskal, D. Kisielewska, C. Curceanu, E. Czerwiński, K. Dulski, et al. (J-PET collaboration). “Feasibility study of the positronium imaging with the J-PET tomograph”. In: *Physics in Medicine and Biology* 64 (2019), p. 055017.

[195] J. Raj, K. Dulski, and E. Czerwiński. “Towards time reversal symmetry test with o-Ps decays using the J-PET detector”. In: *Acta Physica Polonica B* 51 (2020), p. 149.

[196] K. Dulski, S. D. Bass, J. Chhokar, N. Chug, C. Curceanu, et al. (J-PET collaboration). “The J-PET detector—a tool for precision studies of ortho-positronium decays”. In: *Nuclear Instruments and Methods in Physics Research A* 1008 (2021), p. 165452.

[197] D. Schödlbauer, P. Sperr, G. Kögel, and W. Triftshäuser. “A pulsing system for low energy positrons”. In: *Nuclear Instruments and Methods in Physics Research B* 34 (1988), p. 258.

[198] P. Willutzki, J. Störmer, G. Kögel, P. Sperr, D. T. Britton, et al. “An improved pulsed low-energy positron system”. In: *Measurement Science and Technology* 5 (1994), p. 548.

[199] D. B. Cassidy, S. H. M. Deng, R. G. Greaves, and A. P. Mills. “Accumulator for the production of intense positron pulses”. In: *Review of Scientific Instruments* 77 (2006), p. 073106.

[200] C. Hugenschmidt, C. Piochacz, M. Reiner, and K. Schreckenbach. “The NEPOMUC upgrade and advanced positron beam experiments”. In: *New Journal of Physics* 14 (2012), p. 055027.

[201] P. Coleman. *Positron Beams and Their Applications.* WORLD SCIENTIFIC, Jan. 2000.

[202] T. Akahane, T. Chiba, N. Shiotani, S. Tanigawa, T. Mikado, et al. “Stretching of slow positron pulses generated with an electron linac”. In: *Applied Physics A* 51 (1990), pp. 146–150.

[203] J. Paridaens, D. Segers, M. Dorikens, and L. Dorikens-Vanpraet. “Slow positron beam at the 90 MeV linac of Ghent University”. In: *Nuclear Instruments and Methods in Physics Research A* 287 (1990), p. 359.

[204] T. Kurihara, A. Yagishita, A. Enomoto, H. Kobayashi, T. Shidara, et al. “Intense positron beam at KEK”. In: *Nuclear Instruments and Methods in Physics Research B* 171 (2000), p. 164.

[205] P. Guoxi. “Progress of the BEPCII linac upgrade”. In: *Proceedings of the 2005 Particle Accelerator Conference.* IEEE, 2005, p. 2416.

[206] A. Wagner, M. Butterling, M. O. Liedke, K. Potzger, and R. Krause-Rehberg. "Positron annihilation lifetime and Doppler broadening spectroscopy at the ELBE facility". In: *AIP Conference Proceedings* 1970 (2018), p. 040003.

[207] J. Moxom, A. G. Hathaway, E. W. Bodnaruk, A. I. Hawari, and J. Xu. "Performance analysis of the intense slow-positron beam at the NC State University PULSTAR reactor". In: *Nuclear Instruments and Methods in Physics Research A* 579 (2007), p. 534.

[208] H. Schut, A. Van Veen, J. De Roode, and F. Labohm. "Long term performance of the reactor based positron beam POSH". In: *Materials Science Forum* 445-446 (2004), p. 507.

[209] *Decay data search.* URL: `http://nucleardata.nuclear.lu.se/database/nudat/`.

[210] T. D. Lee and C. N. Yang. "Question of Parity Conservation in Weak Interactions". In: *Physical Review* 104 (1956), p. 254.

[211] C. S. Wu, E. Ambler, R. W. Hayward, D. D. Hoppes, and R. P. Hudson. "Experimental Test of Parity Conservation in Beta Decay". In: *Physical Review* 105 (1957), p. 1413.

[212] S. S. Hanna and R. S. Preston. "Positron Polarization Demonstrated by Annihilation in Magnetized Iron". In: *Physical Review* 106 (1957), p. 1363.

[213] J. D. Jackson, S. B. Treiman, and H. W. Wyld. "Possible Tests of Time Reversal Invariance in Beta Decay". In: *Physical Review* 106 (1957), p. 517.

[214] M. Maekawa, K. Wada, and A. Kawasuso. "Development a new positron source for spin-polarized positron beam generation". In: *Nuclear Instruments and Methods in Physics Research B* 480 (2020), p. 49.

[215] H. Olsen and L. C. Maximon. "Photon and Electron Polarization in High-Energy Bremsstrahlung and Pair Production with Screening". In: *Physical Review* 114 (1959), p. 887.

[216] G. Alexander, J. Barley, Y. Batygin, S. Berridge, V. Bharadwaj, et al. "Undulator-based production of polarized positrons". In: *Nuclear Instruments and Methods in Physics Research A* 610 (2009), p. 451.

[217] A. P. Mills. "Experimentation with low-energy positron beams". In: *Positron Solid State Physics, Proceedings of the International School of Physics, Enrico Fermi, Course LXXXIII.* Ed. by W. Brandt and A. Dupasquier. Amsterdam, North-Holland: SIF- Società Italiana di Fisica, 1981, p. 432.

[218] D. E. Groce, D. G. Costello, J. W. McGowan, and D. F. Herring. "Time-of-flight observation of low-energy positrons". In: *Bulletin of The American Physical Society* 13 (1968), p. 1397.

[219] K. F. Canter, P. G. Coleman, T. C. Griffith, and G. R. Heyland. "Measurement of total cross sections for low energy positron-helium collisions". In: *Journal of Physics B* 5 (1972), p. L167.

[220] A. Zecca. "Positron beam development and design". In: *Applied Surface Science* 194 (2002), p. 4.

[221] A. Zecca, L. Chiari, A. Sarkar, S. Chattopadhyay, and M. J. Brunger. “Procedures for conditioning W- and Ni-moderators for application in positron-scattering measurements”. In: *Nuclear Instruments and Methods in Physics Research B* 268 (2010), p. 533.

[222] R. Khatri, M. Charlton, P. Sferlazzo, K. G. Lynn, A. P. Mills, and L. O. Roellig. “Improvement of rare-gas solid moderators by using conical geometry”. In: *Applied Physics Letters* 57 (1990), p. 2374.

[223] G. R. Massoumi, N. Hozhabri, W. N. Lennard, P. J. Schultz, S. F. Baert, et al. “Rare gas moderated electrostatic positron beam”. In: *Review of Scientific Instruments* 62 (1991), p. 1460.

[224] E. M. Gullikson and A. P. Mills Jr. “Positron Dynamics in Rare-Gas Solids”. In: *Physical Review Letters* 57 (1986), p. 376.

[225] A. Zecca, M. Bettonte, J. Paridaens, G. P. Karwasz, and R. S. Brusa. “A new electrostatic positron beam for surface studies”. In: *Measurement Science and Technology* 9 (1998), p. 409.

[226] M. Maekawa, Y. Fukaya, H. Zhang, H. Li, and A. Kawasuso. “Spin polarizations of positron beams generated using electrostatic and magnetic transportation systems with ^{68}Ge and ^{22}Na sources”. In: *Journal of Physics: Conference Series*. Vol. 505. IOP Publishing. 2014, p. 12033.

[227] S. Humphries Jr. *Principles of charged particle acceleration*. Mineola, New York: Dower Publications, Inc., 2012.

[228] H. Liebl. *Applied Charged Particle Optics*. Berlin Heidelberg: Spinger-Varlag, 2007.

[229] S. Aghion, C. Amsler, M. Antonello, A. Belov, G. Bonomi, et al. (AE$\bar{g}$IS collaboration). “Producing long-lived 2^3S positronium via 3^3P laser excitation in magnetic and electric fields”. In: *Physical Review A* 98 (2018), p. 013402.

[230] R. G. Greaves and C. M. Surko. “Positron trapping and the creation of high-quality trap-based positron beams”. In: *Nuclear Instruments and Methods in Physics Research B* 192 (2002), p. 90.

[231] A. P. Mills. “Time bunching of slow positrons for annihilation lifetime and pulsed laser photon absorption experiments”. In: *Applied Physics* 22 (1980), p. 273.

[232] J. P. Sullivan, J. Roberts, R. W. Weed, M. R. Went, D. S. Newman, and S. J. Buckman. “A trap-based positron beamline for the study of materials”. In: *Measurement Science and Technology* 21 (2010), p. 085702.

[233] R. G. Greaves, S. J. Gilbert, and C. M. Surko. “Trap-based positron beams”. In: *Applied Surface Science* 194 (2002), p. 56.

[234] J. Clarke, D. P. Van Der Werf, B. Griffiths, D. C. S. Beddows, M. Charlton, et al. “Design and operation of a two-stage positron accumulator”. In: *Review of Scientific Instruments* 77 (2006), p. 063302.

[235] R. G. Greaves and J. M. Moxom. “Compression of trapped positrons in a single particle regime by a rotating electric field”. In: *Physics of Plasmas* 15 (2008), p. 072304.

[236] R. G. Greaves and C. M. Surko. "Inward transport and compression of a positron plasma by a rotating electric field". In: *Physical Review Letters* 85 (2000), p. 1883.

[237] R. G. Greaves and C. M. Surko. "Radial compression and inward transport of positron plasmas using a rotating electric field". In: *Physics of Plasmas* 8 (2001), p. 1879.

[238] F. J. Mulligan and M. S. Lubell. "A hybrid beam design for slow positron transport". In: *Measurement Science and Technology* 4 (1993), p. 197.

[239] N. Oshima, R. Suzuki, T. Ohdaira, A. Kinomura, T. Narumi, et al. "Brightness enhancement method for a high-intensity positron beam produced by an electron accelerator". In: *Journal of Applied Physics* 103 (2008), p. 094916.

[240] M. Stadlbauer, C. Hugenschmidt, and K. Schreckenbach. "New design of the CDB-spectrometer at NEPOMUC for T-dependent defect spectroscopy in Mg". In: *Applied Surface Science* 255 (2008), p. 136.

[241] D. Gerola, W. B. Waeber, M. Shi, and S. J. Wang. "Quasidivergency-free extraction of a slow positron beam from high magnetic fields". In: *Review of Scientific Instruments* 66 (1995), p. 3819.

[242] M. Shi, D. Gerola, W. B. Waeber, and U. Zimmermann. "Slow positron beam extraction from high magnetic fields". In: *Applied Surface Science* 85 (1995), p. 143.

[243] C. Piochacz and C. Hugenschmidt. "The experimental determination of the phase space distribution of a positron beam". In: *Journal of Physics: Conference Series* 262 (2011), p. 012049.

[244] W. Stoeffl, P. Asoka-Kumar, and R. Howell. "Positron microprobe at LLNL". In: *Applied Surface Science* 149 (1999), p. 1.

[245] S. Golge, B. Vlahovic, and B. Wojtsekhowski. "High-intensity positron microprobe at the Thomas Jefferson National Accelerator Facility". In: *Journal of Applied Physics* 115 (2014), p. 234907.

[246] S. Benson, B. Wojtsekhowski, B. Vlahovic, and S. Golge. "Opportunities and challenges of a low-energy positron source in the LERF". In: *AIP Conference Proceedings* 1970 (2018), p. 050004.

[247] R. E. Honig and H. O. Hook. "Vapor pressure data for some common Gasses". In: *RCA review* 21 (1960), p. 360.

[248] *NIST Chemistry WebBook, SRD 69*. URL: `https://webbook.nist.gov/chemistry/name-ser/`.

[249] B. S. Cooper, A. M. Alonso, A. Deller, T. E. Wall, and D. B. Cassidy. "A trap-based pulsed positron beam optimised for positronium laser spectroscopy". In: *Review of Scientific Instruments* 86 (2015).

[250] S. Ghosh, J. R. Danielson, and C. M. Surko. "Energy distribution and adiabatic guiding of a solid-neon-moderated positron beam". In: *Journal of Physics B* 53 (2020), p. 85701.

[251] S. L. Andersen, R. R. Johansen, J. B. Overgaard, J. K. Mortensen, K. K. Andersen, et al. "Positronium formation from porous silica in backscattering and transmission geometries". In: *The European Physical Journal D* 68 (2014), p. 124.

[252] S. L. Andersen, D. B. Cassidy, J. Chevallier, B. S. Cooper, A. Deller, et al. “Positronium emission and cooling in reflection and transmission from thin mesostructured silica films”. In: *Journal of Physics B* 48 (2015), p. 204003.

[253] R. Guider, C. Traversa, and P. Bettotti. “Mechanical stress relief in porous silicon free standing membranes”. In: *Optical Materials Express* 5 (2015), p. 2128.

[254] F. Guatieri, S. Mariazzi, and R. S. Brusa. “Monte Carlo simulation of the implantation profile of e^+ in nanochanneled silicon”. In: *European Physical Journal D* 72 (2018), p. 198.

[255] D. E. Aspnes and A. A. Studna. “Dielectric functions and optical parameters of Si, Ge, GaP, GaAs, GaSb, InP, InAs, and InSb from 1.5 to 6.0 eV”. In: *Physical Review B* 27 (1983), p. 985.

[256] P. Bettotti. “Porous Silicon”. In: *Springer handbook of nanomaterials.* Ed. by Robert Vajtai. Dordrecht, Heidelberg, London, New York: Springer Science & Business Media, 2013, p. 883.

[257] M. Pałka, P. Strzempek, G. Korcyl, T. Bednarski, Sz Niedźwiecki, et al. “Multichannel FPGA based MVT system for high precision time (20 ps RMS) and charge measurement”. In: *Journal of Instrumentation* 12 (2017), P08001.

[258] G. Korcyl, P. Bialas, C. Curceanu, E. Czerwinski, K. Dulski, et al. “Evaluation of Single-Chip, Real-Time Tomographic Data Processing on FPGA SoC Devices”. In: *IEEE Transactions on Medical Imaging* 37 (2018), p. 2526.

[259] S. Sharma, J. Chhokar, C. Curceanu, E. Czerwiński, M. Dadgar, et al. (J-PET collaboration). “Estimating relationship between the time over threshold and energy loss by photons in plastic scintillators used in the J-PET scanner”. In: *EJNMMI Physics* 7 (2020), p. 39.

[260] P. Moskal, N. Zoń, T. Bednarski, P. Białas, E. Czerwiński, et al. (J-PET collaboration). “A novel method for the line-of-response and time-of-flight reconstruction in TOF-PET detectors based on a library of synchronized model signals”. In: *Nuclear Instruments and Methods in Physics Research A* 775 (2015), p. 54.

[261] L. Raczyński, W. Wiślicki, W. Krzemień, P. Kowalski, D. Alfs, et al. (J-PET collaboration). “Calculation of the time resolution of the J-PET tomograph using kernel density estimation”. In: *Physics in Medicine and Biology* 62 (2017), p. 5076.

[262] N. Krawczyk. “Feasibility Studies of Measurements of Annihilation Photons Polarization with the J-PET Detector”. Master’s Thesis. Jagiellonian University, 2016.

Acknowledgements

I would like to thank prof. R. S. Brusa for his guidance in these years of work. I also thank prof. L. Pancheri for his support in the Trans-disciplinary Program in Quantum Science and Technologies (TPQST). Moreover, I am thankful to Dr. S. Mariazzi who closely followed and guided the research for this thesis.

I am also grateful for the support of Q@TN, the joint laboratory of the University of Trento, FBK-Fondazione Bruno Kessler, INFN National Institute of Nuclear Physics, and the CNR-National Research Council.

I wish to express my gratitude to the other members of the AML group: Luca, Marco, Sushil, and Ruggero. Without their help and support the work described in this thesis would have not been possible and the lunch breaks would have been boring.

Moreover, I have to thank my friends and fellows Damiano, Andrea, and Nicola for their support during the long university years. Without them, the ten years of exams and courses would have been a bare and repetitive landscape.

Finally, most importantly, I express my most sincere thanks to my family for the moral, economic, and emotional support during this long path that is life.